Mines buried in dry and saturated soils : blast experiments, soil modeling and simulations

Eve Roger

UNIVERSITÉ DE GRENOBLE

THÈSE

Pour obtenir le grade de

DOCTEUR DE L'UNIVERSITÉ DE GRENOBLE

Spécialité : **Matériaux, Mécanique, Génie Civil, Electrochimie**

Arrêté ministériel : 7 août 2006

Présentée par

Eve ROGER

Thèse dirigée par **Benjamin LORET**

préparée au sein **du Laboratoire Sols, Solides, Structures et Risques** et de **l'Ecole Doctorale Ingénierie, Matériaux, Mécanique, Energétique, Environnement, Procédés, Production**

Mines buried in dry and saturated soils:

Blast experiments, soil modeling and simulations

Thèse soutenue publiquement le **6 Juillet 2015**,
devant le jury composé de :

M. Jean-Paul CALVEL
Ingénieur à DGA Techniques terrestres, Bourges, Examinateur
M. Ian ELGY
Ingénieur au DSTL, Porton Down, Grande-Bretagne, Examinateur
M. Jean-Marie FLEUREAU
Professeur à l'Ecole Centrale de Paris, Président
M. David M. FOX
Ingénieur à l'ARL, Aberdeen, MD, Etats-Unis, Invité
M. Benjamin LORET
Professeur à l'Institut National Polytechnique de Grenoble, Directeur de thèse
M. Christian MARIOTTI
Ingénieur au CEA-DAM, Bruyères le Chatel, Rapporteur
M. Luc THOREL
Directeur de recherche à l'IFSTTAR, Nantes, Rapporteur

Remerciements

Ma thèse a été effectuée en partie au laboratoire Sols Solides Structures et Risques de Grenoble et à DGA Techniques terrestres, site de Bourges.

Je remercie ma hiérarchie et l'équipe de direction de DGA TT pour m'avoir permis de réaliser cette thèse, en m'accordant un aménagement de mon temps de travail et en me permettant des déplacements réguliers à Grenoble.

J'adresse mes sincères remerciements à mon directeur de thèse, M. Benjamin Loret, pour son aide et sa disponibilité.

Ma thèse présentait un volet expérimental. Les essais réalisés à DGA TT n'auraient pu être menés à bien sans la participation des équipes d'essais et je les en remercie.

Le moyen d'essais utilisé a été conçu et développé avec l'aide de Nexter Systems. Je remercie leur équipe et en particulier M. Benoit Bettencourt pour son implication tout au long de ma thèse.

Je remercie vivement M. Jean-Paul Calvel pour avoir suivi mon travail de thèse à DGA TT, pour ses conseils et son soutien indéfectible.

Je remercie l'ensemble des membres du jury, M. Luc Thorel de l'IFSTTAR de Nantes et M. Christian Mariotti du CEA DAM pour avoir accepté la charge de rapporteurs, M. Jean-Marie Fleureau de l'Ecole Centrale de Paris pour avoir présidé le jury de ma soutenance et M. Ian Elgy du DSTL pour être venu de Grande-Bretagne apporter son expertise dans le domaine des blasts et explosions enfouies.

Je termine cette page en adressant mes remerciements à toutes les personnes qui ont été à mes côtés pendant ces 3 années.

Contents

Nomenclature

α	Initial shear stress involved in the failure surface definition [Pa]
β	Parameter involved in the failure surface definition [Pa^{-1}]
η	Viscosity parameter [s^{-1}]
γ	Parameter involved in the failure surface definition [Pa]
λ	Consistency parameter [-]
ν	Poisson's ratio [-]
ϕ	Friction angle [°]
ρ	Density [$kg.m^{-3}$]
ε	Strain [-]
σ	Stress [Pa]
τ	Time constant [s]
θ	Parameter linked to the friction angle involved in the failure surface definition [-]
c	Sound speed [m/s]
C_c	Coefficient of curvature [-]
C_u	Uniformity coefficient [-]
D	Mean grain size [mm]
D_r	Relative density [-]
E	Young's modulus [Pa]
e	Void ratio [-]
f	Yield surface [Pa]
G	Shear modulus [Pa]

G_s	Specific gravity [-]
I	Impulse [N.s]
I_1	First invariant of stresses [Pa]
J_2	Second invariant of deviatoric stresses [Pa]
K	Bulk modulus [Pa]
k	Volumetric viscoplastic strain [-]
L	Value of I_1 delimiting the interface between the cap and the failure surfaces [Pa]
M	Mass [kg]
N	Perzyna exponent [-]
n	Porosity [-]
P	Pressure [Pa]
q	Deviatoric stress [Pa]
R	Eccentricity of the cap surface [-]
s	Hugoniot parameter [-]
S_r	Degree of saturation [%]
T	Tensile limit of the cutoff surface along the hydrostatic axis [Pa]
U	Shock velocity [m/s]
u	Velocity of the particles [m/s]
V	Volume [m^3]
w	Water content [%]
X	Limit of the cap surface along the hydrostatic axis, preconsolidation pressure [Pa]

Introduction

In recent conflicts (like in Middle East and in Africa) vehicles have been threatened by new devices. They are called IEDs for Improvised Explosive Devices. According to Global Security (globalsecurity.org), at variance with landmines, they can be any homemade devices designed with explosive and with any type of material and intiator. They aim at causing the maximum damage (injury as well as death). They are developed for a specific target and unique in the sense that they are produced with anything that can be found at hand. As a consequence, they are more difficult to detect and to defeat. IEDs can be conventional munitions adapted for a new purpose (bombs, anti-tank mines ...) located by the roadside or buried. They are detonated thanks to a sensor activated with a pressure or a contact, or by a trigger initiated by somebody watching the scene.

Among all IEDs, some can be buried. In this case, the detonation of the buried explosive impacts the belly of the vehicle, deforming it. Then the impulse generated by the explosion is transmitted to the entire vehicle which moves upward subjecting the crew to a severe acceleration. In order to understand the buried explosion phenomenon, the behavior of dynamic soil must be studied.

Since 2001, the topic of buried explosions in the context of vehicle protection has been the object of numerous experimental as well as numerical studies. Some research aimed at modeling buried mines (Wang et al. (2004), Fiserova (2006), Tong and Tuan (2007), Grujicic et al. (2009), An (2010)), with different focuses (deeply buried explosives, study of explosions in cohesive soil, development of an empirical law for various water contents, equations of state for non saturated soils ...). Empirical expressions have been developed to obtain the impulse and the velocity of plates subjected to buried explosions (Westine et al. (1985) numerically compared by Williams and Poon (2000)).

Research have also shown an interest in the craters resulting of buried attacks (Ambrosini et al. (2002, 2004)), and in the stresses the soil can undergo during a detonation (Wang and Lu (2004)).

Objectives of the research

Complementary to the experiments carried out at DGA Techniques Terrestres for the evaluation of vehicle protection, numerical tools are progressively developed. The aim is to manage to simulate the effects of buried detonations on the passengers of a vehicle.

This objective requires to model the detonation of explosives and the propagation of the shock wave in soil. The soil which is targeted is a granular medium composed of three phases: the skeleton (which consists of solid particles), water and air. Water is generally

considered as incompressible. The stresses the soil undergoes are first applied to the pore water before being progressively transferred to the grains. The comments above pertain to standard soil mechanics where strain rates are low. At variance, an explosion is a very fast phenomenon, so quick that only air can be compressed and expelled. Water is considered trapped in the soil.

After the propagation of the shock wave in the soil then in the air, the vehicle loading must be simulated. A mixture of blast, detonation products and soil projections reaches the vehicle. If the previous steps are reliable, the impulse transmitted to the vehicle, its deformation and the effects of the detonation on the crew members can be analyzed.

The correct modeling of the detonation of the buried charge and the vehicle loading is the most important part since it determines the quantity of energy transmitted to the vehicle.

The protection of military vehicles is evaluated with a document produced by NATO countries called STANAG for Standardisation Agreement. STANAG 4569 is about the Protection Levels for Occupants of Logistic and Light Armoured Vehicles. Several levels of threats are referenced up to 10 kg of TNT equivalent. A reference soil called STANAG soil is defined.

The aim of this PhD is to develop a numerical model for STANAG soil with various water contents to simulate buried explosions. The stresses the soil undergoes are very large (more than 10 GPa). The soil stiffening is taken into account to simulate its resistance to this large impact, as a relation between the mean stress and the density of the soil. A viscoplastic cap model previously developed by Tong and Tuan (2007) has been improved and incorporated as a user-defined subroutine in LS Dyna to simulate the behavior of soil.

In an effort to simulate the phenomena that take place during the explosions, two sets of experimental tests have been carried out to feed the data requested in computational simulations. First detonations of small quantities of explosive (100 g of C4) are performed. Pressures are measured at several heights above the soil. Then larger quantities of buried explosives (up to 8 kg of TNT) are detonated. The impulse transmitted to a test rig and the deformation of plates are studied.

The PhD thesis is organized as follows:

First, the physical properties of soils are overviewed. STANAG soil is defined and studied mechanically with granulometry and triaxial tests (chapter 1).

The viscoplasticity which can help the simulations to overcome the difficulties associated with plasticity, in particular in the case of dynamic phenomena like explosions, is overviewed in chapter 2. A viscoplastic model is proposed as a modification of the model developed by Tong and Tuan (2007). Various stress paths (compression, tension and shear) are tested to study the influence of the parameters.

After the detonation of the explosive, a shock wave propagates in the soil and in the air. Chapter 3 presents shock waves and dynamic constitutive relations for soils. The Chapman Jouguet condition is mentioned. Soil compaction due to explosions is reviewed. Since the increase of soil stresses is very large, we developed a soil stiffening

model presented in this chapter to improve the resistance of soil to detonation.

Split Hopkinson Pressure Bar (SHPB) and plate impact experiments are reviewed in chapter 4. They are two devices designed to study the material behavior at high strain rates. In order to avoid the interaction of explosive and soil temporarily, first simulations reproducing SHPB from literature are run with our viscoplastic model using LS Dyna. This software is a non linear explicit finite element commercial code which is also presented in this chapter. To study the propagation of waves, simulations of dynamic loading of a spherical cavity are carried out in an infinite and semi-infinite elastic medium. It is the opportunity to evaluate the influence of a free surface and the mesh borders on the propagation of shock waves.

Experiments with small quantity of explosives are first reviewed in chapter 5. Then our own tests of small charges buried at 3 various depths in dry and saturated STANAG soil are presented. Pressures are measured at various heights, and the shock wave is tracked by a high speed camera using the principle of shadowgraphy. Simulations are then run to reproduce our experiments. The parameters which have the strongest influence on pressures are determined.

Large scale experiments are reviewed in chapter 6. A test rig is used to measure both impulse and deformation of plates. The latter represents vehicle floors. In order to cross-check the JWL parameters of TNT, aerial detonations of 6 kg of TNT are first performed before being reproduced by simulations. Finally our second experimental campaign is presented. We study the influence of various parameters: the explosive mass, its depth of burial, the water content of the soil, the stand off distance of the plate and its thickness. Numerical simulations are then run and detailed in chapter 6 to determine the influence of the viscoplastic model parameters and soil properties on impulse.

Chapter 1

Overview of soil physical properties

Contents

A soil is a porous medium composed of 3 phases as illustrated in figure 1.1 : solid particles (mainly composed of quartz, micas and feldspars in the case of sands) and voids which can be filled with water and air. The soil is dry when the voids only consist of air; conversely, when the voids are only filled with water, the soil is saturated. Between these two extreme states, the soil is non saturated and the proportion of air and water in the voids can be defined by several quantities.

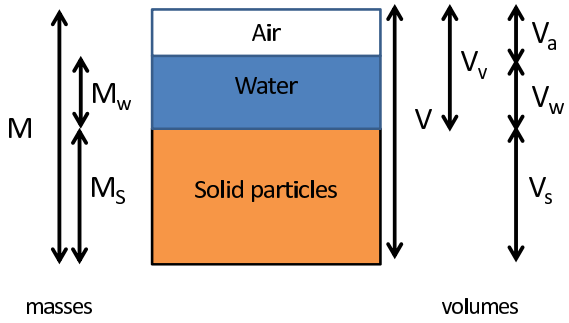

Figure 1.1: The soil is a 3 phase medium composed of solid particles, water and air.

This chapter aims at presenting first the soil physical properties (void ratio, degree of saturation, porosity...) and the relations between the volume, the mass and the density in a three phase soil.

The techniques to obtain the density, the water content and the grain size distribution are described briefly. These techniques derived from international standards are used in the experiments described in chapters 5 and 6. In order to illustrate the grain size distribution, an analysis is presented for STANAG soil, which is the soil used in chapters 5 and 6 in field experiments of buried mines and in the simulations.

One specific property of fine grained soils, the compaction curve (or Proctor curve) is presented. This defines a relation between the dry density and the water content of a soil. For sands, the water content has little influence on the dry density contrary to clays. Still for the STANAG soil, the water content required in the NATO documents for experiments is defined according to the optimum water content of the Proctor curve.

The triaxial test is a traditional quasi-static laboratory experiment developed to obtain stress-strain relationship of soil. This is first described and then used to characterize STANAG soil.

1.1 Definitions of soil physical properties

In this section, basis relations are first presented followed by the standard techniques to obtain the main physical parameters (grain size distribution, water content, void ratio...) which characterize soils.

1.1.1 Volume, mass and density relations in a three phase soil

Let us consider a three phase soil as illustrated in figure 1.1. First the total volume of the soil V is the sum of the volume of the solid grains V_s and of the voids V_v. The volume of voids can be split into a volume of water V_w and a volume of air V_a.

The **void ratio** e is the ratio of the volume of voids V_v to the volume of solid grains V_s:

$$e = \frac{V_v}{V_s} \tag{1.1.1}$$

In the case of sands and gravels, the minimum and the maximum void ratios encountered for a specific soil allow to define the degree of soil compaction with the relative density D_r

$$D_r = \frac{e_{max} - e}{e_{max} - e_{min}} \times 100 \tag{1.1.2}$$

This value varies from 0 to 100%. The soil is all the more compacted as D_r is large.

The **porosity** n is the ratio of the volume of voids to the total volume of a soil sample:

$$n = \frac{V_v}{V} \tag{1.1.3}$$

The **degree of saturation** S_r is the ratio of the volume of water to the volume of void:

$$S_r = \frac{V_w}{V_v} \tag{1.1.4}$$

$S_r = 0$ when the soil is dry and $S_r = 1$ when the soil is fully saturated.

The soil mass M is the sum of the mass of the solid particles M_s and the mass of the water M_w, since the mass of air is negligible.

The density of the soil ρ is the ratio of the total mass M over the volume V of the soil:

$$\rho = \frac{M}{V} \tag{1.1.5}$$

The **specific gravity** G_s is the ratio of the solid grain and water densities:

$$G_s = \frac{\rho_s}{\rho_w} \tag{1.1.6}$$

The **mass water content** w corresponds to the percentage of the water mass M_w over the mass of the solid particles M_s:

$$w = \frac{M_w}{M_s} \times 100\% \tag{1.1.7}$$

The dry density ρ_d is defined as the ratio of the mass of the solid particles M_s over the volume of the soil V:

$$\rho_d = \frac{M_s}{V} \tag{1.1.8}$$

The dry density can also be written

$$\rho_d = \rho_w \frac{G_s}{1+e} = \frac{\rho}{1+w} = \rho_w \frac{G_s}{1+G_s(w/S_r)} \tag{1.1.9}$$

with

$$S_r = \frac{G_s w}{e} \tag{1.1.10}$$

The saturated density is:

$$\rho_{sat} = \frac{M_s + V_v \rho_w}{V} \tag{1.1.11}$$

For a saturated soil,

$$\rho_{sat} = \rho_w \frac{G_s + e}{1+e} = \rho_w \frac{G_s(1+w)}{1+G_s w} \tag{1.1.12}$$

The density of a soil can thus be written as a combination of the physical parameters previously defined:

$$\rho = \rho_w \frac{G_s(1+w)}{1+e} = \rho_w \frac{G_s + S_r e}{1+e} = \rho_w \frac{G_s(1+w)}{1+G_s(w/S_r)} \tag{1.1.13}$$

Table 1.1 sums up the relations between masses, volumes and densities in a three phase soil with typical values.

Term	**Equation**	**Typical range in soil**
Soil density	$\rho = \frac{M}{V}$	1440 - 2250 kg/m^3
Dry density	$\rho_d = \frac{M_s}{V}$	1280 - 2100 kg/m^3
Water content	$w = \frac{M_w}{M_s} \times 100\,\%$	10 - 50 %
Specific gravity of soil solids	$G_s = \frac{M_s}{\rho_w V_s}$	2.65 - 2.80
Void ratio	$e = \frac{V_v}{V_s}$	0.3 - 1.5
Porosity	$n = \frac{V_v}{V} \times 100\,\%$	25 - 60 %
Degree of saturation	$S_r = \frac{V_w}{V_v} \times 100\,\%$	10 - 100 %

Table 1.1: Mass-volume relationships in soils, Kalinski (2011)

Now that the main relations for a three phase soil are established, let us focus on the techniques and the standards to measure the main parameters characterizing a sand: its grain size distribution, its mass water content, and its density in particular when field values are required. These three parameters will be measured before each field test reported in chapters 5 and 6. Moreover the laboratory soil compaction which provides the Proctor curve linking the dry density to the water content is also explained.

1.1.2 The grain size distribution of soil

A soil never contains one particle size only, but a range of sizes, with a quantity of each more or less important. The grain size distribution curve provides the percent (by mass) of the soil grains that are smaller than a grain size. It is obtained passing the soil into sieves with decreasing opening sizes.

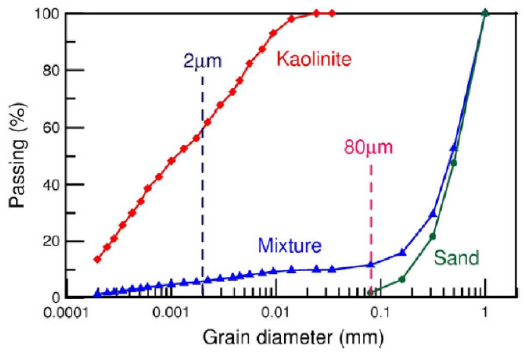

Figure 1.2: Particle size distribution of soil specimen used by Arlery et al. (2010) for plate impact experiments detailed in chapter 4.

An example of grain size distribution is displayed in figure 1.2. It corresponds to the particle size distribution of the soil specimen used by Arlery et al. (2010) for plate impact experiments detailed in chapter 4. This soil specimen is composed of 90% by mass of sand and 10% of kaolinite (clay).

On a grain size distribution curve, some special points can be highlighted:

- A point on the grain size distribution is called D_y which corresponds to the abscissa of the ordinate y: this means that for the average diameter of grains given in abscissa, there exists y% of the total mass of the grains which has a smaller diameter.
- D_{10} is called the efficient diameter : it corresponds to the grain diameter for which 10% of the total mass soil is finer.
- D_{50} is the median of the distribution law.
- The soil average diameter which is an average value of the grain diameters.

Moreover, sands and gravels can also be classified according to the uniformity of their grain sizes: thus, they can be considered as uniform, well-graded or poorly-graded.

A soil is uniform when most of the particles of the soil have almost the same size. The uniformity in soils is characterized by the uniformity coefficient C_u (or HAZEN coefficient):

$$C_u = \frac{D_{60}}{D_{10}} \tag{1.1.14}$$

where D_{10} is the grain size for which 10% of the total mass soil is finer and D_{60} is the grain size for which 60% of the total mass soil is finer. C_u represents the average slope of the grain size distribution curve between 10% and 60%. The coefficient C_u is close to 1 for a uniform soil; on the contrary, when the grain sizes are spread, its value is close to 0.

Soils (sands and gravels only) are considered well-graded when they have a wide range of particle sizes. The grain size distribution curve can be characterized by its curvature, and by its coefficient of curvature C_c:

$$C_c = \frac{(D_{30})^2}{D_{60} \times D_{10}} \tag{1.1.15}$$

where D_{30} is the grain size for which 30% of the total mass soil is finer.

Sands are considered to be well graded when

$$C_u > 6 \quad \text{and} \quad 1 < C_c < 3 \tag{1.1.16}$$

If these inequations are not satisfied, the soils are said to be poorly-graded.

Soils can be classified according to their grain sizes. Various standards such as ASTM (American Society for Testing and Materials), AASHTO (American Association of State Highway and Transportation Officials), USCS (Unified Soil Classification System), and BS (British Standard) provide a classification of soils according to grain sizes, from less than 0.002 mm up to more than 200 mm. The classification is slightly different, table 1.2.

Soil type	BS	USCS	AASHTO	ASTM
Clay	$D < 0.002$		$D < 0.005$	$D < 0.005$
Silt	$0.002 < D < 0.06$	$D < 0.075$	$0.005 < D < 0.075$	$0.005 < D < 0.075$
Sand	$0.06 < D < 2$	$0.075 < D < 4.75$	$0.075 < D < 2$	$0.075 < D < 4.75$
Gravel	$2 < D < 60$	$4.75 < D < 75$	$4.75 < D < 75$	$4.75 < D < 75$
Cobbles	$60 < D < 200$	$75 < D < 300$		$75 < D < 300$
Boulders	$D > 200$	$D > 300$	$D > 75$	$D > 300$

Table 1.2: Classification of the soils for various standards, adapted from Bardet (1997). The dimensions are in millimeters.

Clay and silt are categorized as fine grained soils, whereas sand and gravel are classified as coarse grained soil.

Bardet (1997) provides some typical values of void ratios, porosities, and densities depending on the nature of soil and its state (whether it is dry, saturated or in its natural state). These values are gathered in tables 1.3 and 1.4.

soil type	state of soil	porosity (%)	void ratio	dry density ($kg.m^{-3}$)	natural density ($kg.m^{-3}$)	saturated density ($kg.m^{-3}$)
sandy gravel	loose	38-42	0.61-0.72	1400-1700	1800-2000	1800-2100
	dense	18-25	0.22-0.33	1900-2100	2000-2300	2100-2300
coarse sand,	loose	40-45	0.67-0.82	1300-1500	1600-1900	1700-1900
medium sand	dense	25-32	0.33-0.47	1700-1800	1800-2100	2000-2100
uniform fine	loose	45-48	0.82-0.92	1400-1500	1500-1900	1900-2000
sand	dense	33-36	0.49-0.56	1700-1800	1800-2100	2100-2200

Table 1.3: Typical values of porosity, void ratio, density for various sands, from Bardet (1997).

description	e_{max}	e_{min}	$\rho_{d_{min}}$ ($kg.m^{-3}$)	$\rho_{d_{max}}$ ($kg.m^{-3}$)
standard Ottawa sand	0.80	0.50	1450	1730
clean uniform sand	1.0	0.40	1300	1850
uniform inorganic silt	1.1	0.40	1260	1850
silty sand	0.9	0.3	1370	2000
fine to coarse sand	0.95	0.2	1340	2170
micaceous sand	1.2	0.4	1190	1890
silty sand and gravel	0.85	0.14	1400	2290

Table 1.4: Typical values of maximum and minimum void ratios and dry densities for granular soils, from Bardet (1997).

Determination of particle size distribution:
The grain size analysis is usually performed with a dry soil which is passed through a stack of sieves mechanically shaken. Any number of sieves can be used, but a grain size distribution curve is considered to be obtained from six sieves. The coarsest sieve is placed at the top of the stack, and the size of sieves decreases progressively up to the finest sieve at the bottom of the stack. A pan is placed below the bottom sieve to collect the soil that passes the finest sieve. By weighing the fraction retained by each sieve, the grain distribution curve is obtained.

The procedure is described in more details in the following standards: ASTM D422-63 (Standard Test Method for Particle-Size Analysis of Soils), ASTM D1140 (Standard Test Method for Amount of Material in Soils Finer Than the No. 200 (75 μm) Sieve), BS 1377 (British Standards), AASHTO (American Association of State Highway and Transportation Officials), USCS (Unified Soil Classification System) and AFNOR (NF P 94-056 03/96 and NF P 94-057 05/92).

Hydrometer analysis:
For grains smaller than 75 μm, the sieving technique cannot be used because the clay particles form clods which cannot be evaluated with traditional sieves. Instead, the technique of sedimentation (with an analysis using hydrometer for example), whose basis is Stokes' law is applied. The grain size is calculated from the distance of sedimentation

of particle, since this technique sorts soil particles by size. The percent by mass finer is determined by measuring the density of the soil-fluid suspension.

STANAG soil granulometry

The soil which is the subject of the present study is defined in the NATO procedures AEP 55 (2014) by a granulometry, a density and a water content related to the optimum water content of the Proctor curve:

- 100% of the mass of the soil particles must pass the 40 mm sieve;
- between 60 and 40% must pass the 5 mm sieve;
- a maximum of 10% must pass the 80 μm sieve;
- a density of 2200 $\pm$ 100 kg.m^{-3} and a water content less than 1.5% of the optimum water content of the Proctor curve are required.

According to the material available at the laboratory, ten sieves (with hole sizes of 100, 160, 250, 400, 500, 800 μm, 1, 1.25, 2, and 5 mm) have been used to determine the particule size distribution of our STANAG soil. The standard imposes that the mass M (in kg) of the sample which is poured in the sieves depends on the maximum size D of the grains (in mm) such as $M \geq 0.2D$. Since the maximum size of the grains is 40 mm, it means that a mass of 8 kg of soil should be tested. Two separate tests were performed. The grain size distribution is shown in figure 1.3. The coefficient of curvature C_c is equal to 0.67 and the uniformity coefficient C_u is equal to 7.32 thanks to equations (1.1.15) and (1.1.14) respectively. Since the inequations (1.1.16) are not satisfied, this soil is poorly graded.

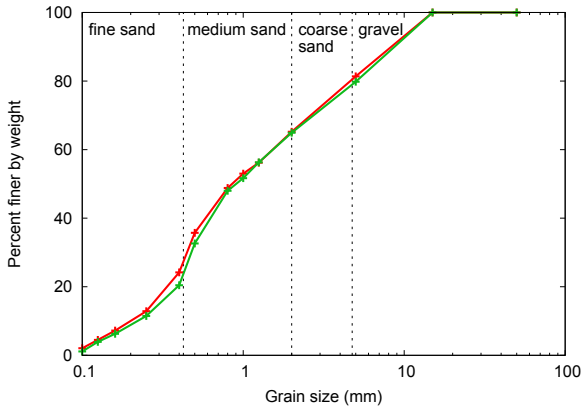

Figure 1.3: Particle size distribution of STANAG soil, obtained from ten sieves, with size holes from 100 μm up to 5 mm. The two curves correspond to a grain size analysis obtained from two separate tests.

1.1.3 Determination of mass water content

The experimental standard procedure to evaluate mass water content is described in ASTM D2216 (Standard Test Method for Laboratory Determination of Water (Moisture) Content of Soil and Rock by Mass).

The water content in mass w is defined as the ratio of the mass of water over to the mass of the solid particles (equation 1.1.7). The value is given as a percentage using two significant figures (for example 15% or 7.5%). The water content for sands and gravels is typically small (between a few percent for dry soils to over 20% in saturated soils) whereas it can reach 100% for highly plastic clays thanks to their ability of absorbing water.

To measure the water content, the oven-drying method is recommended by the standard, with a drying temperature between 105 to 110°C. 105°C corresponds to the temperature at which all the free water of clay has been evaporated. However, some water still remains in clay above 105°C.

To measure mass water content, a test soil sample representative of the soil is selected. The sample should be divided into 2 or 3 samples to average the result of water content. The sample is placed in a container covered by a lid. The mass of the container and the lid is known (M_{c+l}). The mass of the three of them (the container, the wet soil, and the lid) M_{ws} is then determined. The soil sample without its lid is put into an oven, to dry it at a temperature between 105-110°C. When the soil sample is considered to be dry, generally after 12 to 16 hours, the mass of the dried soil sample, the container and the lid M_d must be measured rapidly, not to leave the ambiant atmosphere modify the water content of the soil sample.

The water content is calculated as :

$$w = \frac{M_{ws} - M_d}{M_d - M_{c+l}} \times 100\,\% \tag{1.1.17}$$

1.1.4 Determination of the soil density in the field

Among all the possibilities to determine the soil density in the field, the three following methods are the most used :

- the sand cone method (ASTM D1556: Standard Test Method for Density and Unit Weight of Soil in Place by the Sand-Cone Method),
- the rubber balloon method (ASTM D2167: Standard Test Method for Density and Unit Weight of Soil in Place by Rubber Balloon Method),
- the nuclear density apparatus (ASTM D2922 : Standard Test Method for Density of Soil and Soil-Aggregate in Place by Nuclear Methods and ASTM D3017 : Standard Test Method for Water content of Soil and Rock in Place by Nuclear Methods).

These three methods are described below.

The principle of the **sand cone method** is the following: in the field where the soil density is required, a hole is dug and filled with a sand with a known density. The volume of the sand used to fill the hole is measured. The sample of soil which was extracted from the hole is weighed. Thus the density of the soil in the field is deduced from the mass of the field sample and the volume of the sand used to fill the hole.

First, the density of the sand ρ_{sand} which will be used to fill in the hole has to be determined. The sand must be a clean, dry, poorly graded sand with a coefficient of uniformity ($C_u = D_{60}/D_{10}$) less than 2.0, a maximum particle size (D_{100}) less than 2.0

mm, and less than 3% by mass passing the sieve of 250 μm. The sand should consist of rounded or subrounded particles rather than angular particles. The sand should be stored in an airtight container between tests so that it remains dry.

Once done, this sand is placed in a jar.

Then in the field, where the density is to be determined, a hole is dug with an opening size slightly larger than the base plate opening of the jar. The soil removed from the field is weighed and its water content is measured. The volume of the excavated hole must be smaller the full capacity of the sand cone jar. The full jar with the sand is then weighed. The cone jar is placed so that the valve opening fills the hole with sand. The partially empty jar is weigthed. The density of the soil is then deduced.

Among the other techniques to determine the density, the **balloon density apparatus** has almost the same principle as the sand cone method, except that the balloon fills the hole with water. The volume of the excavation corresponds to the volume of water injected. The quantity of water can be read directly on a graduated cylinder.

Contrary to the two previous methods, the **nuclear density method** is non destructive and allow to determine both density and water content of the soil. The nuclear density gauge is composed of different parts: the device itself which is shielded with two different emitter probes which are located in the soil to test, a detector and a counter on the device.

To determine the density of the soil, a radioactive isotope source (Cesium 137) is sent from the probe in the soil. Photons and more specifically gamma rays are emitted. They are scattered when colliding with soil particles. The larger the density of the soil, the spreader the gamma rays. The difference between the emission and the reception from the scatter is measured by a Geiger counter and related to soil density.

As for the water content, a radioactive source (Americium 241/Beryllium) is released from the probe. The fast neutrons are slowed down when colliding with hydrogen atoms. The number of slow neutrons can be directly linked to the number of hydrogen atoms close to the source, and thus to the water content of the soil since the hydrogen can be mostly found in water in a soil.

The main advantages of the nuclear density method are 1) the speed at which the results of density and water content are known since it takes only a few minutes, and 2) the non destructive aspect of the technique.

1.1.5 Laboratory soil compaction

The experimental standard procedure to evaluate the laboratory soil compaction is described in two standards: first in ASTM D698 (Standard Test Method for Laboratory Compaction Characteristics of Soil Using Standard Effort (12 400 ft-lb/ft^3 (600 kN-m/m^3))) and second in ASTM D1557 (Test Method for Laboratory Compaction Characteristics of Soil Using Standard Effort (56 000 ft-lb/ft^3 (2700 kN-m/m^3))).

The aim of the compaction test is to obtain a curve also known as a Proctor curve

relating the soil dry density to the water content. The test consists in dropping a given number of times a mass from a fixed height (305 mm for the standard test and 457 mm for the modified test) onto the soil. Typical curves are shown in figure 1.4.

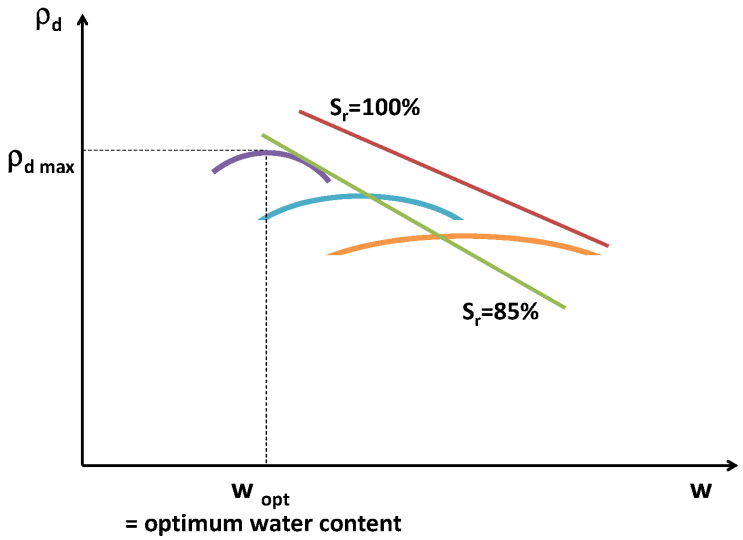

Figure 1.4: Sketch of compaction curves of Proctor tests linking dry density to water content. The orange curve corresponds to a sand with few fines which implies few variations of density with water content. On the contrary, the purple curve corresponds to a soil with fines. The red lines corresponds to the saturation, whereas the degree of saturation of the green line is 85%. The optimum water content of the Proctor curve is the point where the dry density is maximum. The more compressed a soil is, the more it is located on the top left of the figure. For example, the orange curve corresponds to a less compacted soil than the purple one.

The Proctor curve is composed of three parts : an increase of dry density with the water content (because the water fills the voids and soaks clays since fines can absorb water), a maximum (which is called optimum water content of the Proctor curve) and a decrease of dry density as the water content increases (because the volume of the soil increases and all the void of air has vanished). The position of the curve on the graphs depends on the number of blows (which should be equal to 25 in the standard) and on the energy delivered by the hammer which is a little increased for a modified Proctor. As a consequence for a modified Proctor, the curve is displaced to the top left of the graph. Increasing the number of blows also shifts the curve to the left and to the top (in this case, the optimum water content of the Proctor curve occurs for a smaller water content, and the optimum dry density is larger).

The slope of the curve (corresponding to the increase of the dry density as the water content increases) depends on the quantity of fines in the soil. If the soil does not contain any fine-grained soil (which means grains with a size smaller than 80 μm), the Proctor curve will be almost horizontal. For a sand with few fines, the slope is small. In this case, an increase or decrease of water content in the soil changes a little the dry density of the soil and the result is only slightly different from the optimum water content of the Proctor curve.

Standards recommend compaction tests for five different water contents to get the curve between water content and dry density. The water content should be low for the first test points and gradually increased for the other points. The first point should be about 4 to 5 % below the optimum water content whereas the fifth and last point should be 4 to 5 % above the optimum water content.

The soil specimen with a certain water content is placed in a mold so that it is about half full. Then the soil is compacted applying 25 blows of a hammer dropped from the controlled height of 305 mm. Two other layers of soil are added in the mold, and compacted with 25 blows. The entire specimen is extracted, weighed and the water content is measured. With the five compaction points, the dry density-water content curve is obtained.

1.2 Triaxial tests

The triaxial test is performed according to the standards NF P 94-070 and NF P 94-074. It is used to determine the soil characteristics under drained or undrained conditions. Water can be expelled from the sample during drained tests, whereas drainage systems is close for undrained tests, and the water remains in the sample during the whole test.

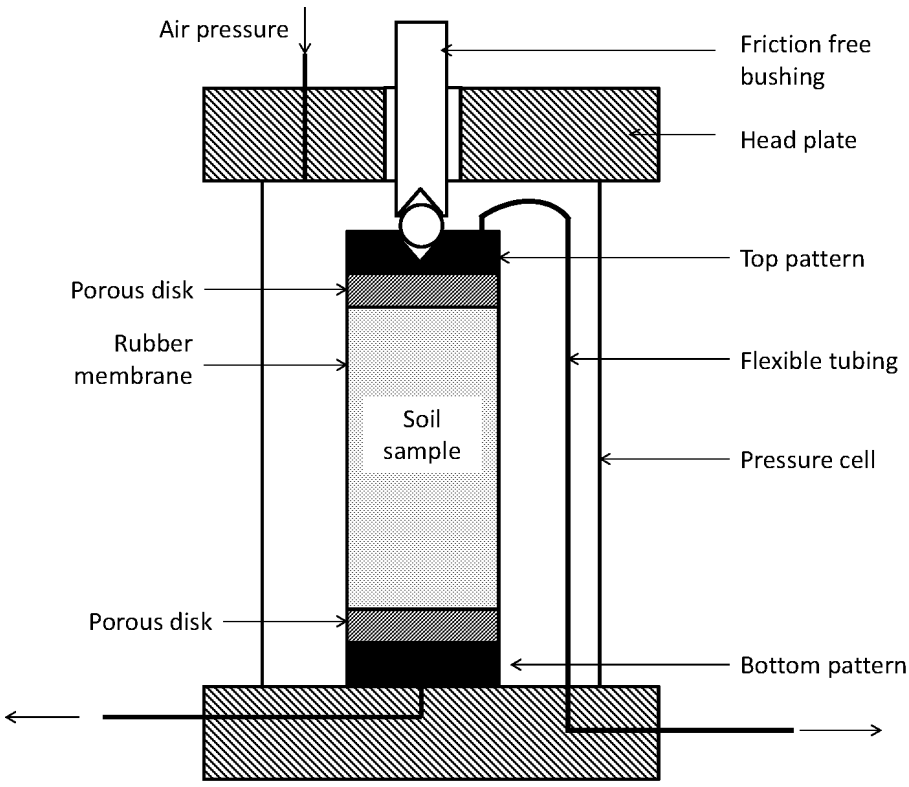

Figure 1.5: Triaxial apparatus, from Bardet (1997).

In a triaxial test, a cylindrical soil sample is placed in a thin membrane of latex between a top and a bottom porous disks which are linked to the drainage system (fig-

ure 1.5). A ratio of 2 between the height and the diameter of the sample is generally adopted. The size of the sample depends on the size of the grains which have to be tested. The cylindrical soil sample surrounded by its membrane and the drainage system are placed below an axial piston in a triaxial cell which is constituted by a cylindrical wall. A hydrostatic pressure of confinement is applied to the sample using a fluid located between the wall and the sample.

The triaxial tests can be unconsolidated or consolidated, drained or undrained. Two letters are used to describe the test: C or U for the consolidation phase (Consolidated or Unconsolidated), and D or U for drainage conditions during the shear phase (Drained or Undrained). Drained tests are always consolidated. So there are three main types of triaxial tests, which are labeled CD, UU, and CU.

The consolidated and drained test (CD) is composed of two stages: first the isotropic compression phase, then the shear phase.

During the first phase, an isotropic stress state is applied to the sample test ($\sigma_1 = \sigma_3$, with the axis 1 corresponding to the vertical axis of the cylindrical sample and the axis 3 corresponding to a perpendicular axis to the first one). The internal drainage remains open during the isotropic compression phase and the shear phase.

The shear phase consists in imposing an axial load to the sample thanks to the piston ($\sigma_1 > \sigma_3$). This stage can be drained or not. When it is drained, the drainage system which is connected to the porous disks is open. The water can be exit without any change in pore pressure. When this stage is undrained, the drainage system is closed and the pressure buids up.

The membrane, according to Abu Sayeed et al. (2011) is an important factor which adds extra shear stress on the specimen. Therefore to obtain accurate values of the friction angle ϕ, the effect of membrane force should be properly measured. Practically, it is very difficult to take it into account experimentally.

Figure 1.6 is a sketch of the typical relation between the stress deviator defined by $q = \sigma_1 - \sigma_3$ in relation to the axial strain ε_1 for triaxial tests for loose and dense soils. The deviatoric curves of a dense soil increases up to a maximal value (whereas the curve from a loose soil does not have any peak) before stabilizing at a residual value which is the same for dense and loose samples.

The density dependent response can also be observable on the curves of volumetric deformations. A dense soil has a contractance phase (where the volume of the sample decreases) much less important than a loose material, and a dilatance phase (during which the volume increases) much more important. During the shear test, a loose sample experiences a decrease of volume whereas a dense sample increases in volume, a phenomenon known as dilatancy.

The response of a dense sample can be explained as follows: First, the sample undergoes contraction, which corresponds to a volume decrease. Then some dilatation occurs: the volume of the sample increases. Finally the sample does not change volume anymore.

During the contraction and the dilatation steps, the stress increases. At larger axial strain, the soil tends to the critical state, which is characterized by a constant stress ratio (ratio of shear stress over mean stress) and constant volume.

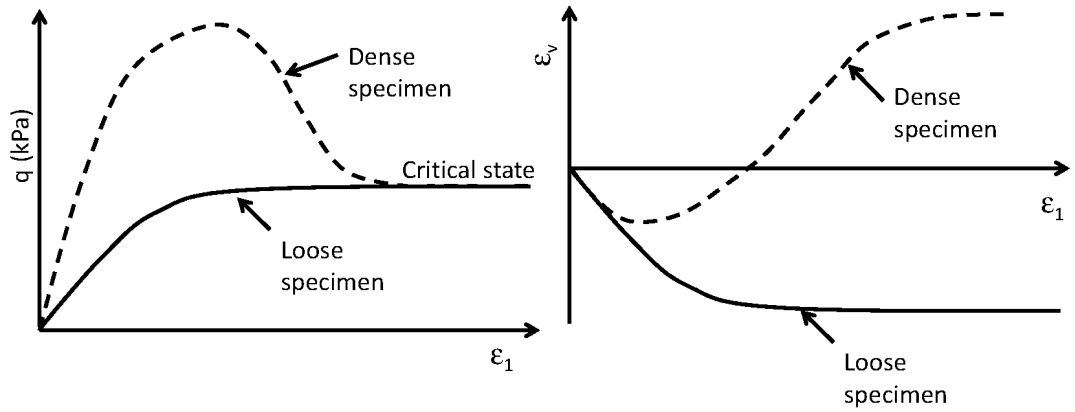

Figure 1.6: Sketch of curves from triaxial tests for a loose and a dense soils. Adapted from Salot (2007).

Triaxial tests with our STANAG soil

What follows corresponds to our triaxial tests carried out with our STANAG soil. The aim of these tests was to study our soil and to get its friction angle ϕ defined by

$$\sin \phi = \frac{\sigma_1 - \sigma_3}{\sigma_1 + \sigma_3} = \frac{q}{q + 2\,\sigma_3} \tag{1.2.1}$$

with σ_1 the axial stress in the direction of the piston, σ_3 the lateral stress, and $q = \sigma_1 - \sigma_3$ the deviatoric stress.

In a triaxial test, the size of the larger grains is limited by the size of the sample. Kim and Ha (2014) adviced to use a maximum particle diameter of coarse grained soil below 1/8 to 1/10 of the size of the test sample. In our case, the radius of the sample was 7 cm and the height was 15 cm, so the maximum admissible size for the grains was 1.4 cm ($7 \times 2/10$). However the grains were very sharp. So in order to avoid damaging the membrane during the shear stage of the test, the maximum size of the grains was reduced to 800 μm.In order to study the resistance to shear of the grains, we tested three sub-samples with uniform grain sizes D ($250 < D < 400\,\mu$m, $400 < D < 500\,\mu$m and $500 < D < 800\,\mu$m), and another sample with grain sizes smaller than 800 μm (with a grain size distribution representative to the STANAG soil).

At this point, it is worth reporting the two observations below that address the effects of the maximum particle size and the grain size distribution curve on the macroscopic properties of a granular soil:

1. Kim and Ha (2014) noticed that the maximum particle size of a sample has an influence on the friction angle and the shear behavior. The friction angle, the maximum shear stress and the shear strength increase with the maximum particle size.

2. For Lun (2011), well graded soils experience higher shear strength compared to

uniform graded soils, because in well graded soils, the finer particles fill the void between the coarse grains, providing more interlocking in the material.

Ideally, we had like to prepare soil specimen with the same density as the soil which is filling the tank used in our blast tests described in chapters 5 and 6. Given the size of the tank (about 1x1x1m^3), the soil for these field tests was compacted using a grooming machine. The soil sample here was thus compressed as much as possible. The density obtained for the cylindrical tests was around 1670 kg.m^{-3}.

During the triaxial tests, a vertical piston progressively moved at a speed of 1 mm per minute. The force applied to the sample, and the displacement of the piston were recorded. The test was stopped when there was no more volume change. The lateral confinement consisted in a pressure between 100 and 400 kPa.

The curves relating the deviatoric stress q and the axial strain ε_1 are reported in figure 1.7. The axial strain ε_1 is calculated from the recorded displacement of the piston over the initial height. As the strain is gradually increased, the deviatoric stress q and the shearing resistance increase until a peak stress is reached and failure starts. During the failure, the arrangement of the soil particles is disturbed and the packing is loosened.

The maximum shear stress is observed to increase with the confinement. In agreement with Abu Sayed et al (2011), we notice that the confining pressure change the shear strength of a soil: an increase of the confining pressure decrease the friction angle (ϕ) and increase the deviatoric stress.

However, at variance with the observations of Kim and Ha (2014), for a given confining pressure, the maximum value of the deviatoric stress is almost the same whatever the maximum size of the particle of the sample is. Perhaps the grain size difference between the samples is too small to provoke a clear change.

From these results, the friction angles ϕ are calculated with the equation (1.2.1) and provided in table 1.5.

Grain size	**Confinement pressure**	**Friction angle**
$250 < D < 400\mu$m	200 kPa	46.3°
$250 < D < 400\mu$m	300 kPa	45.32°
$250 < D < 400\mu$m	390 kPa	44.03°
$400 < D < 500\mu$m	200 kPa	46.1°
$400 < D < 500\mu$m	300 kPa	44.37°
$400 < D < 500\mu$m	390 kPa	43.49°
$500 < D < 800\mu$m	200 kPa	46.73°
$500 < D < 800\mu$m	290 kPa	45.21°
$500 < D < 800\mu$m	390 kPa	44.32°
$D < 800\mu$m	200 kPa	46.63°
$D < 800\mu$m	300 kPa	45.37°
$D < 800\mu$m	400 kPa	42.82°

Table 1.5: Friction angles obtained for various grain sizes.

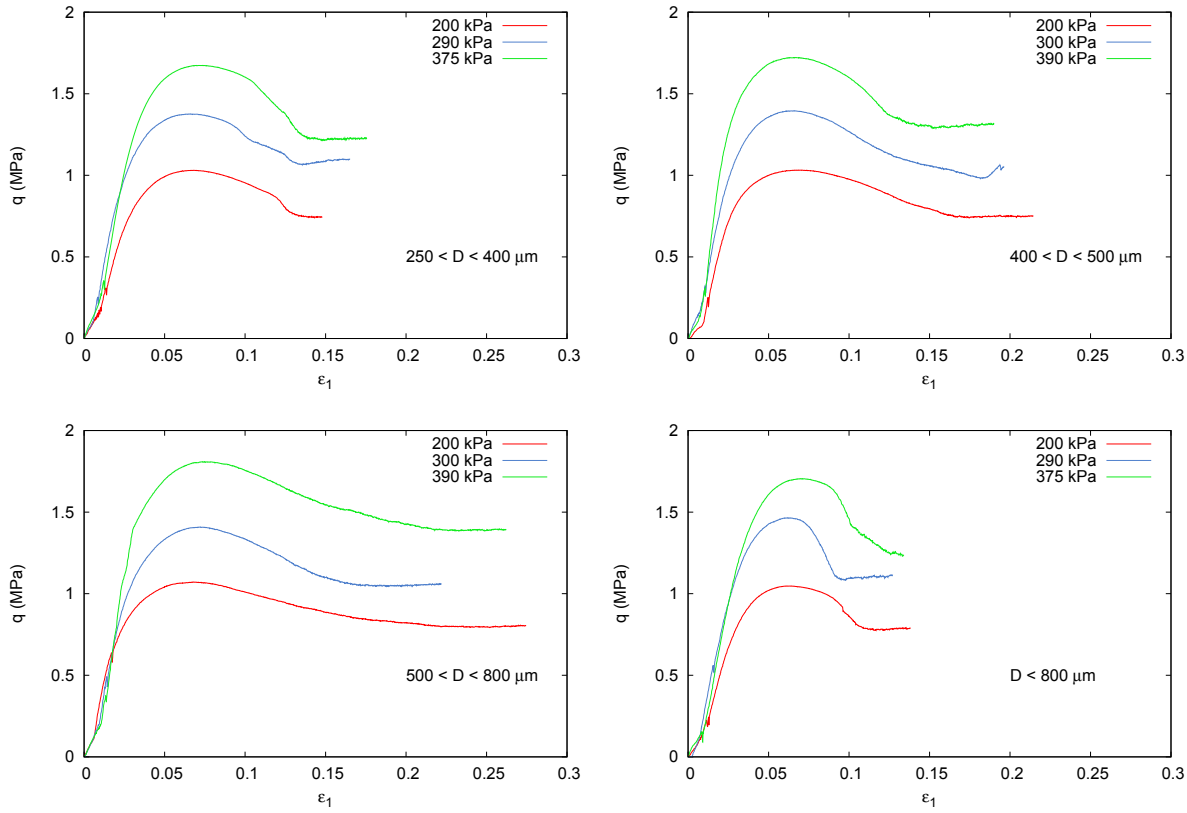

Figure 1.7: Curves relating the deviatoric stresses to the axial strain with uniform grain sizes D ($250 < D < 400\,\mu$m (top left), $400 < D < 500\,\mu$m (top right) and $500 < D < 800\,\mu$m (bottom left)), and another sample (bottom right) with grain sizes smaller than $800\,\mu$m (with a grain size repartition representative to the STANAG soil)

As a final note to these triaxial tests, they are clearly preliminary since

1. the entire grain size distribution of the STANAG soils could not be tested;
2. the range of confinement that was used ($< 1\,$MPa) is way below the stress range (10 GPa) to which the soil close to the explosive is subjected in the field tests to be described in chapters 5 and 6.

It is challenging to design a triaxial device that can accommodate these requirements. Indeed, to apply large stresses, the natural solution is to make use of small specimens (to minimize the applied force). This requirement is contradictory with the presence of large particles in the STANAG soil (up to 4 cm) which would require specimen of $10 \times 4\,\text{cm} = 40\,\text{cm}$ in diameter.

Chapter 2

Development of a viscoplastic cap model

Contents

In many constitutive equations, the time which is introduced does not refer to the duration of the phenomenon. It is just an artificial parameter that helps to sequence the loading events. Elastic and elastoplastic materials are two conspicuous examples.

On the other hand, some materials are endowed with an intrinsic time which is related to the viscosity of the material. Viscous fluids, viscoelastic and viscoplastic solids enter this class of materials. As a matter of fact, the responses of elastic and elastoplastic materials are instantaneous: they can be conceived as limits of time dependent materials whose intrinsic time tends to zero.

As for soils, the constitutive behavior of dry sand is mostly time independent. Still, time comes into picture in experiments with saturated (or partially saturated) sands and in physical processes like consolidation problems. This is due to the fact that water diffuses through the solid skeleton.

The comments above pertain to standard soil mechanics where strain rates are low. For high strain rates, the standard assumption of soil mechanics that the intrinsic time scale of the sand is zero has to be revised. One potential source of time dependence that is advocated for granular materials, even in absence of water, is the fact that grain crushing is not instantaneous but is endowed with a representative intrinsic time.

In this chapter, we address first the basic properties of viscoelasticity and viscoplasticity, and we have a brief look at how the viscoplasticity is taken into account in literature models for simulations of buried explosions.

Next, we derive our own viscoplastic cap model. It is composed of three parts: a hardening cap surface, a failure surface to limit shear stresses and a cut off surface to limit tension. The entire yield surface is smooth so that plastic strain increments are continuous. Typical stress paths (isotropic compression, isotropic tension and shear) are tested. A parametric study is performed to evaluate the influence of the various model parameters on the stress response. As expected, the parameters defining the shape and the size of the yield surface influence the most the stress response.

2.1 Viscoelasticity

Viscoelasticity corresponds to a behavior which introduces time dependence but remains elastic. A viscoelastic material can be modeled with springs representing elasticity, and with dashpots representing viscosity.

Springs react instantaneously, with a deformation proportional to the load. They are defined with a stiffness E whereas dashpots have an instrinsic time of reaction and are characterized by a viscosity coefficient η. The rate at which the deformation is produced with dashpots is proportional to the load. The result is thus not instantaneous.

In this section, three rheological models are presented: the Maxwell, the Voigt and the "standard linear solid" models. The exposition follows Fung (1977).

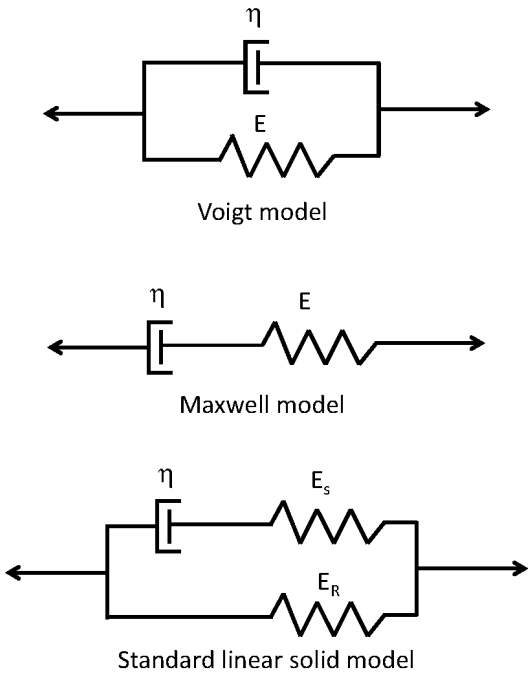

Figure 2.1: Three models of linear viscoelasticity. They are constituted by springs and dashpots. Dashpots have a coefficient of viscosity η, and thus an intrinsic time to react, whereas the deformation obtained with the spring and its stiffness E is instantaneous.

These three models are illustrated in figure 2.1. For each, a different relationship between the stress σ and the strain ε can be defined depending on the model:

- For the Maxwell model

$$\dot{\varepsilon} = \frac{\dot{\sigma}}{E} + \frac{\sigma}{\eta} \quad \text{with} \quad \varepsilon(0^+) = \frac{\sigma(0^+)}{E} \tag{2.1.1}$$

- For the Voigt model

$$\sigma = E\,\varepsilon + \eta\,\dot{\varepsilon} \quad \text{with} \quad \varepsilon(0^+) = 0 \tag{2.1.2}$$

- For the standard linear solid model

$$\sigma + \tau_\varepsilon\,\dot{\sigma} = E_R\,(\varepsilon + \tau_\sigma\,\dot{\varepsilon}) \quad \text{with} \quad \tau_\varepsilon\,\sigma(0^+) = E_R\,\tau_\sigma\,\varepsilon(0^+) \tag{2.1.3}$$

τ_σ and τ_ε are two time constants which can be defined by $\tau_\varepsilon = \eta/E_S$ and $\tau_\sigma = (1 + E_S/E_R)\,\tau_\varepsilon = \eta\,(1/E_R + 1/E_S)$. The notations E_R and E_S are the same as in figure 2.1.

The Maxwell model is the limit of the standard linear solid for $E_R \to 0$. The Kelvin model is the limit of the standard linear solid for $E_S \to \infty$.

2.1.1 Creep functions

The creep functions are defined as the deformation obtained by the application of a unit step function $\mathbf{1}(t)$:

$$\mathbf{1}(t) = \begin{cases} 1 & \text{when} \quad t > 0 \\ 1/2 & \text{when} \quad t = 0 \\ 0 & \text{when} \quad t < 0 \end{cases} \tag{2.1.4}$$

The creep functions of the three models in figure 2.1 are the following:

- For the Maxwell model:

$$c(t) = \left(\frac{1}{E} + \frac{1}{\eta}\, t\right) \mathbf{1}(t) \tag{2.1.5}$$

- For the Voigt model:

$$c(t) = \frac{1}{E}(1 - e^{-(E/\eta)\, t})\, \mathbf{1}(t) \tag{2.1.6}$$

- For the standard linear solid model:

$$c(t) = \frac{1}{E_R}\left[1 - \left(1 - \frac{\tau_\varepsilon}{\tau_\sigma}\right) e^{-t/\tau_\sigma}\right] \mathbf{1}(t) \tag{2.1.7}$$

The deformation curves obtained for each of the three models are presented in figure 2.2.

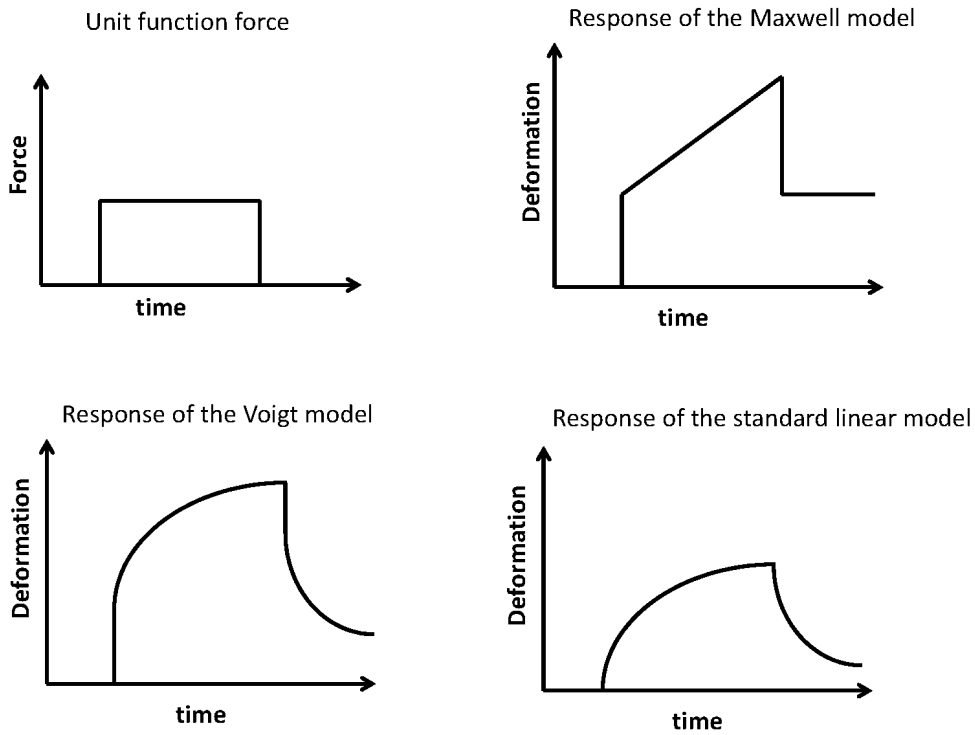

Figure 2.2: Creep functions obtained for the three viscoelastic models submitted to a unit step function force.

2.1.2 Relaxation functions

At variance with the creep functions, the relaxation functions are the force responses of the models subjected to a unit elongation $u(t) = \mathbf{1}(t)$. The unit function takes and keeps the unit value. For the three models, the relaxation functions are the following:

- For the Maxwell model:

$$k(t) = E\, e^{-(E/\eta)t}\, \mathbf{1}(t) \tag{2.1.8}$$

- For the Voigt model:

$$k(t) = \eta\, \delta(t) + E\mathbf{1}(t) \tag{2.1.9}$$

- For the standard linear solid model:

$$k(t) = E_R \left[1 - \left(1 - \frac{\tau_\sigma}{\tau_\varepsilon}\right) e^{-t/\tau_\varepsilon}\right] \mathbf{1}(t) \tag{2.1.10}$$

They are illustrated in figure 2.3.

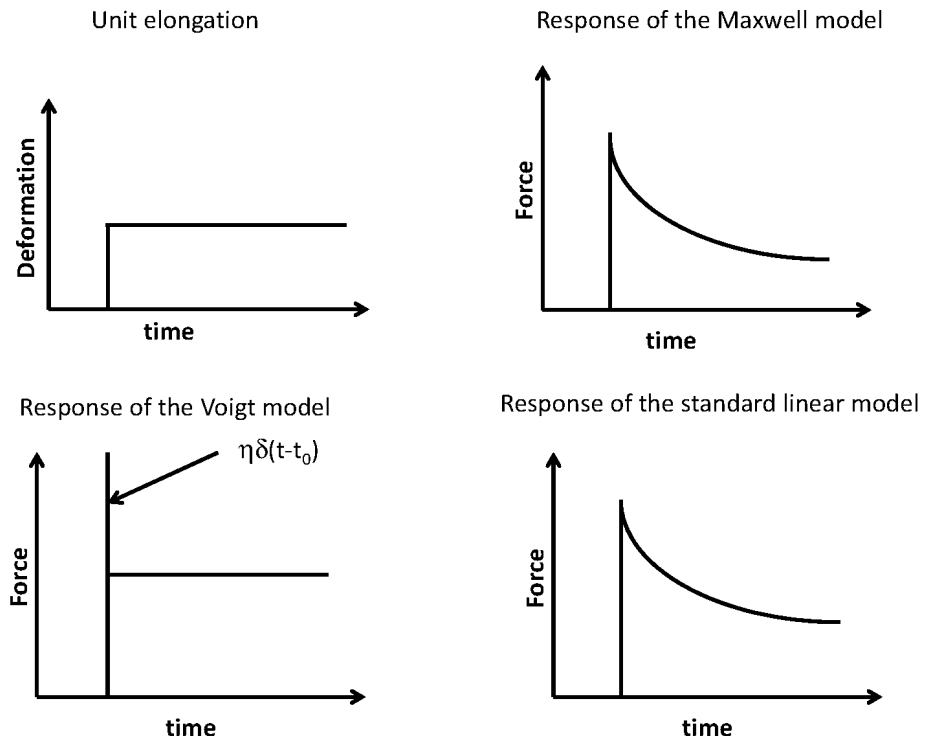

Figure 2.3: Relaxation function obtained for the three viscoelastic models submitted to a unit elongation.

$\delta(t)$ corresponds to a unit impulse function (which is called Dirac function):

$$\begin{cases} \delta(t) = 0 \quad (\text{for} \quad t < 0 \quad \text{and} \quad t > 0) \\ \int_{-\epsilon}^{\epsilon} f(t)\delta(t)\, dt = f(0) \quad (\epsilon > 0) \end{cases} \tag{2.1.11}$$

Thus, τ_σ and τ_ε appear as the characteristic times associated respectively with creep and relaxation. For a Maxwell model, $\tau_\varepsilon = \eta/E$, $\tau_\sigma = \infty$. For a Kelvin model, $\tau_\varepsilon = 0$, $\tau_\sigma = \eta/E$.

2.2 Overstress models

For plastic materials, in the stress space, the plastic solution must lie inside or on the yield surface. In viscoplasticity, the solution may be outside the yield surface due to rate effects.

Plasticity can be considered as a special case of viscoplasticity when the characteristic time of loading is large with respect to the intrinsic material characteristic time.

In the following, two formulations of viscoplasticity are presented: the formulation based on Perzyna's theory (1966) and another one based on Duvaut-Lions' theory (1972). The first one has been used in various papers to model viscoplasticity in a context of buried explosions, whereas the second one is mostly a prototype easily amenable to time-stepping algorithmic solutions.

2.2.1 The Perzyna model

In the small strain theory, the total strain rate $\dot{\boldsymbol{\varepsilon}}$ can be decomposed in an elastic strain rate $\dot{\boldsymbol{\varepsilon}}^e$ and a viscoplastic strain rate $\dot{\boldsymbol{\varepsilon}}^{vp}$:

$$\dot{\boldsymbol{\varepsilon}} = \dot{\boldsymbol{\varepsilon}}^e + \dot{\boldsymbol{\varepsilon}}^{vp} \tag{2.2.1}$$

Considering the elastic part, the elastic strain rate is linked to the stress rate with the tensor moduli $\mathbb{E}$ which is assumed to be constant:

$$\dot{\boldsymbol{\sigma}} = \mathbb{E} : \dot{\boldsymbol{\varepsilon}}^e \tag{2.2.2}$$

As for the viscoplastic part, a flow rule is defined between the viscoplastic strain rate, λ a non-negative plasticity multiplier (also known as the consistency parameter, Simo and Hughes (1998)) which gives a magnitude of $\dot{\boldsymbol{\varepsilon}}^{vp}$, and a second order tensor $\boldsymbol{m}$ which provides the direction of $\dot{\boldsymbol{\varepsilon}}^{vp}$:

$$\dot{\boldsymbol{\varepsilon}}^{vp} = \lambda\, \boldsymbol{m} \tag{2.2.3}$$

The second order tensor $\boldsymbol{m}$ is usually obtained from the derivation of the potential function g:

$$\boldsymbol{m} = \frac{\partial g}{\partial \boldsymbol{\sigma}} \tag{2.2.4}$$

In the Perzyna's theory (1966), the viscoplastic strain rate $\dot{\boldsymbol{\varepsilon}}^{vp}$ is written

$$\dot{\boldsymbol{\varepsilon}}^{vp} = \frac{< \phi(f) >}{\eta}\, \boldsymbol{m} \tag{2.2.5}$$

η is a viscosity parameter (so that a rate-independent elasto-plastic model is recovered if $\eta \to 0$) and ϕ is an overstress function which depends on the rate-independent yield surface f. The overstress function ϕ must fulfill the following conditions:

$$\begin{cases} \phi(f) & \text{is} & \text{continuous} & \text{in} & [0, \infty[, \\ \phi(f) & \text{is} & \text{convex} & \text{in} & [0, \infty[, \\ & & \phi(0) = 0 & & \end{cases} \tag{2.2.6}$$

So the overstress function ϕ is written as

$$\phi(f) = \left(\frac{f}{\alpha}\right)^N \tag{2.2.7}$$

with α defined as a reference yield surface, generally chosen as the initial yield surface f_0, and N a calibration exponent which must be an integer at least equal to 1 to fulfil the convex condition of the overstress function.

The function $< . >$ means

$$< \phi(f) >= \begin{cases} \phi(f) & \text{if} \quad \phi(f) \geq 0 \\ 0 & \text{if} \quad \phi(f) < 0 \end{cases} \tag{2.2.8}$$

The Perzyna's theory is called the overstress model. This is an elasto-viscoplasticity theory: viscosity is only applied to plasticity, once the material yields, not to elasticity.

2.2.2 The Duvaut-Lions one dimensional viscoplastic model

The following explanation follows Simo and Hughes (1998).

In section 2.1 about viscoelasticity, we defined two devices to model elasticity and viscosity. Here a frictional device is added with its yield stress σ_Y in order to model plasticity.

The viscoplastic behavior of a material can be represented with the rheological model of figure 2.4.

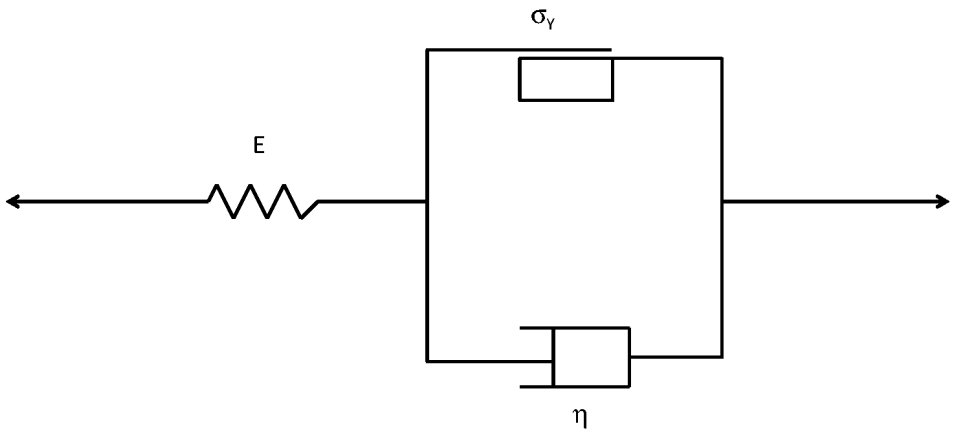

Figure 2.4: Rheological model for a viscoplastic material.

Let us define a time constant (as in section 2.1) also known as relaxation time:

$$\tau = \frac{\eta}{E} \tag{2.2.9}$$

and a loading function $f(\boldsymbol{\sigma}) = |\boldsymbol{\sigma}| - \boldsymbol{\sigma}_Y \geq 0$ applied on the device illustrated in figure 2.4. Its viscoplastic strain rate can be written from the Maxwell model, equation (2.1.1):

$$\dot{\boldsymbol{\varepsilon}}^{vp} = \frac{1}{\eta} f(\boldsymbol{\sigma}) \text{sign}(\boldsymbol{\sigma}) \tag{2.2.10}$$

with sign(σ) the negative or positive sign of the stress σ.

$$\dot{\boldsymbol{\varepsilon}}^{vp} = \frac{E^{-1}}{\tau} [|\boldsymbol{\sigma}| \text{sign}(\boldsymbol{\sigma}) - \boldsymbol{\sigma}_{\text{Y}} \text{sign}(\boldsymbol{\sigma})] \tag{2.2.11}$$

$$= \frac{E^{-1}}{\tau} [\boldsymbol{\sigma} - \boldsymbol{\sigma}_{Y} \text{sign}(\boldsymbol{\sigma})] \tag{2.2.12}$$

Let us introduce the operator $\boldsymbol{P}$ such as $\boldsymbol{P\sigma} = \boldsymbol{\sigma}_{Y} \text{sign}(\boldsymbol{\sigma})$. Equation (2.2.12) becomes

$$\dot{\boldsymbol{\varepsilon}}^{vp} = \frac{E^{-1}}{\tau} [\boldsymbol{\sigma} - \boldsymbol{P\sigma}] \tag{2.2.13}$$

The operator $\boldsymbol{P}$ can be seen as a projection since

$$\boldsymbol{P}(\boldsymbol{P\sigma}) = \boldsymbol{P}^2\boldsymbol{\sigma} = \boldsymbol{P\sigma} \Leftrightarrow \boldsymbol{P}^2 = \boldsymbol{P} \tag{2.2.14}$$

The operator $\boldsymbol{P}$ allows to obtain the stress state $\boldsymbol{\sigma}$ which corresponds to the closest point of the yield surface.

2.2.3 Viscoplastic models applied to soil dynamics

Several papers mention viscoplasticity when modeling buried explosions. In fact, it is taken into account in two different ways: either with one of the two viscoplastic models previously presented or by incorporating viscoplasticity in the definition of the yield surface.

The model developed by Tong and Tuan (2007), then used by An et al. (2011) and Grujicic et al. (2009) is based on the Perzyna model. An (2010) compared the two viscoplastic models and found that there exists a set of parameters for both models which allow to get the same results.

At variance, Wang et al. (2004) modified the Drucker Prager cap model which can be written

$$f = \sqrt{J_2} - \alpha I_1 - k = 0 \tag{2.2.15}$$

where α and k are material constants and I_1 and J_2 are the first stress invariant and the second deviatoric stress invariant respectively.

Strain rate effects were taken into account in the elastoplastic constitutive relation of the soil skeleton:

$$f = \sqrt{J_2} - (\alpha I_1 + k) \left(1 + \beta \ln \frac{\dot{\varepsilon}_{\text{eff}}}{\dot{\varepsilon}_0}\right) = 0 \tag{2.2.16}$$

$\dot{\varepsilon}_0$ is a reference strain rate, β is a material parameter, and $\dot{\varepsilon}_{\text{eff}}$ is the effective strain rate defined as

$$\dot{\varepsilon}_{\text{eff}} = \sqrt{\frac{2}{3} \dot{\boldsymbol{\varepsilon}} : \dot{\boldsymbol{\varepsilon}}} \tag{2.2.17}$$

In the following, we will use the Perzyna model.

2.3 A viscoplastic cap model

A viscoplastic cap model is presented in this section. The yield surface is divided into three regions: a cap surface defined by a preconsolidation pressure for compressive stresses, a failure surface to limit shear stresses and a tensile cut off to limit tensile stresses. This is an isotropic model and only the cap can harden, but it cannot soften. The tensile cut off and the failure surface do not harden nor soften. Moreover, the entire yield surface is smooth so that the plastic strain increments are continuous.

This section addresses the equation of the three parts of the yield surface and of the hardening law. The step by step integration for a strain driven controlled path is exposed since this ingredient is required for finite element simulations. Finally the model is tested for several stress paths, and a parameter sensitivity is described.

2.3.1 The viscoplastic constitutive equations

The total strain rate can be divided into an elastic and a viscoplastic parts:

$$\dot{\boldsymbol{\varepsilon}} = \dot{\boldsymbol{\varepsilon}}^e + \dot{\boldsymbol{\varepsilon}}^{vp} \tag{2.3.1}$$

The elastic stiffness is not constant due to elastic stiffening. In terms of the tangent elastic stiffness, the elastic constitutive equation can be expressed in rate form as:

$$\dot{\boldsymbol{\sigma}} = \mathbb{E} : \dot{\boldsymbol{\varepsilon}}^e \tag{2.3.2}$$

Adopting the Perzyna overstress format, the viscoplastic strain rate is:

$$\dot{\boldsymbol{\varepsilon}}^{vp} = \eta < \phi(f) > \frac{\partial f}{\partial \boldsymbol{\sigma}} \tag{2.3.3}$$

η corresponds to the inverse of a characteristic time (1/s)

The function $< . >$ is defined such as $< x >= x + |x|/2$. f is the yield function (Pa) and $\phi(f)$ is a dimensionless viscous flow function defined such as:

$$\phi(f) = \left(\frac{f}{f_0}\right)^N \tag{2.3.4}$$

with f_0 a normalizing constant with the same unit as f and $N \geq 1$ the Perzyna exponent.

In the following, the plastic yield function is defined with I_1 the first invariant of stress $\boldsymbol{\sigma}$ (with I_1 positive in compression) and with J_2 the second invariant of the deviatoric stress $\boldsymbol{s} = \boldsymbol{\sigma} - \frac{1}{3}\,\mathrm{tr}\,\boldsymbol{\sigma}\,\boldsymbol{I}$:

$$I_1 = -\boldsymbol{I} : \boldsymbol{\sigma} = -\mathrm{tr}\boldsymbol{\sigma} \quad ; \quad \mathrm{J}_2 = \frac{1}{2}\boldsymbol{s} : \boldsymbol{s} \tag{2.3.5}$$

The volumetric viscoplastic strain

$$k = -\mathrm{tr}\boldsymbol{\varepsilon}_{vp} \tag{2.3.6}$$

is positive in compression.

As shown in figure 2.5, the yield surface is divided into three regions: the cap surface $f_1 = \sqrt{J_2} - F_c(I_1, k)$, the failure surface $f_2 = \sqrt{J_2} - F_e(I_1)$ and the cut off surface $f_3 = \sqrt{J_2} - F_{co}(I_1)$.

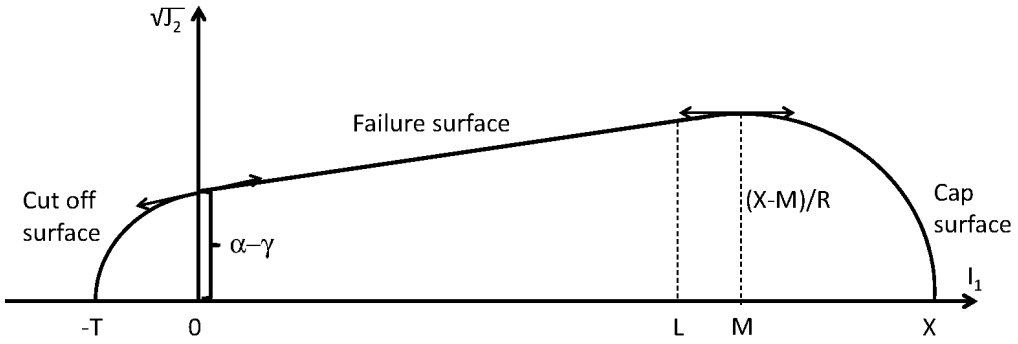

Figure 2.5: Representation of the yield surface in the plane $(I_1, \sqrt{J_2})$.

2.3.1.1 The cap surface

The region where $I_1 \geq L$ corresponds to the cap surface. It is defined as an ellipse with R its eccentricity, and $(M; 0)$ its center. Its intersection with the I_1 axis is noted X and can be seen as the preconsolidation pressure. The point $(L\ ;\ F_e(L) = F_c(L))$ corresponds to the intersection between the failure and the cap surfaces. The cap surface can harden (but not soften).

Viewed as a piece of an ellipse, the cap admits the equation

$$\frac{(I_1 - M)^2}{(X - M)^2} + \frac{(\sqrt{J_2})^2}{(X - M)^2/R^2} = 1 \tag{2.3.7}$$

where $X = X(k)$ is given by the hardening rule in equation (2.3.28). L and M are two unknowns.

The equation of the cap surface can be re-written:

$$f_1(I_1, \sqrt{J_2}, k) = \sqrt{F_{c1}(I_1, \sqrt{J_2})} - \frac{1}{R}(X - M) \tag{2.3.8}$$

$$\text{with} \quad F_{c1}(I_1, \sqrt{J_2}) = J_2 + \frac{1}{R^2}(I_1 - M)^2 \tag{2.3.9}$$

The whole yield surface is smooth. The continuity between the failure and the cap surfaces at the intersection point $(I_1 = L(k)\ ;\ F_e(L) = F_c(L))$ implies

$$\frac{(L - M)^2}{(X - M)^2} + \frac{(F_e(L))^2}{(X - M)^2/R^2} = 1 \tag{2.3.10}$$

which provides the definition of $M(k)$ once $L(k)$ is known:

$$M = \frac{1}{2}(X + L) - R^2 \frac{(F_e(L))^2}{2(X - L)} \tag{2.3.11}$$

whereas the continuity of the tangent at the same point implies

$$\frac{dF_c(L)}{dI_1} = -\frac{1}{R^2}\frac{L-M}{F_c(L)} = -\frac{1}{R^2}\frac{L-M}{F_e(L)} = \frac{dF_e(L)}{dI_1} \tag{2.3.12}$$

Inserted into equation (2.3.11), this relation provides an equation for L:

$$\rho(L) = -(X-L)^2 + 2R^2F_e(L)\frac{dF_e(L)}{dI_1}(X-L) + R^2(F_e(L))^2 = 0 \tag{2.3.13}$$

Equation (2.3.13) can be solved through Newton iterations starting for example from $L = X/2$, namely

$$\rho(L) + \frac{d\rho}{dL}\delta L = 0 \tag{2.3.14}$$

with

$$\begin{aligned}\frac{d\rho}{dL} &= 2(X-L) + 2R^2\left(\left(\frac{dF_e(L)}{dI_1}\right)^2(X-L)\right. \\ &\quad + F_e(L)\frac{d^2F_e(L)}{dI_1^2}(X-L) \\ &\quad \left. - F_e(L)\frac{dF_e(L)}{dI_1}\right) + 2R^2F_e(L)\frac{dF_e(L)}{dI_1}\end{aligned} \tag{2.3.15}$$

which can be simplified to

$$\frac{d\rho}{dL} = 2(X-L)\left[1 + R^2\left(\left(\frac{dF_e(L)}{dI_1}\right)^2 + F_e(L)\frac{d^2F_e(L)}{dI_1^2}\right)\right] \tag{2.3.16}$$

Figure 2.6 shows the actual size of the cap surface.

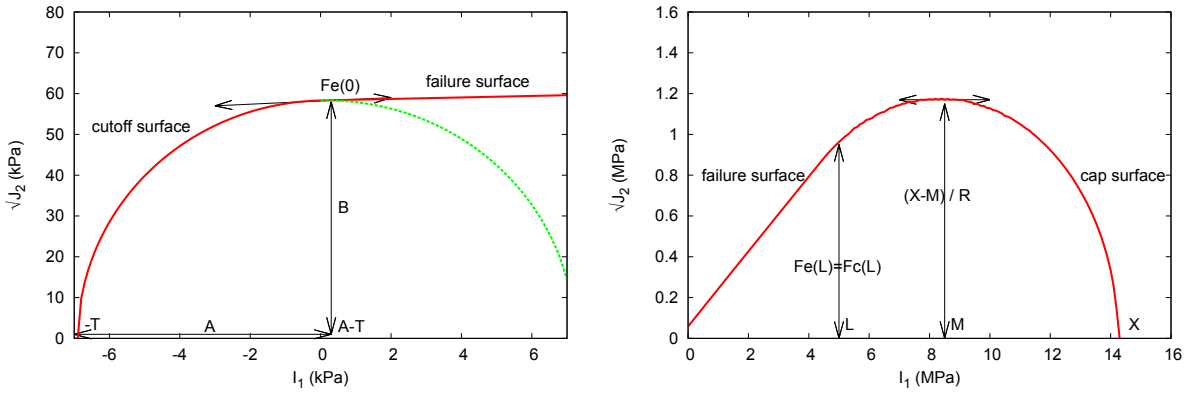

Figure 2.6: Cut off surface (left) and cap surface (right) in actual size. The interface with the failure surface is smoothed and the plastic potential continuous. The ordinate and abscissa axes are not at the same scale on purpose, to make the notations visible.

2.3.1.2 The failure surface

The region $L > I_1 \geq 0$ corresponds to the failure surface, see figure 2.5,

$$f_2(I_1) = \sqrt{J_2} - F_e(I_1) = 0 \tag{2.3.17}$$

$$= \sqrt{J_2} - [\alpha - \gamma \exp(-\beta I_1) + \theta I_1] \tag{2.3.18}$$

with α (Pa), β (Pa^{-1}) and γ (Pa) (such as $\alpha \geq \gamma \geq 0$) and θ (unitless and positive) four material parameters. The failure surface is a non hardening surface.

2.3.1.3 The cut off surface

The region $I_1 < 0$ corresponds to the cut off surface. In order to have a smooth interface between the failure and the cut off surfaces and to provide a continuity of the plastic potential, the cut off surface is defined as an elliptical surface, shown in actual size in figure 2.6.

The central point of the ellipse is $(A-T;0)$ where A is defined as the minor semi-axis and $(-T;0)$ is the point of intersection of the cut off surface with the I_1 axis. The major semi-axis is denoted by B. The ellipse crosses $\sqrt{J_2}$ axis at $(0;F_e(0))$.

The equation of the elliptical cut off is

$$\frac{(I_1 - (A-T))^2}{A^2} + \frac{(\sqrt{J_2})^2}{B^2} = 1 \tag{2.3.19}$$

The equation of the cut off surface can be re-written

$$f_3(I_1, \sqrt{J_2}) = \sqrt{F_{co1}(I_1, \sqrt{J_2})} - B \tag{2.3.20}$$

with

$$F_{co1}(I_1, \sqrt{J_2}) = J_2 + \frac{B^2}{A^2}(I_1 - (A-T))^2 \tag{2.3.21}$$

At point $(0;F_e(0))$, the continuity of failure and cut off surfaces requires

$$F_{co}(0) = B\sqrt{1 - \frac{(A-T)^2}{A^2}} = F_e(0) \quad \text{with} \quad F_{co}(I_1) = B\sqrt{\frac{1 - (I_1 - (A-T))^2}{A^2}} \tag{2.3.22}$$

and the continuity of the slope of failure and cut off surfaces imposes

$$\frac{dF_e(I_1 = 0)}{dI_1} = \frac{dF_{co}(I_1 = 0)}{dI_1} \tag{2.3.23}$$

where F_{co} is defined as

$$f_3(I_1, \sqrt{J_2}) = \sqrt{J_2} - F_{co}(I_1) = 0 \tag{2.3.24}$$

Equation (2.3.23) becomes

$$\frac{dF_{co}}{dI_1}(0) = \frac{B\,(A-T)}{A^2} \frac{1}{\sqrt{1 - \frac{(A-T)^2}{A^2}}} = \frac{dF_e(0)}{dI_1} \tag{2.3.25}$$

which leads to the expressions of the minor and major semi-axes:

$$A = \frac{T^2\, dF_e(0)/dI_1 - T\, F_e(0)}{2T\, \dfrac{dF_e(0)}{dI_1} - F_e(0)} \tag{2.3.26}$$

and

$$B = \frac{A^2}{A-T}\sqrt{1 - \frac{(A-T)^2}{A^2}}\frac{dF_e(0)}{dI_1} \tag{2.3.27}$$

with T the tension cut off ($T \geq 0$).

2.3.1.4 The hardening law

The following hardening law is proposed

$$X(k) - X_0 = \frac{1}{D}\left(\left|1 - \frac{k}{W}\right|^{-1} - 1\right), \quad k = W\left(1 - [1 + D(X(k) - X_0)]^{-1}\right) \tag{2.3.28}$$

Thus

$$X' = \frac{\partial X}{\partial k} = \frac{1}{WD}\left|1 - \frac{k}{W}\right|^{-2} \tag{2.3.29}$$

The volumetric viscoplastic strains tend toward W. X_0 (Pa) is the initial cap position which can be also considered as the preconsolidation pressure and D is a material parameter (Pa^{-1}) which provides the rate at which the hardening occurs.

When the stress state is related to any dilatant part of the yield surface (either to the cut off, to the failure surface or to the part of the cap surface where $L < I_1 < M$), it was chosen that the cap does not soften. It means that k defined by equation (2.3.6) is actually not changed if plastic dilatancy takes place. However the point is questionable: this assumption consists in pretending that plastic dilatancy does not degrade the material properties. The alternative would deserve to be considered.

When the soil is compressed and the cap hardens, this surface moves to the right. Thanks to the equation (2.3.28), when the compression is very important and the soil is highly compacted, the preconsolidation pressure $X(k)$ tends to the infinity. Therefore the yield surface is very large. In this case, the soil is in a highly compacted state where no void remains. Therefrom, one can consider that the compacted soil undergoes the elastic behavior of the solid particles. If the soil contains initially water, the compacted material would consist in a mixture of grains and water with a bulk modulus K_{wg} detailed in equation (3.6.9), page 76.

2.3.2 Step by step integration of the viscoplastic equations

The objective is to implement the model previously described in LS Dyna to simulate buried explosions. In a context of finite elements, the paths are strain driven. So the following step by step integration is written with this point of view. Each step corresponds to a time increment Δt. The state at the time t_n is characterized by stresses $\boldsymbol{\sigma_n}$, strains $\boldsymbol{\varepsilon_n}$ and viscoplastic strains $\boldsymbol{\varepsilon_n^{vp}}$.

Over a time interval Δt, the incremental stresses and strains can be expressed:

$$\Delta\boldsymbol{\varepsilon} = \Delta\boldsymbol{\varepsilon}^e + \Delta\boldsymbol{\varepsilon}^{vp} = \boldsymbol{\varepsilon}_{n+1} - \boldsymbol{\varepsilon}_n = \dot{\boldsymbol{\varepsilon}}\Delta t \tag{2.3.30}$$

and

$$\Delta\boldsymbol{\sigma} = \mathbb{E} : \Delta\boldsymbol{\varepsilon}^e = \mathbb{E} : (\Delta\boldsymbol{\varepsilon} - \Delta\boldsymbol{\varepsilon}^{vp}) \tag{2.3.31}$$

The viscoplastic strain is integrated over a time step:

$$\Delta\boldsymbol{\varepsilon}^{vp} = \boldsymbol{\varepsilon}^{vp}_{n+1} - \boldsymbol{\varepsilon}^{vp}_n = \eta \ < \phi(f) > \ \Delta t \frac{\partial f}{\partial \boldsymbol{\sigma}} \tag{2.3.32}$$

Let us introduce a plastic multiplier $\Delta\lambda$ such as

$$\Delta\lambda = \eta < \phi(f) > \Delta t \tag{2.3.33}$$

The viscoplastic strain increment can be rewritten

$$\Delta\boldsymbol{\varepsilon}^{vp} = \Delta\lambda \frac{\partial f}{\partial \boldsymbol{\sigma}} = \Delta\lambda \boldsymbol{P} \tag{2.3.34}$$

with $\boldsymbol{P}$ the normal to the plastic potential.

We search the new state at step $n+1$, ie we look for $\boldsymbol{\sigma}_{n+1}$ and $\boldsymbol{\varepsilon}^{vp}_{n+1}$: the stress and the viscoplastic strain are two unknowns. From equation (2.3.32), $\Delta\lambda$ can be used instead of $\Delta\boldsymbol{\varepsilon}^{vp}$. Consequently the two unknowns are $\boldsymbol{\sigma}_{n+1}$ and $\Delta\lambda = \lambda_{n+1} - \lambda_n$. Two equations are thus necessary:

1. the constitutive viscoplastic equation :

$$\Delta\boldsymbol{\sigma} = \mathbb{E} : \left(\Delta\boldsymbol{\varepsilon} - \Delta\lambda \frac{\partial f}{\partial \boldsymbol{\sigma}}\right) \tag{2.3.35}$$

2. the definition of $\Delta\lambda$ such as

$$\frac{\Delta\lambda}{\eta\Delta t} - \phi(f) = 0 \tag{2.3.36}$$

To solve these two equations, Newton's iterations are used: we must write them for two successive iterations i and $i+1$ at time $n+1$ and the difference is calculated. For any quantity a, this difference is written:

$$\delta a = a^{i+1}_{n+1} - a^i_{n+1} \tag{2.3.37}$$

The equation (2.3.35) becomes

$$\begin{aligned} \Delta\boldsymbol{\sigma}^{i+1} &= \mathbb{E}^{i+1} : (\Delta\boldsymbol{\varepsilon}^{i+1} - \Delta\lambda^{i+1}\boldsymbol{P}^{i+1}) \\ \Delta\boldsymbol{\sigma}^{i} &= \mathbb{E}^{i} : (\Delta\boldsymbol{\varepsilon}^{i} - \Delta\lambda^{i}\boldsymbol{P}^{i}) \end{aligned} \tag{2.3.38}$$

The difference between the two iterations yields

$$\delta\boldsymbol{\sigma} = \mathbb{E} : (\delta\boldsymbol{\varepsilon} - \delta(\Delta\lambda)\boldsymbol{P} - \Delta\lambda\delta\boldsymbol{P}) + \delta\mathbb{E} : (\mathbb{E}^{-1} : \Delta\boldsymbol{\sigma}) \tag{2.3.39}$$

A priori $\boldsymbol{P}$ depends on the two unknowns $\boldsymbol{\sigma}$ and $\Delta\lambda$. Expression (2.3.39) becomes

$$\delta\boldsymbol{\sigma} = \mathbb{E} : (\delta\boldsymbol{\varepsilon} - \delta(\Delta\lambda)\boldsymbol{P} - \Delta\lambda\left(\frac{\partial \boldsymbol{P}}{\partial \boldsymbol{\sigma}} : \delta\boldsymbol{\sigma} + \frac{\partial \boldsymbol{P}}{\partial \Delta\lambda}\delta(\Delta\lambda)\right)) + \left(\frac{\partial \mathbb{E}}{\partial \boldsymbol{\sigma}} : \delta\boldsymbol{\sigma}\right) : (\mathbb{E}^{-1} : \Delta\boldsymbol{\sigma}) \tag{2.3.40}$$

which can be expressed by

$$\delta\boldsymbol{\sigma} = \mathbb{E}_{alg} : (\delta\boldsymbol{\varepsilon} - \delta(\Delta\lambda)\boldsymbol{P}_{alg}) \tag{2.3.41}$$

with

$$\mathbb{E}_{alg} = \left(\boldsymbol{I} + \frac{1}{K}\frac{\partial K}{\partial I_1}\Delta\boldsymbol{\sigma} \otimes \boldsymbol{I} + \Delta\lambda\mathbb{E} : \frac{\partial \boldsymbol{P}}{\partial \boldsymbol{\sigma}}\right)^{-1} \tag{2.3.42}$$

and

$$\boldsymbol{P}_{alg} = \boldsymbol{P} + \Delta\lambda\frac{\partial \boldsymbol{P}}{\partial \Delta\lambda} \tag{2.3.43}$$

K is the tangent bulk modulus which is defined from the stiffening curve in equation (3.6.5) page 75. Because we assume a constant Poisson's ratio, we can write $\mathbb{E} = (K/K_0)\mathbb{E}_0$, with $\mathbb{E}_0$ the initial elastic stiffness and $K = K(I_1)$. Therefore $\delta\mathbb{E} = (\delta K/K)\mathbb{E}$. Thanks to the expression of the bulk modulus in relation of I_1,

$$\frac{1}{K}\frac{\partial K}{\partial I_1} = \frac{2}{3}\frac{ab}{(1 + b < I_1 > /3)^3}\frac{K}{K_{wg}} \tag{2.3.44}$$

A second equation is required for the plastic multiplier $\Delta\lambda = \eta < \phi(f) > \Delta t$. By differentiation of the expression of the residual in equation (2.3.36), it comes:

$$\rho + \frac{\delta\Delta\lambda}{\eta\Delta t} - \frac{\partial\phi}{\partial f}(\frac{\partial f}{\partial \boldsymbol{\sigma}}\delta\boldsymbol{\sigma} + \frac{\partial f}{\partial\Delta\lambda}(\delta\Delta\lambda)) = 0 \tag{2.3.45}$$

which can be rearranged to:

$$\left(\frac{1}{\eta\Delta t} - \frac{\partial\phi}{\partial f}\frac{\partial f}{\partial\Delta\lambda}\right)\delta(\Delta\lambda) - \frac{\partial\phi}{\partial f}\frac{\partial f}{\partial\boldsymbol{\sigma}} : \delta\boldsymbol{\sigma} = -\rho^{(i)} \tag{2.3.46}$$

with $\rho^{(i)}$ the residual which is calculated at each iteration i.

It can also be seen as a linearizing of the residual:

$$\rho^{(i+1)} = \rho^{(i)} + \left(\frac{\partial\rho}{\partial\boldsymbol{\sigma}}\right) : \delta\boldsymbol{\sigma} + \left(\frac{\partial\rho}{\partial\Delta\lambda}\right)\delta\Delta\lambda \tag{2.3.47}$$

The result is set to 0 which yields to equation (2.3.45).

Now we have obtained the two equations (2.3.41) and (2.3.46) to find $\delta\boldsymbol{\sigma}$ and $\delta(\Delta\lambda)$. Inserting equation (2.3.41) into equation (2.3.46) yields a scalar equation for $\delta(\Delta\lambda)$:

$$\left(\frac{1}{\eta\Delta t} - \frac{\partial\phi}{\partial f}\frac{\partial f}{\partial\Delta\lambda}\right)\delta(\Delta\lambda) = \frac{1}{H_{alg}}\left(-\frac{1}{\partial\phi/\partial f}\rho + \boldsymbol{P} : \mathbb{E}_{alg} : \delta\boldsymbol{\varepsilon}\right) \tag{2.3.48}$$

with

$$H_{alg} = \frac{1}{\eta\Delta t}\frac{1}{\partial\phi/\partial f} - \frac{\partial f}{\partial\Delta\lambda} + \boldsymbol{P} : \mathbb{E}_{alg} : \boldsymbol{P}_{alg} \tag{2.3.49}$$

Inserting the expression of $\delta(\Delta\lambda)$ into equation (2.3.41) yields $\delta\boldsymbol{\sigma}$ and $\delta\boldsymbol{\varepsilon}^{vp}$ since $\delta\boldsymbol{\sigma}$ is equal to $\mathbb{E} : (\delta\boldsymbol{\varepsilon} - \delta\boldsymbol{\varepsilon}^{vp})$:

$$\delta\boldsymbol{\varepsilon}^{vp} = (\boldsymbol{I}^{(4)} - \mathbb{E}^{-1} : \mathbb{E}_{alg}) : \delta\boldsymbol{\varepsilon} + \delta(\Delta\lambda)\mathbb{E}^{-1} : \mathbb{E}_{alg} : \boldsymbol{P}_{alg} \tag{2.3.50}$$

The iterative process is stopped when the residual and $\delta\boldsymbol{\sigma}$ are smaller than some tolerance. In a completely strain driven process $\delta\boldsymbol{\varepsilon} = \mathbf{0}$.

To sum up, the logic which is followed for a step-by-step integration of the visco-plastic equations is:

1. Initialization: $i = 0$, $\Delta\lambda^i_{n+1} = 0$, $k_{n+1} = k_n$, $\boldsymbol{\varepsilon}^{vp}_{n+1} = \boldsymbol{\varepsilon}^{vp}_n$.

2. Trial test: For a strain driven process, the total strain is increased by the strain increment: $\boldsymbol{\varepsilon}_{n+1} = \boldsymbol{\varepsilon}_n + \Delta\boldsymbol{\varepsilon}$. The trial stress is derived:

   $\boldsymbol{\sigma}^{trial}_{n+1} = \mathbb{E} : (\boldsymbol{\varepsilon}_{n+1} - \boldsymbol{\varepsilon}^{vp}_{n+1})$. The yield functions are estimated. If the stress trial is in the elastic region, it means if $f^i_{n+1} \leq 0$ then go to (1).

3. The plastic potential, the derivatives of the yield function and the residual are calculated:

$$f^i_{n+1}, \boldsymbol{P}^i_{n+1}, \left(\frac{\partial f}{\partial(\Delta\lambda)}\right)^i_{n+1}, \left(\frac{\partial \boldsymbol{P}^i_{n+1}}{\partial\boldsymbol{\sigma}}\right), \left(\frac{\partial \boldsymbol{P}^i_{n+1}}{\partial(\Delta\lambda)}\right) \tag{2.3.51}$$

$$= \left(f, \frac{\partial f}{\partial\boldsymbol{\sigma}}, \frac{\partial f}{\partial(\Delta\lambda)}, \frac{\partial \boldsymbol{P}}{\partial\boldsymbol{\sigma}}, \frac{\partial \boldsymbol{P}}{\partial(\Delta\lambda)}\right)(\boldsymbol{\sigma}^i_{n+1}, k^i_{n+1}) \tag{2.3.52}$$

$$\rho^i_{n+1} = \frac{\Delta\lambda^i_{n+1}}{\eta\Delta t} - \phi(f^i_{n+1}) \tag{2.3.53}$$

4. The viscoplastic multiplier is calculated:

$$\delta(\Delta\lambda) = \frac{1}{H_{alg}{}^i_{n+1}}\left(-\frac{1}{\partial\phi^i_{n+1}/\partial f}\,\rho\right) \tag{2.3.54}$$

5. The viscoplastic strain and the hardening variable are updated:

$$\delta\boldsymbol{\varepsilon}^{vp} = \delta(\Delta\lambda)\mathbb{E}^{-1} : (\mathbb{E}_{alg})^i_{n+1} : (\boldsymbol{P}_{alg})^i_{n+1} \tag{2.3.55}$$

$$(\boldsymbol{\varepsilon}^{vp})^{i+1}_{n+1} = (\boldsymbol{\varepsilon}^{vp})^i_{n+1} + \delta\boldsymbol{\varepsilon}^{vp} \tag{2.3.56}$$

$$k^{i+1}_{n+1} = k^i_{n+1} - \mathrm{tr}\delta\boldsymbol{\varepsilon}^{\mathrm{vp}} \tag{2.3.57}$$

$$\delta\boldsymbol{\sigma} = \mathbb{E}_{alg} : (\delta\boldsymbol{\varepsilon} - \delta(\Delta\lambda)\boldsymbol{P}_{alg}) \tag{2.3.58}$$

   If $|\rho^i_{n+1}| \leq$ TOL and $|\delta\boldsymbol{\sigma}| \leq$ TOL2 where TOL and TOL2 are two tolerances, then go to (1).

6. $\boldsymbol{\sigma}^{i+1}_{n+1} = \mathbb{E}^{i+1}_{n+1} : (\boldsymbol{\varepsilon}_{n+1} - (\boldsymbol{\varepsilon}^{\boldsymbol{vp}})^{i+1}_{n+1})$, $i \to i+1$ and go to (3)

2.3.3 Calculations of required derivatives

What follows provides the first and second derivatives that are required during the step by step integration.

2.3.3.1 Derivatives of stress and deviatoric stress invariants

Let us start with the first invariant of stresses:

$$I_1 = -\mathrm{tr}\boldsymbol{\sigma}, \quad \frac{\partial I_1}{\partial \boldsymbol{\sigma}} = -\boldsymbol{I}, \quad \frac{\partial^2 I_1}{\partial \boldsymbol{\sigma}^2} = \boldsymbol{0} \tag{2.3.59}$$

and with the second invariant of the deviatoric stresses:

$$J_2 = \frac{1}{2}\boldsymbol{s} : \boldsymbol{s}, \quad \frac{\partial \sqrt{J_2}}{\partial \boldsymbol{\sigma}} = \frac{\boldsymbol{s}}{2\sqrt{J_2}}, \quad \frac{\partial^2 \sqrt{J_2}}{\partial \boldsymbol{\sigma}^2} = \frac{\boldsymbol{J}^{(4)}}{2\sqrt{J_2}} - \frac{1}{\sqrt{J_2}}\frac{\boldsymbol{s}}{2\sqrt{J_2}} \otimes \frac{\boldsymbol{s}}{2\sqrt{J_2}} \tag{2.3.60}$$

$\otimes$ is the dyadic product: for example, $(\boldsymbol{s} \otimes \boldsymbol{s})_{ijkl} = s_{ij}s_{kl}$.

$\boldsymbol{J}^{(4)}$ is the fourth order identity tensor over second order deviatoric tensors such as:

$$\boldsymbol{J}^{(4)} = \boldsymbol{I}^{(4)} - \frac{1}{3}\boldsymbol{I} \otimes \boldsymbol{I} \tag{2.3.61}$$

For example: $\boldsymbol{J}^{(4)} : \boldsymbol{s} = \boldsymbol{s}$ and $\boldsymbol{J}^{(4)} : \boldsymbol{\sigma} = \boldsymbol{s}$.

$\boldsymbol{I}^{(4)}$ is the fourth order identity tensor over second order stress tensors such as $\boldsymbol{I}^{(4)} : \boldsymbol{s} = \boldsymbol{s}$ and $\boldsymbol{I}^{(4)} : \boldsymbol{\sigma} = \boldsymbol{\sigma}$.

In cartesian axes, the two fourth order identity tensors write componentwise:

$$I^{(4)}_{ijkl} = \frac{1}{2}\left(I_{ik}I_{jl} + I_{il}I_{jk}\right), \quad J^{(4)}_{ijkl} = \frac{1}{2}\left(I_{ik}I_{jl} + I_{il}I_{jk}\right) - \frac{1}{3}I_{ij}I_{kl} \tag{2.3.62}$$

Using the Voigt convention, it is useful to record both fourth order tensors in their matrix forms. Depending whether they are associated with the stiffness (when the identity applies to a strain like tensor) or whether they are associated with the compliance (when the identity applies to a stress like tensor), their expressions are different due to the presence of the "2" coefficient in front of the shear strains.

$$[\boldsymbol{I}^{(4)}_E] = \begin{bmatrix} 1 & 0 & 0 & 0 & 0 & 0 \\ 0 & 1 & 0 & 0 & 0 & 0 \\ 0 & 0 & 1 & 0 & 0 & 0 \\ 0 & 0 & 0 & \frac{1}{2} & 0 & 0 \\ 0 & 0 & 0 & 0 & \frac{1}{2} & 0 \\ 0 & 0 & 0 & 0 & 0 & \frac{1}{2} \end{bmatrix} \quad ; \quad [\boldsymbol{I}^{(4)}_S] = \begin{bmatrix} 1 & 0 & 0 & 0 & 0 & 0 \\ 0 & 1 & 0 & 0 & 0 & 0 \\ 0 & 0 & 1 & 0 & 0 & 0 \\ 0 & 0 & 0 & 2 & 0 & 0 \\ 0 & 0 & 0 & 0 & 2 & 0 \\ 0 & 0 & 0 & 0 & 0 & 2 \end{bmatrix} \tag{2.3.63}$$

$$[\boldsymbol{J}_E^{(4)}] = \begin{bmatrix} \frac{2}{3} & -\frac{1}{3} & -\frac{1}{3} & 0 & 0 & 0 \\ -\frac{1}{3} & \frac{2}{3} & -\frac{1}{3} & 0 & 0 & 0 \\ -\frac{1}{3} & -\frac{1}{3} & \frac{2}{3} & 0 & 0 & 0 \\ 0 & 0 & 0 & \frac{1}{2} & 0 & 0 \\ 0 & 0 & 0 & 0 & \frac{1}{2} & 0 \\ 0 & 0 & 0 & 0 & 0 & \frac{1}{2} \end{bmatrix} \quad ; \quad [\boldsymbol{J}_S^{(4)}] = \begin{bmatrix} \frac{2}{3} & -\frac{1}{3} & -\frac{1}{3} & 0 & 0 & 0 \\ -\frac{1}{3} & \frac{2}{3} & -\frac{1}{3} & 0 & 0 & 0 \\ -\frac{1}{3} & -\frac{1}{3} & \frac{2}{3} & 0 & 0 & 0 \\ 0 & 0 & 0 & 2 & 0 & 0 \\ 0 & 0 & 0 & 0 & 2 & 0 \\ 0 & 0 & 0 & 0 & 0 & 2 \end{bmatrix} \tag{2.3.64}$$

2.3.3.2 Dyadic product stiffness and compliance matrixes

The dyadic product of two identity matrices write:

$$[\boldsymbol{I} \otimes \boldsymbol{I}] = \begin{bmatrix} 1 & 1 & 1 & 0 & 0 & 0 \\ 1 & 1 & 1 & 0 & 0 & 0 \\ 1 & 1 & 1 & 0 & 0 & 0 \\ 0 & 0 & 0 & 0 & 0 & 0 \\ 0 & 0 & 0 & 0 & 0 & 0 \\ 0 & 0 & 0 & 0 & 0 & 0 \end{bmatrix} \tag{2.3.65}$$

For the record, the expression $\boldsymbol{\sigma} = \mathbb{E} : \boldsymbol{\varepsilon}$, $\sigma_{ij} = E_{ijkl}\varepsilon_{kl}$ is written with the Voigt convention in the format:

$$\begin{bmatrix} \sigma_{11} \\ \sigma_{22} \\ \sigma_{33} \\ \sigma_{23} \\ \sigma_{13} \\ \sigma_{12} \end{bmatrix} = \begin{bmatrix} E_{1111} & E_{1122} & E_{1133} & E_{1123} & E_{1113} & E_{1112} \\ E_{2211} & E_{2222} & E_{2233} & E_{2223} & E_{2213} & E_{2212} \\ E_{3311} & E_{3322} & E_{3333} & E_{3323} & E_{3313} & E_{3312} \\ E_{2311} & E_{2322} & E_{2333} & E_{2323} & E_{2313} & E_{2312} \\ E_{1311} & E_{1322} & E_{1333} & E_{1323} & E_{1313} & E_{1312} \\ E_{1211} & E_{1222} & E_{1233} & E_{1223} & E_{1213} & E_{1212} \end{bmatrix} \begin{bmatrix} \varepsilon_{11} \\ \varepsilon_{22} \\ \varepsilon_{33} \\ 2\,\varepsilon_{23} \\ 2\,\varepsilon_{13} \\ 2\,\varepsilon_{12} \end{bmatrix} \tag{2.3.66}$$

with the isotropic elastic stiffness $E_{ijkl} = \lambda\, I_{ij} I_{kl} + 2\mu I_{ijkl}^{(4)}$ and in the Voigt convention:

$$[\mathbb{E}] = \begin{bmatrix} \lambda + 2\mu & \lambda & \lambda & 0 & 0 & 0 \\ \lambda & \lambda + 2\mu & \lambda & 0 & 0 & 0 \\ \lambda & \lambda & \lambda + 2\mu & 0 & 0 & 0 \\ 0 & 0 & 0 & \mu & 0 & 0 \\ 0 & 0 & 0 & 0 & \mu & 0 \\ 0 & 0 & 0 & 0 & 0 & \mu \end{bmatrix} \tag{2.3.67}$$

The inverse of the stiffness is called the compliance such as $\boldsymbol{\varepsilon} = \mathbb{S} : \boldsymbol{\sigma}$ with $\mathbb{E}^{-1} = \mathbb{S}$. In the Voigt convention the expression can be written:

$$\begin{bmatrix} \varepsilon_{11} \\ \varepsilon_{22} \\ \varepsilon_{33} \\ 2\,\varepsilon_{23} \\ 2\,\varepsilon_{13} \\ 2\,\varepsilon_{12} \end{bmatrix} = \begin{bmatrix} S_{1111} & S_{1122} & S_{1133} & 2\,S_{1123} & 2\,S_{1113} & 2\,S_{1112} \\ S_{2211} & S_{2222} & S_{2233} & 2\,S_{2223} & 2\,S_{2213} & 2\,S_{2212} \\ S_{3311} & S_{3322} & S_{3333} & 2\,S_{3323} & 2\,S_{3313} & 2\,S_{3312} \\ 2\,S_{2311} & 2\,S_{2322} & 2\,S_{2333} & 4\,S_{2323} & 4\,S_{2313} & 4\,S_{2312} \\ 2\,S_{1311} & 2\,S_{1322} & 2\,S_{1333} & 4\,S_{1323} & 4\,S_{1313} & 4\,S_{1312} \\ 2\,S_{1211} & 2\,S_{1222} & 2\,S_{1233} & 4\,S_{1223} & 4\,S_{1213} & 4\,S_{1212} \end{bmatrix} \begin{bmatrix} \sigma_{11} \\ \sigma_{22} \\ \sigma_{33} \\ \sigma_{23} \\ \sigma_{13} \\ \sigma_{12} \end{bmatrix} \tag{2.3.68}$$

with the isotropic elastic compliance $E^{-1}_{ijkl} = -\frac{\nu}{E} I_{ij} I_{kl} + \frac{1+\nu}{E} I^{(4)}_{ijkl}$; in the Voigt convention:

$$[\mathbb{E}]^{-1} = \begin{bmatrix} \frac{1}{E} & -\frac{\nu}{E} & -\frac{\nu}{E} & 0 & 0 & 0 \\ -\frac{\nu}{E} & \frac{1}{E} & -\frac{\nu}{E} & 0 & 0 & 0 \\ -\frac{\nu}{E} & -\frac{\nu}{E} & -\frac{1}{E} & 0 & 0 & 0 \\ 0 & 0 & 0 & \frac{1}{\mu} & 0 & 0 \\ 0 & 0 & 0 & 0 & \frac{1}{\mu} & 0 \\ 0 & 0 & 0 & 0 & 0 & \frac{1}{\mu} \end{bmatrix} \tag{2.3.69}$$

Also, for a stress like dyadic product(that multiplies a strain),

$$[\boldsymbol{a} \otimes \boldsymbol{b}] = \begin{bmatrix} a_{11}b_{11} & a_{11}b_{22} & a_{11}b_{33} & a_{11}b_{13} & a_{11}b_{12} \\ a_{22}b_{11} & a_{22}b_{22} & a_{22}b_{33} & a_{22}b_{13} & a_{22}b_{12} \\ a_{33}b_{11} & a_{33}b_{22} & a_{33}b_{33} & a_{33}b_{13} & a_{33}b_{12} \\ a_{23}b_{11} & a_{23}b_{22} & a_{23}b_{33} & a_{23}b_{13} & a_{23}b_{12} \\ a_{13}b_{11} & a_{13}b_{22} & a_{13}b_{33} & a_{13}b_{13} & a_{13}b_{12} \\ a_{12}b_{11} & a_{12}b_{22} & a_{12}b_{33} & a_{12}b_{13} & a_{12}b_{12} \end{bmatrix} \tag{2.3.70}$$

The expression of a dyadic product which multiplies a stress is given by

$$[\boldsymbol{a} \otimes \boldsymbol{b}] = \begin{bmatrix} a_{11}b_{11} & a_{11}b_{22} & a_{11}b_{33} & 2a_{11}b_{23} & 2a_{11}b_{13} & 2a_{11}b_{12} \\ a_{22}b_{11} & a_{22}b_{22} & a_{22}b_{33} & 2a_{22}b_{23} & 2a_{22}b_{13} & 2a_{22}b_{12} \\ a_{33}b_{11} & a_{33}b_{22} & a_{33}b_{33} & 2a_{33}b_{23} & 2a_{33}b_{13} & 2a_{33}b_{12} \\ 2a_{23}b_{11} & 2a_{23}b_{22} & 2a_{23}b_{33} & 4a_{23}b_{23} & 4a_{23}b_{13} & 4a_{23}b_{12} \\ 2a_{13}b_{11} & 2a_{13}b_{22} & 2a_{13}b_{33} & 4a_{13}b_{23} & 4a_{13}b_{13} & 4a_{13}b_{12} \\ 2a_{12}b_{11} & 2a_{12}b_{22} & 2a_{12}b_{33} & 4a_{12}b_{23} & 4a_{12}b_{13} & 4a_{12}b_{12} \end{bmatrix} \tag{2.3.71}$$

2.3.3.3 Derivatives of the cap surface

The cap surface is defined as:

$$f_1(I_1, \sqrt{J_2}, k) = \sqrt{F_{c1}(I_1, \sqrt{J_2}, k)} - \frac{1}{R}(X(k) - M(k)) \tag{2.3.72}$$

with

$$F_{c1}(I_1, \sqrt{J_2}, k) = J_2 + \frac{1}{R^2}(I_1 - M(k))^2 \tag{2.3.73}$$

Its derivatives are thus:

$$\frac{\partial F_{c1}}{\partial \boldsymbol{\sigma}} = \boldsymbol{s} - \frac{2}{R^2}(I_1 - M)\boldsymbol{I} \quad ; \quad \frac{\partial^2 F_{c1}}{\partial \boldsymbol{\sigma}^2} = \boldsymbol{J}^{(4)} + \frac{2}{R^2}\boldsymbol{I} \otimes \boldsymbol{I} \tag{2.3.74}$$

$$\frac{\partial F_{c1}}{\partial k} = \frac{2}{R^2}(M - I_1)\frac{\partial M}{\partial k} \quad ; \quad \frac{\partial^2 F_{c1}}{\partial \boldsymbol{\sigma} \partial k} = \frac{2}{R^2}\frac{\partial M}{\partial k}\boldsymbol{I} \tag{2.3.75}$$

with

$$\begin{aligned} \frac{\partial M}{\partial k} &= \frac{\partial L}{\partial k} + \frac{1}{2}\left(\frac{\partial X}{\partial k} - \frac{\partial L}{\partial k}\right) \\ &\quad -R^2\left[F_e(L)\frac{dF_e(L)}{dI_1}\frac{\partial L}{\partial k}(X - L) - \frac{1}{2}(F_e(L))^2\left(\frac{\partial X}{\partial k} - \frac{\partial L}{\partial k}\right)\right]\frac{1}{(X-L)^2} \end{aligned} \tag{2.3.76}$$

Since $k = -\operatorname{tr}\boldsymbol{\varepsilon}^{vp} = -\boldsymbol{I} : \boldsymbol{\varepsilon}^{vp}$, with $\Delta\boldsymbol{\varepsilon}^{vp} = \Delta\lambda\boldsymbol{P}$:

$$\delta k = -\delta(\Delta\lambda)\operatorname{tr}\boldsymbol{P} - \Delta\lambda\,\delta(\operatorname{tr}\boldsymbol{P}) \tag{2.3.77}$$

The expression of the normal to the plastic potential $\boldsymbol{P}$ and its derivatives are

$$\boldsymbol{P} = \frac{\partial f_1}{\partial\boldsymbol{\sigma}} = \frac{1}{2\sqrt{F_{c1}}}\frac{\partial F_{c1}}{\partial\boldsymbol{\sigma}} \tag{2.3.78}$$

$$\frac{\partial\boldsymbol{P}}{\partial\boldsymbol{\sigma}} = \frac{\partial^2 f_1}{\partial\boldsymbol{\sigma}^2} = \frac{1}{2\sqrt{F_{c1}}}\frac{\partial^2 F_{c1}}{\partial\boldsymbol{\sigma}^2} - \frac{1}{4(F_{c1})^{3/2}}\frac{\partial F_{c1}}{\partial\boldsymbol{\sigma}}\otimes\frac{\partial F_{c1}}{\partial\boldsymbol{\sigma}} \tag{2.3.79}$$

$$\frac{\partial f_1}{\partial(\Delta\lambda)} = \left(\frac{1}{2\sqrt{F_{c1}}}\frac{\partial F_{c1}}{\partial k} - \frac{1}{R}\frac{\partial}{\partial k}(X - M)\right)(-\operatorname{tr}\boldsymbol{P}) \tag{2.3.80}$$

$$\frac{\partial\boldsymbol{P}}{\partial(\Delta\lambda)} = \left(\frac{1}{2\sqrt{F_{c1}}}\frac{\partial^2 F_{c1}}{\partial\boldsymbol{\sigma}\partial k} - \frac{1}{4(F_{c1})^{3/2}}\frac{\partial F_{c1}}{\partial k}\frac{\partial F_{c1}}{\partial\boldsymbol{\sigma}}\right)(-\operatorname{tr}\boldsymbol{P}) \tag{2.3.81}$$

2.3.3.4 Derivatives of the failure surface

The failure surface can be written

$$f_2(I_1, \sqrt{J_2}) = \sqrt{J_2} - F_e(I_1) = \sqrt{J_2} - (\alpha - \gamma\exp(-\beta\, I_1) + \theta\, I_1) \tag{2.3.82}$$

Its derivatives are thus

$$\frac{\partial F_e}{\partial I_1} = \beta\gamma\exp(-\beta\, I_1) + \theta \quad ; \quad \frac{\partial^2 F_e}{\partial I_1^2} = -\beta^2\gamma\exp(-\beta\, I_1) \tag{2.3.83}$$

The expressions of the normal to the plastic potential $\boldsymbol{P}$ and its derivative relative to the stress tensor are

$$\boldsymbol{P} = \frac{\partial f_2}{\partial\boldsymbol{\sigma}} = \frac{\partial\sqrt{J_2}}{\partial\boldsymbol{\sigma}} - \frac{\partial F_e}{\partial I_1}(-\boldsymbol{I}) = \frac{\partial\sqrt{J_2}}{\partial\boldsymbol{\sigma}} + \frac{\partial F_e}{\partial I_1}\boldsymbol{I} \tag{2.3.84}$$

$$\frac{\partial\boldsymbol{P}}{\partial\boldsymbol{\sigma}} = \frac{\partial^2 f_2}{\partial\boldsymbol{\sigma}^2} = \frac{\partial^2\sqrt{J_2}}{\partial\boldsymbol{\sigma}^2} - \frac{\partial^2 F_e}{\partial I_1^2}\boldsymbol{I}\otimes\boldsymbol{I} \tag{2.3.85}$$

The previous expression multiplies a stress, so its matrix form is given by equation 2.3.71. Since the failure surface does not harden:

$$\frac{\partial f_2}{\partial(\Delta\lambda)} = 0 \quad \text{and} \quad \frac{\partial\boldsymbol{P}}{\partial(\Delta\lambda)} = \boldsymbol{0} \tag{2.3.86}$$

2.3.3.5 Derivatives of the tension cut off

The tension cut off is defined as follows:

$$f_3(I_1, \sqrt{J_2}) = \sqrt{F_{co1}(I_1, \sqrt{J_2})} - B \tag{2.3.87}$$

with

$$F_{co1}(I_1, \sqrt{J_2}) = J_2 + \frac{B^2}{A^2}(I_1 - (A - T))^2 \tag{2.3.88}$$

Its derivatives are thus

$$\frac{\partial F_{co1}}{\partial \boldsymbol{\sigma}} = \boldsymbol{s} - 2\frac{B^2}{A^2}(I_1 - (A - T))\boldsymbol{I} \quad ; \quad \frac{\partial^2 F_{co1}}{\partial \boldsymbol{\sigma}^2} = \boldsymbol{J}^{(4)} + 2\frac{B^2}{A^2}\boldsymbol{I} \otimes \boldsymbol{I} \tag{2.3.89}$$

The expressions of the normal to the plastic potential $\boldsymbol{P}$ and its derivatives are

$$\boldsymbol{P} = \frac{\partial f_3}{\partial \boldsymbol{\sigma}} = \frac{1}{2\sqrt{F_{co1}}}\frac{\partial F_{co1}}{\partial \boldsymbol{\sigma}} \tag{2.3.90}$$

$$\frac{\partial \boldsymbol{P}}{\partial \boldsymbol{\sigma}} = \frac{\partial^2 f}{\partial \boldsymbol{\sigma}^2} = \frac{1}{2\sqrt{F_{co1}}}\frac{\partial^2 F_{co1}}{\partial \boldsymbol{\sigma}^2} - \frac{1}{4(F_{co1})^{3/2}}\frac{\partial F_{co1}}{\partial \boldsymbol{\sigma}} \otimes \frac{\partial F_{co1}}{\partial \boldsymbol{\sigma}} \tag{2.3.91}$$

$$\frac{\partial f_3}{\partial(\Delta\lambda)} = 0 \quad \text{and} \quad \frac{\partial \boldsymbol{P}}{\partial(\Delta\lambda)} = \boldsymbol{0} \tag{2.3.92}$$

Expressions (2.3.89) and (2.3.91) multiply a stress and the matrix form of their expressions is given by equation (2.3.71).

2.3.4 Response of the model to typical stress-strain paths

Before using this viscoplastic model in LS Dyna, let us test it in a strain driven context. The parameters required are given in table 2.1. They are taken from Tong and Tuan (2007). In the article, they were defined to model sand to reproduce experiments of Bergeron et al. (1998) consisting in the detonation of small quantity of explosive buried in sand.

In the following, two stress paths are tested:

- an isotropic compressive stress followed by a shear stress path,
- an isotropic tensile stress path.

These two stress paths end with a relaxation step. Since the model is controlled in strain, the strain components are imposed with either a positive value in the case of elongation, or a negative value in the case of contraction. During the relaxation step, all the components of the strain are set equal to zero.

failure surface parameters			
α	β	γ	θ
0.0642 MPa	0.34283 MPa^{-1}	0.00589 MPa	0.18257

cap surface parameters	
R	X_0
5.0	1 MPa

tensile cut off parameter
T
6.9 kPa

hardening parameters	
D	W
9.52 $\times 10^{-9}$ Pa^{-1}	0.5

viscoplastic parameters		
η	f_0	N
$200\,\text{s}^{-1}$	100 kPa	1

rigidification parameters					
ρ_0	ρ^*	P^*	K_0	K_{wg}	ν_0
$1592\,\text{kg.m}^{-3}$	1710 kg.m^{-3}	1.075 GPa	100 MPa	36 GPa	0.25

Table 2.1: Soil parameters taken from Tong and Tuan (2007) and considered in the following as reference parameters for the parametric study.

2.3.4.1 Isotropic compression and shear test

The first stress path is composed of three steps:

- an isotropic compression,
- a shear stress,
- a relaxation.

The strain increments are thus imposed in the following way:

$$\begin{cases} \Delta\varepsilon_{11} = \Delta\varepsilon_{22} = \Delta\varepsilon_{33} = -1 \times 10^{-6} \quad \text{if} \quad t \leq 1\,\mu\text{s} \\ \Delta\varepsilon_{11} = -1 \times 10^{-6}, \quad \Delta\varepsilon_{22} = \Delta\varepsilon_{33} = 0 \quad \text{if} \quad 1 < t \leq 10\,\mu\text{s} \\ \Delta\varepsilon_{11} = \Delta\varepsilon_{22} = \Delta\varepsilon_{33} = 0 \quad \text{if} \quad t > 10\,\mu\text{s} \end{cases} \tag{2.3.93}$$

All the strain increments $\Delta\varepsilon_{ij}$ with $i \neq j$ are equal to zero during the whole test and the time step is fixed to 10^{-10} s. Therefore the imposed strain rate is equal to 10 000 s^{-1}.

The resulting stress path, and the time history of the first invariant of stresses I_1, the second invariant of deviatoric stresses $\sqrt{J_2}$ and the cap extremity X are presented in figure 2.7.

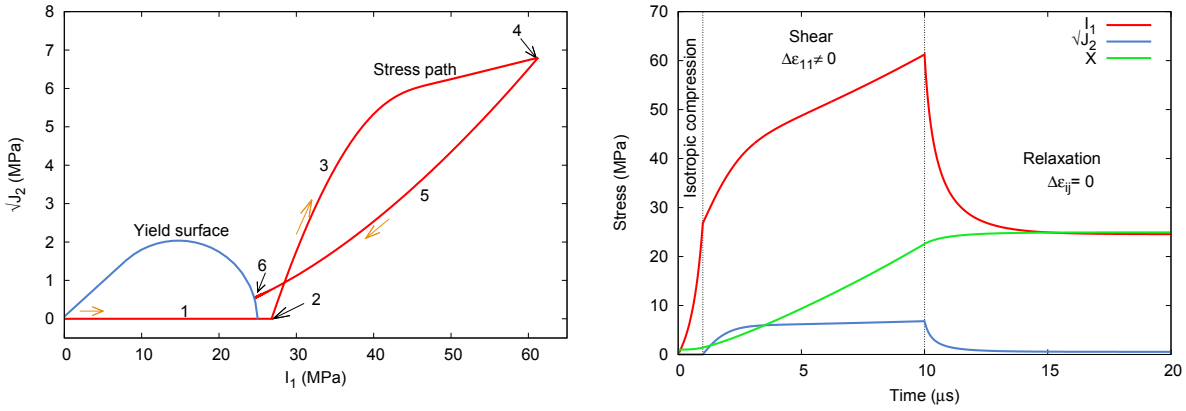

Figure 2.7: On the left, stress path composed of an isotropic compression, followed by shear and a relaxation step. Strain rate: 10 000 s^{-1}. The various setps are: 1-isotropic compression where $\Delta\varepsilon_{11} = \Delta\varepsilon_{22} = \Delta\varepsilon_{33} \neq 0$; 2-start of shear; 3-shear where $\Delta\varepsilon_{11} \neq 0$; 4-start of relaxation; 5-relaxation where all strain increments are equal to 0; 6-final stress state. On the right, time history of the first invariant of stresses I_1, the second invariant of deviatoric stresses $\sqrt{J_2}$ and the cap extremity X for the stress path presented on the left figure.

First, the same constant value for the principal strain increments $\Delta\varepsilon_1$, $\Delta\varepsilon_2$, $\Delta\varepsilon_3$ is imposed whereas the other components of the strain increments are set to zero. Therefore, an isotropic compression is tested. The stress path follows the I_1 axis first inside the yield surface. The behavior is thus elastic and the cap does not move. Once I_1 reaches the cap surface, the stress can be outside the yield surface since the model is viscoplastic. At this moment, the cap hardens and tries to catch up the stress. The rate at which the cap hardens is defined in the hardening law, in particular by the parameter D.

Then a shear stress path is imposed: here since the model is viscoplastic, the shear stress path occurs outside the yield surface, with a slope which is not constant because

of viscoplasticity. At variance, when the shear takes place in the yield surface, the slope is equal to $1/\sqrt{3}$ in the plane $(I_1, \sqrt{J_2})$.

Finally all the strain increments are set to zero. So the stress goes back toward the cap surface while the cap keeps on hardening until the stress state is on the cap. The time of relaxation (time for the stress state to go back to the cap surface) is directly proportional to a characteristic time defined by η: if η is 10 times larger, the time of relaxation is 10 times faster.

2.3.4.2 Tensile test

In the case of explosions, the soil part above the explosive which expands at detonation undergoes tensile stresses.

Here an isotropic tensile stress path is studied with the following imposed strain increments:

$$\begin{cases} \Delta\varepsilon_{11} = \Delta\varepsilon_{22} = \Delta\varepsilon_{33} = 1 \times 10^{-6} & \text{if} \quad t \leq 1\,\mu\text{s} \\ \Delta\varepsilon_{11} = \Delta\varepsilon_{22} = \Delta\varepsilon_{33} = 0 & \text{if} \quad t > 1\,\mu\text{s} \end{cases} \tag{2.3.94}$$

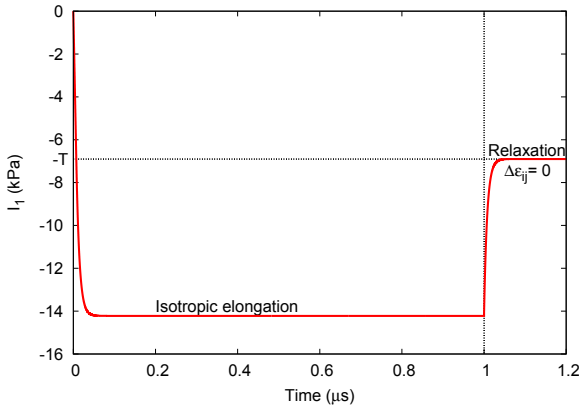

Figure 2.8: Time history of the first invariant of stresses I_1 for a tensile stress path followed by a relaxation step.

Figure 2.8 shows the time course of the first invariant of stresses I_1. During isotropic elongation, the stress path follows the I_1 axis in the plane $(I_1, \sqrt{J_2})$, and the value of I_1 increases, even above the value of the limit $I_1 = -T$ of the cut off surface because of the viscoplastic behavior of the model. But after a certain time, the value of I_1 remains equal, probably because the viscoplasticity does not allow to increase indefinitely. During the relaxation step, when all the strain increments are set to zero, the stress state goes back to the cut off surface and the value of I_1 is equal to $-T$.

2.3.5 Parametric study of the model

The model is defined by twelve parameters (α, β, γ, θ, D, R, W, T, X_0, f_0, N, η). Thanks to a parametric study, we are going here to evaluate the influence of each of them on the stress path.

The same strain increments are imposed for the test of all the parameters: the stress path is composed first of an isotropic compression and then of shear stress. The strain increments are the same as in equation (2.3.93). Only one parameter is changed at a same time. The other parameters are the same as those provided in table 2.1 and tested in section 2.3.4. The strain rate is equal to 10 000 s^{-1} (reduced to 10 s^{-1} in some special cases to have a better readibility in the figures).

When the stress is inside the yield surface during shear, the slope of the stress path is known and equal to $1/\sqrt{3}$. Because of the viscoplastic behavior of the model, the stress state can be outside the yield surface. There the direction of the stress path is controlled by the normal to the yield surface, since an associated flow rule was considered. Therefore, among the parameters, those which affect the shape of the yield surface influence the direction of the stress path.

Three parameters modify the shape of the yield surface: θ from the definition of the failure surface, R from the cap surface, and T from the cut off surface. The influence of θ and R on the stress path is illustrated in figure 2.9.

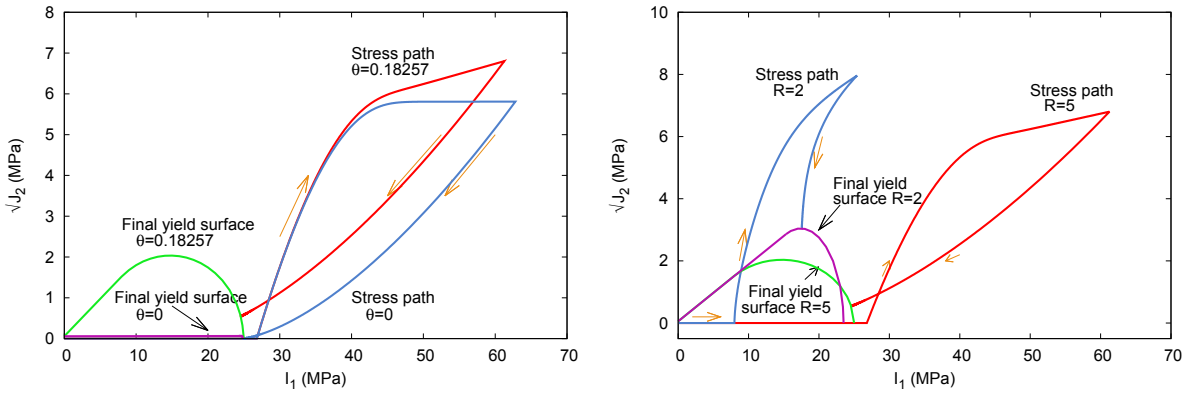

Figure 2.9: On the left, comparison of the stress paths obtained for $\theta = 0$ and for $\theta = 0.18257$. On the right, comparison of the stress paths obtained for $R = 2$ and $R = 5$. Both parameters change the shape of the yield surface which has a direct influence on the direction of the stress path.

θ defines the slope of the failure surface when I_1 is large enough. It can be related to the friction angle of the soil ϕ:

$$\theta = \frac{2}{\sqrt{3}} \frac{\sin \phi}{3 - \sin \phi} \tag{2.3.95}$$

or in inverse form

$$\sin \phi = \frac{3\sqrt{3}\,\theta}{2 + \sqrt{3}\,\theta} \tag{2.3.96}$$

The failure surface is close to a horizontal asymptote for $\theta = 0$ which is its minimum

value. It means that once a stress state reaches the failure surface defined with $\theta = 0$, the behavior keeps on evolving without any change of volume.

A test has been performed with $\theta = 0$ and with $\theta = 0.18257$ corresponding to a friction angle of 24.2°. The resulting stress paths and yield surfaces are presented in figure 2.9. The failure surface for $\theta = 0$ is horizontal. Thus when the cap hardens, the yield surface only widens along the hydrostatic axis. For a strain rate of 10 000 s^{-1}, the final yield surface with $\theta = 0.18257$ is much larger. This difference of the size of the yield surface influences the shape of the stress path and the final stress state.

The R parameter corresponds to the eccentricity of the ellipse defining the cap surface. Two values of R are tested: 2 and 5. A large R flattens the cap. The yield surfaces and the stress paths obtained are presented in figure 2.9. As shown in this figure, $R = 2$ not only modifies the shape of the cap surface but also changes the size of the failure surface along the hydrostatic axis. With $R = 2$, the failure surface is larger and the size of the cap surface is much reduced. This shape deeply modifies the direction of stress path.

Two parameters play a role in the size of the yield surface: the parameter α from the failure surface, and X_0 from the cap surface. Their influence on the stress path is illustrated in figure 2.10.

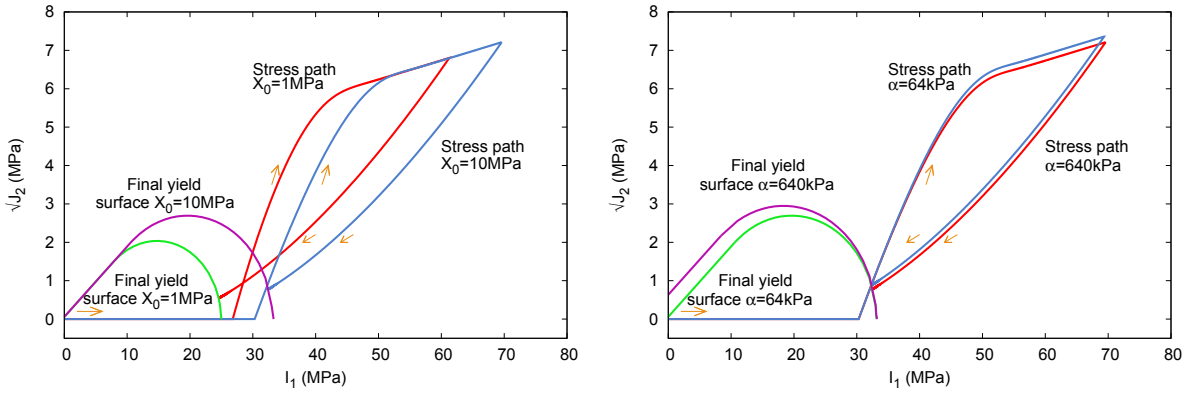

Figure 2.10: On the left, comparison of the stress paths obtained for $X_0 = 1\,\text{MPa}$ and $X_0 = 10\,\text{MPa}$. On the right, comparison of the stress paths obtained for $\alpha = 64.2\,\text{kPa}$ and $\alpha = 642\,\text{kPa}$. When the value of X_0 is ten times larger, the yield surface is ten times wider, so the stress path is translated further on the I_1 axis. The stress path obtained for a value of α ten times larger is slightly changed, because of the small modifications induced on the cap surface by the increase of the failure surface.

X_0 corresponds to the preconsolidation pressure and to the initial cap position. An increase of X_0 makes the elastic zone wider. Two values for X_0 (1 and 10 MPa) are tested and compared in figure 2.10. Since the shape of the cap surface has not changed, the direction of the stress path is the same for the two sets of parameters. For $X_0 = 10\,\text{MPa}$, the stress path is just translated along the hydrostatic axis of 10 MPa.

α corresponds to the initial shear stress. In the definition of the failure surface, α corresponds to the ordinate to the origin. All the values cannot fit for α. The inequality

$M < X - (\alpha - \gamma)R$ must be verified. Otherwise, if the value of α is too large, the value of M becomes negative. To be sure the value of M does not become negative, a value of X_0 ten times larger is chosen.

A change in the initial shear stress α translates the failure surface along the deviatoric stress axis. In order to compare the influence of α, two values are tested: 64.2 kPa and 642 kPa. For $\alpha = 642$ kPa, the failure surface is translated along the deviatoric axis which modifies a little the cap surface. Therefore, the stress path is slightly changed because of this modification.

In the hardening law in equation (2.3.28), except for X_0, two other parameters, D and W, are involved.

D (MPa^{-1}) defines the rate at which the cap hardens: the larger the value of D, the slower the displacement of the cap. Two values of D (0.00952 and 0.113 MPa^{-1}) are tested and the result is presented in figure 2.11: with these two different values of D, the cap hardens at two different rates. Thus, the direction of the stress paths is different since the cap surface changes of shape at different rates. With $D = 0.113$ MPa^{-1}, the cap hardens so slowly that during the relaxation step the stress path ends its way almost on the hydrostatic axis.

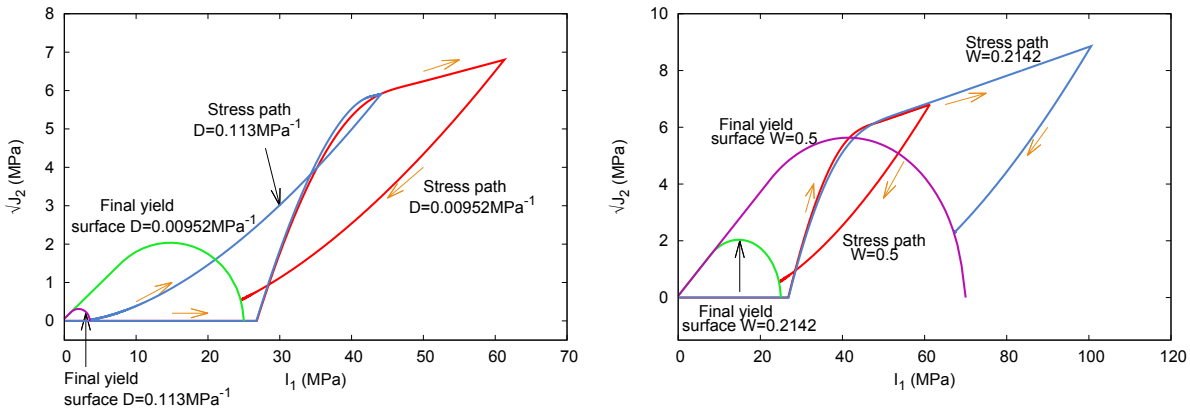

Figure 2.11: On the left, the stress paths obtained for $D = 0.00952$ and 0.113 MPa^{-1} are compared. The larger the value of D is, the slower the displacement of the cap is. With $D = 0.113$ MPa^{-1}, the cap hardens so slowly that during the relaxation step the stress path ends its way almost on the hydrostatic axis. On the right, comparison of the stress paths obtained for $W = 0.2142$ and $W = 0.5$. The smaller the value of W is, the more the cap hardens.

According to the definition of the hardening law in equation (2.3.28), when the value of W increases, the value of X decreases, which means that the smaller the value of W is, the larger the displacement of the cap is (or the more the cap hardens). This is illustrated in figure 2.11.

Three parameters (N, η and f_0) define the viscoplastic strain rate, and thus have an

influence on the viscoplastic behavior of the model. For the tests with these parameters, the strain rate is decreased to 10 s^{-1}.

f_0 is involved in the definition of the overstress function. If this parameter is larger, the behvavior is more viscoplastic: the material acts as if it did not see the yield surface, and thus continues its path with a quasi elastic behavior. Moreover, the slope of the stress path gets closer to an elastic slope (and equal to $1/\sqrt{3}$), even outside the yield surface. As f_0 increases, the stress path goes farther, out of the yield surface, for a same sollicitation. This is illustrated in figure 2.12.

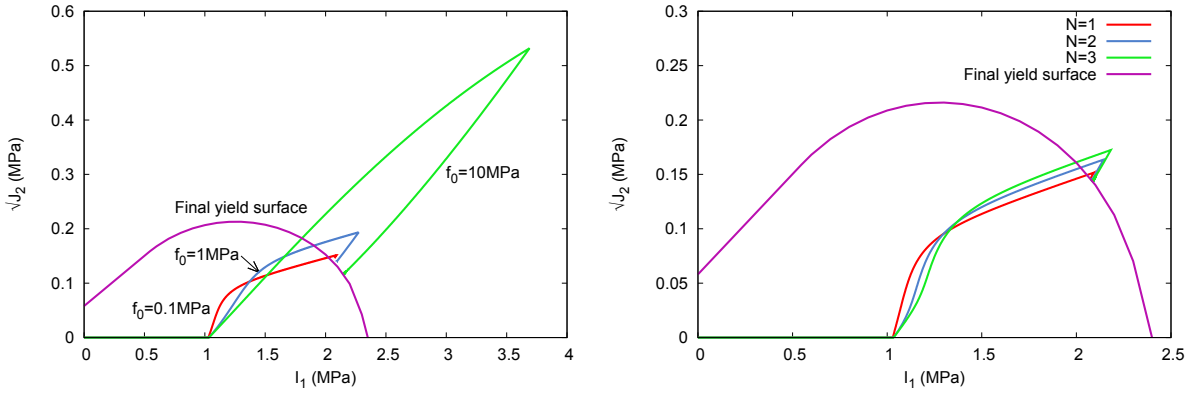

Figure 2.12: On the left, the stress paths obtained for $f_0 = 0.1$, 1 and 10 MPa with a strain rate of 10 s^{-1} are compared. As f_0 increases, the slope of the stress path gets closer to an elastic slope (and equal to $1/\sqrt{3}$), even outside the yield surface. Moreover the stress path goes farther, out of the yield surface, for a same sollicitation. On the right, comparison of the stress paths obtained for $N = 1$, $N = 2$ and $N = 3$ with a strain rate of 10 s^{-1}. The value of N accentuates the effect of f_0: the larger the value of N is, the more viscoplastic the behavior is.

The parameter N is the exponent of the ratio f/f_0. Its value thus accentuates the effect of f_0: the larger the value of N is, the more important the effect of f_0 is. A larger value of N makes the material more viscoplastic. This is shown in figure 2.12.

η corresponds to the inverse of a characteristic time. Its influence is the inverse of f_0 due to its definition in equation (2.3.3). The smaller the value of η, the more viscoplastic and thus elastic the behavior of the material is. This is illustrated in figure 2.13 where two values of η are tested.

Finally, the two last parameters (β and γ) from the definition of the failure surface have little influence on the stress path.

The β and the γ parameters are used in the expression of the exponential of the failure surface. In the failure surface definition in equation (2.3.18), the dominating term is the term with θ: with an increase of I_1 (due to compression for example) this term rapidly increases whereas the exponential term becomes negligible. As a result, the values of both parameters have little influence on the stress path: a change of order of magnitude for those both parameters has hardly any consequence.

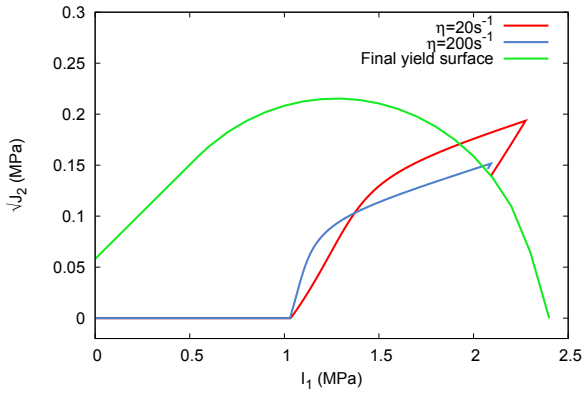

Figure 2.13: Comparison of the stress paths obtained for $\eta = 20$ and $\eta = 200$ s^{-1} with a strain rate of $10\,s^{-1}$. The effects of η are the contrary of those observed for f_0: the smaller the value of η, the more viscoplastic and thus elastic the behavior of the material is.

Chapter 3

Specific constitutive equations for soil dynamics

Contents

When an explosive detonates, a large quantity of energy is released subjecting the soil to stresses up to several gigapascals at high strain rates (between 1 000 and 100 000 s^{-1}) and a shock wave propagates. It is in fact a discontinuity that divides the medium into two regions (the region behind the shock wave which has been shocked, and the region ahead the shock wave which is in its natural conditions) with different densities, pressures and velocities as illustrated in figures 3.1 and 3.2.

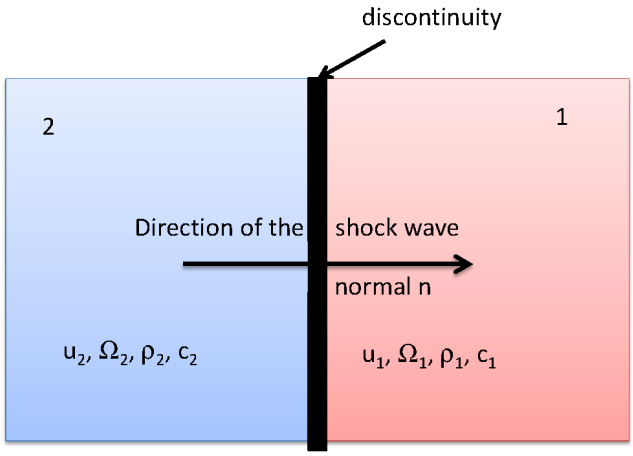

Figure 3.1: Propagation of a shock wave, dividing the medium into two domains with different densities, pressures and velocities.

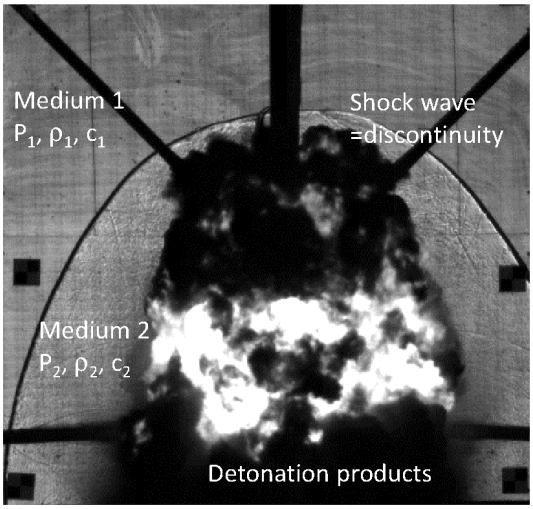

Figure 3.2: Propagation of a shock wave emanated by the detonation of 100 g of C4.

In such conditions, the mechanical constitutive response of the soil is different from the standard soil mechanics description and is here closer to a fluid.

In this chapter, the shock relations and the constitutive equations are addressed from a mechanical point of view. They are detailed for a liquid and a perfect gas. The

Chapman Jouguet condition which is used for the explosive modeling in simulations is also mentioned.

Considering the soil with a fluid-like behavior, dynamic equations for soils are reviewed. General expressions of equations of state and the Mie Grüneisen coefficient are derived. An actual soil is a three phase medium. In constitutive equations, and in particular in equations of state, this can be taken into account through mixture rules. Models for non saturated soils are detailed.

However, our approach does not make use of the above "equations of state". Instead, we pursue a pure continuum mechanics approach but we introduce some sophistication to the standard soil mechanics to account for the specific conditions that prevail in a soil close to the explosive: the stress is huge (up to 10 GPa) and the strain rate reaches considerable values ($10^5\,\mathrm{s}^{-1}$). One of the tool that we have to develop is linked to the stiffening of the elastic response. A stiffening soil model is thus proposed in this chapter.

Besides, during such a dynamic phenomenon, while air is expelled/compressed, water is trapped in the soil. The aim of this PhD is to run buried explosive simulations with saturated and partially saturated sand. In our model, the water content is taken into account in the definition of the stiffening curve of the soil in two different ways:

- First in the initial bulk modulus of the curve: at this stage, the soil is a three phase medium. So the initial bulk modulus and the rest of the curve are defined depending on the initial void ratio ;

- Second, in the final bulk modulus of the curve: at this stage, the soil is highly compacted and no more air remains, but only solid grains and water: so the final bulk modulus is defined with the volume fractions of both constituents.

3.1 Conservation laws in a continuum

Except at the location of the shock, the flow ahead and behind the shock wave shock is assumed to be isentropic, and hence adiabatic if there is no dissipation. The equations of conservation of mass, momentum and energy are reminded here.

- The balance of mass can be written:

$$\begin{cases} \dfrac{d\rho}{dt} + \rho\,\mathrm{div}\mathbf{v} = 0 \\ \Leftrightarrow \quad \dfrac{\partial\rho}{\partial t} + \mathrm{div}(\rho\mathbf{v}) = 0 \end{cases} \tag{3.1.1}$$

  where ρ is the density ($\mathrm{kg.m}^{-3}$).

- The balance of momentum is:

$$\left\{\begin{array}{rl} & \mathrm{div}\boldsymbol{\sigma} + \rho\left(\boldsymbol{b} - \dfrac{\mathrm{d}\mathbf{v}}{\mathrm{dt}}\right) = 0 \\ \Leftrightarrow & -\nabla p + \mathrm{div}\boldsymbol{s} + \rho\left(\boldsymbol{b} - \dfrac{\mathrm{d}\mathbf{v}}{\mathrm{dt}}\right) = \mathbf{0} \\ \Leftrightarrow & \mathrm{div}\boldsymbol{\sigma} + \rho\boldsymbol{b} - \dfrac{\partial(\rho\mathbf{v})}{\partial \mathrm{t}} - \mathrm{div}(\rho\mathbf{v})\mathbf{v} = \mathbf{0} \end{array}\right. \tag{3.1.2}$$

where the stress $\boldsymbol{\sigma} = -p\boldsymbol{I} + \boldsymbol{s}$ has been decomposed in its isotropic and deviatoric parts. $\boldsymbol{b}$ can be any body force like gravity.

- The balance of energy can be written:

$$\left\{\begin{array}{rl} & \rho\dfrac{du}{dt} - \boldsymbol{\sigma} : \dfrac{d\boldsymbol{\varepsilon}}{dt} + \mathrm{div}\boldsymbol{Q} - \Theta = 0 \\ \Leftrightarrow & \rho\dfrac{du}{dt} - p\dfrac{d\varepsilon_v}{dt} - \boldsymbol{s} : \dfrac{d\boldsymbol{e}}{dt} + \mathrm{div}\boldsymbol{Q} - \Theta = 0 \\ \Leftrightarrow & \dfrac{\partial}{\partial t}(\rho(u + \dfrac{1}{2}\mathbf{v}^2)) + \mathrm{div}(\rho(u + \dfrac{1}{2}\mathbf{v}^2) - \boldsymbol{\sigma}.\mathbf{v}) - \rho\,\boldsymbol{b}.\mathbf{v} + \mathrm{div}\boldsymbol{Q} - \Theta = 0 \end{array}\right. \tag{3.1.3}$$

where $\boldsymbol{Q}$ is the heat flux, Θ the internal heat supply, u the internal energy per unit mass (J/kg), and s the entropy per unit mass (J/kg/K). The strain $\boldsymbol{\varepsilon} = -\varepsilon_v\boldsymbol{I} + \boldsymbol{e}$ has been decomposed in its isotropic and deviatoric parts.

Moreover, the entropy production per unit volume $\hat{s}$ can be expressed such as:

$$\hat{s} = \rho\frac{ds}{dt} + \mathrm{div}\left(\frac{\mathrm{Q}}{\mathrm{T}}\right) - \frac{\Theta}{\mathrm{T}} \geq 0 \tag{3.1.4}$$

where T is the temperature (K).

Inside the shock, the flow is not isentropic. To express the discontinuity relations, the field equations need to respect the Hadamard compatibility relations which are detailed in the following section.

3.2 Discontinuity relations

Let us consider the propagation of the shock wave in the direction of the unit normal $\mathbf{n}$, as in figure 3.1. The material particles move with the velocity $\mathbf{v}$. The absolute speed of the wave front is called W whereas the normal speed of the wave relative to the material in its current configuration is denoted Ω,

$$W = \Omega + \mathbf{v}.\mathbf{n} \tag{3.2.1}$$

In order to evaluate the jump of velocities, pressures and densities, let us detail the Hadamard compatibility relations and apply them to the field equations through the wave front. The shock relations in an ideal compressible fluid and in a perfect gas are then derived.

3.2.1 Hadamard compatibility relations

Let us consider $\phi(\boldsymbol{x}, t)$ a scalar function, continuous through the wave front which moves at the speed Ω in the direction $\boldsymbol{n}(\boldsymbol{x}, t)$, and differentiable on both sides of the front. However, some of its derivatives are not continuous through the wave front.

The Hadamard compatibility relations show the existence of a scalar η such as:

$$\left[\!\left[\frac{\partial \phi}{\partial \boldsymbol{x}}\right]\!\right] = \eta \mathbf{n}, \quad \left[\!\left[\frac{d\phi}{dt}\right]\!\right] = -\Omega\eta \tag{3.2.2}$$

The discontinuity operator $[\![a]\!] = a_1 - a_2$ is defined as the difference of the values of the quantity a in front of the wave and behind the wave.

Discontinuity relations can be of first order or of second order. If the relations are discontinuous at the first order, the velocity $\mathbf{v}$ and the stress $\boldsymbol{\sigma}$ are discontinuous. If the relations are discontinuous at the second order, $\mathbf{v}$ and $\boldsymbol{\sigma}$ are continuous but their derivatives ($d\mathbf{v}/dt$, $d\boldsymbol{\sigma}/dt$, and $\operatorname{div}\boldsymbol{\sigma}$) are not continuous.

The absolute speed of the wave front W is continuous through the wave front but neither are the relative speed Ω nor the speed of particles $\mathbf{v}$:

$$\begin{cases} [\![W]\!] & = 0 = & [\![\Omega]\!] + [\![\mathbf{v}]\!].\mathbf{n} \\ W_1 - W_2 & = 0 = & \Omega_1 - \Omega_2 + (\mathbf{v_1} - \mathbf{v_2}).\mathbf{n} \end{cases} \tag{3.2.3}$$

3.2.2 Field equations through the wave front

Applying Hadamard compatibility relations to the field equations yields the discontinuity relations that should be satisfied across the shock wave

$$\begin{cases} \text{balance of mass} & [\![\rho\Omega]\!] = 0 \\ \text{balance of momentum} & [\![\boldsymbol{\sigma}]\!] + (\rho\Omega)[\![\mathbf{v}]\!] = \mathbf{0} \\ \text{balance of energy} & (\rho\Omega)[\![u + \mathbf{v}^2/2]\!] + [\![\mathbf{v}.\boldsymbol{\sigma} - \boldsymbol{Q}]\!].\mathbf{n} = 0 \end{cases} \tag{3.2.4}$$

Similarly, the jump of entropy production across the wave takes the form

$$[\![\boldsymbol{Q}/T]\!].\mathbf{n} - (\rho\Omega)[\![s]\!] \geq 0 \tag{3.2.5}$$

Under adiabatic conditions, the heat flux $\boldsymbol{Q}$ vanishes so $[\![s]\!] \leq 0$ which means that the entropy increases through the wave front : $s_2 > s_1$.

3.2.3 Shock relations in an ideal compressible fluid

Now that we presented the field equations through the wave front, let us apply them to an ideal compressible fluid: its viscosity and its temperature loss by thermal conductivity are not taken into account.

The aim of this section is to derive the two main shock relations for an ideal compressive fluid. They are called the Rayleigh Michelson straight line and the Rankine

Hugoniot curve. The first one corresponds to mass and momentum conservation across the shock wave whereas the second one means an energy conservation across the shock wave.

For an ideal fluid, the stress $\boldsymbol{\sigma} = -p\boldsymbol{I}$ is isotropic. Consequently, from equation (3.2.4), the particle velocity jump is in the same direction as the propagation of the wave front: $[\![\mathbf{v}]\!] = -[\![\Omega]\!]\mathbf{n}$.

If the propagation of the wave front is considered with axes attached and moving with the wave, the absolute speed of the wave speed is equal to zero : $W = 0$, so $\mathbf{v}.\mathbf{n} = -\Omega$ or $\mathbf{v} = -\Omega\mathbf{n}$.

h is the enthalpy per unit mass such as $h = u + p/\rho$. The discontinuity relations for the field equations become:

$$\begin{cases} \text{balance of mass} & [\![\rho\Omega]\!] = 0 \\ \text{balance of momentum} & [\![\mathbf{v} + \Omega\mathbf{n}]\!] = \mathbf{0}, \quad [\![p + \rho\Omega^2]\!] = 0 \\ \text{balance of energy} & [\![h + \Omega^2/2]\!] = 0 \\ \text{entropy inequality} & [\![s]\!] \leq 0 \end{cases} \tag{3.2.6}$$

As defined previously, the domains ahead and behind the shock are called 1 and 2 respectively.

Let us call $w = 1/\rho$ (m^3/kg) the specific volume. The discontinuity relation for the balance of mass and the balance of momentum, using the specific volume, yields:

$$-(\rho_1\Omega_1)^2 = -(\rho_2\Omega_2)^2 = \frac{p_2 - p_1}{w_2 - w_1} = -\rho D^2 \tag{3.2.7}$$

with D the shock wave velocity.

This equation is a particular expression of the **Rayleigh Michelson straight line** for a fluid.

From the previous equation and the discontinuity relation for the balance of energy we obtain:

$$-(\rho_1\Omega_1)^2 = -(\rho_2\Omega_2)^2 = 2\frac{h_2 - h_1}{w_2^2 - w_1^2} \tag{3.2.8}$$

From the two previous equations, the changes of enthalpy and internal energy through the wave front can be deduced:

$$h_2 - h_1 = \frac{1}{2}(p_2 - p_1)(w_1 + w_2), \quad u_2 - u_1 = \frac{1}{2}(p_2 + p_1)(w_1 - w_2) \tag{3.2.9}$$

The jump of enthalpy across the shock wave is also known as the **Rankine Hugoniot curve**.

From the discontinuity relation of mass and equation (3.2.7), we obtain the following relation for the particle velocities:

$$[\![\mathrm{v}.\mathrm{n}]\!] = -[\![\Omega]\!] = -(\rho\Omega)[\![w]\!] = \frac{[\![p]\!]}{\rho\Omega} \Rightarrow [\![\mathrm{v}.\mathrm{n}]\!]^2 = -[\![p]\!][\![w]\!] \tag{3.2.10}$$

3.3 The Chapman Jouguet theory

This theory was developed by Chapman and Jouguet at the beginning of the 20th century. According to this theory, a detonation wave is the propagation of a physical and chimical discontinuity at a supersonic velocity in relation to the ahead medium, and at a sonic velocity in relation to the downstream medium. It transforms instantaneously the reactive medium (initial medium noted 0) into burnt gases (medium behind the detonation wave noted CJ) which are at a thermodynamic equilibrium. The thickness of the reactive zone is considered negligible.

The thermodynamic parameters like the pressure, temperature, particle velocity are subjected to a discontinuity through the detonation wave. As developed previously in section 3.2.3, the discontinuity relations allow to obtain the Rankine Hugoniot (equation (3.2.9)) which links the enthalpy to the pressure and the density. This curve is called the Crussard curve and defines all the possible equilibrium states of the products from a complete burning.

From the combination of the balance of mass and momentum, we obtained in equation (3.2.7) the Rayleigh Michelson straight line. The intersection of the Crussard curve with the Rayleigh Michelson straight line drawn from the initial state provides the thermodynamic characteristics of the final state of the detonation wave (illustrated in figure 3.3). If the initial velocity is zero, the slope of the Rayleigh Michelson is governed by the detonation velocity. Chapman and Jouguet showed that the point where the Rayleigh Michelson straight line is tangent to the Crussard curve is the only possible state which defines the conditions for the propagation of an ideal detonation. The velocity of discontinuity is then constant and equal to the detonation velocity D_{cj}.

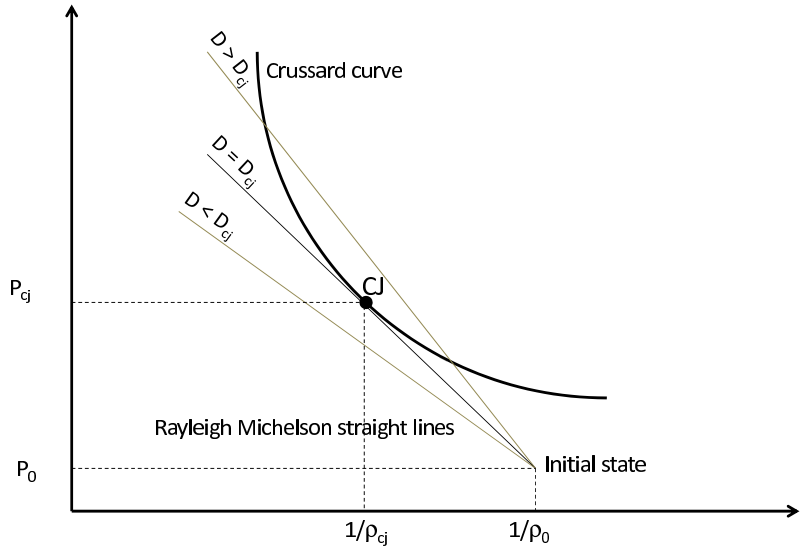

Figure 3.3: Rayleigh Michelson straight line positions in relation to the Crussard adiabatic curve according to the velocity D of the detonation wave.

3.4 Equation of state

An equation of state relates the state variables (the pressure p, the density ρ and the internal energy u). It is required when the behavior of a material is close to a fluid. It is especially the case when the material is subjected to shock waves.

The stress of a material can be decomposed into a deviatoric and an hydrostatic parts such as $\boldsymbol{\sigma} = \boldsymbol{s} - p\,\boldsymbol{I}$ with $\boldsymbol{s}$ the deviatoric stresses, p the pressure which is also equal to minus the third of the first stress invariant I_1 and $\boldsymbol{I}$ the identity matrix.

In the following, general expressions of an equation of state are detailed. The Mie Grüneisen equation of state in particular is derived.

3.4.1 General expressions of equations of state

The relation of discontinuity for the balance of mass gives $\rho\Omega = \rho_1\Omega_1$.

For an ideal fluid, $[\![\Omega]\!] = -[\![\mathbf{v}.\mathbf{n}]\!]$. Through the wave front,

$$d\rho/\rho_1 = \rho/\rho_1 - 1 = -y/(1+y) \quad \text{with} \quad y = [\![\mathbf{v}.\mathbf{n}]\!]/\Omega_1 \tag{3.4.1}$$

The discontinuity relation for the balance of momentum for an ideal compressible fluid is $[\![p]\!] = (\rho\Omega)[\![\mathrm{v.n}]\!]$. At the second order around the state 1, this discontinuity relation becomes:

$$p_1 + p_1^{'} d\rho + \frac{1}{2} p_1^{''} (d\rho)^2 - p_1 = -(\rho_1\,\Omega_1)[\![\mathrm{v.n}]\!] \tag{3.4.2}$$

Since $dp/d\rho = c^2$, then $p_1^{'} = c_1^2$, with c_1 the speed of the sound ahead of the front.

From the expression (3.4.1) of $d\rho/\rho_1$ and the second order expansion for p_1, the relation for Ω can be obtained:

$$\frac{\Omega_1^2}{c_1^2} = \frac{1 + (1 - \rho p_1^{''}/(2c_1^2))y}{(1+y)^2} \tag{3.4.3}$$

This expression may be linearized to

$$\Omega_1 = c_1 + \frac{1}{2}\left(1 + \frac{\rho_1 p_1^{''}}{2c_1^2}\right)(\mathbf{v}_2 - \mathbf{v}_1).\mathbf{n} \tag{3.4.4}$$

This affine relation between the particle velocity $\mathbf{v}_2.\mathbf{n}$ behind the shock and the speed of the wave Ω_1 ahead of the shock is well verified in experiments.

For a gas under isentropic condition: $p/p_1 = (\rho/\rho_1)^\gamma$. The speed of the sound of the gas is:

$$c^2 = \frac{dp}{d\rho} = \gamma\frac{p}{\rho} = \gamma\frac{K}{\rho} \tag{3.4.5}$$

with K the bulk modulus and γ the adiabatic coefficient.

$$\frac{d^2p}{d\rho^2} = \gamma(\gamma-1)\frac{p}{\rho^2} = -\gamma\frac{K}{\rho^2} = -\frac{c_1^2}{\rho} \tag{3.4.6}$$

The linearized expression of Ω_1 becomes:

$$\Omega_1 = c_1 + \frac{1}{4}(\gamma+1)(\mathbf{v}_2 - \mathbf{v}_1).\mathbf{n} \tag{3.4.7}$$

which is known as equation of state (eos) in its general form:

$$\Omega_1 = c_1 + s_{\text{eos}}(\mathbf{v}_2 - \mathbf{v}_1).\mathbf{n} \tag{3.4.8}$$

From equations (3.4.4) and (3.4.7), under isentropic conditions, the theoretical expression of the expression of s_{eos} is :

$$s_{eos} = \frac{1}{2}\left(1 + \frac{\rho_1 (d^2p/d\rho^2)_1}{2(dp/d\rho)_1}\right) \tag{3.4.9}$$

However, this coefficient is almost always determined experimentally from plate impact experiments. Examples of this coefficient have been given in section 4.1.2 where plate impact experiments have been addressed.

3.4.2 The Mie Grüneisen equation of state

Before focusing on the Mie Grüneisen equation of state, let us have a look at the Mie Grüneisen coefficient.

3.4.2.1 The Mie Grüneisen coefficient

The Mie Grüneisen coefficient Γ is defined from the internal energy. It is a dimensionless coefficient which can be expressed such as:

$$\Gamma \equiv -\frac{w}{T}\frac{\partial^2 u}{\partial w \partial s} = \frac{w}{T}\frac{\partial p}{\partial s}_{|w} = -\frac{w}{T}\frac{\partial T}{\partial w}_{|s} \tag{3.4.10}$$

Since $du = -pdw + Tds$, then at constant specific volume, $du = Tds$. Then

$$\Gamma = w\frac{\partial p}{\partial u}_{|w} \tag{3.4.11}$$

3.4.2.2 The related equation of state

The Mie Grüneisen equation of state is an equation of state often used to determine the pressure in a shock-compressed solid. It is derived from the expression of the Mie Grüneisen parameter (equation (3.4.11)), considering Γ/ρ constant, and by integration from a reference point on the isentrope :

$$p = p_{isen} + \frac{\Gamma}{w}(u - u_{isen}) \tag{3.4.12}$$

In numerical codes, the Mie Grüneisen equation of state used is an approximation of the original expression. It can either be a polynomial expression

$$p = c_0 + c_1\mu + c_2\mu^2 + c_3\mu^3 + (c_4 + c_5\mu + c_6\mu^2)E, \quad \mu = w_0/w - 1 \tag{3.4.13}$$

in which the c's are constants. This polynomial expression seems to come from a fitted curve of the Mie Grüneisen expression.

Or it can be a more complex expression, like the Mie Grüneisen equation of state expression given in the LS Dyna theoretical manual:

$$p = \frac{\rho_0 c^2 \mu[1 + (1 - \Gamma_0/2)\mu - (a/2)\mu^2]}{1 - (s_1 - 1)\mu - s_2(\mu^2/(\mu + 1)) - s_3(\mu^3/(\mu + 1)^2)} + (\Gamma_0 + \alpha\mu)E \tag{3.4.14}$$

with E the internal energy per initial volume, c the sound of speed, s_1, s_2, s_3 the coefficients of the slope of the $U_s - u_p$ curve (cf. section 4.1.2), Γ_0 the constant Mie Grüneisen coefficient, a a first order of correction of Γ_0 and $\mu = \rho/\rho_0 - 1$.

3.5 Models for the compaction of granular media

A soil is a three phase medium with a skeleton constituted by solid grains, air and water. When a shock is applied to a granular soil, this medium behaves as if it was undrained. The load is first carried by the pore water and then progressively transmitted to the grains which may be crushed. This compaction of soil has been taken into account differently in literature according to authors.

In the following, the compaction models for soils are first reviewed. Then equations of state and in particular the $P - \alpha$ compaction model which can be used to model non saturated soils are detailed, and the Kandaur model which is often referred to in literature is explained.

3.5.1 Review of the compaction models for soils

Several models of soil compaction have been proposed in literature:

- An (2010) and An et al. (2011) simulated the explosion of buried charges. They considered two different areas for the soil modeling: a first one around the explosive which is highly compacted during the detonation, and a second one further away from the detonation area and thus not submitted to very large stresses. So the soil of the second zone was modeled with continuum mechanics only. On the contrary, for the first zone with a size which may depend on the quantity of explosive, An (2010) used the Mie Grüneisen equation of state ((equation (3.4.14)). The three phase model of the soil was simulated with the Kandaur model (described in section 3.5.4).
- Laine and Sandvik (2001), Fiserova (2006) and Niroumand and Kassim (2010) used a compaction equation of state described by $p = c^2(\rho)\,\rho$ so that the bulk modulus depends on the density. Above a density considered as the theoretical maximum density, the curve $p(\rho)$ follows a straight line defined by $p = c_s^2(\rho - \rho_{TMD})$ where ρ_{TMD} corresponds to the theoretical maximum density and c_s is the bulk sound speed of the fully compacted material. Moreover, an expression $G(\rho) = \rho\, V_s^2$ was also defined to make the shear modulus dependent on the density, where V_s is the shear wave speed.
- Like An (2010), Zakrisson et al. (2012) developed a three phase model based on the Kaudaur theory. But as for the soil stiffening of the soil, they obtained from

experiments a curve relating the pressure to the density (shown in figure 3.6), which allows to derive the bulk modulus. Like Laine and Sandvik (2001), above a certain density, the pressure-density curve becomes a straight line where the soil is highly compacted and no more air remains.

- Thanks to compaction curves, the elastic moduli increase as stresses become very large. Instead, Grujicic et al. (2009) chose a very large initial bulk modulus to avoid taking into account the stiffening of the soil due to the detonation wave.
- At variance with the equation of compaction of Laine and Sandvik (2001), other equations of compaction have been developed with a parameter α defining the degree of soil compaction: $\alpha = \alpha_0$ corresponds to an initial state, and $\alpha = 1$ corresponds to a soil where no air remains. The model is called $P - \alpha$ by Riedel et al. (2008), Wardlaw et al. (1996) and $\varepsilon_v - \alpha$ by Wünnemann et al. (2006). The α quantity allows an evolution of the fraction of each phase (air, and mixture of water and solid grains) in the medium.
- Wang (2001) used the "soil foam model" of LS Dyna to simulate buried mines. In this model, the soil compaction is taken into account with a curve defining the evolution of pressure in relation to volumetric strain. As a result, the bulk modulus also evolves with an increase of pressure.

3.5.2 Porous material (grain-water)-air mixture: $P-\alpha$ equation of state

In this model, the volume fraction of each phase is known explicitly and changes during compaction. The behavior of the medium is first elastic then rapidly becomes elastoplastic.

The compaction of the granular medium has two main steps. During the first one, the pores collapse and the soil particles rearrange: the volume fraction of the void tends to zero progressively. During the second step, the granular medium itself is compacted; no void still remains. If the compaction continues, the grains can be crushed. Unloading does not re-open the void.This model is divided into two parts as illustrated in figure 3.4. One part consists of a mixture of water and grain particles. The second one consists of air. The soil particles and the water are modeled with the Mie Grüneisen equation of state, and the mixture of the porous medium and the air are modeled with the $P - \alpha$ model.

This model is based on the work of Herrmann (1969), Carroll and Holt (1972), Wardlaw et al. (1996) and Buxton (2009). Wardlaw et al. (1996) and Buxton (2009) employed these models for underwater explosion applications, whereas the two first authors used it for porous metallic materials.

The pressure is assumed uniform over the different phases. Moreover, to use the $P-\alpha$ equation of state, the granular medium is supposed statistically homogeneous, isotropic.

The porosity of the soil medium also called distention parameter is defined as:

$$\alpha \equiv \frac{\rho_{gw}}{\rho} = \frac{w}{w_{gw}}, \quad \alpha \geq 1 \tag{3.5.1}$$

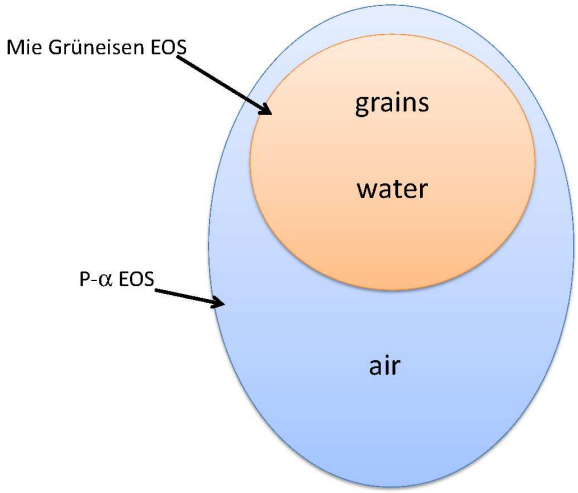

Figure 3.4: A three phase medium modeled by the compaction equation of state $P-\alpha$. This model is described by Wardlaw et al. (1996).

The subscript gw means grain-water and corresponds to a matrix property. $\alpha = 1$ means the soil does not have any air. It is fully compacted and saturated. This distention parameter highlights the irreversible volume change.

For $\alpha > 1$, the sound speed of the porous material is defined as a linear function of porosity according to the sound of speed c_{gw} of the fully compacted soil, and to c_{el}, the bulk sound of speed of the initial soil, with its initial porosity:

$$c = c_{gw} + (c_{el} - c_{gw})\frac{\alpha - 1}{\alpha_0 - 1} \tag{3.5.2}$$

When $\alpha = 1$, $c = c_{gw}$ is calculated from the Mie Grüneisen relations.

The $P-\alpha$ equation of state makes a link between the properties of the grain-water mixture and the properties of the porous medium. It has the following form, expressed by Carroll and Holt (1972):

$$P(\alpha, \rho, u) = \frac{1}{\alpha} P_{gw}(\rho_{gw}, u) \tag{3.5.3}$$

The $P-\alpha$ model is illustrated in figure 3.5. As for any elasto-plastic material, the porous material first experiences an elastic zone, and once the elastic limit is reached, the porous medium undergoes some hardening. The elastic limit increases progressively with the hardening. Meanwhile, the slope $dP/d\alpha$ tends to the infinity obtained for $\alpha = 1$.

The elastic slope of the $P-\alpha$ curve is given by:

$$\frac{d\alpha_{el}}{dP} = \frac{\alpha^2}{\rho_{isen}\, c_{gw}^2}\left(1 - \frac{1}{h^2}\right), \quad h = 1 + \frac{c_{el} - c_{gw}}{c_{gw}}\,\frac{\alpha - 1}{\alpha_0 - 1} \tag{3.5.4}$$

$$\alpha_{el}(P, \alpha_{min}) = \alpha_{min} + \frac{d\alpha_{el}}{dP}(\alpha_{min})(P - P_{min}) \tag{3.5.5}$$

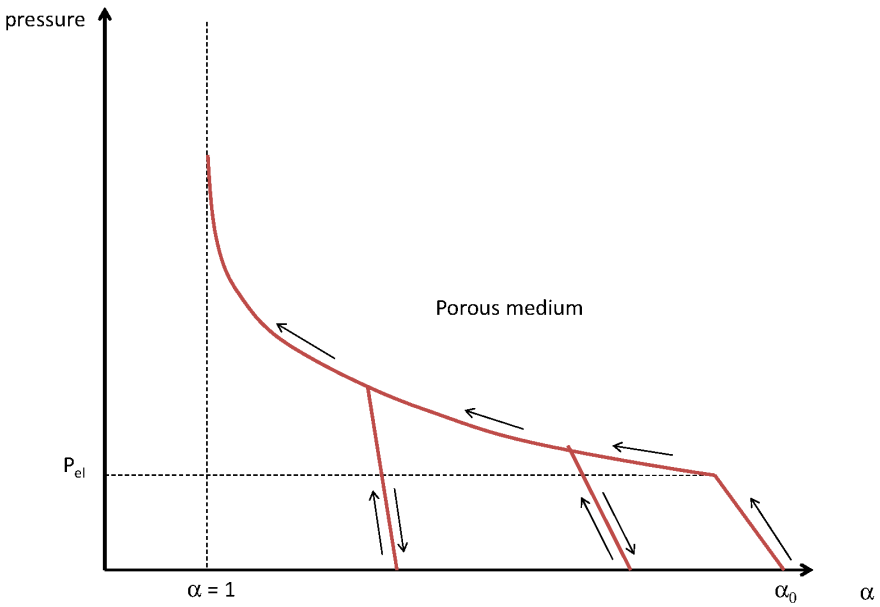

Figure 3.5: The $P-\alpha$ model. P is the pressure of the grain-water mixture. α is the ratio of this mixture phase over all the phases. When $\alpha = 1$, no air remains in the medium: the soil is fully compacted. For $\alpha > 1$, some porosity exists inside the medium.

The equation for the plastic zone (Wardlaw et al. (1996)) is given by:

$$\alpha_{pl}(P) = 1 + (\alpha_{el} - 1)\left(\frac{P_{gw} - P}{P_{gw} - P_{el}}\right)^2, \quad P_{pl}(\alpha) = P_{gw} - (P_{gw} - P_{el})\left[\frac{\alpha - 1}{\alpha_{el} - 1}\right]^{1/2} \tag{3.5.6}$$

For the elastic part of the curve $P-\alpha$, equation (3.5.5) can be rearranged to give the expression of P_{el}:

$$P_{el}(\alpha, \alpha_{min}) = P_{pl}(\alpha_{min}) + \frac{\alpha - \alpha_{min}}{d\alpha_{el}/dP(\alpha_{min})} \tag{3.5.7}$$

α_{min} corresponds to the elastic limit. $\alpha > \alpha_{min}$ corresponds to the elastic part whereas $\alpha < \alpha_{min}$ corresponds to the plastic part.

3.5.3 Non saturated soils modeled by equations of state

Non linear elastic pressure-volume relations for each phase of the soil have been used by various authors (An (2010), An et al. (2011), Wang et al. (2004), Fiserova (2006)).

In this model, the soil is considered as a three phase medium with grain particles, water and air. The pressures of the constituents are not uniform unlike in the compaction models, but each phase has its own pressure.

The pressure of air is calculated considering adiabatic conditions:

$$P_a = P_0\left(\frac{V_{a0}}{V_a}\right)^{\gamma_a} = P_0\left(\frac{\rho_a}{\rho_{a0}}\right)^{\gamma_a} \tag{3.5.8}$$

with P_0 the atmospheric pressure, ρ_{a0} the density of air at atmospheric pressure, and ρ_a the density of air at the pressure P.

The pressures of water P_w and of the grains P_g are non linear elastic equations, written in a similar form as the expression of the pressure of air.

$$P_w = P_0 + \frac{\rho_{w0}\, c_{w0}^2}{\gamma_w}\left[\left(\frac{\rho_w}{\rho_{w0}}\right)^{\gamma_w} - 1\right] \tag{3.5.9}$$

$$P_g = P_0 + \frac{\rho_{g0}\, c_{g0}^2}{\gamma_g}\left[\left(\frac{\rho_g}{\rho_{g0}}\right)^{\gamma_g} - 1\right] \tag{3.5.10}$$

The volume fraction of phase $k = a, w, g$, is noted $n_k = V_k/V$. a is for air, w for water and g for grain respectively, the sum of the volume fractions equals 1 at each time :

$$n_g + n_w + n_a = 1 \tag{3.5.11}$$

Besides the ratios like ρ_k/ρ_{k0} may be written in different ways

$$\frac{\rho_k}{\rho_{k0}} = \frac{M_k}{M_{k0}}\frac{V_{k0}}{V_k} = \frac{M_k}{M_{k0}}\frac{v_{k0}}{v_k} = \frac{M_k}{M_{k0}}\frac{n_{k0}}{n_k}\frac{V_0}{V} \tag{3.5.12}$$

where v_k is the volume content which can be defined like

$$v_k = \frac{V_k}{V_0}, \quad n_k = v_k\frac{V_0}{V} \tag{3.5.13}$$

This model assumes no diffusion of matter (water and gas in relation to the grains) nor transformation of the state of water (vaporization or condensation) take place. Thus the mass of each species remains the same: $M_k = M_{k0}$. Therefore relations (3.5.12) can be simplified to

$$\frac{\rho_k}{\rho_{k0}} = \frac{V_{k0}}{V_k} = \frac{v_{k0}}{v_k} = \frac{n_{k0}}{n_k}\frac{V_0}{V} \tag{3.5.14}$$

The volume fraction of each phase is given by

$$\frac{n_a}{n_{a0}} = \frac{V_0}{V}\left(\frac{P_a}{P_0}\right)^{-1/\gamma_a} = \frac{\rho_{a0}}{\rho_a}\frac{V_0}{V} \tag{3.5.15}$$

$$\frac{n_w}{n_{w0}} = \frac{V_0}{V}\left(\frac{\gamma_w(P_w - P_0)}{\rho_{w0}c_{w0}^2} + 1\right)^{-1/\gamma_w} = \frac{\rho_{w0}}{\rho_w}\frac{V_0}{V} \tag{3.5.16}$$

$$\frac{n_g}{n_{g0}} = \frac{V_0}{V}\left(\frac{\gamma_g(P_g - P_0)}{\rho_{g0}c_{g0}^2} + 1\right)^{-1/\gamma_g} = \frac{\rho_{g0}}{\rho_g}\frac{V_0}{V} \tag{3.5.17}$$

From equation (3.5.11), a relation on the pressures of each phase can be written

$$n_{a0}\,\frac{V_0}{V}\left(\frac{P_a}{P_0}\right)^{-1/\gamma_a} + n_{w0}\,\frac{V_0}{V}\left(\frac{\gamma_w(P_w - P_0)}{\rho_{w0}c_{w0}^2} + 1\right)^{-1/\gamma_w} + n_{g0}\,\frac{V_0}{V}\left(\frac{\gamma_g(P_g - P_0)}{\rho_{g0}c_{g0}^2} + 1\right)^{-1/\gamma_g} = 1 \tag{3.5.18}$$

Another equivalent relation can be written on volume contents considering

$$\rho_0/\rho = V/V_0 = v_a + v_w + v_g \tag{3.5.19}$$

such as

$$v_a+v_w+v_g = n_{a0}\left(\frac{P_a}{P_0}\right)^{-1/\gamma_a}+n_{w0}\left(\frac{\gamma_w(P_w-P_0)}{\rho_{w0}c_{w0}^2}+1\right)^{-1/\gamma_w}+n_{g0}\left(\frac{\gamma_g(P_g-P_0)}{\rho_{g0}c_{g0}^2}+1\right)^{-1/\gamma_g} \tag{3.5.20}$$

3.5.4 Kandaur model

Many works refer to the concept of Kandaur (Henrych (1979)) for the modeling of a three phase soil with equations of state (Wang et al. (2004), An (2010, 2011), Fiserova (2006)).

In fact, three independent pressures P_a, P_b and P_c and two independent volumes (V_s and V_p) are defined. P_a corresponds to the frictions between solid particles, P_b is the sum of the water and air pressures whereas P_c is the pressure associated to the bonds between particles.

As for the volume V of the soil, it is equal to the sum of the two volumes V_s and V_p which correspond to the volume of the skeleton (solid grains) and the pores (air and water) respectively.

In the Kandaur model, the pressure of the solid grains P_s is considered equal to the total pressure P of the soil.

Then relations derived in section 3.5.3 are used: Equation (3.5.18) written slightly differently provides a relation between dP_s and $dV = dV_s + dV_p$. The constitutive relation (equation (3.5.10)) provides another relation between dP_s and dV_p which gives a relation between dV_p and dV and thus between dV_s and dV.

Two constitutive relations are proposed for dP_a and dP_b as a function of dV_p. These relations allow to obtain the changes of grain, water and air pressures, dP_s, dP_w and dP_a respectively as a function the total volume dV.

3.6 Development of a model of soil stiffening

Due to the detonation energy, the soil undergoes large stresses (around 10 gigapascals) close to the explosive which stiffens it.

Zakrisson et al. (2012) and Laine and Sandvik (2001) have performed laboratory experiments that show that the material response stiffens significantly as air is expelled/compressed due to the increasing stress levels. These experiments are isotropic (they involve only the mean stress and the volume change), quasi-static and the soil was dry. Their results are reported in figure 3.6. Note that these curves represent the total volume change. The elastic-plastic decomposition remain to be attempted, without additional information.

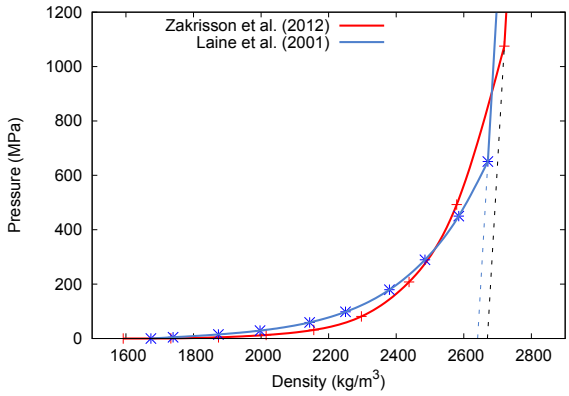

Figure 3.6: Pressure - density curves of Laine and Sandvik (2001) and Zakrisson et al. (2012). These data are based on laboratory experiments. Both curves end with a straight line. It corresponds to a soil state so compacted where all the air has been expelled/compressed. Thus the slope of these straight lines is direclty linked to the bulk modulus of the final highly compacted grain-water mixture.

Our stiffening model has been derived from the curve patterns shown in figure 3.6: initially the density of the soil is ρ_0 and the bulk modulus is K_0. When the detonation initiates, the pressure increases exponentially with the density; then all the air is expelled/compressed while the water is trapped. The soil is packed and the curve tends to a straight line defining a bulk modulus K_{wg} equal to the bulk modulus of grains and water weighted by their volume fractions. The shear modulus is derived from the Poisson's ratio which is kept constant, and from the bulk modulus. The elastic moduli thus become pressure dependent.

3.6.1 Relation between the soil bulk modulus and the soil pressure

In this part, we define the expression relating the bulk modulus K of the soil to the pressure P of the soil which is equal to the third of the soil stresses.

Density, pressure and temperature are related, which can be expressed as follows:

$$\ln \frac{\rho}{\rho_0} = \frac{P}{K(P)} + c_T(T - T_0) \tag{3.6.1}$$

with c_T the coefficient of thermal expansion. Isothermal conditions are considered and the density-pressure relation can be written

$$\ln \frac{\rho}{\rho_0} = \left(1 + \frac{a}{1 + b < P >}\right) \frac{P}{K_{wg}} \tag{3.6.2}$$

where ρ_0 is the initial density. K_{wg} is the final bulk modulus of the soil when the air has been expelled. K_{wg} depends on the bulk moduli of solid grains and water and on their

proportions. $< P >$ can be defined as

$$< P >= \begin{cases} P & \text{if} \quad P > 0 \\ 0 & \text{if} \quad P \leq 0 \end{cases} \tag{3.6.3}$$

with $P = I_1/3 = -\text{tr}\boldsymbol{\sigma}/3$[1]. The bulk modulus is related to the pressure and density as:

$$K = \rho \frac{dP}{d\rho} = \frac{dP}{d\ln\rho} \tag{3.6.4}$$

Derivation of the secant relation (3.6.2) yields the tangent bulk modulus,

$$K = \frac{K_{wg}}{1 + \dfrac{a}{(1 + b < P >)^2}} \tag{3.6.5}$$

The parameter a is

$$a = \frac{K_{wg}}{K_0} - 1 \tag{3.6.6}$$

where K_0 is the initial bulk modulus (at zero stress).

To obtain the parameter b, we need an experimental curve of soil stiffening or at least one point (ρ^*, P^*). The parameter b can be written

$$b = \frac{1}{< P^* >} \frac{a}{\dfrac{K_{wg}}{P^*} \ln \dfrac{\rho}{\rho_0} - 1} - \frac{1}{< P^* >} \tag{3.6.7}$$

The stiffening curve is therefore totally defined thanks to equations (3.6.5), (3.6.6) and (3.6.7), and to one experimental point (ρ^*, P^*).

3.6.2 Bulk modulus of the grain-water mixture K_{wg}

We are now going to define more precisely the bulk modulus of the grain-water mixture K_{wg} involved in equation (3.6.5).

The parameter K_{wg} can either be expressed in terms of volume fraction of water or with the water content since we assumed that the air has been expelled/compressed, and that the step of air expulsion takes place at constant water content, the same from the beginning to the end of detonation. In the following, we use the superscript ∞ for the final value of the parameters, that is when air is totally expelled/compressed.

Let us consider the final volume fraction of water $n^\infty = V_w/V^\infty$. We can write it differently in relation to parameters which are available during the entire simulation:

$$n_w^\infty = \frac{w\,\rho_g/\rho_w}{1 + w\,\rho_g/\rho_w} \tag{3.6.8}$$

[1]Actually in a porous medium context the total stress should be replaced by the effective stress.

w is the mass water content defined in equation (1.1.7).

Once the final volume fraction of water is known, the bulk modulus K_{wg} can be obtained if it is written in the following manner

$$K_{wg}(w) = K_g(1 - \sqrt{n_w^\infty})^2 + K_w\, n_w^\infty \tag{3.6.9}$$

K_g is the bulk modulus of soil grains. For grains made of quartz this parameter is equal to 36 GPa. K_w is the bulk modulus of water which is equal to 2 GPa.

Relation (3.6.9) is illustrated in figure 3.7.

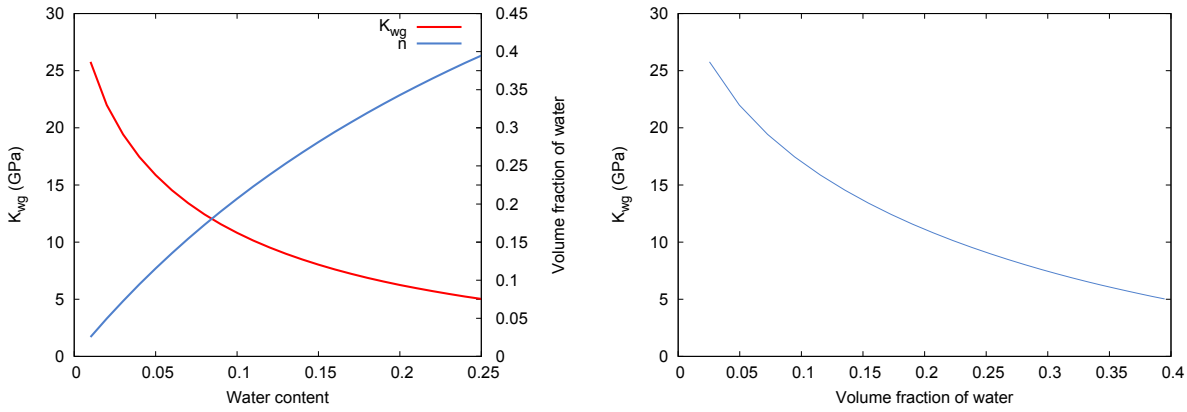

Figure 3.7: On the left, bulk modulus of the grain-water mixture K_{wg} and volumetric fraction n_w^∞ in relation to the water content w. On the right, grain-water mixture K_{wg} in relation to volumetric fraction n_w^∞. A density of 2610 kg.m^{-3} was used for the density of the grains.

3.6.3 Dependence of the stiffening curve on the initial void ratio

The soil stiffening curve and the bulk modulus of the grain water mixture have been defined in previous sections. The value K_{wg} can be modified according to the field measure of the soil water content. We also need to have a stiffening curve which depends on the initial state of the soil. As shown in equation (1.1.13), the soil can be described by two quantities, like the void ratio e and the water content w.

In this section, we are going to explain the approach to obtain a stiffening curve for a given initial void ratio e.

First, let us assume that both bulk moduli K_0 and K_{wg} depend on the water content w in the same way, such as

$$K_0(w, e_0) = \frac{K_{wg}(w)}{K_{wg}(0)}\, K_{01}(e_0) \tag{3.6.10}$$

$K_{wg}(0)$ corresponds to the bulk modulus of the grains, which is 36 GPa. However $K_{01}(e_0)$ is not known. The pressure-density curve associated to the largest void ratio e_{max} (or to the smallest density) will help us to build this dependence.

3.6.3.1 Stiffening curve for the largest void ratio e_{max}

We are interested in the stiffening curve for the largest void ratio e_{max}. So we have to give a value to $K_{01}(e_{max})$ for equation (3.6.10).

According to typical values of Bardet (1997) for Young's modulus and Poisson's ratio (tables 3.1 and 3.2), bulk moduli for loose sandy gravel rank between 33 to 100 MPa whereas they rank from 67 to 133 MPa for the same dense soil. We chose 100 MPa for loose sandy gravel from literature (Tong and Tuan (2007), Grujicic et al. (2009)), and 133 MPa for dense sandy gravel. For the latter soil, literature values were too large (An et al. (2011), Grujicic et al. (2009)) so we chose for $K_{01}(e_{max})$ the maximum value provided by Bardet (1997).

Soil group	Soil type	Bowles (1988)	Cernica (1995)	Converse (1962)	Hallam et al. (1978)	Hunt (1986)
Sand	Loose	10-25	15	10-21	20-80	10-29
	Medium				50-150	29-48
	Dense	50-81	80	52-83	49-78	48-77
	Silty	5-20				
Gravel	Loose	50-150	100			29-77
	Dense	100-200	150	102-204		96-192
Gravel	Without sand				100-200	
	Coarse gravel				150	
	sharp edged				300	

Table 3.1: Young's moduli (Bardet (1997)) expressed in MPa, for various soil types and groups.

Soil group	Soil type	Bowles (1988)	Cernica (1995)	Converse (1962)	Hallam et al. (1978)	Hunt (1986)
Sand	Loose		0.2		0.2-0.35	0.35-0.4
	Medium					0.3-0.35
	Dense	0.3-0.4	0.3	0.3-0.36	0.3-0.4	0.25-0.2
Gravel	Loose		0.2			
	Dense		0.3			

Table 3.2: Poisson's ratios (Bardet (1997)) for various soil types and groups.

In equation (3.6.10), the ratio $K_0(w, e_0)/K_{wg}(w)$ is known thanks to $K_0(e_{max})$. We now need to define a_{min} and b_{min} relative the smallest density (ρ_{min}) due to the largest void ratio e_{max}. a_{min} is obtained from equation (3.6.6)

$$a_{min} = \frac{K_{wg}(w)}{K_0(w, e_0)} - 1 = \frac{K_{wg}(0)}{K_{01}(e_{max})} - 1 \tag{3.6.11}$$

To deduce b, we must select a point (P^*, ρ^*) the stiffening curve must cross.

Two points (P^*, ρ^*) are selected, whether the soil is loose or dense. For a loose soil, the point $(P^*, \rho^*) = (1075\,\text{MPa},\ 1710\,\text{kg.m}^{-3})$ has been chosen from Zakrisson et al.

(2012). For a dense soil, the point $(P^*, \rho^*) = (1075\,\text{MPa},\ 2300\,\text{kg.m}^{-3})$ was selected in order to have positive values of a_{min} and b_{min}.

The expression of b from equation (3.6.7) becomes

$$b_{min} = \frac{1}{< P^* >} \frac{a_{min}}{\dfrac{K_{wg}(w)}{P^*} \ln \dfrac{\rho^*}{\rho_{min}} - 1} - \frac{1}{< P^* >} \tag{3.6.12}$$

Thanks to the expressions of a_{min} and b_{min} in equations (3.6.11) and (3.6.12), the stiffening curve for the largest void ratio e_{max} is defined. Let us now define stiffening curves for other void ratios (necessarily smaller) and other densities (necessarily larger).

3.6.3.2 Stiffening curves for other void ratios

First we have to determine the inverse of expression (3.6.2),

$$P = \frac{1}{2\,b}\left(-(1 + a - b\,c) + \sqrt{\Delta}\right),\ \ \Delta = (1 + a - b\,c)^2 + 4\,b\,c,\ \ c\,=\,K_{wg} \ln \frac{\rho}{\rho_0} \tag{3.6.13}$$

For other densities ρ_{new} with a water content w, the pressure P_0 is calculated solving equation (3.6.13) with parameters a_{min} and b_{min}. Then the new initial bulk modulus is obtained with equation (3.6.5) which becomes

$$K_{0,new}(w, e_0) = \frac{K_{wg}(w)}{1 + \dfrac{a_{min}}{(1 + b_{min}\ < P_0 >)^2}} \tag{3.6.14}$$

The value of the bulk modulus of the grain-water mixture $K_{wg}(w)$ is calculated from equation (3.6.9) with the volume fraction of water defined in equation (3.6.8).

a_{new} and b_{new} are obtained thanks to the new initial bulk modulus $K_{0,new}(w, e_0)$, the bulk modulus of the grain water mixture $K_{wg}(w)$ and the density ρ_{new} to build the new stiffening curve,

$$a_{new} = \frac{K_{wg}(w)}{K_0(w, e_0)} - 1 \tag{3.6.15}$$

and

$$b_{new} = \frac{1}{< P^* >} \frac{a_{new}}{\dfrac{K_{wg}(w)}{P^*} \ln \dfrac{\rho^*}{\rho_{new}} - 1} - \frac{1}{< P^* >} \tag{3.6.16}$$

The point (P^*, ρ^*) may be changed as a function of e_0 such as $\rho^*_{new} = \rho^* \times \rho_{new}/\rho_0$.

We tested various initial void ratios (from 0.2 to 0.33 for a dense soil and from 0.61 to 0.72 for a loose soil) which correspond to the minimum and maximum values provided by Bardet (1997) for sandy gravel, and various water contents (0, 0.5, 1.5, 3, 5, 7.5%). The last one corresponds to the water content used at DGA TT for the saturated STANAG soil which is a sandy gravel. The various curves are presented in figures 3.8 and 3.9.

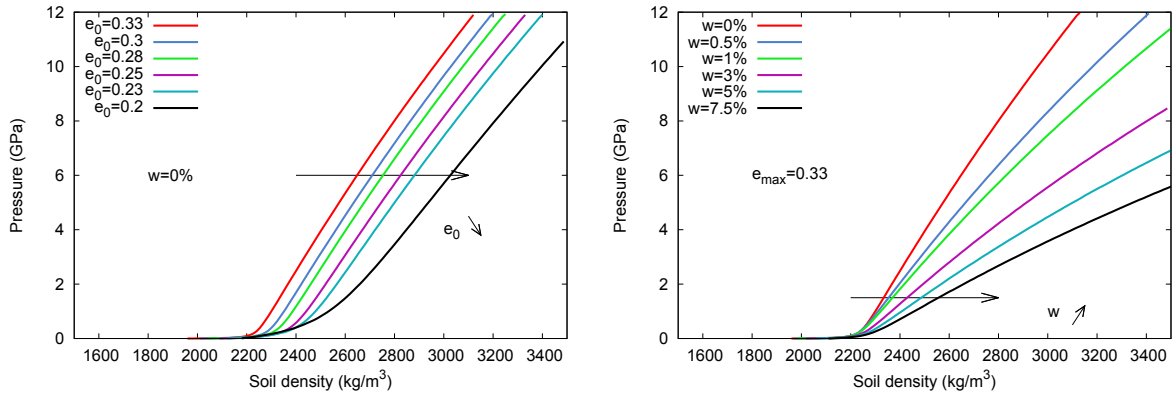

Figure 3.8: Pressure-density curves for dry dense sandy gravel with various initial void ratios (left) and with a maximum void ratio value of 0.33 and various water contents (right).

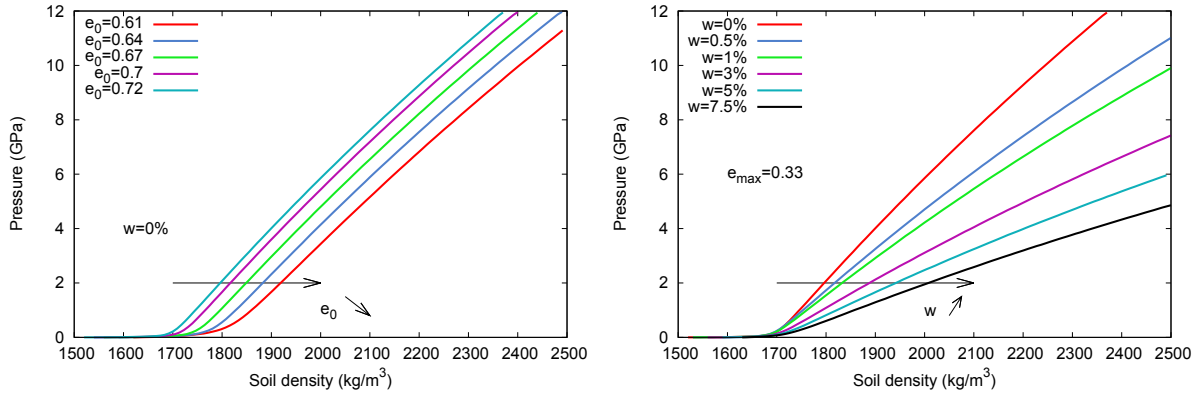

Figure 3.9: Pressure-density curves for dry loose sandy gravel with various initial void ratios (left) and with a maximum void ratio value of 0.72 and various water contents (right).

3.6.4 Parameters of the stiffening curve

Since we did not carry out experimental tests to get the pressure-density curve of our sandy gravel soil, in the following, we took the experimental curve of Zakrisson et al. (2012) shown in figure 3.6 as a reference. Therefrom, we derived the stiffening parameters of table 3.3.

Let us carry out quasi static tests with our non linear viscoplastic cap model (the model is detailed in chapter 2).

For a quasi static regime, the curves of the elastic and the total volumetric strains are drawn in figure 3.10. The total volumetric strain is obtained directly from the strains imposed during the test. The pressure is equal to the third of the trace of the stress tensor. As for the elastic strain curve, it is deduced from the total volumetric strain and the viscoplastic volumetric strain k.

The gap between the elastic and the total volumetric strain curves corresponds to the

K_{wg} (GPa)	K_{01} (MPa)	ρ_0 (kg.m^{-3})	ρ^* (kg.m^{-3})	P^* (MPa)	e_0
36	100	1592	1710	1075	0.64

Table 3.3: Parameters of the stiffening curve derived from the experimental curve of Zakrisson et al. (2012).

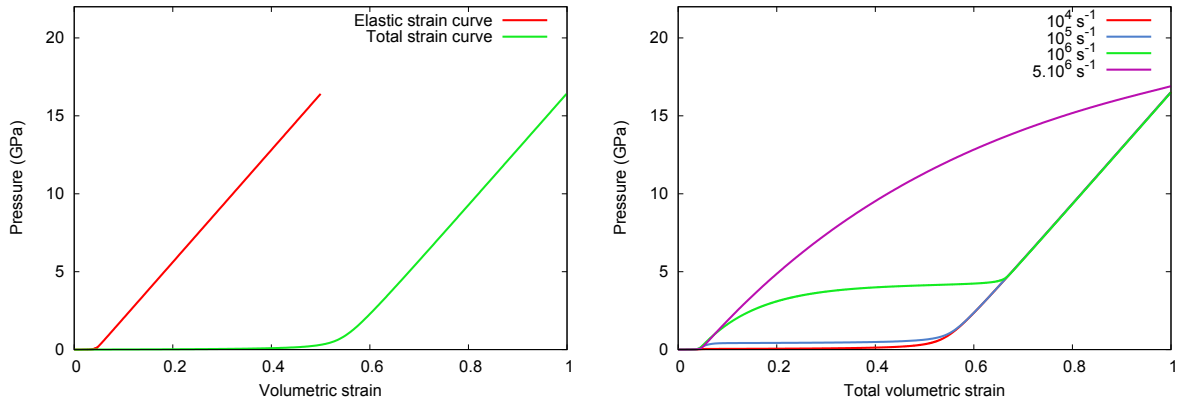

Figure 3.10: On the left, elastic and total volumetric strain, for a quasi static regime. The difference between the two curves corresponds to the volumetric viscoplastic strain k. On the right, total volumetric strain curves for four strain rates (from 10^4 s^{-1} to 5×10^6 s^{-1}. For low strain rates the pressure is low and close to the quasi-static curve. As the strain rate becomes larger, the soil temporarily reacts as if it was elastic. However, as time goes by, relaxation takes place, and the quasi-static (plastic) curve is approached.

viscoplastic volumetric strain k. As stresses become larger, due to the definition of the hardening law (equation (2.3.28)), k tends toward W. The final viscoplastic volumetric strain is thus equal to W. Initially we chose $W = 0.2142$ which is the value provided in Tong and Tuan (2007) to simulate the experiments of buried explosion of Bergeron et al. (1998). The proportion of elastic volumetric strain obtained with $W = 0.2142$ was too important: when the soil pressure reached 10 GPa which is a common value close to the explosive at detonation, the volumetric elastic strain was equal to 60% which is very large. To have less volumetric elastic strain, W was changed to 0.5 which increases the part of the volumetric viscoplastic strain in the total volumetric strain and decreases the elastic part.

Figure 3.10 shows four curves of pressure in relation to total volumetric strain for four strain rates from 10^4 to 5×10^6 s^{-1}. For low strain rates the pressure is low and close to the quasi-static curve. As the strain rate becomes larger, the soil temporarily reacts as if it was elastic. However, as time goes by, relaxation takes place, and the quasi-static (plastic) curve is approached.

Chapter 4

Preliminary finite element simulations

Contents

Chapter 4. Preliminary finite element simulations

This chapter first presents a brief overview of two main testing devices, the Split Hopkinson Pressure Bar (SHPB) and the plate impact. The order of magnitude of the stress and strain rate that can be reached through these devices is much higher than in quasi static regime as shown in figure 4.1. These experiments develop strain rate regimes close to what occurs in an explosion (1 000 - 100 000 s^{-1}).

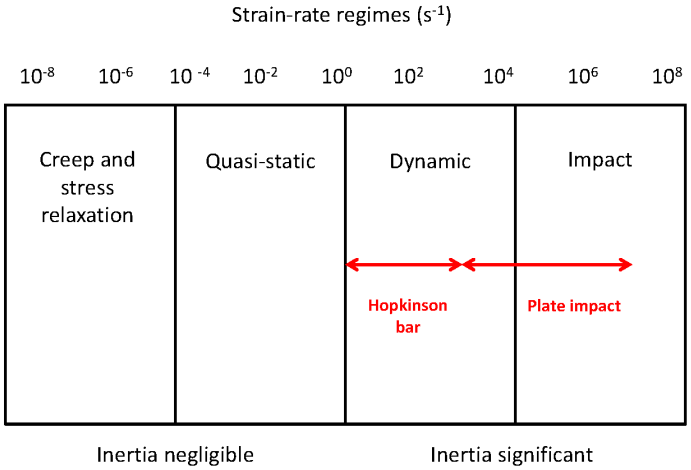

Figure 4.1: Schematic diagram of strain rate regimes and associated techniques (adapted from Curran et al.(1987) and Field et al.(2004)). The Split Hopkinson Pressure Bar and plate impact experiment techniques are two main laboratory setups used to obtain material properties typical of high strain rates.

LS Dyna is the finite element software which has been used during this PhD. So a brief presentation is addressed. Then numerical simulations of SHPB impacts are run with LS Dyna. The objective of these simulations is twofold: becoming familiar with the software, and starting studying the soil numerically, with a simple laboratory example, knowing the kind of results we should expect. The LS Dyna software has already several laws dedicated to soil modeling. SHPB simulations were run, first with metallic samples, then with soil samples to test the two main laws of LS Dyna and to compare with our model. We found out that the elastic moduli are very important and influential on the results.

To study the propagation of waves in soil, we started with simulations without explosive, avoiding the interaction soil/explosive modeling. We applied a small pressure (10 MPa) to a spherical cavity located in an elastic soil, first in an infinite soil medium, to be able to compare theoretical and numerical results, then in a finite soil medium, in order to study issues we met during buried explosion experiments: the free surface (and the possible reflection of the wave at the border between the soil and the air, since the explosive is buried), and reflective borders (corresponding to the borders of the soil tank).

Finally, the propagation of the shock wave during a detonation in a soil was simulated to explore the various options of Eulerian simulations. Two advections methods were studied.

4.1 Soil testing devices at high strain rates

From the 19th century, dynamic tests started developing even if few experimental techniques existed at that time (Field et al. (1994)). At the beginning of the 20th century, Hopkinson designed an experimental device constituted by a long rod (known as Hopkinson pressure bar), in order to study the pulses caused by the impact of bullets. Later in 1949, Kolsky modified the device and placed two rods in a row to measure stress and strain of metallic samples (Kolsky (1949)). During the second half of the 20th century, his device was improved to diversify its application, not only to study mechanical behavior of samples in compression, but also in tension, torsion, and for other materials than metals.

This device is now known as Split Hopkinson Pressure Bar and is often used to characterize dynamic behavior of samples at strain rates between 10 to 10^3 s^{-1}.

For larger strain rates (up to $10^7\,s^{-1}$), plate impact experiments have been developed to study the behavior of samples in a special thermodynamic state where the stresses are so large that the sample almost behaves like a fluid, losing its shear resistance, and equations of state can be applied. Plate impact experiments allow to determine the sound of speed in the sample and the coefficient s, cf. chapter 3.

The Split Hopkinson Pressure Bar and plate impact experiment techniques are briefly described below.

4.1.1 Split Hopkinson Pressure Bar tests

The Split Hopkinson Pressure Bar (SHPB) is an experimental setup that provides the history of axial strains and stresses of a sample at high strain rates.

4.1.1.1 Principle

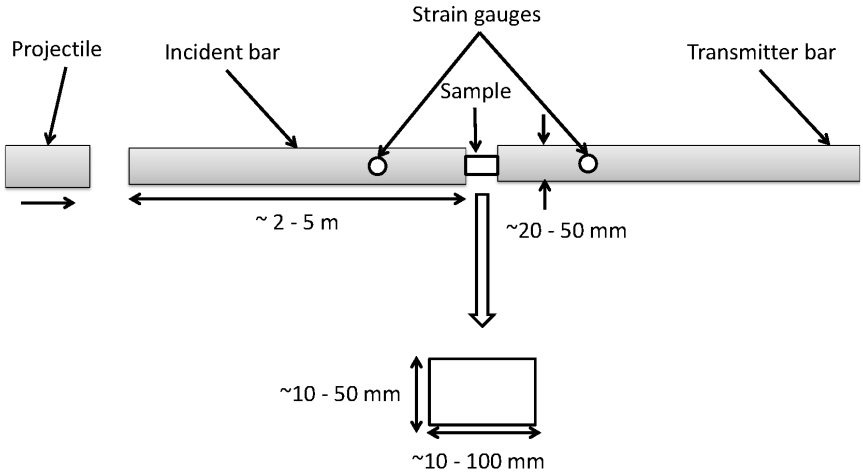

Figure 4.2: The Split Hopkinson Pressure Bar setup consists of 4 parts: a projectile, an incident bar, a transmitter bar and the sample. The sample is sandwiched between the two bars and assumed to remain in contact with them.

The Split Hopkinson Bar setup is composed of a projectile, two bars called the incident bar and the transmitter bar, and a specimen sandwiched between the two bars, as illustrated in figure 4.2.

During a SHPB test, the projectile is launched generally by a gas gun at a speed between ten to thirty meters per second towards the incident bar. The impact leads to the propagation of a compressive wave in the incident bar, and through the specimen which deforms plastically. At the interface between the specimen and the transmitter bar, a part of the pulse is transmitted into the transmitter bar and a part of the pulse is reflected back into the incident bar. Strain gauges are located on the incident bar, and on the transmitter bar to measure the direct incident, reflected and transmitted pulses. The pulses are converted into stresses to get the stress-strain histories of the specimen. The position of the gauges is crucial to avoid overlapped signals. The typical strain signals obtained at both gauges is presented in figure 4.3.

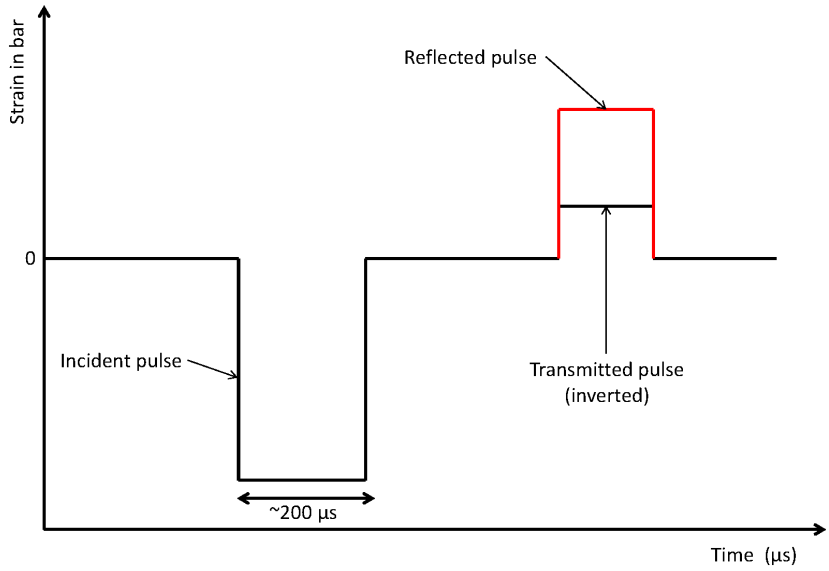

Figure 4.3: Time profiles of the strain for the two gauges (contraction is counted negative).

In order to be able to exploit strain-stress results to study the behavior of the sample, some assumptions must be made. First the stresses in the sample must be homogeneous: the axial and the radial stresses must be uniform in the length of the sample. The material of the bar must be chosen to be considered as elastic so that the waves could propagate without dispersion. In order to study the axial strain-stress behavior, the stress state in the cross sectional area of the bars must be one-dimensional. And finally, to consider a perfect transmission of the signal between the bars and the sample, the interfaces between the bars and the sample must be frictionless. All these assumptions correspond to the basic hypotheses Kolsky made in 1949.

If all these conditions are fulfilled, the equilibrium of the forces applied at the ends of the specimen is assumed. The following relations, based on Meyers (1994), explain how the strain and the strain rate of the sample are deduced from the measurements in the experiments (shown in figure 4.4).

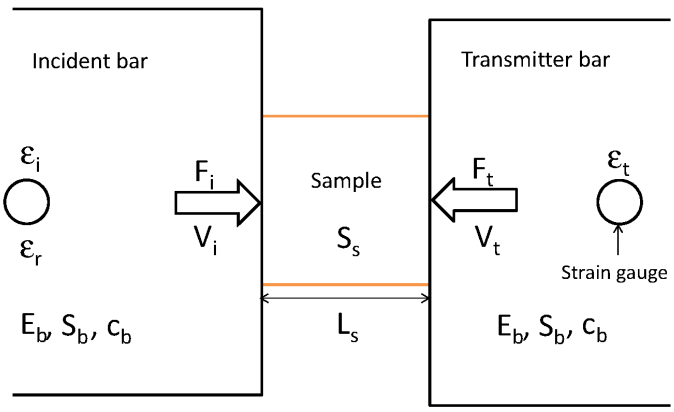

Figure 4.4: Parameters of the bars and the sample used to derive the strain rate in the specimen.

Let us call F_i and F_t the forces applied to the specimen by the incident bar and the transmitter bar respectively:

$$F_i(t) = F_t(t) \tag{4.1.1}$$

The axial stress $\sigma_s(t)$ in the specimen is assumed to be uniform at equilibrium and can be written as follows:

$$\sigma_s(t) = \frac{F_i(t) + F_t(t)}{2\,S_s} \tag{4.1.2}$$

where the section of the specimen S_s is assumed to change little during the test. The two bars are assumed to be elastic, to have the same section and to be made of the same material.

So the force applied by the incident bar to the specimen is the product of the Young's modulus of the bar E_b times its section S_b and times the sum of the incident strain ε_i and the reflected strain ε_r. These two strains are measured on the strain gauge of the incident bar:

$$F_i(t) = E_b\,S_b\,(\varepsilon_i + \varepsilon_r) \tag{4.1.3}$$

The force applied by the transmitter bar to the specimen at the interface is the product of the Young's modulus times the section of the bar, and times the strain measured with the strain gauge of the transmitter bar ε_t:

$$F_t(t) = E_b\,S_b\,\varepsilon_t \tag{4.1.4}$$

So equilibrium (4.1.1) implies

$$\varepsilon_i + \varepsilon_r = \varepsilon_t \tag{4.1.5}$$

and therefore:

$$\sigma_s(t) = \frac{S_b}{2\,S_s}\,E_b\,(\varepsilon_i + \varepsilon_r + \varepsilon_t) = \frac{S_b}{S_s}\,E_b\,\varepsilon_t(t) \tag{4.1.6}$$

The strain rate of the specimen $\dot{\varepsilon}_s(t)$ can be defined as the difference of velocities of the incident bar and the transmitter bar, V_i and V_t respectively, divided by the length of the specimen L_s:

$$\dot{\varepsilon}_s(t) = \frac{d\varepsilon_s}{dt} = \frac{V_i(t) - V_t(t)}{L_s} \tag{4.1.7}$$

The velocity of the incident bar $V_i(t)$ at the interface is expressed as the product of the wave speed in the bar c_b by the difference of the incident strain and the reflected strain:

$$V_i = c_b \left(\varepsilon_i - \varepsilon_r\right) \tag{4.1.8}$$

whereas the velocity of the transmitter bar $V_t(t)$ at the interface is expressed as the product of the wave speed in the bar by the transmitted strain:

$$V_t = c_b \, \varepsilon_t \tag{4.1.9}$$

so

$$\frac{d\varepsilon_s}{dt} = \frac{c_b \left(\varepsilon_i - \varepsilon_r\right) - c_b \, \varepsilon_b}{L_s} \tag{4.1.10}$$

$$\frac{d\varepsilon_s}{dt} = \frac{c_b}{L_s} \left(\varepsilon_i - \varepsilon_r - \varepsilon_t\right) \tag{4.1.11}$$

Using equation (4.1.5),

$$\dot{\varepsilon}_s(t) = -\frac{2\, c_b}{L_s} \, \varepsilon_r \tag{4.1.12}$$

Thus

$$\varepsilon_s(t) = -\frac{2\, c_b}{L_s} \int_0^t \varepsilon_r \, \mathrm{dt} \tag{4.1.13}$$

which leads to the strain and the strain rate of the sample from the properties of the bar and the sample, and from the measure of the strain gauges.

4.1.1.2 SHPB for soil experiments

To study a soil specimen, the SHPB technique must be adapted. First the sound of speed in soils is much lower than in metals (about 400 m/s in sands and about 5000 m/s in steel for example) which implies that the size of the soil specimen must be chosen in consequence, in order to have uniform stresses over the specimen. When the wave enters the specimen, a stress gradient is created between the two faces of the specimen. The uniform stress distribution is reached thanks to the numerous reflections which occur in the specimen. Moreover, the aspect ratio has to be small, the length of the specimen short, and the duration of the applied stress wave long enough. A pulse shaping technique was also developed dedicated to soil experiments: the time of the stress wave is lengthened using a copper or a steel disk plate placed at the end of the incident bar hit by the projectile.

Besides, a soil specimen requires to be confined during the experiments because of the absence of cohesion. But the results of the stress-strain history are changed according

to the stiffness of the material of the holder. The stiffness of the soil specimen is all the more important since the stiffness of the holder is large (Song et al. (2009)).

However, SHPB experiments with soil specimens provide the following results:

- Song et al. (2009) and Felice (1986) found that a dry soil is not sensitive to strain rate. Song et al. (2009) tested soils at 470, 900 and 1450 s^{-1}, whereas Felice (1986) tested strain rates up to 5000 s^{-1}.
- According to Martin et al. (2009) and Ross et al. (1989), the change of the soil stiffness regarding the water content is non monotonic: from dry to partially saturated sand, the soil stiffness decreases. At variance, from a water content of 8 %, the soil stiffness gradually increases. For low water contents, the water helps the sand particles to move more easily. When the water content has increased significantly, the water occupies more space in the sample providing large displacement of air and sand particle from moving, stiffening the sample.
- The initial density of the sand has an effect on the stiffening of the stress-strain history, and is the principal parameter that governs the stress-strain response (Felice et al. (1987), Song et al. (2009)): a sand with a higher density behaves stiffer. These studies were performed with a dry soil.

4.1.2 Plate impact experiments

Plate impact experiments are complementary to Hopkinson experiments. In Hopkinson bar tests, the strain rate involved is less than 10^3 s^{-1} and the stresses are about 100 to 500 MPa. At variance, plate impact experiments involve stresses greater than 1 GPa, and the strain rates can go up to 10^7 s^{-1}.

Plate impact experiments are used to obtain Hugoniot characteristics (the speed of sound c_0 and the coefficient s) of a specimen, when the Hugoniot properties of all the other materials involved in the test are known. The Hugoniot curve (detailed theoretically in chapter 3 and expressed in equation (3.4.11)) is often experimentally simplified to an affine relationship between the shock speed U_s and the particle velocity u_p in the specimen:

$$U_s = c_0 + s\, u_p \tag{4.1.14}$$

The two Hugoniot characteristics c_0 and s are found from the impedance technique also called the reverberation technique which is explained below.

4.1.2.1 The experiment

A plate impact experiment is composed of a projectile and a target. The material of the projectile is generally chosen in relation to its known Hugoniot properties (copper, aluminium, PMMA...). Its dimensions are such that the shock wave produced by the impact in the projectile does not have the time to reflect during the period of interest. Generally between 20 to 30 mm thick, the projectile is mounted on a discarded sabot.

A gas gun gives its initial speed to the projectile which impacts the target under uniaxial strain conditions. The load ranges generally between 1 to 10 GPa. With a

length of several meters and diameters between 50 mm and 110 mm, this gas gun can provide initial speeds from several hundred meters per second up to 1200 m/s.

As for the target, it contains the soil specimen confined between a front and a rear plates with a thickness of a few millimeters (between 3 and 5 mm). These plates are made of the same material as the one used in the target, as illustrated in figure 4.5. The thickness of the soil specimen varies from 3 mm to 15 mm. The diameter of the target is usually the same as the projectile, (between 76 mm and 100 mm) which is dimensioned by the gas gun equipment.

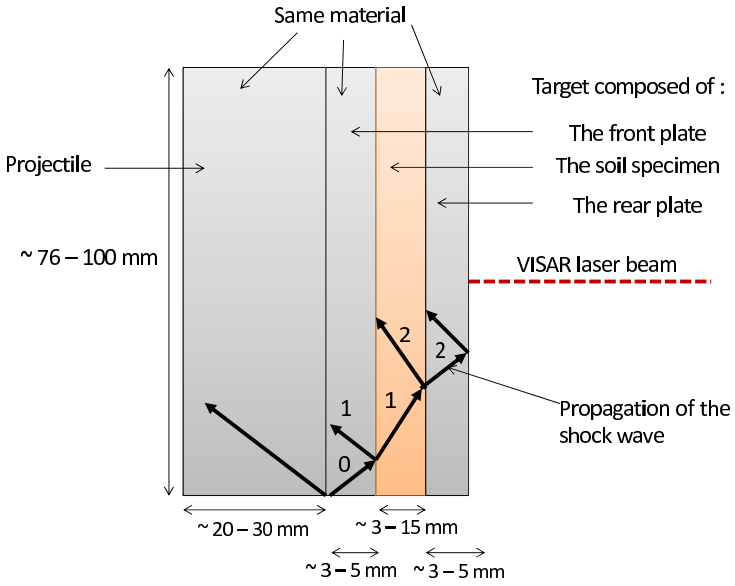

Figure 4.5: Events inside the target after the impact. State 0 : load of the front plate ; State 1 : release of the front plate and load of the soil specimen ; State 2 : reload of the soil specimen and load of the rear plate. Gauges are generally inserted in the front and rear plates to obtain the shock wave speed in the soil specimen.

The front and the rear plates surrounding the soil specimen are generally equipped with gauges (piezo electric pins or manganin stress gauges) to detect the wave motion, and the time of arrival of the shock wave, close enough to the soil specimen to deduce the shock speed in this medium.

On top of recording the shock velocity in the soil specimen, the impact velocity is also estimated and a VISAR (Velocity Interferometer System for Any Reflector) system can be used to record the free surface velocity on the back target. A laser light is emitted and collected by the device after its reflection on the surface of the target. The frequency of the reflected light changes in direct ratio with the velocity of the surface.

These measures allow to characterize the shock and the re-shock states.

4.1.2.2 Impedance matching technique (or reverberation technique)

This technique aims at determining the Hugoniot properties of the specimen and is based on the relations between the impedances of each part of the experiment (the target, the

front and rear plates, and the specimen). The impedance Z is the product of the density times the sound speed of the material i: $Z_i = \rho_i \, c_i$.

For the impedance matching technique, it is assumed that at each interface of the experiment parts (the target, the front and rear plates, and the specimen), the axial components of the particle velocities and the stresses are continuous.

From the continuity of normal stress components at the interface between the projectile and the target, at the shock impact :

$$\sigma_{x_{projectile}} = \sigma_{x_{front\,plate}} \tag{4.1.15}$$

Moreover the normal stress is proportional to the particle velocity u_p :

$$\sigma_x = \rho \, U_s \, u_p \tag{4.1.16}$$

with ρ the density and U_s the shock velocity.

The projectile impacts the target with a velocity V, which corresponds to the velocity of its particles. After the impact, the particle velocity in the compressed region of the projectile is u_{pr} whereas the particle velocity in the compressed region of the target is u_0 such as $V = u_{pr} + u_0$ assuming that the target and the specimen remain in contact.

In equation (4.1.15), the pressure is substituted by its expression:

$$\rho_{pr} \, U_{s_{pr}} \, u_{pr} = \rho_0 \, U_0 \, u_0 \tag{4.1.17}$$

which can also be written using equation (4.1.14)

$$\rho_{pr} \, (c_{o_{pr}} + s_{pr} \, u_{pr}) \, u_{pr} = \rho_0 \, (c_0 + s \, u_0) \, u_0 \tag{4.1.18}$$

Generally the projectile and the plate confining the soil specimen are built in the same material. So $\rho_{pr} = \rho_0$, $c_{0_{pr}} = c_0$ and $s_{pr} = s$:

$$(c_0 + s \, u_{pr}) \, u_{pr} = (c_0 + s \, u_0) \, u_0 \tag{4.1.19}$$

Since $u_{pr} = V - u_0$,

$$(c_0 + s \, (V - u_0)) \, (V - u_0) = (c_0 + s \, u_0) \, u_0 \tag{4.1.20}$$

which gives

$$u_0 = \frac{V}{2} \tag{4.1.21}$$

As a result, when the impact occurs, a shock wave propagates both in the projectile and in the front plate, in a symmetric way.

The impedance match technique is schematically illustrated in figures 4.5 and 4.6.

The projectile has a velocity V. It impacts the front plate. The projectile and the front plate are driven to state 0 (figures 4.5 and 4.6). The particle velocity for this state is known and equal to half the impact velocity. The shock wave propagates in the front plate up to the interface with the soil specimen. This time the front plate and the soil

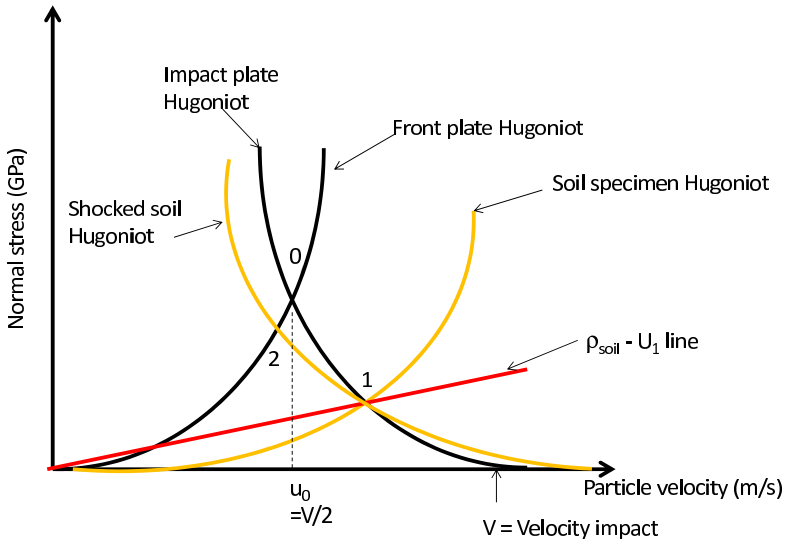

Figure 4.6: Hugoniot curves to obtain soil properties. The numbers are related to the different states defined in figure 4.5. They correspond to intersections between Hugoniot curves of the different parts involved in the plate impact experiment (front, rear plates and soil).

specimen are driven to state 1. This state 1 can be found in figure 4.6 at the intersection between the release Hugoniot of the front plate passing by the state 0 (corresponding to the previous state of the front plate) and the Hugoniot of the soil passing by (0,0). The shock wave moves through the soil specimen and reaches the interface with the rear plate, loading the rear plate and reloading the soil, both to state 2. Finally the shock wave reaches the back surface of the rear plate, and makes it move. This displacement can be measured by a VISAR.

Deduction of Hugoniot parameters

Let us consider state 1. Two parts of the device undergoes this state: the soil specimen and the front plate. This state appears in figure 4.6 at the intersection of the Hugoniot curve of the soil and of the release Hugoniot curve of the front plate. The state 1 is also on the line $\sigma_{x_1} = \rho_{soil} U_1 u_1$ which corresponds to the conservation of the momentum for the soil specimen from equation (4.1.16). U_1 can be obtained from the experiment: gauges are generally inserted in the front and rear plates close enough to the soil specimen to determine the shock velocity U_1 (Chapman et al. (2006), Brown et al. (2007), Bragov et al. (2008)). The release Hugoniot curve of the front plate is known, which provides the value of u_1. The point (U_1, u_1) is thus deduced for a specific impact velocity. The Hugoniot curve of the soil specimen is obtained by repeating this experiment for other impact velocities.

Various authors have studied the plate impact experiments for dry, partially and saturated samples. The relation between the shock and the particle velocities is drawn in figure 4.7. Tables 4.1 and 4.2 provides the values of the Hugoniot parameters (c_0 and

s) with the respective water content of the soil. The curves for dry specimens are rather close, less for partially and saturated samples but the samples do not have the same water contents, which could explain the discrepancy. Besides, Arlery et al.(2010) made a distinction whether the sample is dry or not, and for watered samples, whether the particle velocity is less or more than 750 m/s. As a result they provided three Hugoniot sets of parameters (c_0 and s). Chapman et al. (2006) tested sands with several water contents, and each water content led to a specific set of Hugoniot parameters.

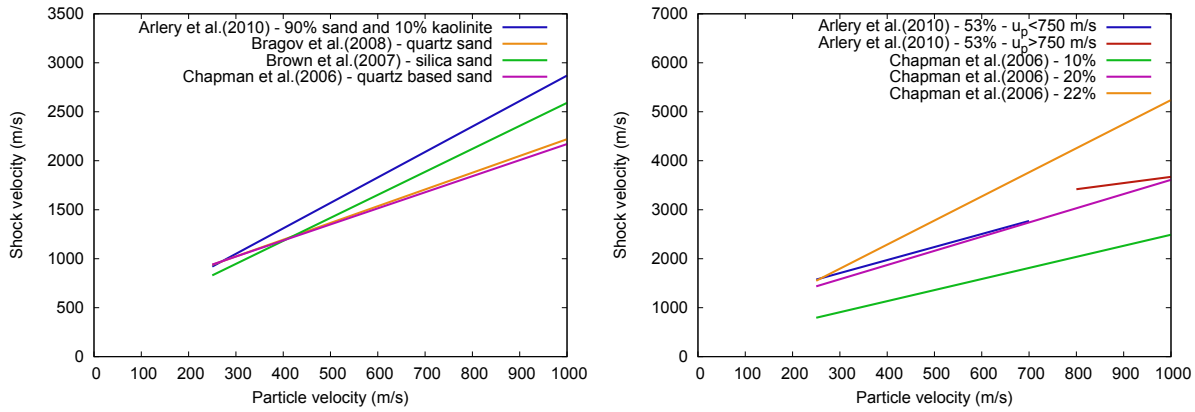

Figure 4.7: Shock velocity - particle velocity from different works with dry soil specimens (left) and with soil specimens with different water contents (right)

water content	density (kg/m3)	c_0 (km/s)	s	correlation coefficient
0 %	1430 ± 50	0.53	1.64	0.899
10 %	1530 ± 50	0.23	2.26	0.971
20 %	1810 ± 50	0.71	2.90	0.951
22 %	1840 ± 50	0.32	4.92	0.979

Table 4.1: Hugoniot data obtained by Chapman et al. (2006) with quartz based sand

Reference	soil composition	water content	density (kg/m^3)	c_0 (m/s)	s
Bragov et al. (2008)	quartz sand	dry	1500	510	1.71
Arlery et al. (2010)	90% sand, 10% kaolinite	dry	1730	270	2.6
		53%	1911	908	2.66 ($u_p \leq 750$ m/s)
				2411	1.26 ($u_p > 750$ m/s)
Brown et al. (2007)	silica sand	dry	1570	243	2.348

Table 4.2: Hugoniot parameters for soil specimen from different works.

4.2 Specific tools for blast available in LS Dyna

The finite element code used in this PhD is LS Dyna. It is a commercial software created by John Hallquist in 1976 at Lawrence Livermore National Laboratory.

This non linear solver allows to run implicit and explicit simulations. Among the various possible applications, dynamic simulations (in the field of automobile, defense, aeronautics ...) can be run thanks to Lagrangian, Eulerian and ALE models.

The conservative equations are solved with the method of centered differences: the velocities are estimated with half a time step shift in relation to the displacements and the accelerations.

The time step of explicit integration scheme must be less than the time physically necessary for a wave to cross an element, in order to ensure the stability of the integration scheme. This time step is given by the condition of Courant Friedrich Levy such as

$$\Delta t_{CFL} = \frac{l_e}{c_e} \tag{4.2.1}$$

with l_e the characteristics length of the element and c_e the sound speed of the material inside the element. The smallest time step of all the elements of a mesh corresponds to the stable time step. To ensure the stability of the integration scheme, LS Dyna applies a scale factor, which is in general equal to 0.9. This factor can be modified by the user.

4.2.1 Soil models

The material laws available in LS Dyna are referenced in the user's manual. The two LS Dyna laws which are of interest for soil simulations are detailed below.

4.2.1.1 The soil and foam model

This model has been tested by various authors (Wang (2001), Swensen et al. (2006), Barsotti et al. (2012)). Wang (2001) used this law to model a buried explosion in soil, in order to reproduce the experiments of Bergeron et al. (1998). These simulations were run with a Eulerian formulation. Swensen et al. (2006) tested the soil and foam model to simulate buried explosions and their effects on structures. Barsotti et al. (2012) modeled buried mine blast with smoothed particle hydrodynamics with this law, reproducing the experiments of Anderson et al. (2009). The parameters of Wang (2001) and Barsotti et al. (2012) are listed in the tables 4.3 and 4.4.

This law is a non linear Drucker Prager plasticity criterion. For this law, LS Dyna requires the density, the shear modulus and the bulk modulus for unloading when a volumetric crushing option is activated. When this option is not activated, the loading and unloading paths are the same. To take into account tension, a pressure cutoff for tensile fracture is required.

Parameter	ρ (kg.m^{-3})	G (MPa)	K (GPa)	a_0	a_1	a_2 (GPa)	p_c (kPa)
values	1600	63.9	30	3.4×10^{-13}	7.03×10^{-7}	0.3	-6.9
Parameter	ε_1 (-)	ε_2 (-)	ε_3 (-)	ε_4 (-)	ε_5 (-)	ε_6 (-)	ε_7 (-)
value	0	0.104	0.161	0.192	0.224	0.246	0.271
Parameter	ε_8 (-)	ε_9 (-)	ε_{10} (-)				
value	0.283	0.29	0.4				
Parameter	P_1 (GPa)	P_2 (GPa)	P_3 (GPa)	P_4 (GPa)	P_5 (GPa)	P_6 (GPa)	P_7 (GPa)
value	0	0.02	0.04	0.06	0.12	0.2	0.4
Parameter	P_8 (GPa)	P_9 (GPa)	P_{10} (GPa)				
value	0.6	0.8	4.1				

Table 4.3: Values of the parameters of Wang (2001) for the soil and foam model of LS Dyna.

Parameter	ρ (kg.m^{-3})	G (kPa)	K (-*)	a_0	a_1	a_2 (GPa)	p_c (kPa)
values	1370	3.6	- *	2.56×10^{-8}	0	0	-34.5
Parameter	ε_1 (-)	ε_2 (-)	ε_3 (-)	ε_4 (-)	ε_5 (-)	ε_6 (-)	ε_7 (-)
value	0	0.005	0.01	0.015	0.02	0.025	0.03
Parameter	ε_8 (-)	ε_9 (-)	ε_{10} (-)				
value	0.06	0.105	0.115				
Parameter	P_1 (kPa)	P_2 (kPa)	P_3 (kPa)	P_4 (kPa)	P_5 (kPa)	P_6 (kPa)	P_7 (kPa)
value	0	200	284	320	360	380	400
Parameter	P_8 (kPa)	P_9 (kPa)	P_{10} (kPa)				
value	440	450	450				

Table 4.4: Values of the parameters of Barsotti et al. (2012) for the soil and foam model of LS Dyna. * no value of unloading bulk modulus: the loading and unloading paths are the same.

The yield function is defined as $f = J_2 - (a_0 + a_1 I_1 + a_2 I_1^2)$, with three constant coefficients a_0, a_1, and a_2 provided by the user. I_1 is the first invariant of stresses whereas J_2 is the second invariant of the devatoric stresses. The yield surface does not harden.

A curve of the evolution of mean stress as a function of the volumetric strain is required. This curve can be obtained from a hydrostatic compression test.

4.2.1.2 The geologic cap model

This law is very close to the model of Tong and Tuan (2007), except that no viscosity is taken into account in the model of LS Dyna. The definition of the yield surface is the same. It is composed of three parts: a cap, a failure envelope, and a tension cutoff. Like the model described by Tong and Tuan (2007), the cap can harden isotropically. Moreover, the failure surface can harden kinematically. 14 parameters are required in this model (the initial density, the bulk and the shear moduli, four parameters for the failure surface, one parameter for the cap surface, one parameter for the cut off surface, three parameters for the hardening law and two parameters for the kinematic hardening).

This law has not been used directly in simulations of buried mines, but the model of Tong and Tuan (2007) is referred to in several papers (Tong and Tuan (2007), Grugijic et al. (2009), An et al. (2011)). Our model is a modification of this law.

4.2.2 The Johnson Cook law

To model the steel plates standing for the belly of vehicles, the empirical law developed by Johnson and Cook (1983) is typically used in the literature. The Johnson Cook law models plasticity with strain rate dependency. It is valid for impact velocities up to 1 km/s.

In this law, the yield stress is expressed such as

$$\sigma_y = \left(A + B\,\bar{\varepsilon}_p^{\,n}\right)\left(1 + c\,\ln\frac{\dot{\bar{\varepsilon}}}{\dot{\varepsilon}_0}\right)\left(1 - T^{*^m}\right) \tag{4.2.2}$$

A represents the initial yield stress, B and n are hardening coefficients. c and m are parameters linked to the strain rate and to thermal softening respectively.

$\bar{\varepsilon}_p$ is the effective plastic strain whereas $\dot{\bar{\varepsilon}}$ is the effective strain rate which can be defined such as:

$$\dot{\bar{\varepsilon}} = \sqrt{\frac{2}{3}\dot{\boldsymbol{\varepsilon}} : \dot{\boldsymbol{\varepsilon}}} \tag{4.2.3}$$

$\dot{\varepsilon}_0$ is a reference strain rate ($\dot{\varepsilon}_0 = 1\,\mathrm{s}^{-1}$), and T^* is equal to

$$T^* = \min\left[\max\left(0, \frac{T - T_0}{T_m}\right), 1\right] \tag{4.2.4}$$

T is the material temperature, T_0 is the ambient temperature, and T_m is the melting temperature. The evolution of temperature is illustrated in figure 4.8.

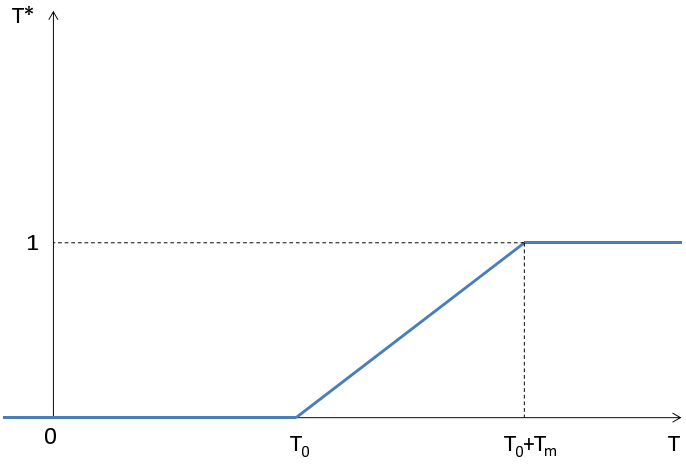

Figure 4.8: Evolution of T^* from equation (4.2.2) in relation with the temperature T.

A (MPa)	B (MPa)	n (-)	m (-)	c (-)
844	622.7	0.164	1.058	0.0087

Table 4.5: Coefficients of Johnson Cook parameters for RHA, Gailly (1996).

Table 4.5 provides the parameters which have been used to model RHA (Rolled Homogeneous Armour, an armour steel) plates.

In LS Dyna, the Johnson Cook law requires to be associated with an equation of state, like the Mie Grüneisen equation of state. The parameters of this equation of state which were used in simulations are provided in table 4.6.

c	s	Γ_0
4578 m/s	1.33	1.67

Table 4.6: Parameters of the Mie Grüneisen equation of state for steel, Steinberg (1996).

4.2.3 Explosive modeling

Explosives are traditionally modeled with the Jones Wilkins Lee (JWL) equation of state derived from the expression of an ideal gas, to take into account the non-idealities of detonation gases. The parameters of this equation are found in Dobratz and Crawford (1985) for many explosives. The JWL equation of state defines the pressure of the detonation products as a function of the specific volume of the explosive V and of the internal energy per initial volume E.

$$p = A\left(1 - \frac{\omega}{R_1\,V}\right)\,\mathrm{e}^{-\mathrm{R_1\,V}} + \mathrm{B}\left(1 - \frac{\omega}{\mathrm{R_2\,V}}\right)\,\mathrm{e}^{-\mathrm{R_2\,V}} + \omega\,\frac{\mathrm{E}}{\mathrm{V}} \tag{4.2.5}$$

$V = \rho_0/\rho$. ρ_0 is the initial density of the solid explosive and ρ is the current density of the explosive. Six parameters are required A, B, R_1, R_2, ω and $E = \rho_0 e_{int}$ where e_{int} is the current internal energy per unit mass.

The pressure before the shock is equal to 0 and the pressure behind the shock is defined by the JWL equation of state weighted by a burn fraction F such as $p = F\ p_{JWL}$. The value of F controls the energy release. At detonation, the time of ignition t_i of each element is calculated by dividing the distance from the detonation point to the center of the element by the detonation velocity D. The burn fraction F is the maximum of the two following expressions:

$$\begin{cases} F_1 &= \dfrac{2\,(t - t_i)\,D\,A_e}{3\,v_e} \\ F_2 &= \dfrac{1 - V}{1 - V_{cj}} \end{cases} \tag{4.2.6}$$

where t is the current time, A_e is the surface and v_e the volume of the element. V is the actual specific volume whereas V_{cj} is the Chapman Jouguet specific volume. This burn fraction calculation is based on the work of Wilkins (1964).

Apart from the JWL equation of state, LS Dyna also requires Chapman Jouguet parameters (the detonation speed D_{cj}, and the pressure P_{cj}) to model explosives.

In all the simulations run in this PhD, two explosives are modeled: the C4 and the TNT explosives. The TNT parameters are taken from Dobratz and Crawford (1985) whereas the C4 parameters are taken from Thompson et al. (2010). Both sets of parameters are listed in table 4.7

Explosive	A (GPa)	B (GPa)	R_1	R_2	ω	ρ_0 (kg.m^{-3})	D_{cj} (m/s)	P_{cj} (GPa)	E_0 (GPa)
C4	609.770	12.950	4.5	1.4	0.25	1601	8193	28	9.0
TNT	371.2	3.231	4.15	0.95	0.3	1630	6900	21	7

Table 4.7: JWL parameters used for all the simulations run in this PhD. The TNT parameters are from Dobratz and Crawford (1985) whereas the C4 parameters are from Thompson et al. (2010).

4.2.4 Air modeling

In LS Dyna, the air is modeled with a polynomial linear equation of state using parameters which correspond to the perfect gas equation. The linear polynomial equation is

$$p = c_0 + c_1\mu + c_2\mu^2 + c_3\mu^3 + (c_4 + c_5\mu + c_6\mu^2)E \tag{4.2.7}$$

where $\mu = \rho/\rho_0 - 1$ with ρ the current density, ρ_0 the initial density. $E_0 = \rho_0 c_v T_0$ with c_v the heat capacity at constant volume. Since the temperature is kept constant, the time evolution of the internal energy may be $E = \rho c_{v_0} T_0$.

In the simulations, $c_0 = c_1 = c_2 = c_3 = c_6 = 0$, $c_4 = c_5 = \gamma - 1 = 0.4$, $\rho_0 = 1.18\,\mathrm{kg.m^{-3}}$. γ is the adiabatic constant.

4.2.5 Lagrangian contacts

For the Lagrangian simulations reproducing Split Hopkinson Pressure Bar tests (section 4.3), contacts are required between the soil and the bars. The contact takes place between two planar faces, with the same surface dimension.

For the contact, first LS Dyna looks for a penetration from one part in the other one. When it happens, a penalty method is applied: virtual springs are created between the slave nodes and their theoretical locations on the master surface, and nodal forces are applied to move the nodes back from the master part.

4.2.6 Transmitting boundaries

In order to simulate an infinite medium, transmitting boundaries have been considered for the outer boundaries of the mesh: they are defined to avoid reflections there. An impedance matching function is computed for the required elements of the mesh, under the assumption that the material law at the boundary is linear.

4.2.7 The Eulerian / ALE method

The Eulerian/ALE method is the same as the Lagrangian formulation but at the end of each time step, once the mesh has been deformed, it is either smoothed for ALE simulations or taken back to its original place for Eulerian simulations (this stage is called smoothing or relaxation step). The history values (momentum, energy, stress tensor and other history variables) are moved to the closest Gauss point (advection step). With this formulation, the problem of crushed mesh disappears. However because of the displacement of the mesh at each time step and the projections of the physical values, the results are less accurate. This is explained in the sketch 4.9. Several Lagrangian steps are possible before the advection step.

For the advection step, two methods are available in LS Dyna: the first order method called Donor Cell and the second order method called Van Leer (LSTC, 2014). Advection algorithms must be monotonic, conservative, non dissipative (to avoid blurring/excessive smoothing) and non dispersive (to avoid creating new extrema).

The Donor Cell algorithm is monotonic, conservative and fast. It is a first order method, so it is very dissipative. The Van Leer algorithm is monotonic, conservative and much slower: it is a second order method, so it is more precise.

On top of these two algorithms, an algorithm of Half Index Shift is always used added to any of the two advection scheme. The algorithm of Half Index Shift consists of the advection of the nodal velocities. It is monotonic and complex but conservative. It

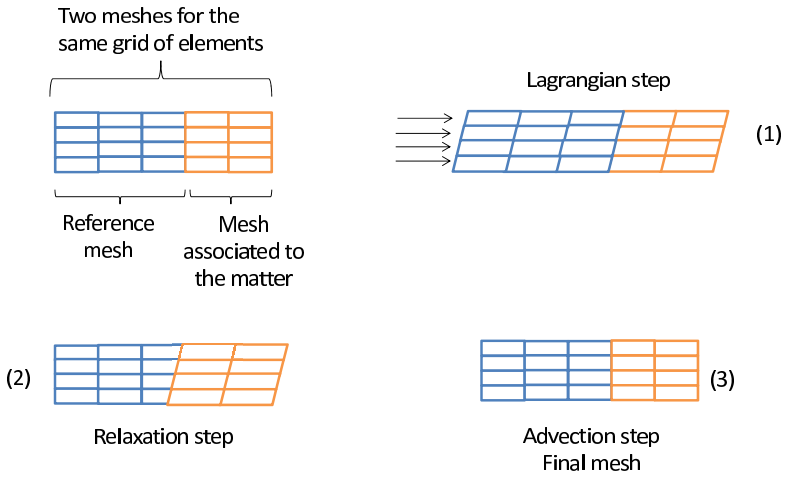

Figure 4.9: ALE/Eulerian formulation: Superposition of two meshes: one spatial reference mesh and one mesh associated to the matter. Step 1: Lagrangian phase: both meshes move simultaneously in the direction of the movement of the matter. The physical quantities are stored. Step 2: Relaxation phase: The grid is fully relaxed and the matter is detached. Step 3: Advection phase: transport of state variable of the matter to the reference mesh; final mesh with the superposition of the two meshes, ready for the new time step (adapted from LS Dyna training by Dyna AS+).

minimizes the dispersion. The principle of this method is to move the nodal values to integration points before the advection, to move them back to the nodes after.

In case of ALE simulations, elements are under integrated, which triggers hourglass, and therefore requires the Hourglass cure.

4.2.8 Eulerian/Lagrangian coupling - Fluid Structure Interaction

When both Lagrangian and Eulerian elements are used in the same simulations, it is necessary to define a coupling between them. This is the case when modeling the detonation of a buried explosive and its effects on a structure above: Lagrangian elements are used for the structure whereas all the other parts (explosive, soil and air) are Eulerian.

This coupling, also called Fluid Structure Interaction (FSI), is defined as a traditional contact, except in this case the master is always the Eulerian part, and the slave the Lagrangian part. It is a penalty coupling: the algorithm looks for penetrations of the Eulerian part inside the Lagrangian one, and applies a proportional effort to make the fluid and the surface interact. A number of points of coupling is defined in each Lagrangian element.

For this interaction, the parameters of LS Dyna which are given by default have been used in all the simulations.

4.3 Preliminary finite element simulations

The aim of this part is twofold: first to become familiar with LS Dyna, the finite element code which will be used later to run numerical simulations of buried mines, second to perform numerical simulations in relatively simple settings corresponding to what has been described in the literature review. The geometries and loadings in these preliminary simulations are as simple as possible so as to entail as much as possible spatial homogeneity. This homogeneity allows to address the influence of material parameters involved in the constitutive equations.

In the literature review, the Split Hopkinson Pressure Bar (SHPB) was referred to as a technique to study high speed impacts and constitutive material responses under high strain rates. In the following, in a first step, we are going to use a detailed analysis reported by Tasneem (2005) on metallic samples to get familiar with the input files and output of LS Dyna. Next, simulations of SHPB involving soil samples have been run in order to test the two LS Dyna soil laws presented in section 4.2.1, and our soil model. All the parameters are taken from literature.

4.3.1 Numerical simulations of SHPB with a metal specimen

The principle of the Split Hopkinson Pressure Bar is detailed in section 4.2, and can be summed up as follows: Split Hopkinson Pressure Bar experiments consist of a specimen sandwiched between two bars called the incident and the transmitter bars. A striker is launched against the incident bar. A wave propagates in the incident bar, in the specimen and in the transmitter bar. At each interface, a part of the signal of the wave is reflected. Strain gauges are placed in the two bars in order to measure incident, reflected and transmitted strains. Considering equilibrium inside the sample and at the interfaces, the strain rate inside the sample can be deduced.

4.3.2 Input data

Since the final objective is to simulate SHPB tests with a soil specimen, the dimensions of the device presented in figure 4.10 are taken from the articles of Song et al. (2009) and Martin et al. (2009) from soil SHPB experiments. In the first simulations, the soil specimen is replaced by an aluminum one. All the mechanical properties have been taken from Tasneem (2005). All the parts of the device (striker, bars and sample) are considered elastic. In LS Dyna, the elastic law requires the density, the Young's modulus and the Poisson's ratio. The aluminum specimen is modeled with a Young's modulus of 68.95 GPa, a density of 2700 $kg.m^{-3}$ and a Poisson's ratio of 0.285, whereas all the other parts are made in steel and modeled with a Young's modulus of 206.91 GPa, a density of 7850 $kg.m^{-3}$ and a Poisson's ratio of 0.3. The element mesh is equal to 2 mm.

Two striker velocities have been tested: 5 m/s and 25.4 m/s. These two values have been been used by Tasneem (2005) (25.4 m/s) for metallic samples and by Song et al. (2009) for soil ones (5 m/s).

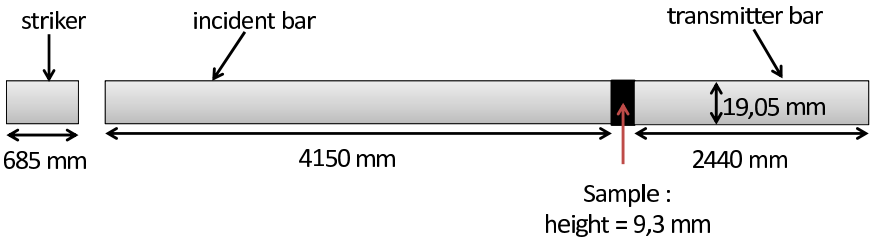

Figure 4.10: SHPB disposal used for the simulations.

4.3.3 Stress propagation in the bars and in the specimen, and evaluation of strain rate

First, in order to control the propagation of the wave along the incident bar, the axial stress was plotted in figure 4.11 in various elements along the incident bar (at 30 cm from the front and the back faces of the incident bar, and in the middle of the incident bar). As shown in this figure, the signal loss along the bar is negligible.

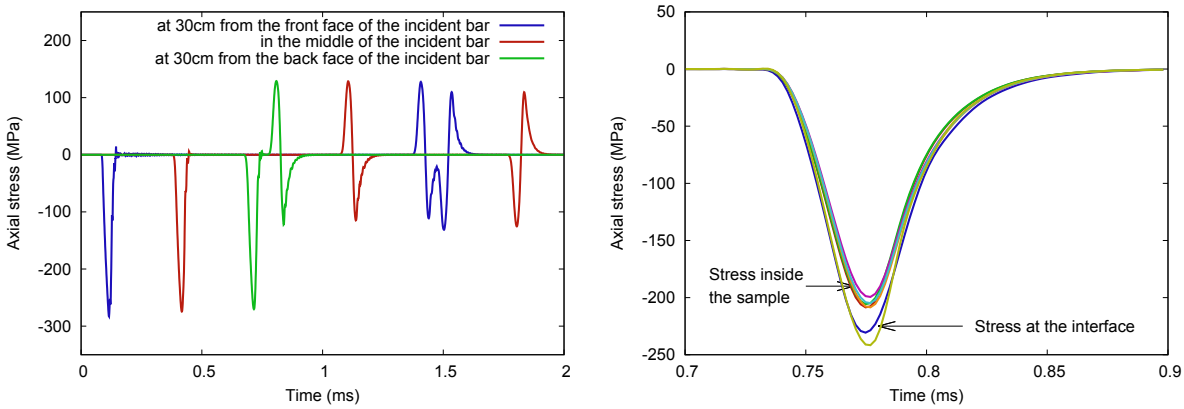

Figure 4.11: Time history of the stress propagation across the incident bar (left) and across the sample (right). The impact velocity was 25.4 m/s.

The signal was also recorded in the sample. Larger stresses were obtained in the elements at the extremities of the sample (figure 4.11): inhomogeneity occured close to the two interfaces with the bars. This may be caused by the vibrations of the contact between the bars and the sample, or by the displacement of the bars due to the propagation of the wave. Except at these interfaces, the stress was well spread across the sample.

In all the simulations, the stresses and the strains were measured in an element in the middle of the incident bar, in the middle of the sample, and at 30 cm from the front face of the transmitter bar, since we can consider that the stresses in each part is uniform except at the interfaces.

The time history of the stresses in the bars and the sample is presented in figure 4.12.

Since the material of the sample is a little less stiff than the bars, a large part of the signal is transmitted to the sample then to the transmitter bar.

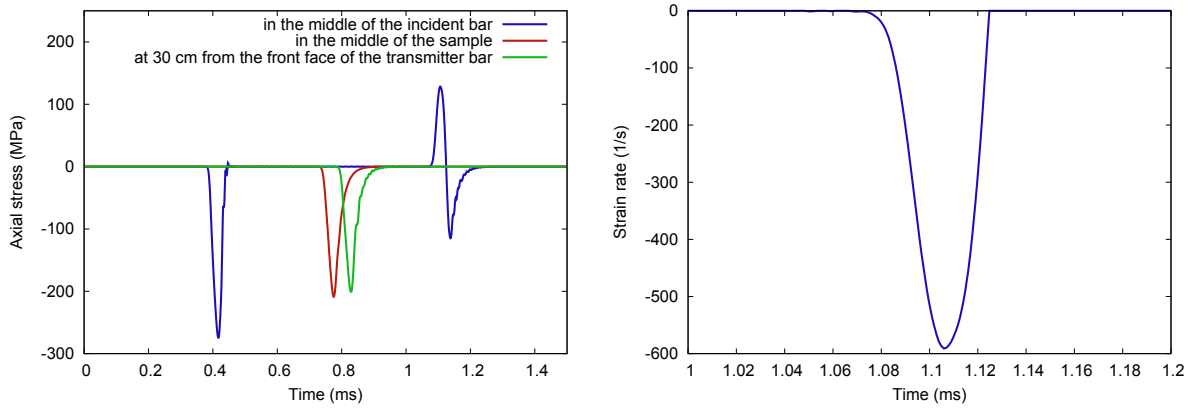

Figure 4.12: On the left, time history of the stresses in the bars and in the sample. On the right, time history of the strain rate in the sample. The impact velocity was 25.4 m/s.

In section 4.1, we saw that if the sample was at the equilibrium, the strain rate in the sample could be expressed by

$$\dot{\varepsilon}_s(t) = -\frac{2\,c_b}{L_s}\,\varepsilon_r \tag{4.3.1}$$

with c_b the sound speed in the bar, L_s the length of the sample and ε_r the reflected strain measured in the incident bar. In our case, except at the interfaces, the stresses are uniformly spread in the sample. The strain rate calculated in the sample using equation (4.3.1) is shown in figure 4.12.

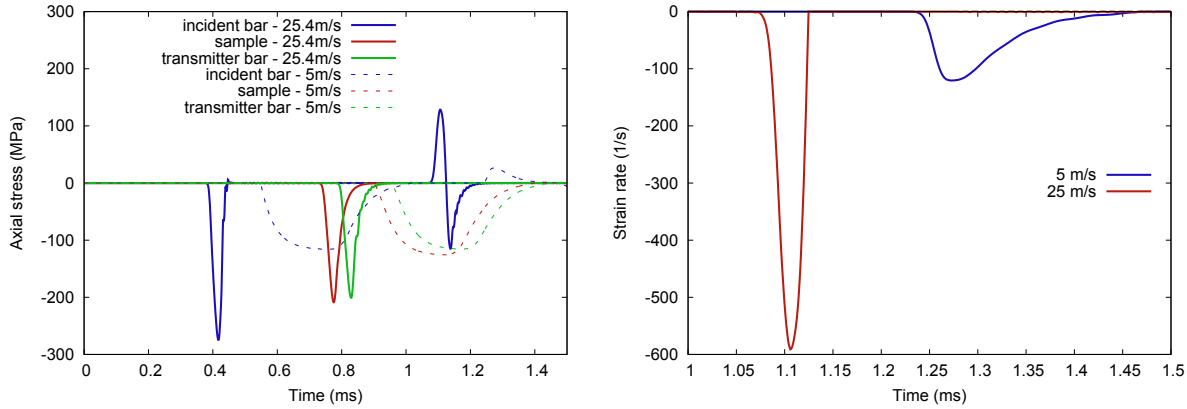

Figure 4.13: On the left, time history of the stresses in the bars and in the sample for two impact velocities (5 and 25.4 m/s). On the right, time history of the strain rate in the sample for two impact velocities (5 and 25.4 m/s).

4.3.4 Influence of the velocity of the striker

Two velocities of striker were tested: 5 and 25.4 m/s.

A slower impact provokes smaller stresses that last longer in the bars and in the sample. In this case, the duration of the contact between the projectile and the incident bar is longer which explains why the stresses last a longer time for a lower velocity of impact, as shown in figure 4.13. The strain rate in the sample is also 5 times smaller.

4.3.5 Numerical simulations of SHPB with a soil specimen

In this section, simulations of SHPB with soil specimens have been run to test the two models of LS Dyna presented in section 4.2.1 and our model. The dimensions of the simulated device remain those presented in figure 4.10.

4.3.5.1 Simulations with the soil and foam law

Wang (2001) and Barsotti et al. (2012) modeled buried mines with the soil and foam law of LS Dyna. So we ran simulations of SHPB impacts with samples of soil defined by parameters taken from these two references. The velocity of the projectile was equal to 5 m/s.

This model consists in a Druger Prager law ($f = J_2 - (a_0 + a_1 I_1 + a_2 I_1^2)$). A curve relating pressure to volumetric strain is required. The initial bulk and shear moduli, and the initial density are also input.

The elastic moduli used by Barsotti et al. (2012) are totally different from those of Wang (2001). The shear modulus of Barsotti et al. (2012) is equal to 3.6 kPa, whereas Wang (2001) used a very large value (30 GPa) which almost corresponds to the bulk modulus of solid grains: the bulk modulus of quartz is equal to 36 GPa. Moreover, the curve relating mean stresses in the soil to the volumetric strains provides a much stiffer soil from the parameters of Wang (2001) than from the parameters of Barsotti et al. (2012).

Small values of elastic moduli lead to a very soft sample. The quasi totality of the wave is reflected back to the incident bar (figure 4.14) and very little signal is transmitted to the second bar.

At variance, with the soil parameters of Wang (2001), the propagation of the wave in the sample is well visible in the history of stresses shown in figure 4.14. With an impact velocity of 5 m/s, the wave crosses the sample during about 0.5 ms, subjecting the sample to about 40 MPa.

Various values of density and of the parameters of the Druger Prager model were tested. Little influence was noticed on the propagation wave in the sample.

What can be concluded from these tests is that the stiffness of the material defined by its elastic moduli and the pressure-volumetric strain curve are very influential on the behavior of the sample, and on the propagation of the wave.

Moreover different impact velocities have been tested with the stiff model of Wang (2001) (3 m/s, 5 m/s, 10 m/s and 16 m/s). This leads to a strain rate of about 250 s^{-1} for an

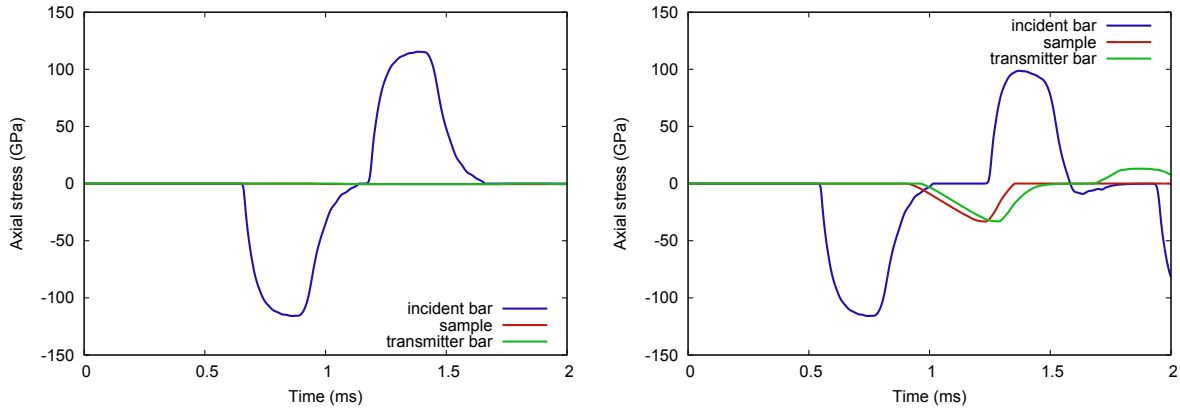

Figure 4.14: On the left, time history of the stresses in the incident and in the transmitter bars, and in the sample, using the parameters of Barsotti et al. (2012): the almost entire signal is reflected to the incident bar. On the right, time history of the stresses in the incident and in transmitter bars, and in the sample using the parameters of Wang (2001). The elastic moduli are larger. The reflection in the incident bar is less important.

impact of 3m/s, 390 s^{-1} for an impact of 5m/s, 750 s^{-1} for an impact of 10m/s and 1050 s^{-1} for an impact of 16 m/s (figure 4.15).

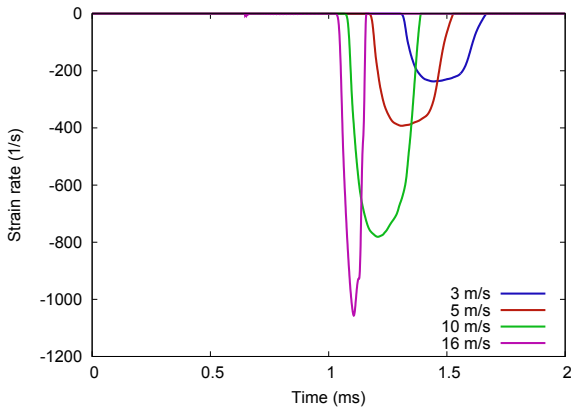

Figure 4.15: Time history of the strain rate in the sample calculated from the reflected strain based on equation (4.3.1) for four different impact velocities of the striker. The soil specimen is described with the stiff model of Wang (2001).

4.3.5.2 Simulations with the geologic cap model

The geologic cap model of LS Dyna is a hardening cap model close to the model described by Tong and Tuan (2007) and An et al. (2011) and to our model. The major difference in the model of LS Dyna remains in the absence of viscoplasticity, and that the failure surface can harden kinematically.

Parameters can be found in Jackson et al. (1980), Tong and Tuan (2007) and An et al. (2011) for this LS Dyna law. In the last two papers, the aim was to simulate buried

mines: in Tong and Tuan (2007) a first data set corresponds to sandy soil to repeat the experiments of Bergeron et al. (1998). A second data set was for clayey soil to repeat experiments of Materials Sciences Corporation (2006). An et al. (2011) considered first data for a dry sand, and second for a saturated sand. As for the data set from Jackson et al. (1980), they are used to model uniaxial strain and triaxial compression tests. All these parameters are in table 4.8.

	Sand Jackson et al. (1980)	Sandy soil Tong and Tuan (2007)	Clayey soil Tong and Tuan (2007)	Dry sand An et al. (2011)	Saturated sand, An et al. (2011)
K	2,500 MPa	106.4 MPa	320 MPa	1,064 MPa	5,000 MPa
G	1,500 MPa	63.85 MPa	200 MPa	63.85 MPa	20.0 MPa
α	3.654 MPa	0.0642 MPa	1.371 MPa	0.0642 MPa	0.0625
β	0.003 MPa^{-1}	0.34283 MPa^{-1}	0.0 MPa^{-1}	0.34283 MPa^{-1}	0.36430
γ	3.5 MPa	0.00589 MPa	0.0 MPa	0.00589 MPa	0.00320 MPa
θ	0.263	0.18257	0.000557	0.18257	0.249
W	0.109	0.2142	0.0993	0.2142	0.2250
D	0.05 MPa^{-1}	0.00952 MPa^{-1}	0.0773 MPa^{-1}	0.00952 MPa^{-1}	0.00884 MPa^{-1}
R	1.5	5.0	4.45	5.0	5.32
X_0	0.3 MPa	0.01 MPa	0.0 MPa	0.01 MPa	0.01 MPa
T	-	0.0069 MPa	0.0 MPa	0.0069 MPa	0.0012 MPa
η	0.002 ms^{-1}	2×10^{-4} μs^{-1}	$0.1 \times 10^{-6} \mu\text{s}^{-1}$	2×10^{-4} μs^{-1}	1×10^{-4} μs^{-1}
N	1.5	1.0	0.8	1.0	1.0
f_0	1.0 MPa	100,000 MPa	1.0 MPa	100,000 MPa	120,000 MPa

Table 4.8: Values of the parameters of Tong and Tuan (2007), An et al. (2011) and Jackson et al. (1980), depending on the soil used.

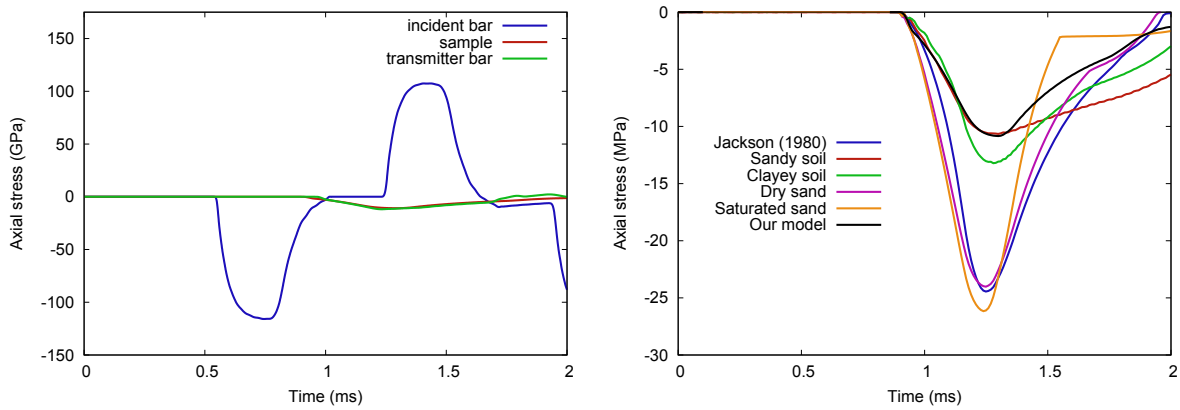

Figure 4.16: On the left, time history of stresses in the bars and in the sample modeled with our viscoplastic cap law. On the right, time history of stresses in the sample for various sets of parameters with the geologic cap model of LS Dyna and with our model.

Figures 4.16, 4.17, and 4.18 illustrate the time histories of stress, strain, strain rate and the stress-strain curve in the sample. All the simulations were run with an impact at 5 m/s and with an initial soil density of 1800 $\mathrm{kg.m^{-3}}$. Whatever the soil parameters are, the strain rate has the same order of magnitude, around 500 $\mathrm{s^{-1}}$. With the parameters of An et al. (2011) and Jackson et al. (1980), the stresses in the sample are twice as much as with those of Tong and Tuan (2007) and with our model. In fact, the bulk moduli of Jackson et al. (1980) and An et al. (2011) are 10 times more important than our initial bulk modulus and what Tong and Tuan (2007) used.

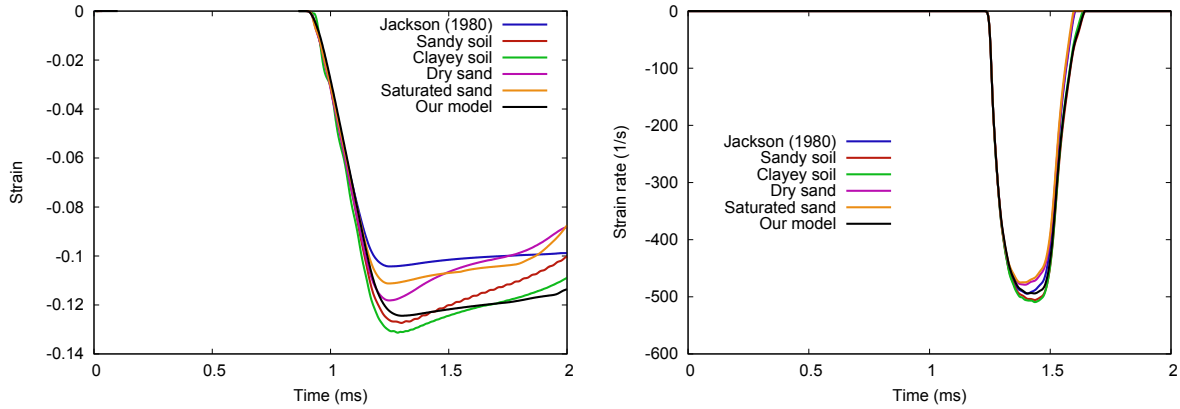

Figure 4.17: On the left, time history of strains in the sample for various sets of parameters with the geologic cap model of LS Dyna and with our model. On the right, time history of strain rates in the sample for various sets of parameters with the geologic cap model of LS Dyna and with our model.

Moreover, simulations were also run with various impact velocities of the striker with our model to get an order of magnitude of the strain rate undergone by the sample. This led to strain rates in the sample in the same order of magnitude as with the parameters of

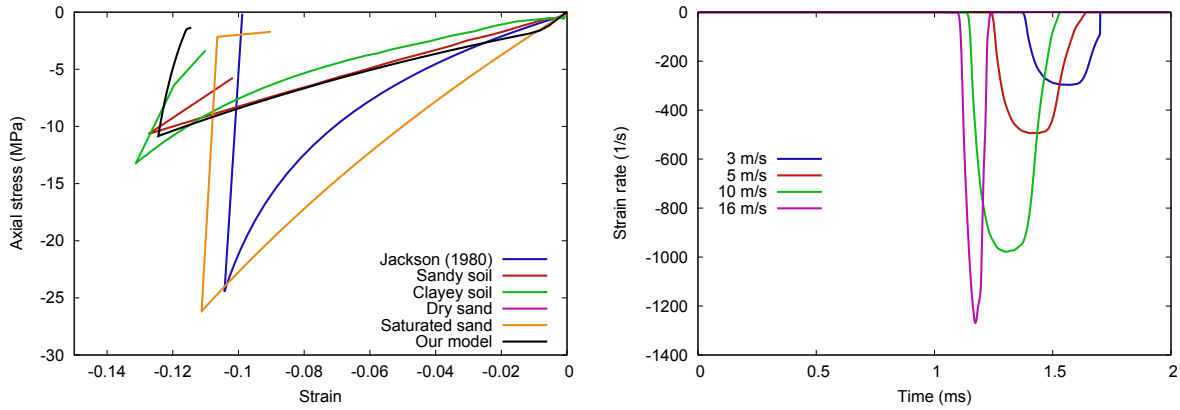

Figure 4.18: On the left, stress-strain curve in the sample for various sets of parameters with the geologic cap model of LS Dyna and with our model. On the right, time history of strain rates in the sample for various impact velocities, with our soil model.

Wang (2001) shown in figure 4.15: about 300 s^{-1} for an impact velocity of 3 m/s, 500 s^{-1} for 5 m/s, 950 s^{-1} for 10 m/s, 1300 s^{-1} for 16 m/s (figure 4.18). A larger impact velocity leads to a larger strain rate in the sample (the maximum value is reached earlier), to a larger value, and to the shortest time duration of the strain rate since the duration of the contact between the projectile and the incident bar is quicker.

4.4 Dynamic loading of a spherical cavity in an infinite or semi-infinite elastic solid

The aim of the simulations here is to study the propagation of waves in soil. Simulations of a pressure applied to a spherical cavity in elastic soil are run. The propagation of the wave is studied at various distances from the cavity up to 9 radii. Two kinds of simulations are run: the pressure is applied to a cavity in an infinite and in a semi-infinite medium. In the first case, the simulations can be compared to the theoretical results. In the second case, the influence of a free surface and of mesh borders can be studied. The free surface is similar to the interface between the soil and air for buried simulations. Borders can lead to reflections like those which occur at the border of a soil tank.

4.4.1 Spherical coordinates

In LS Dyna, all the outputs are given in the Cartesian system. Given the geometry of the problem, it is more interesting to work in polar coordinates. What follows explains the transformations from the Cartesian outputs to spherical coordinates.

We want to study the propagation of waves. Let us pick up either the coordinates of a Gauss point, or of the center of gravity of an element. We have the coordinates (x_1, x_2, x_3) of a given point x. We want to obtain the angles θ and ϕ (figure 4.19).

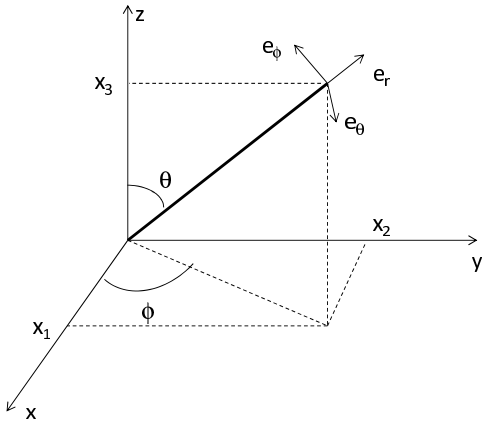

Figure 4.19: Position of the point x with the cartesian coordinates (x_1, x_2, x_3) and the angles $\theta \in [0, \pi[$ and $\phi \in [0, 2\pi[$.

First we have to norm x:

$$\hat{x} = \frac{x}{||x||} = \frac{1}{\sqrt{x_1^2 + x_2^2 + x_3^2}} \begin{pmatrix} x_1 \\ x_2 \\ x_3 \end{pmatrix} = \begin{pmatrix} \hat{x}_1 \\ \hat{x}_2 \\ \hat{x}_3 \end{pmatrix} \tag{4.4.1}$$

$\cos\theta = \hat{x}_3$ gives $\theta = \arccos \hat{x}_3 \in [0,\pi[$ ($\hat{x}_3$ must be between -1 and 1.).

To get the angle ϕ, we have to notice that $\sin\theta \cos\phi = \hat{x}_1$ which leads to $\phi = \arccos\left(\frac{\hat{x}_1}{\sin\theta}\right) \in [0,2\pi[$ if $\theta \neq 0$.

We obtain the spherical vectors which can be expressed in the cartesian axes :

$$\boldsymbol{e_r} = \begin{pmatrix} \sin\theta\cos\phi \\ \sin\theta\sin\phi \\ \cos\theta \end{pmatrix}; \quad \boldsymbol{e_\theta} = \begin{pmatrix} \cos\theta\cos\phi \\ \cos\theta\sin\phi \\ -\sin\phi \end{pmatrix}; \quad \boldsymbol{e_\phi} = \begin{pmatrix} -\sin\phi \\ \cos\phi \\ 0 \end{pmatrix} \tag{4.4.2}$$

To get the polar stresses, we have to apply the stress tensor to the polar vectors of the basis :

$$\begin{cases} \text{radial stress:} & \sigma_{rr} = \boldsymbol{e_r} \cdot \boldsymbol{\sigma} \cdot \boldsymbol{e_r} = \sum_{i,j=1}^{3} \sigma_{ij} (e_r)_i (e_r)_j \\ \text{orthoradial stress:} & \sigma_{\theta\theta} = \boldsymbol{e_\theta} \cdot \boldsymbol{\sigma} \cdot \boldsymbol{e_\theta} = \sum_{i,j=1}^{3} \sigma_{ij} (e_\theta)_i (e_\theta)_j \end{cases} \tag{4.4.3}$$

4.4.2 Dynamic loading of a spherical cavity in an infinite elastic solid

The numerical simulations of the dynamic loading of a spherical cavity in an infinite elastic solid can be compared to the analytical solution.

In order to save computation time, a quarter of model is meshed. The mesh is obtained from an axisymmetric mesh by spinning on 90 degrees. The volume obtained is therefore a cylinder minus the hole representing the cavity as shown in figure 4.20. A first 10 mm

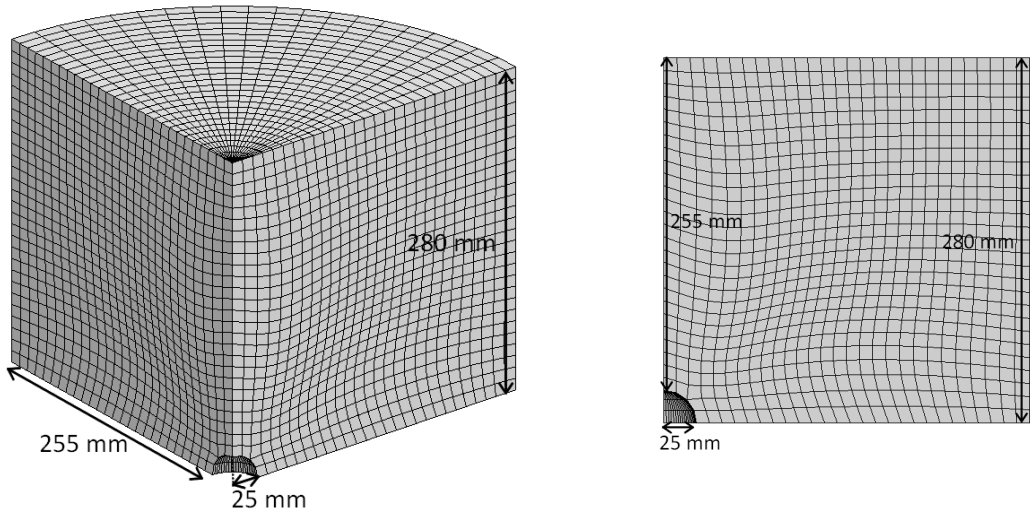

Figure 4.20: Mesh of the infinite solid with a spherical cavity. Left: global view of the mesh. Right: side view of the mesh.

mesh has been chosen to limit the number of elements in the domain. Then, a second and finer mesh of 5mm was tested.

The size of the cavity has been chosen to be closer to experiments already recorded in literature. In the report of Bergeron et al. (1998), the explosives consisted in cylinders of 100 g of C4. If we consider the same charge but with a spherical geometry, the radius of the cavity obtained is 25 mm, which has been chosen as the radius of the cavity for the simulations.

Since we want to analyze the effects up to 9 radii to the cavity, the radius and the height of the soil cylinder are 280 mm.

In order to simulate an infinite medium, transmitting boundaries have been considered for the outer borders of the domain: they are defined to avoid reflections. An impedance matching function is computed for the required elements of the mesh, under the assumption that the material law at the boundary is linear. Since the soil we simulate is modeled by a linear elastic law, we should not have any problem of reflection with the transmitting boundaries.

The soil is modeled with an elastic behavior with the parameters provided in table 4.9 which leads to a longitudinal wave speed of 353 m/s.

Density ($kg.m^{-3}$)	Young's modulus (MPa)	Poisson's ratio (-)
1520	158	0.25

Table 4.9: Elastic soil parameters taken from An et al. (2011), considering a bulk modulus ten times smaller than the value in the article ($K = 106.4$ MPa, and $G = 63.85$ MPa).

In LS Dyna, a smooth approximation of the Heaviside function through a cubic polynomial is available

$$H(t) = \begin{cases} h_0 & t \leq t_0 \\ h_0 + (h_1 - h_0)\left(\dfrac{t - t_0}{t_1 - t_0}\right)^2 \left(3 - 2\dfrac{t - t_0}{t_1 - t_0}\right) & t_0 < t < t_1 \\ h_1 & t \geq t_1 \end{cases} \tag{4.4.4}$$

which is illustrated in figure 4.21.

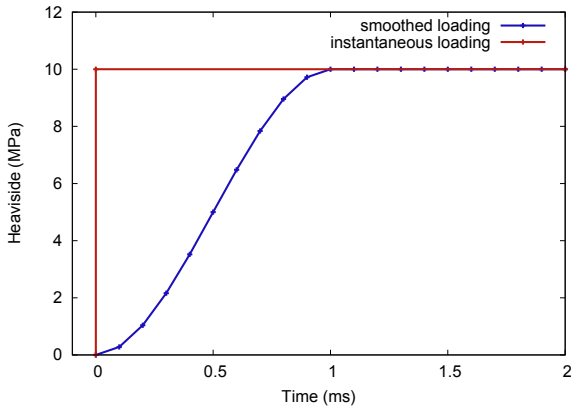

Figure 4.21: Smoothing of the Heaviside step function implemented in LS Dyna.

The approximation of the Heaviside in LS Dyna does not provide an instantaneous loading but a progressive one over a time $t_1 - t_0$. The main advantage of this smoothing is that no oscillation troubles the wave signal (which is the case when an instantaneous loading is used) which can be studied properly.

h_0 is taken equal to 0 and h_1 to 10MPa. Note that this last value is low compared to the values of pressure encountered close to explosives which are in the range of the gigapascal. But the aim here is not to simulate explosion but to study the propagation of the wave. A smaller value is thus not an issue since the material behavior is linear elastic.

In order to test a more realistic Heaviside function, an instantaneous loading was also simulated. It was defined by two points: at $t = 0$, the value of the pressure applied was directly 10 MPa, and with a second point at the infinity with the same value of pressure.

The radial and the orthoradial stress components have been picked up in elements near the cavity and at 1, 3 and 9 radii from the cavity and on two different planes as sketched in figure 4.22.

The simulations were run over 3 ms which leaves the wave to cross the soil medium 3.5 times.

4.4.3 Comparison of LS Dyna Heaviside function results with the analytical expected values

The figure 4.23 illustrates the comparison of the analytical and numerical results for the elements with a barycenter located at 3 and 9 radii from the cavity.

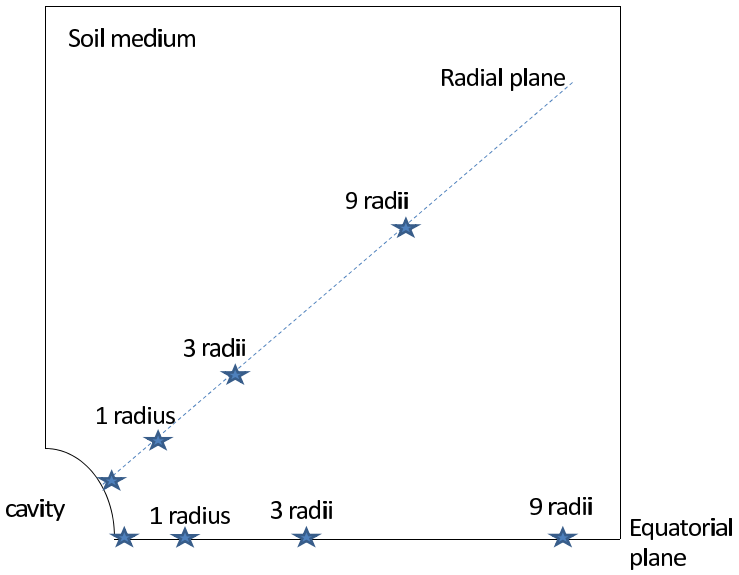

Figure 4.22: Points where the radial and orthoradial stresses are plotted in an infinite medium.

The analytical radial stress begins with a brutal decrease which corresponds to the passage of the dynamic peak to tend toward the static solution. The radial stress is compressive all time long whatever the distance of the element from the cavity is.

As for the orthoradial stress, the analytical signal begins with a compressive peak followed by a tensile peak to finally tend toward the tensile static solution.

On the equatorial plane, the radial and orthoradial stress results are closer to the analytical expected values than on the radial plane. In the radial plane, the wave propagates from one element to the next element diagonally which can lead to dispersion of the signal, whereas in the equatorial plane, the wave propagates horizontally, following the mesh, allowing a better propagation of the signal.

The figure 4.24 illustrates the comparison between analytical and numerical results of radial and orthoradial stresses once the static value is reached. The difference which exists is due to the progressive loading. Thus the maximum value which is reachable dynamically cannot be obtained here.

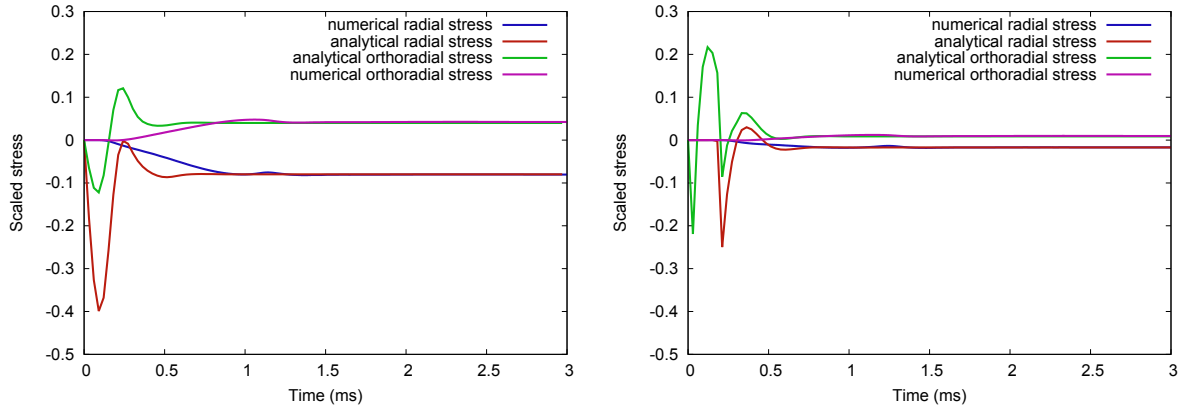

Figure 4.23: Analytical and numerical radial and orthoradial stresses at 3 radii (left) and at 9 radii (right) from the center of the cavity (on the equatorial plane) for scaled stresses with the initial pressure (10MPa).

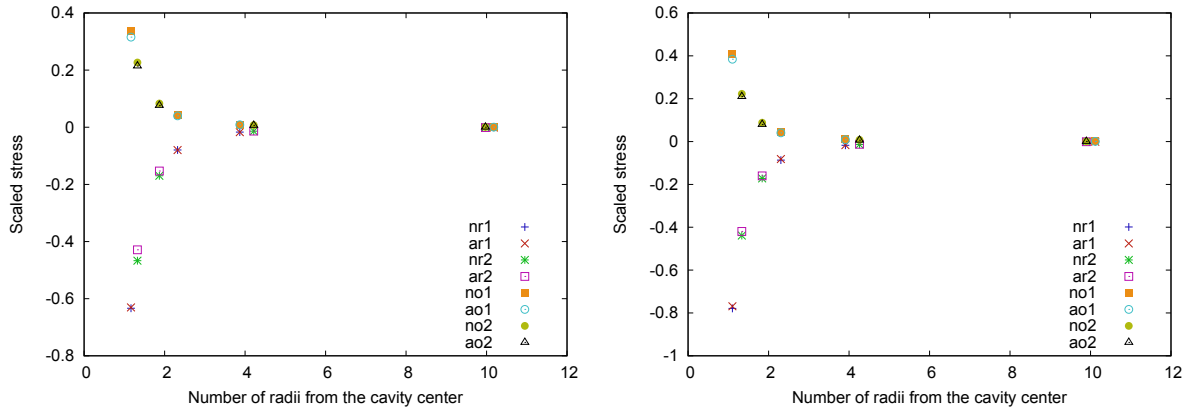

Figure 4.24: Static value of radial and orthoradial stresses at various radii from the cavity center with a mesh size of 10 mm (left) and 5 mm (right). The stresses have been scaled with the initial pressure (10MPa). (n: numerical solution; a: analytical solution; r: peak of the radial stress; o: peak of the orthoradial stress; 1: equatorial plane; 2: radial plane)

4.4.4 Comparison of the (instantaneous) Heaviside function results with the analytical expected values

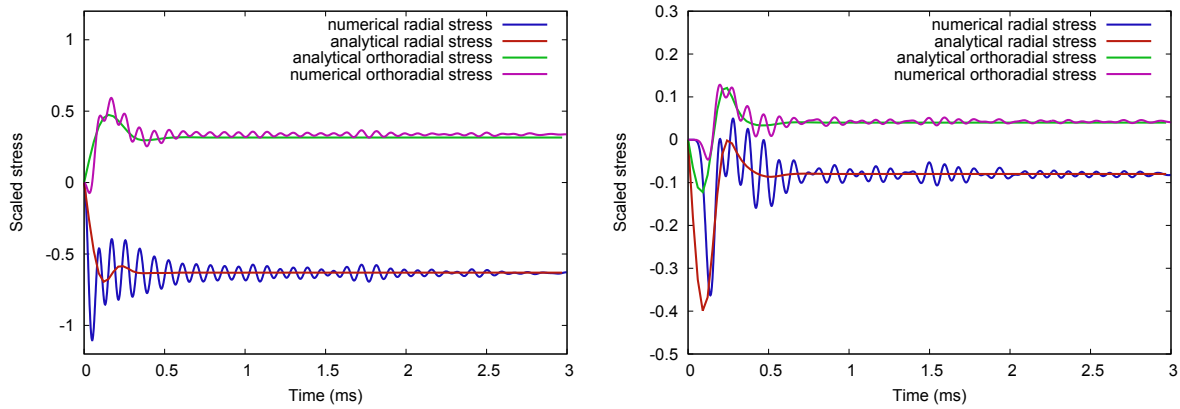

Figure 4.25: Analytical and numerical results of the radial and orthoradial stresses at 3 radii (left) and 9 radii (right) from the center of the cavity (element on the equatorial plane). The stresses have been scaled with the initial pressure (10MPa).

An instantaneous loading leads to results where the peak is well marked and provides the closest results to the analytical solution (amplitude and time of the peak in particular).

But the instantaneous loading also provokes oscillations, which progressively decrease with time and distance. The solution of the instantaneous loading oscillates around the analytical solution as illustrated in figure 4.25. The oscillations are less pronounced with a finer mesh. In the simulations of semi-infinite medium, whether fixed or transmitting boundaries are used, the vibrations prevent to study correctly the wave.

The intensity of the peaks, illustrated in figure 4.26, (compressive for the radial stress, compressive and tensile for the orthoradial stress) decreases with time and distance. But the compressive peak of the orthoradial stress decreases slower than the tensile peak. So away from the cavity, the compressive peak is getting more and more important compared to the tensile peak, to finally at a large distance from the cavity, be greater than the tensile peak.

The times of arrival of the compressive peaks for the radial and the orthoradial stresses on the equatorial and radial planes, shown in figure 4.26, follow the theoretical line given by the longitudinal wave times the distance.

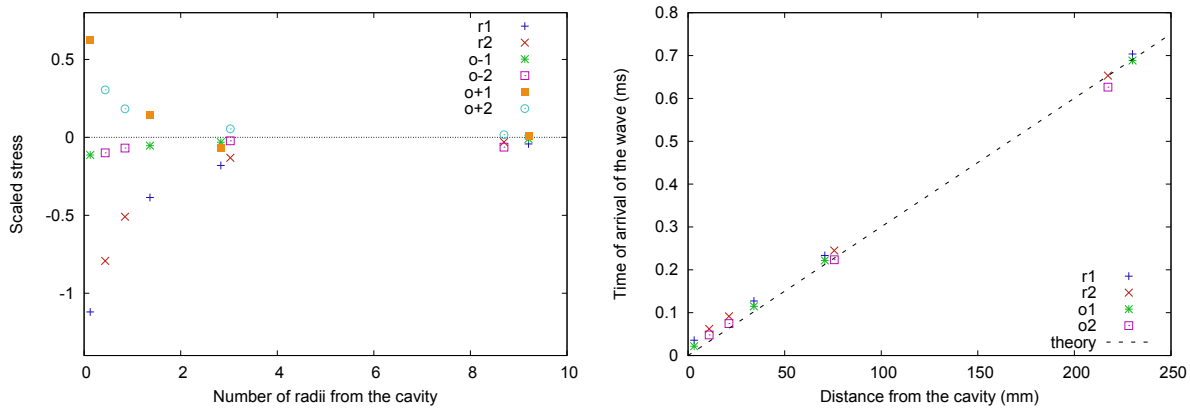

Figure 4.26: On the left, amplitude of the compressive peak for the radial stress, and compressive and tensile peak for the orthoradial stress at various distances from the center of the cavity. The stresses have been scaled with the initial pressure (10MPa). (r: peak of the radial stress; o+: tensile peak of the orthoradial stress; o-: compressive peak of the orthoradial stress; 1: element in the plane passing through the center of the cavity; 2: element in another plane). On the right, time of arrival of the compressive peaks at various distances from the center of the cavity (for the radial and the orthoradial stresses). For both figures the mesh size was 10 mm and the loading was instantaneous, displaying a peak close to the analytical solution.

Stress path

Figure 4.27 illustrates the stress paths in an infinite medium at various distances from the cavity. Close to the cavity, at first, the medium experienced deviatoric compressive stresses. Once the wave is gone, the stress path goes back with a lower slope to finally reach the tension region. At 9 radii from the cavity, after the compressive deviatoric behavior, a tensile deviatoric behavior appears which is in fact due to spurious reflections.

When the static regime is established, the mean stress I_1 vanishes like the volume change.

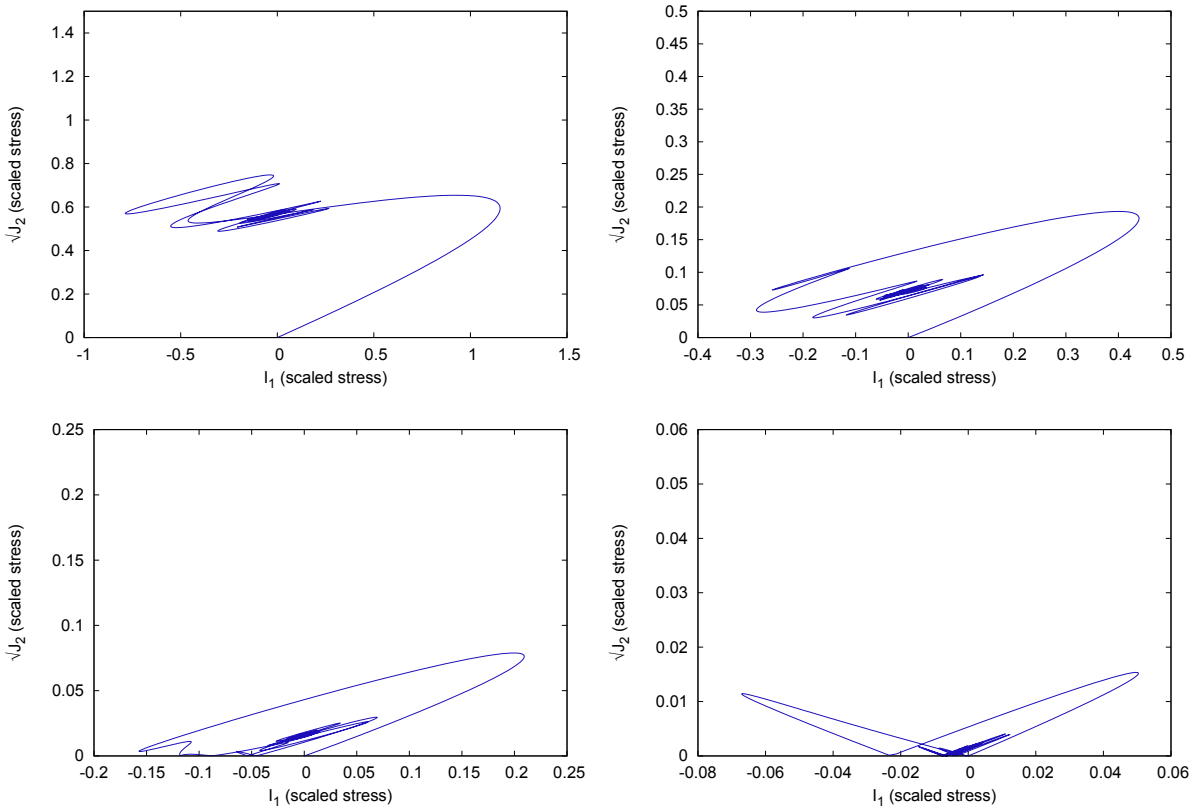

Figure 4.27: Stress path in an infinite medium for an instantaneous loading with a 10-mm mesh for scaled stresses with the initial pressure (10MPa) (near the cavity for the figure on the top left, at one radius from the cavity for the figure on the top right, at 3 radii for the figure on the bottom left, and at 9 radii for the figure on the bottom right).

4.4.5 Dynamic loading of a spherical cavity in a semi-infinite elastic solid

The spherical cavity in a semi-infinite elastic solid allows to study a free surface (which could be the surface between the air and the soil for buried mine simulations) and the reflections (which occur at the border of a soil tank).

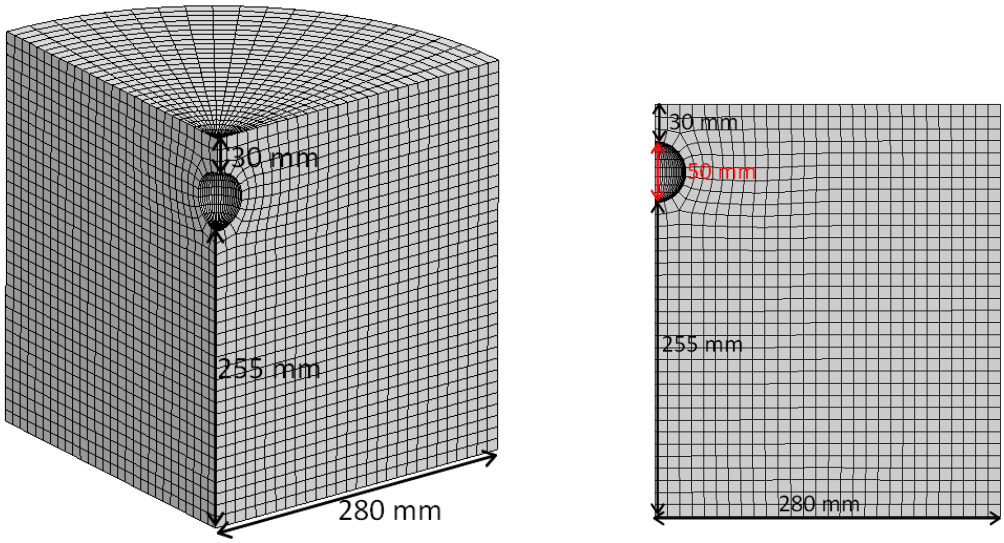

Figure 4.28: Mesh of the semi-infinite solid with a spherical cavity. Left: global view of the mesh. Right: side view of the mesh.

The same size of cavity was kept (with a radius equal to 25 mm). A mesh size of 10 mm was used, and a quarter of the geometry was simulated. The cavity was buried in the soil at a distance equal to 30 or to 80 mm from the free surface. These two distances correspond to the two depths of burial used by Bergeron et al. (1998) in their experiments.

The mesh is obtained by spinning an axisymmetric surface (so the volume obtained is a cylinder). On the top surface of the mesh, conditions of free surface are applied. On the two other surfaces (the external radius and the bottom of the cylinder), two conditions were tested: either transmitting boundaries or fixed boundaries (meaning a zero displacement condition). The first conditions are representative of a free field, whereas the second ones are representative of the border of a test bed.

The radial and the orthoradial stress components have been picked up near the cavity and at 1, 3 and 9 radii from the cavity, on an equatorial plane and on a radial plane as shown in figure 4.29.

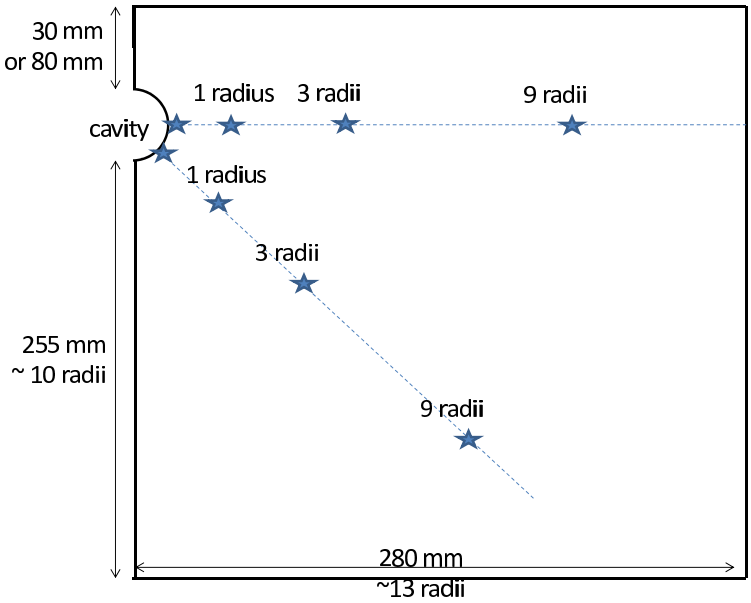

Figure 4.29: Points where the radial and orthoradial stresses are output in a semi-infinite medium ; two planes are considered : the first one passes through the center of the cavity, and the second one is orthogonal to the cavity, following a diagonal in the medium.

4.4.5.1 Influence of the free surface and of the boundary conditions

The simulations run with the semi-infinite medium can provide two kinds of information: first regarding the influence of the free surface on the propagation of waves and second, regarding the effects of the fixed boundaries (on the external radial border and at the bottom of the mesh).

Influence of the free surface

The influence of the free surface seems negligible. It may be responsible for little stress peaks (figure 4.30).

Influence of the fixed boundary conditions

In figure 4.31, the influence of the fixed boundary conditions can be clearly seen. The radial boundary of the mesh is located at 255 mm from the cavity. With a longitudinal speed of 353 m/s, it takes about about 1.44 ms for the wave to go to the boundary and return to the cavity. This can explain the time when the first differences occur between the stress results with fixed and with transmitting boundaries. At one radius from the cavity (so about 25 mm from the cavity), it takes about 1.30 ms for the longitudinal wave to go to the boundary and return to the place of the element. These times can be read in the figure.

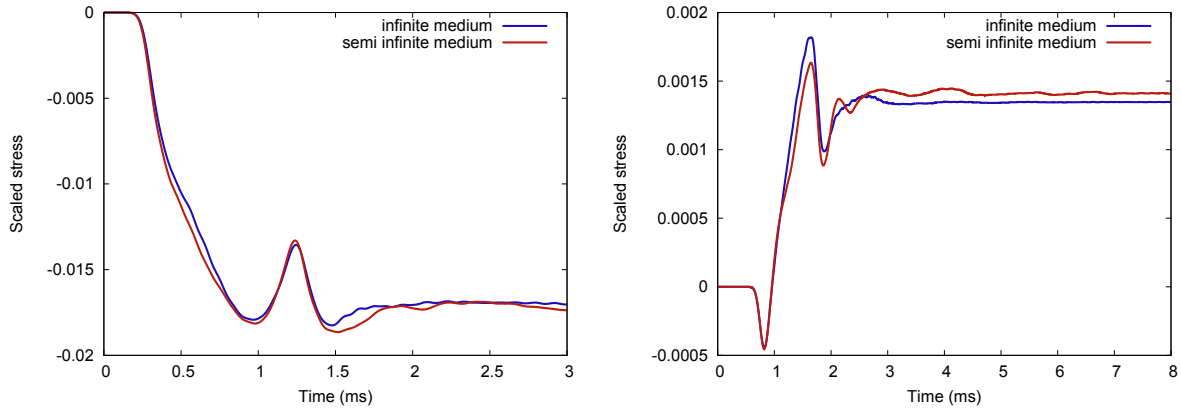

Figure 4.30: Radial stresses at 3 radii (left) and orthoradial stresses at 9 radii (right) from the cavity for the Heaviside loading of LS Dyna. The stresses have been scaled with the initial pressure, 10MPa. Very small peaks can be noticed due to the presence of the free surface which has therefore a negligible influence on stresses. The meshes of the infinite and semi infinite medium do not coincide perfectly which explains some differences on the curves.

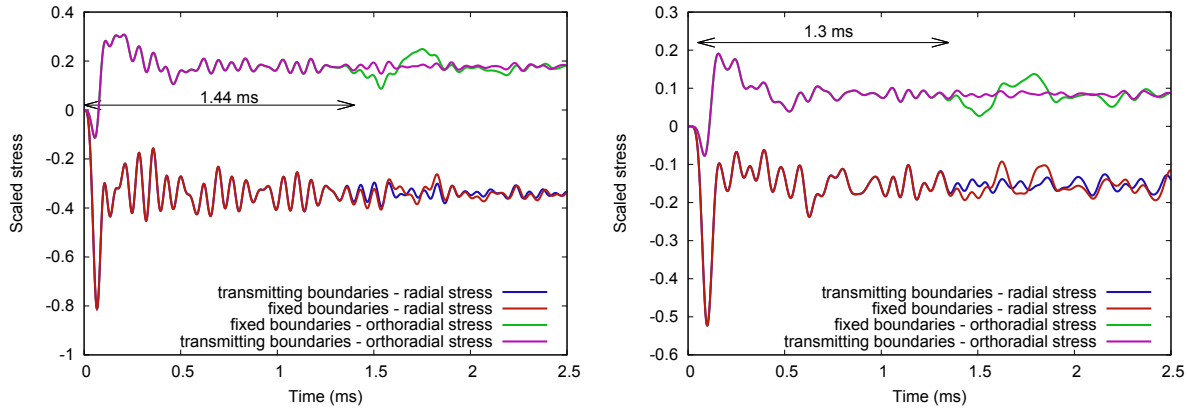

Figure 4.31: Radial and orthoradial stresses close to the cavity (on the left) and at one radius to the cavity (on the right) for an instantaneous loading with transmitting or fixed boundaries. The influence of the boundaries can be cleary noticed on the stresses.

4.5 First Eulerian simulations of explosion in soil

In the following, the aim is to get closer to simulations with buried explosives. Previously, we simulated the pressure inside a cavity in an infinite and in a semi-finite elastic soil medium. Now rather than applying a pressure to a cavity, we simulate the detonation of an explosive. Its radius is the same as in the previous simulations: it is equal to 25 mm and corresponds to 100 g of C4. The explosive is modeled with a JWL equation of state. Its point of detonation is located at the origin of the mesh. The simulations are axisymmetric. They are the opportunity to test Eulerian parameters.

Radial and orthoradial stresses are plotted in the soil at 1, 2, 3, 4 and 10 radii from the interface between the soil and the explosive. The pressure in the explosive is also output at 5, 10, 15 and 20 mm from the detonation point. The mesh domain is 300 mm side to minimize the influence of the borders even when stresses are picked up at 10 radii from the interface with the explosive (so at 250 mm from the interface with the explosive).

An elastic soil model with parameters provided in table 4.9 is chosen. Two boundary conditions are tested: fixed borders (which means that reflections occur) and transmitting boundaries. The two advection algorithms available in LS Dyna are tested (Donor Cell of first order, and Van Leer of second order).

4.5.1 Influence of the boundary conditions

Figure 4.32 shows the time history of radial stresses for fixed and transmitting boundaries. Distinct peaks are visible in the figure. They correspond to reflections on the border of the mesh when fixed boundaries are used. With transmitting boundaries, reflections are less visible, even if they are not completely vanished. However, oscillations which seem purely numerical appear when the transmitting boundaries are used.

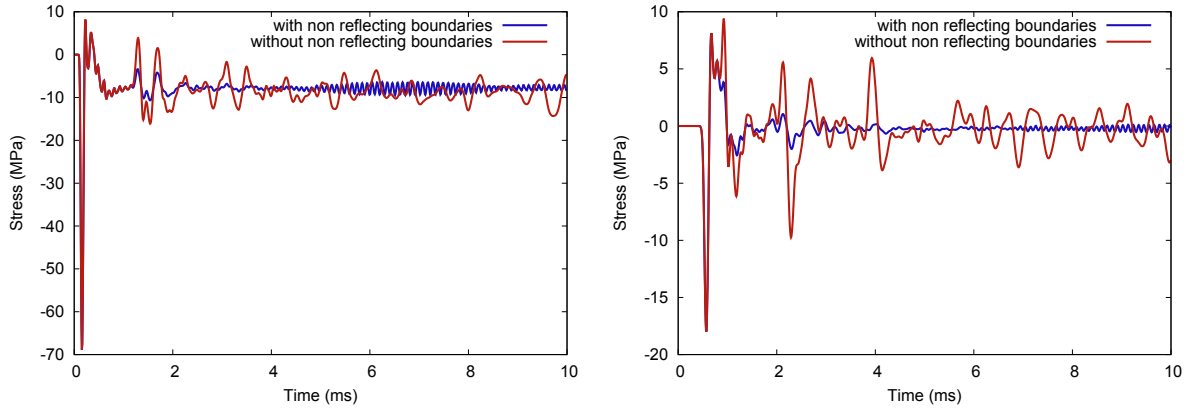

Figure 4.32: Time history of the radial stresses at 100 mm from the explosive or 4 radii from the detonation point (left), and 250 mm from the explosive or 10 radii from the detonation point (right). Simulations are run with fixed boundary conditions (so reflections can occur), and with transmitting boundaries (reflections are prevented).

4.5.2 Influence of the order of the advection method

The influence of the order of accuracy of the advection method can be noticed on the first compression peak provoked by the shock wave in the soil (shown in figure 4.33): the second order method seems to increase the value of the peak, and to produce large oscillations which seem purely numerical.

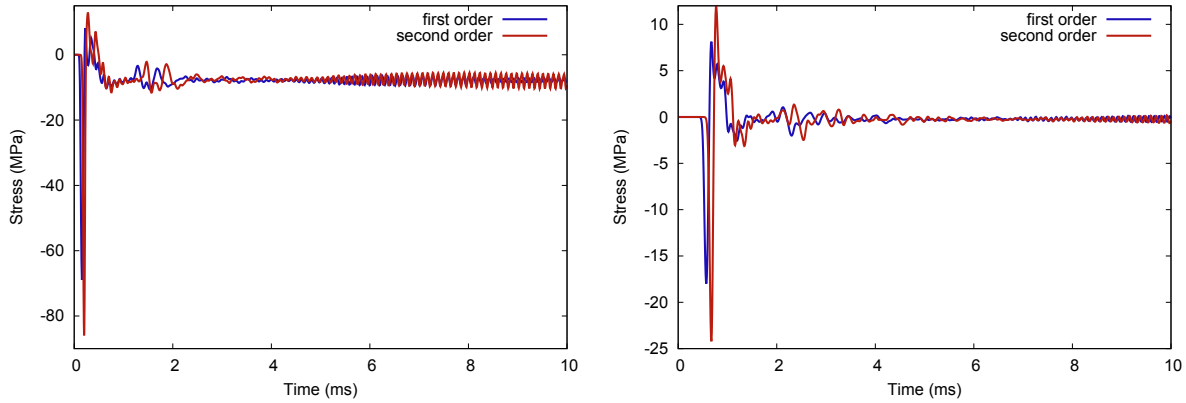

Figure 4.33: Time history of the radial stresses at 100 mm (left) and 250 mm (right) from the explosive for simulations with the first order accurate method and with the second order accurate method.

4.5.3 Propagation of the detonation in a granular soil: simulation of a cylindrical explosion

In order to better understand the interaction between the explosive and the soil, axisymmetric simulations of a disk have been carried out, focusing on the interface explosive/soil.

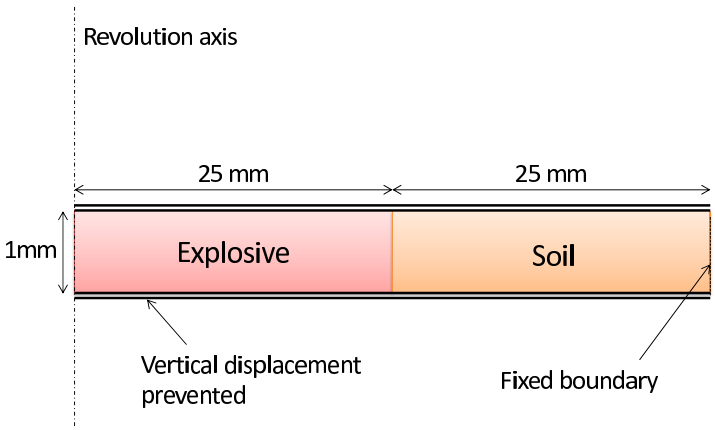

Figure 4.34: Sketch of the simulation for the study of the interaction between explosive and soil.

The simulations consist of the detonation of a disk of explosive and soil. Both are 25 mm long. This value has been chosen because the radius of the explosive in the previous simulations was 25 mm. This length of soil allows to have enough distance to avoid early reflections. Two element sizes are tested (0.1 and 1 mm). The transverse displacements of the top and of the bottom of the mesh are prevented so that the displacement is only allowed radially along the propagation of the shock wave as illustrated in figure 4.34. Besides the radial outer boundary is fixed.

The explosive is modeled with a JWL equation of state. The parameters come from Thompson et al. (2010) and are given in table 4.7. The detonation point is located on the axis of rotational symmetry, at 0.5 mm (which is at the middle of the height of the mesh) in order to have the shock wave as planar as possible.

Our viscoplastic model is used with the parameters provided in table 2.1.

4.5.3.1 Propagation of the shock wave in the explosive charge

The pressure has been output in the explosive at 4 fixed points (at 5, 10, 15 and 20 mm from the detonation point) and is displayed in figure 4.35.

The pressure decreases once the shock wave is gone, but not to zero: it remains at 4.6 GPa for several microseconds at the three first points. This constant pressure is not visible at the last point.

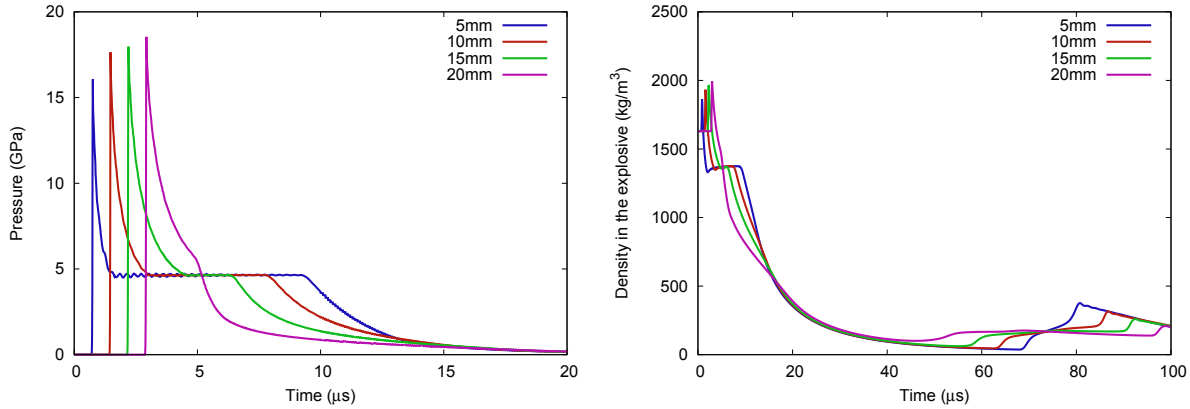

Figure 4.35: Time courses of the pressure (left) and the explosive density (right) in four fixed points in the explosive (at 5, 10, 15 and 20 mm from the detonation point). The pressure in the first three points remains with the same value for a certain time, which corresponds to the time required by the shock wave to go to the interface and come back to the point. The pressure decreases when the gas can expand in the soil. The density of the explosive increases due to the shock wave and decreases towards a very small value (close to 0) because the explosive after the detonation is a gas.

This phenomenon is not visible if the displacements of the top and of the bottom of the mesh are allowed: since the confinement of the explosive charge prevents the detonation products to escape, the pressure cannot decrease to zero. Because of the confinement of the explosive, a large pressure remains until the shock wave has reached the interface

with the soil. At this moment, the detonation products expand which allows the pressure to decrease to a very small value.

Apart from the pressure, the density was picked up in the explosive in the four same points as previously (at 5 mm, 10 mm, 15 mm and 20 mm from the detonation point). The density course is shown in figure 4.35. Once the shock wave has crossed the medium, the density tends to a value which is very small. In fact, this very small value of density (close to 1) shows that once the shock wave is passed, the solid explosive behaves as a gaseous medium.

4.5.3.2 Propagation of the shock wave in the soil

The stresses produced in the soil by the explosion are very high (the order of magnitude is the gigapascal). Such values lead to a stiffening of the soil. Thus its density increases and so should the elastic moduli. However, with the linear elastic law and the geologic cap model of LS Dyna, the elastic moduli keep the same value from the beginning to the end of the simulation. So the user has to choose between values representative of the soil before the explosion (which means standard values of soils) or high elastic moduli representing the values which can be reached by the soil just at the moment of the detonation.

At variance, our model accounts for the stiffening: the elastic moduli are defined such as they depend on the first inviariant of stresses I_1.

The history of density and pressure is shown in figure 4.36 in 3 fixed points in the soil (at the interface between the explosive and the soil, and at 5 and 15 mm from this interface). The density in the first two points tends towards the density of gas since the explosive has reached them. At variance, in the third point, the pressure and the density remain high because the explosive has not expanded so much.

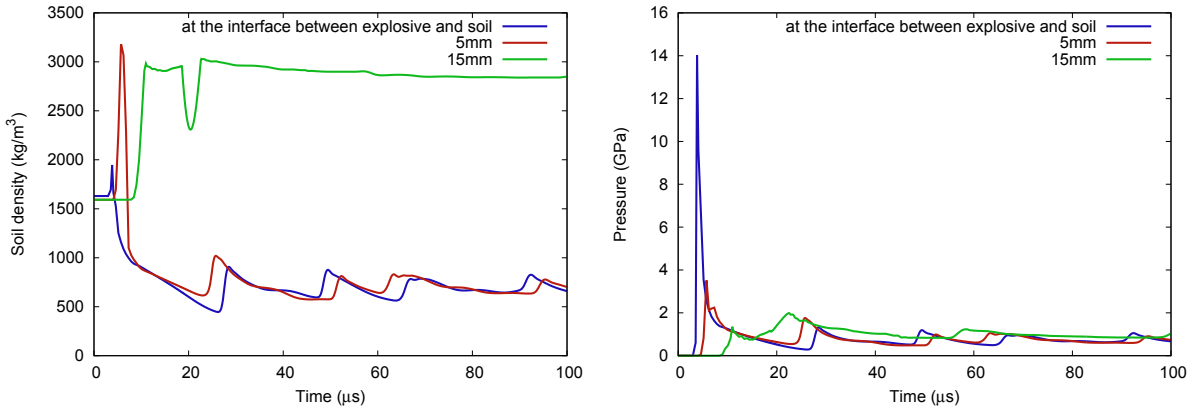

Figure 4.36: Time course of the density (left) and of the pressure (right) in the soil in three fixed points (at the interface with the explosive, at 5 mm and 15 mm from the interface in the soil). Our model is used for the soil.

If constant elastic moduli had been used, very large densities would have been obtained. They correspond in fact to numerical artefacts since they are much larger than the soil particle density (equal to 2700 $kg.m^{-3}$). Here the soil density remains reasonable.

Chapter 5

Pressure and shock wave propagation emanating from small buried charges - experiments and simulations

Contents

When an explosion takes place in the soil, a part of the energy is used to break the soil and let the detonation products move upwards. However the energy that reaches the surface is still important, and the shock wave keeps propagating in the air. The resulting crater depends on various parameters like the depth of burial, the size of the explosive, the degree of saturation of the soil. In this chapter, experiments of the detonation of small buried charges taken from literature are described and the state of the art of craters is briefly presented.

The aim of the PhD is to develop a model of soil for various water contents that can reproduce the measurements obtained in experiments. To test the model, two sets of experiments were carried out. The first one is detailed in this chapter whereas the second one is exposed in chapter 6.

In this chapter, our experiments address the propagation of the shock wave and the resulting aerial pressures due to the detonation of small quantities of explosive (100 g of C4) buried at three various depths in dry and saturated STANAG soil.

Because of too few differences on water content between dry and saturated soil, negligible influence of water is visible on pressures. The resulting craters, at variance, are larger when the shot takes place in dry soil.

In this chapter, our experiments with small charges are compared to numerical simulations. For that purpose, we use our nonlinear elasto viscoplastic cap model developed in chapter 2. A parametric study is performed to determine the influence of the model parameters on pressure.

The simulations provide results in quantitative and qualitative agreement with the experiments. The density and the size of the yield surface defined by the initial cap position X_0 are the parameters that have the largest influence on pressures.

5.1 The phenomenon of buried mine explosion

When a buried charge explodes, the resulting energy transmitted in the air depends on the conditions of the burial: if the charge is buried too deeply, there will not be enough energy for the shock wave to reach the surface. The detonation products remain in the soil, and the explosion is called a camouflet. At variance, when an explosive lays on a frozen soil, very little energy is transmitted to the soil, and if a structure is close to the detonation, most of the energy emanating from the blast is transferred to move and deform the structure. Between these two extrema, a broad range of conditions exists where, in some of them, the energy of the detonation generates soil ejecta which have non negligible kinetic energy and can provoke considerable damage on closeby structures.

The buried explosion generates three types of waves in the soil: compression, shear and Rayleigh waves. The intensity of the induced soil displacement decreases as they propagate. While the compressive and shear waves propagate in a spherical manner, the expansion of the Rayleigh waves is cylindrical. The decay of the compression and shear waves is proportional to $1/r^2$, r being the distance to the center of the charge. Rayleigh waves decrease slower in $1/\sqrt{r}$. For the three waves, the rate of decay depend on the soil properties, in particular the density (which can amplify the shock intensity up to two orders of magnitude, according to Bergeron et al. (1998)), and the water content.

A saturated soil has a larger stiffness and strength, and the shock propagates faster and more easily.

According to Ramasamy et al. (2011) and Bergeron et al. (1998), a buried explosion involves three main stages: first, the detonation of the explosive and the early interaction between the explosive and the soil; second, the gas expansion and the first ejecta from the soil; finally, the momentum transferred from the whole soil initially located above the explosive broken in ejecta. These phenomena are highlighted in figure 5.1.

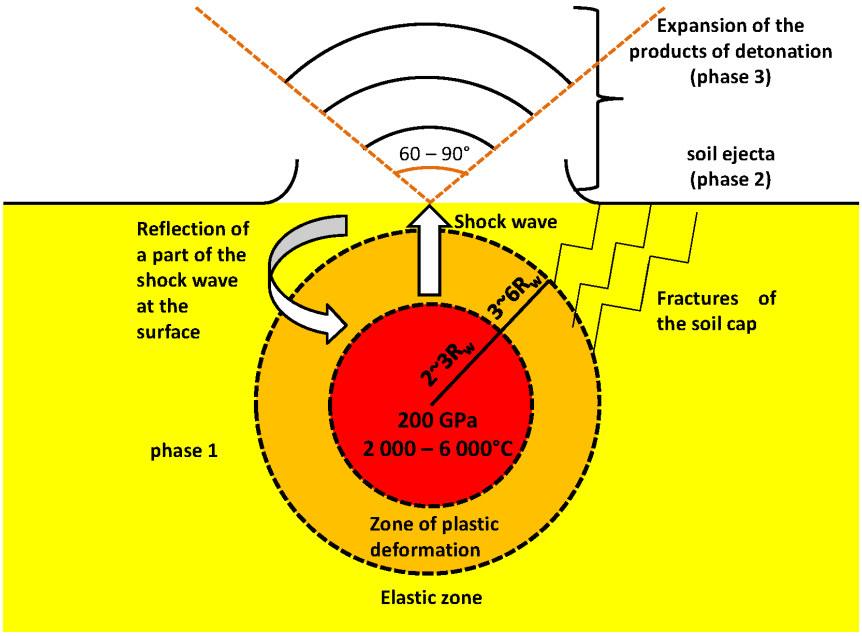

Figure 5.1: The three stages that take place during a buried explosion from the detonation of the buried mine to the transfer of momentum, adapted from Bangash (1993) and Ramasamy et al. (2011). First, the solid explosive is transformed into hot gases at a high pressure. A shock wave propagates upwards to the surface. A part is transmitted in the air, whereas the rest is reflected in the soil as a tensile wave. The detonation products drive all the soil above the explosive at speeds of hundreds of meters per second.

5.1.1 First stage: detonation and early interaction between the explosive and the soil

At detonation, according to Ramasamy et al. (2011), the solid explosive is transformed into detonation gases at high pressure (around 200 GPa) and high temperature (between 2 000 and 6 000°C). In the soil, three areas shown in figure 5.1 can be observed depending on the distance from the detonation point.

According to Bangash (1993), very close and along a distance of two or three explosive radii, the soil is so crushed with a so high temperature and pressure that the propagation of the shock wave can be considered independent on the medium properties.

According to Drake and Little (1983) a plastic zone is extended from three to six radii of the explosive where the shock wave has provoked irreversible soil compression. The density and the volume fraction of the air have notably changed and can be two key parameters to determine the size of the zone.

Outside these two zones, the soil can be considered as elastic since the explosion has caused mostly reversible changes.

The early interaction between the explosive and the soil is the most important stage because it determines the quantity of energy which will be available to generate the impulse on a target located above the soil. The depth of burial of the explosive, the water content of the soil, and its physical properties are thought to have the largest influence on the impulse.

5.1.2 Second stage: Gas expansion and early ejecta

After the early interaction between the explosive and the soil, the shock wave propagates up to the surface. There, a large difference of impedance exists between the soil and the air. The impedance corresponds to the product of the density times the sound speed of the medium. As a consequence, a part of the shock wave is transmitted in the air whereas the other part is reflected in the soil as a tensile wave.

When propagating in the air, the shock wave drives a little part of the soil from the surface. They are the early ejecta.

5.1.3 Third stage: Transfer of momentum from soil ejecta

The propagation of the shock wave weakens the soil which is now fractured. The detonation products can find a way to the surface through the soil fractures and drive finally all the soil above the explosive upward at speeds of hundreds of meters per second. The soil projections have non negligible kinetic energy which contributes to the impulse. The set of soil ejecta have a conical geometrical form with an angle from 60 to 90°. This angle decreases as the depth of burial and the soil density increase.These three steps occur in a few milliseconds.

5.2 Conventional description of the blast wave

When an explosive detonates, a shock wave propagates. This shock wave is in fact a discontinuity dividing two media with different properties (pressures, densities, ...). When the shock wave arrives, the pressure suddenly increases. The typical shape of the pressure curve is shown in figure 5.2.

The pressure rise takes only a few microseconds. After the shock wave, the pressure decreases below the atmospheric pressure to finally return to its initial value. The intensity of the peak is all the more important that the measure is close to the detonation point. Far away, the duration of the peak is longer but the intensity is smaller.

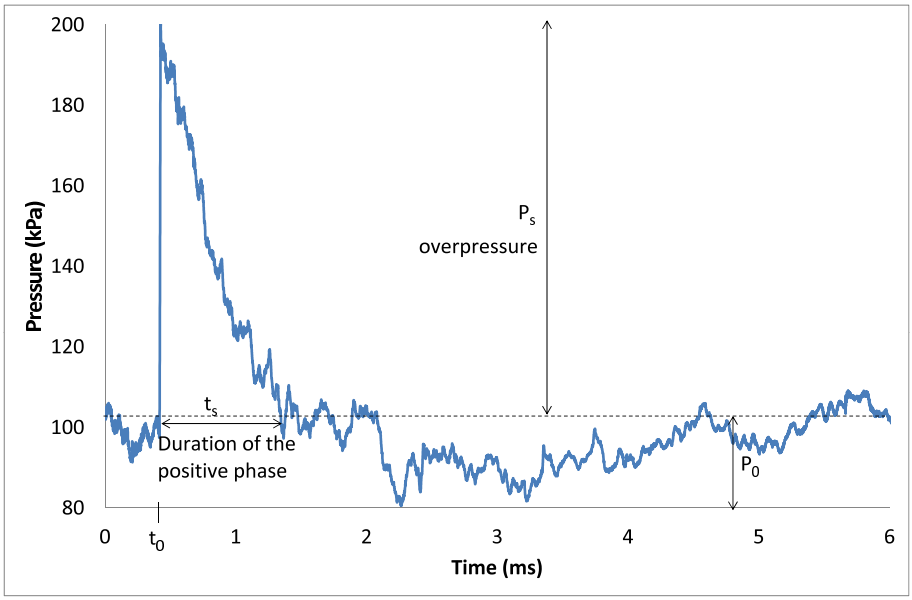

Figure 5.2: Time profile of pressure due to a blast wave: the shock wave arrives at time t_0 provoking a sudden increase of pressure with an overpressure P_s which lasts a duration t_s. The shock wave is followed by a release which explains the decrease of the pressure curve below the atmospheric pressure. After the shock wave, the pressure curve finally returns to its original value. This curve is obtained from the detonation of 100 g of C4 buried at 3 cm below the soil surface, see section 5.5 for details. The pressure was measured at 190 cm above the soil surface.

The time dependence of the pressure due to a blast is often expressed using the Frielander equation (Baker 1973), namely

$$P(t) - P_0 = P_s \left[1 - \frac{t - t_0}{t_s}\right] \exp\left(-\frac{b\,(t - t_0)}{t_s}\right) \quad \text{for} \quad t > t_0 \tag{5.2.1}$$

where b is a positive constant called the waveform parameter that depends on the peak overpressure P_s, P_0 is the atmospheric pressure, t_s corresponds to the duration of the positive phase and t_0 is the time of arrival of the shock wave.

5.3 Crater formation: brief state of the art

When a detonation occurs in the soil, a crater delimited by soil lips (small amounts of soil around the crater zone) and resulting from the space left by the soil ejecta is formed. However determining the size of the crater is not easy because a part of the ejecta falls back in the crater. Its diameter should normally be measured from the size of the lips which is not always easy to distinguish clearly. Therefore the notions of depth and diameter of the crater are defined with two different adjectives **actual** and **apparent** whether they are the real ones that should be obtained theoretically or those which are actually measured. The point is illustrated in figure 5.3.

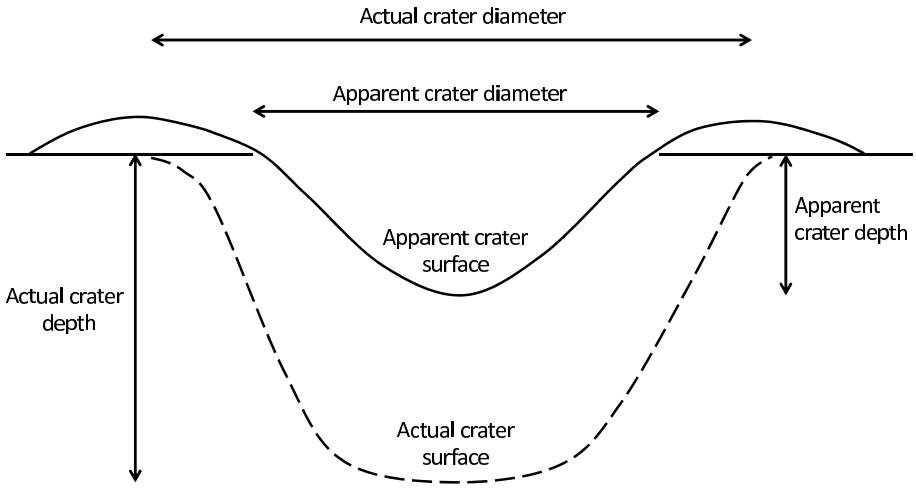

Figure 5.3: Apparent and actual craters. Adapted from Luccioni and Ambrosini (2006).

The three important parameters influencing the shape of the crater are the soil strength, the mass of the explosive, and its depth of burial. When this latter parameter increases, the explosive must expel a larger amount of soil, provoking a wider and deeper crater. Still beyond a certain depth of burial, the size of the crater decreases.

As far as IED threat is concerned, it is interesting to be able to determine the amount of explosive used and at which depth it was buried given the size of the crater discovered after an attack. However the mechanism of the crater formation is very complex and depends on the physical properties of the soil. Bull and Woodford (1998) noticed that, even very carefully performed, cratering tests give dispersions in the measured dimensions of the order of 30% to 40%.

Some authors have nevertheless tried to establish an empirical relation for the ratio of the radius R of the crater to the depth of burial d as a function of the mass of explosive W and of two mechanical properties of the soil (σ related to soil strength, and K to account for gravitational effects.)

The expression proposed by Baker et al. (1991)

$$\frac{R}{d} = f\left(\frac{W^{7/24}}{\sigma^{1/6}\, K^{1/8}\, d}\right) \tag{5.3.1}$$

is illustrated in figure 5.4. The experiments of Luccioni and Ambrosini (2006) agree with this formula. However, the formula of equation (5.3.1) seems to have a problem of unit, since the ratio of the right term has dimension $(\text{second/meter})^{7/12}$.

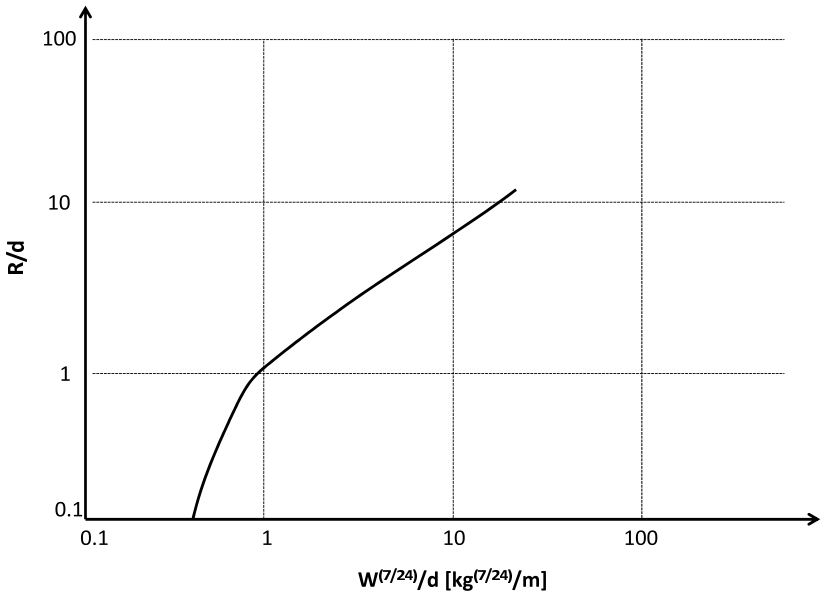

Figure 5.4: Variation of the ratio of the crater radius by the depth of burial of the explosive as a function of the entity proposed by Luccioni and Ambrosini (2006).

5.4 A short review of experiments with small buried charges with emphasis on aerial pressures

In order to study the effects of buried explosion, Bergeron et al. (1998) and Materials Sciences Corporation (2006) reported by An et al. (2011) have carried out experiments and measured the resulting aerial pressures at several heights and various angles above the detonation (figures 5.5 and 5.6). Both experiments address the detonation of 100 g of C4 at three depths (0, 3 and 8 cm) in a dry sand for Bergeron et al. (1998) and in dry and saturated sands for Materials Sciences Corporation (2006). The data recorded included overpressures and the times of arrival of the shock wave at several places in the soil and in the air.

Pressure can be measured in two different ways depending on the orientation of the gauge as sketched by figure 5.7. The pressure gauge can be parallel to the direction of the shock wave. In this case, the obtained measure is said to be a **side-on pressure**. If the pressure gauge is embedded in some rigid material and placed perpendicularly to the direction of the shock wave, the pressure is called **reflected pressure**.

Side-on pressures were recorded at 5 heights above the ground (30, 70, 110, 150 and 190 cm) for Bergeron et al. (1998), whereas three heights and various angles were considered by Materials Sciences Corporation (2006) for the pressure gauges. The five first gauges were placed at 30 cm above the soil and pointing toward the center of the explosive at 0°, ± 22,5°, and ± 45° angles; two other gauges were located at 70 cm and at 0° and ± 30° angles, and the last gauge at 113 cm and at 0° angle. Pressure records

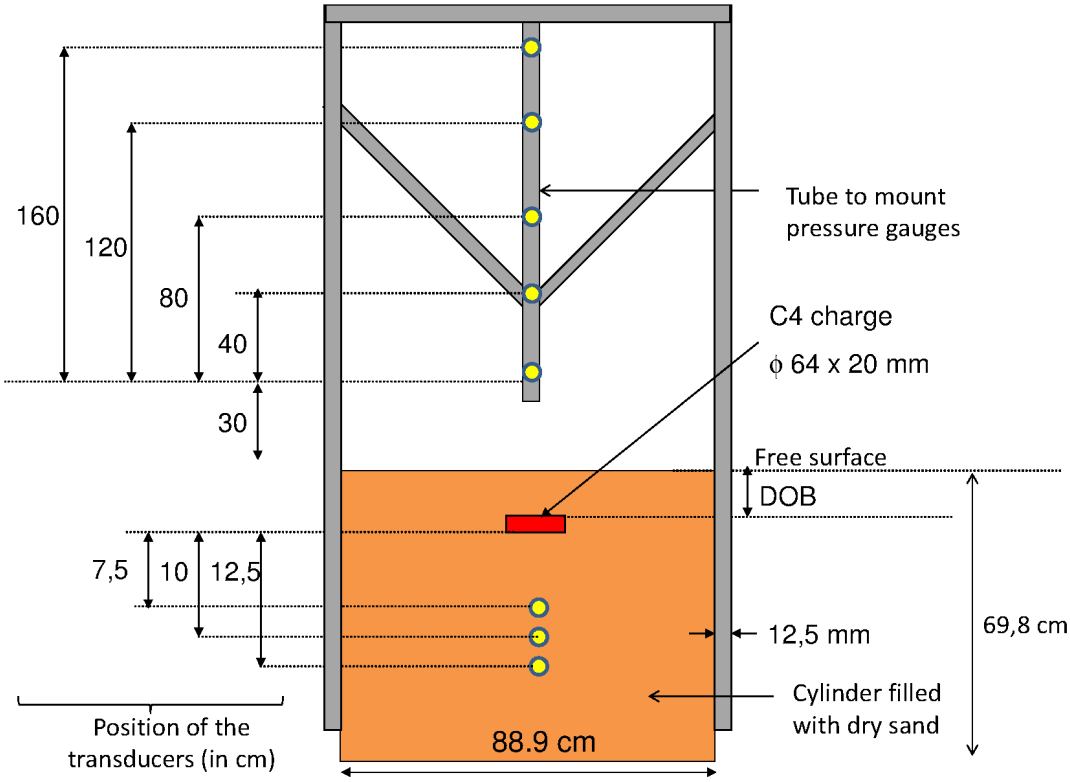

Figure 5.5: Small scale experimental setup of Bergeron et al. (1998) and position of the pressure transducers. Dry sand was used.

provide the time course of the pressure, including times of arrival and amplitudes.

In the experiments of Bergeron et al. (1998), the soil was simply poured in the soil tank. They controlled the soil density and water content with a nuclear density method.

Apart from aerial pressures, Bergeron et al. (1998) also used soil transducers at three different depths (7, 10 and 12 cm).

These two sets of experiments have served as a basis for the design of our experiments, especially to help selecting gauges with appropriate pressure ranges according to the distance from the charge.

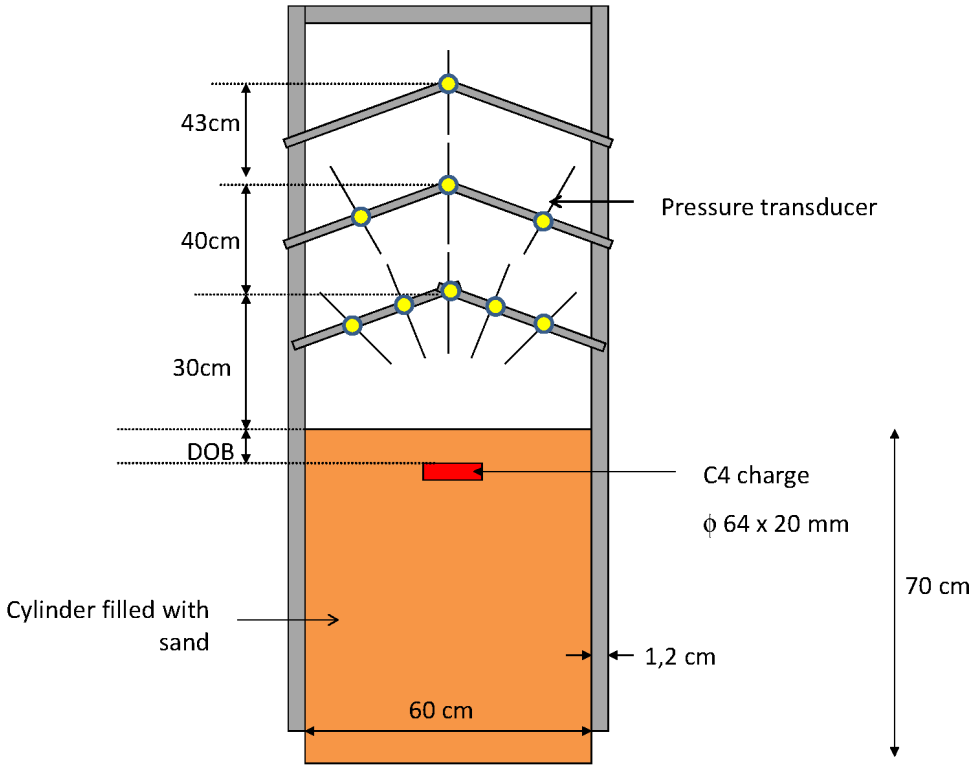

Figure 5.6: Experimental setup used by for Materials Sciences Corporation (2006). The sand was either dry or saturated.

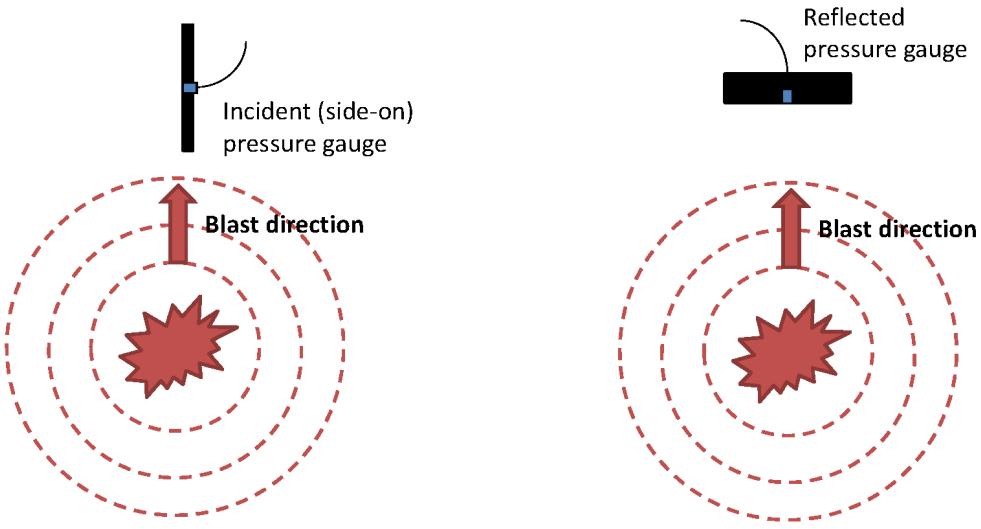

Figure 5.7: Side-on and reflected pressures. If the pressure gauge is parallel to the direction of the shock wave, this is a side-on pressure, whereas if the pressure gauge is embedded in a rigid material perpendicularly to the direction of the shock wave, this is a reflected pressure.

5.5 Overview of our experiments with small buried explosives

Our own experiments are close to those carried out by Bergeron et al. (1998). Our tests consisted in the detonation of small charges (100 g of C4) buried at three different depths (0 mm, 3 mm and 8 mm) in dry and saturated sandy gravel soil. Air pressure gauges were mounted above the explosive charge and the soil was placed in a 1m x 1m x 0.5m tank as sketched in figure 5.8. Twelve tests were shot, the first seven in April 2013, and the last five in January 2014. The weather was sunny during the tests in April, but was rainy in January. The table 5.1 sums up all the tests carried out during this experimental campaign.

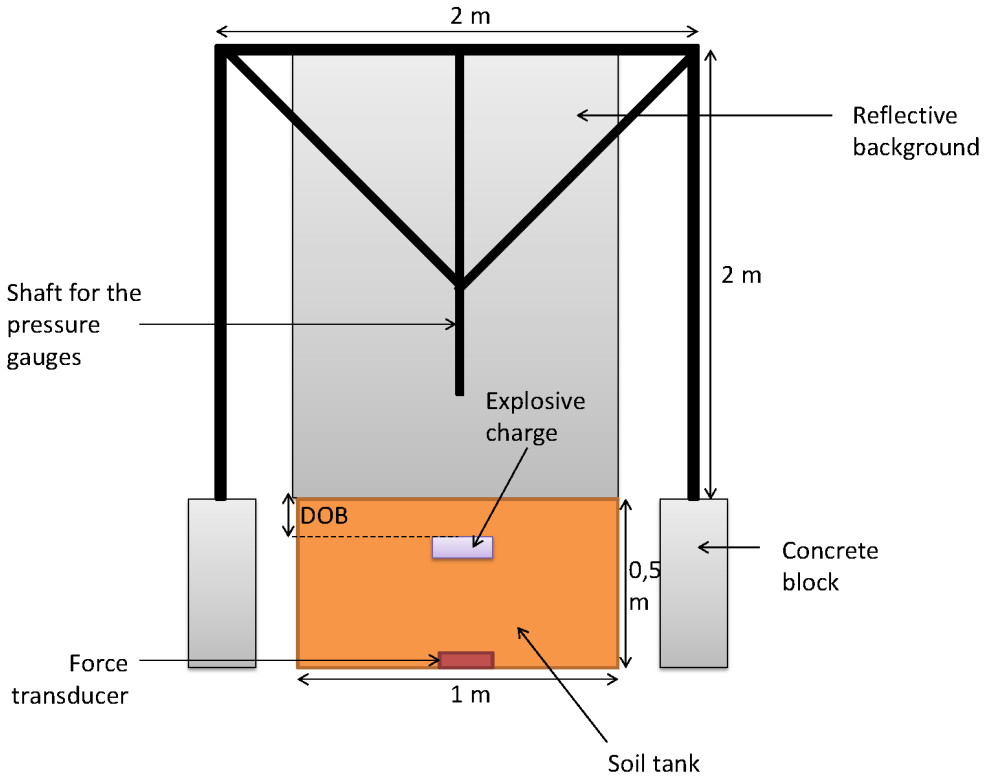

Figure 5.8: Setup of our experiments addressing the detonation of small explosive charges (100 g of C4) buried at various depths of burial (DOB). Air gauges are mounted at the vertical of the explosive charge and provide a continuous measurement of the pressure over time. A reflecting panel is placed in the background. A force transducer is laid at the bottom of the tank to estimate the soil pressure. Density and water content are measured with the nuclear density method before and after the detonation and with a sample of soil removed from the tank. A high speed camera located in front of the experimental setup tracks the shock wave and the projection of ejecta.

The **soil** was composed of a sandy gravel soil named STANAG soil defined in AEP 55 with a granulometry curve drawn in figure 1.3: 100% of the mass of the soil particles must pass the 40 mm sieve, between 40 and 60% must pass the 5mm sieve and a maximum of

Shot number	Date	DOB	State of the soil
Shot 1	16th April AM	0 cm	Dry
Shot 2	16th April PM	0 cm	Dry
Shot 3	17th April AM	0 cm	Wet ($\sim$ 45 L of water added)
Shot 4	17th April PM	0 cm	Wet ($\sim$ 55 L of water added)
Shot 5	18th April AM	3 cm	Dry
Shot 6	18th April PM	3 cm	Wet ($\sim$ 25 L of water added)
Shot 7	19th April AM	3 cm	Dry
Shot 8	8th January PM	3 cm	Wet ($\sim$ 45 L of water)
Shot 9	9th January AM	8 cm	Wet ($\sim$ 45 L of water)
Shot 10	10th January AM	8 cm	Wet ($\sim$ 60 L of water)
Shot 11	10th January PM	8 cm	Dry
Shot 12	13th January PM	8 cm	Dry

Table 5.1: List of tests carried out during the campaign with small buried charges.

10% of the soil mass must pass the 80 μm sieve.

Two **water contents** were tested: the soil (stored outside) was either tested with its natural water content, or saturated. The quantity of water added to the soil was measured with a calibrated bucket.

Density and water content were measured with two methods:

- with traditional laboratory analysis: a specific volume of soil was weighed for the density, and oven dried to determine its water content.
- with a nuclear gauge at several places and depths before and after the shots in April. The nuclear density method is described in details in section 1.1.4. For all the shots in January, the nuclear density method was not used.

A rectangular **soil tank** was chosen with a height equal to 0.5 m and a side of 1 m. The soil was poured in a first layer of half the height. When a saturated soil was used, water was added. Then the first layer was compacted. Some soil was poured to form the second layer and a container (radius: 66.5 mm and height: 300 mm) was placed in order to determine later the density, the water content and to check the granulometry. Water was added again in the case of saturated soil, and the soil was compacted. Once the second layer was ready, the container was extracted from the soil and transported to the laboratory for analyses. Some soil was added to complete the soil tank in order to have a full test tank. Figure 5.9 illustrates the different steps of the soil tank filling, and shows how the soil was moistened. A grooming machine was used for the soil compaction.

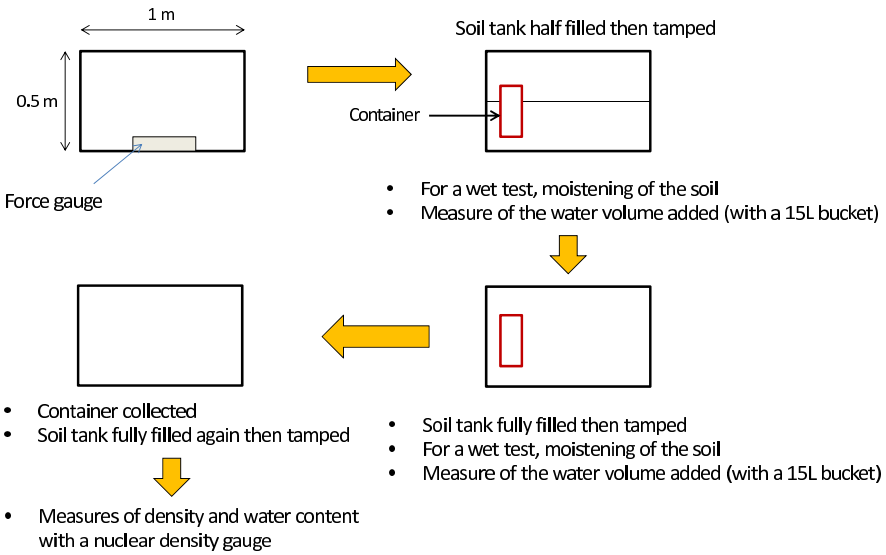

Figure 5.9: Systematic steps followed in the preparation of the soil in order to optimize reproducibility.

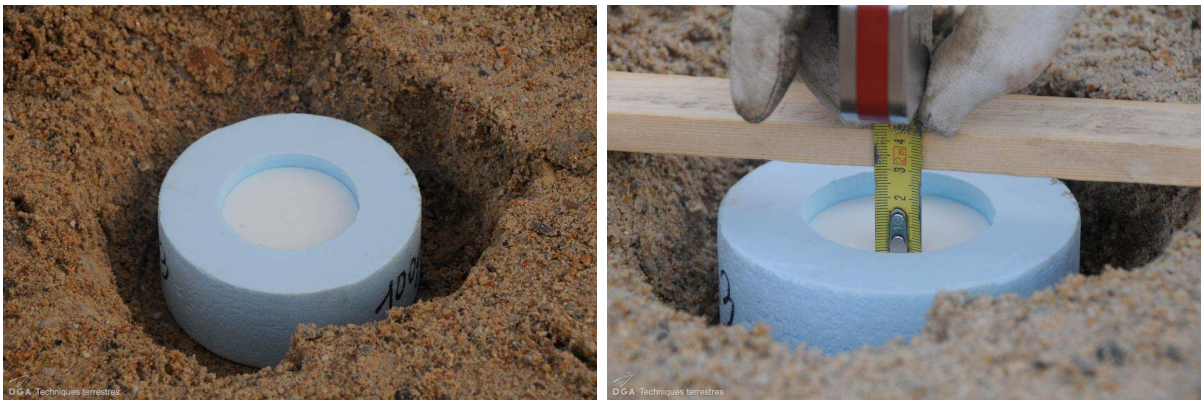

Figure 5.10: Photos of the C4 explosive with a diameter of 64 mm and a height of 20 mm. The charge was surrounded by polystyrene with a thickness of 25 mm. The photo on the right shows that the depth of burial refers to the top surface of the explosive itself.

Before the test, once the density and water content measures were performed, the explosive charge was placed in the soil. For a buried charge, a hole was dug in the soil to position the explosive. Then, some soil was placed on the top of the charge. The explosive was a 20 mm high cylinder of C4 with a diameter of 64 mm. It was surrounded radially and on the bottom by polystyrene with a density of 31 kg.m^{-3} and a thickness of 25 mm, see figure 5.10.

The polystyrene is required because C4 does not have enough stiffness and a container prevents it from spreading. The explosive charge was initiated at the center of its bottom face. The detonator was sunk into the C4 explosive.

Five side-on pressure gauges were placed on a 2 m long crossbar. The places of the pressure gauges were the same as in Bergeron et al. (1998). The closest gauge was placed at 30 cm above the soil surface; the four other gauges were located above the first one, every 40 cm (see figure 5.11).

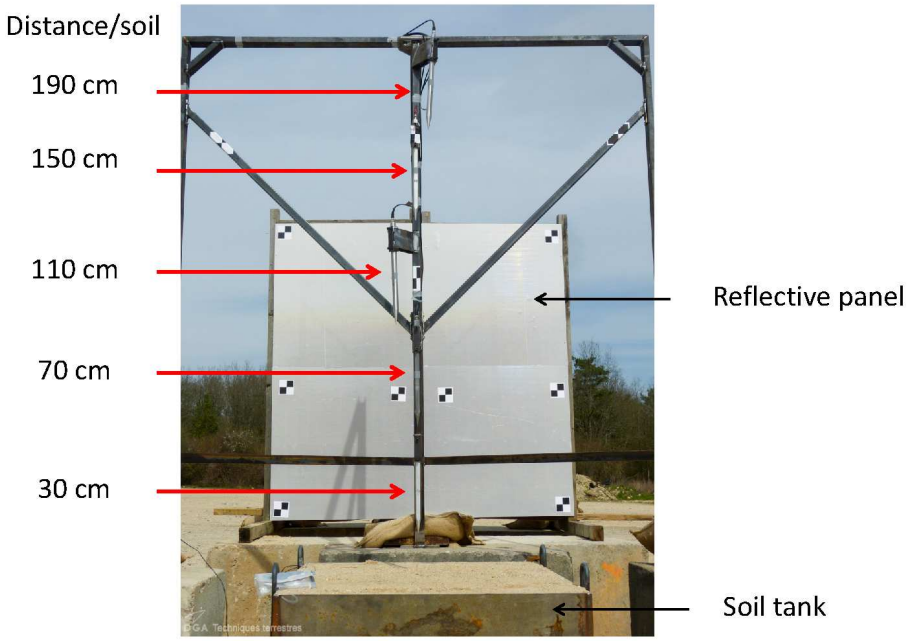

Figure 5.11: Position of the 5 pressure gauges with their respective distances to the free surface of the soil tank. These gauges were used for the shots with flush explosives and charges buried at 3 cm.

For the explosives buried at 3 cm and the flush charges, the pressure gauges were made of quartz. The deformation of the quartz provides an electric current which is directly linked to the pressure. Fat and aluminium powder can be added on the pressure gauges. These two products prevent the gauges from being disturbed by the light and the heat of the explosion.

Figure 5.12: Pressure gauges used for the shots with explosives buried at 8 cm. In this case, the pressure gauges are piezoresistive: the resistance of the gauge is modified because of the shock wave which changes the voltage which is linked to the pressure. The edge of the shaft is sharp, so that it does not disturb the propagation of the shock wave.

For the detonation of buried charges at 8 cm, the pressure gauges were changed. In this configuration, these pressure gauges were piezoresistive (as shown in figure 5.12): the resistance is modified due to the shock wave which changes the voltage which is linked to the pressure. This kind of gauge measures low pressures more accurately. Since these gauges are very sensitive, fat and aluminium powder was not used.

A **reflecting panel** was placed behind the crossbar so that the high speed camera could better follow the propagation of the shock and the projection of ejecta.

A **force gauge** with a diameter equal to 70 mm was placed at the bottom of the tank. It could measure forces up to 120 kN. Figure 5.13 shows the force gauge that was used during the shot in January.

Figure 5.13: The force gauge with a diameter of 70 mm used for the shots in January. This device was placed at the bottom of the soil tank.

To synchronise all measurements, two aluminium sheets were placed on the buried explosive. At detonation, the two sheets are put in contact which closes an electric circuit, thus providing the time when the shock wave arrives at the border of the explosive. This time is very close to the time of detonation.

After the shot, the **crater** was recorded with a 3D scan and pictured. Density and water content were measured. Once all measures were finished, the tank was emptied and prepared for the next test (figure 5.14).

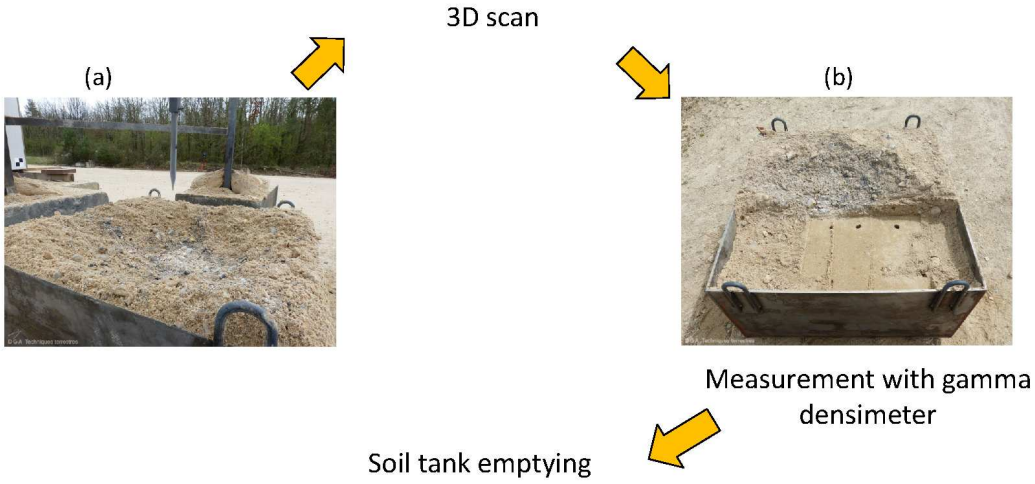

Figure 5.14: Systematic steps after the shots: the crater resulting from the shot (a) is scanned. The soil tank is partly emptied to measure density and water content with the neutron density gauge (b).

5.6 Pressure, density and water content for the detonation of small explosive masses

This section emphasizes the pressures results and the soil measurements (water content and density) obtained with the nuclear density method shot by shot. The conditions of each shot are also detailed. These results are analysed in section 5.7.

5.6.1 Points of measures with the nuclear density method after the shot

The nuclear density method allows to measure density and water content at various points and depths in the soil. This device was used during the shot campaign in April 2013, before and after each shot. In the following, the points of the measures after the shot regarding the depth of burial of the explosive are discussed.

5.6.1.1 Case of a flush charge

The nuclear density method needs to be used on a flat surface. Four points of measure were selected after the shot: one on the lip of the crater, one at the deepest point of the crater and the two other ones at the same deep as the second point but after the soil was removed. These points are illustrated in figure 5.15.

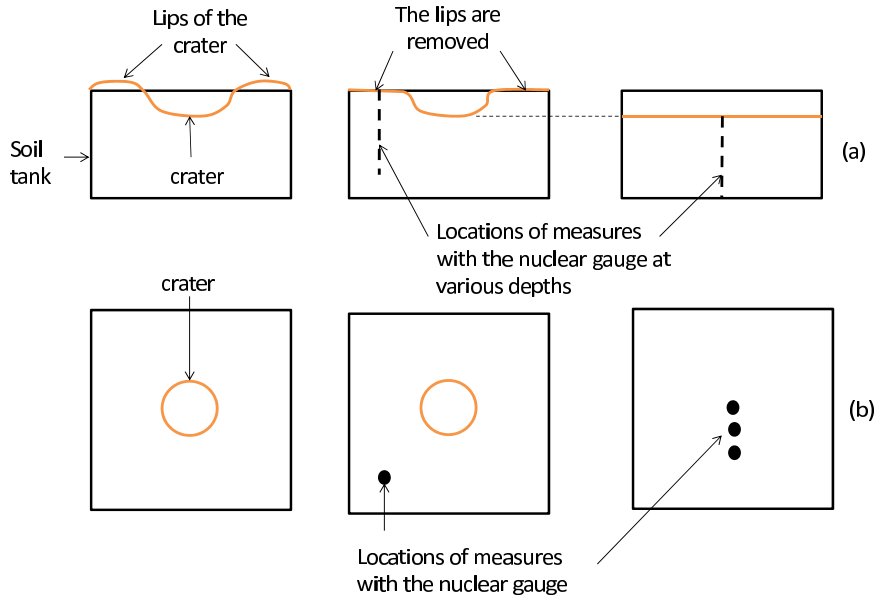

Figure 5.15: Points of measures of density and water content with the nuclear density method for a crater with lips large enough to enable measurement. (a): side views. (b): top views.

5.6.1.2 Case of a buried charge

For the shots with explosives buried at 3 and 8 cm, the lips were too small to place the nuclear density gauge above them. So all the measures were performed at the bottom of the crater. The points of measures are recorded in figure 5.16.

5.6.2 Pressures and nuclear density measures for each shot of the first campaign

In the following, the preparation of each shot is detailed. The measures obtained with the neutron density method and the time histories of each pressure gauge are provided. The first pressure gauge P1 corresponds to the point of measure at 30 cm. The other gauges P2 to P5 are above.

5.6.2.1 First shot - flush charge with a dry soil

The soil was prepared with dry conditions, so no water was added. However, the soil was stored outdoors under a waterproof tarp, so it already contained natural humidity and was not completely dry.

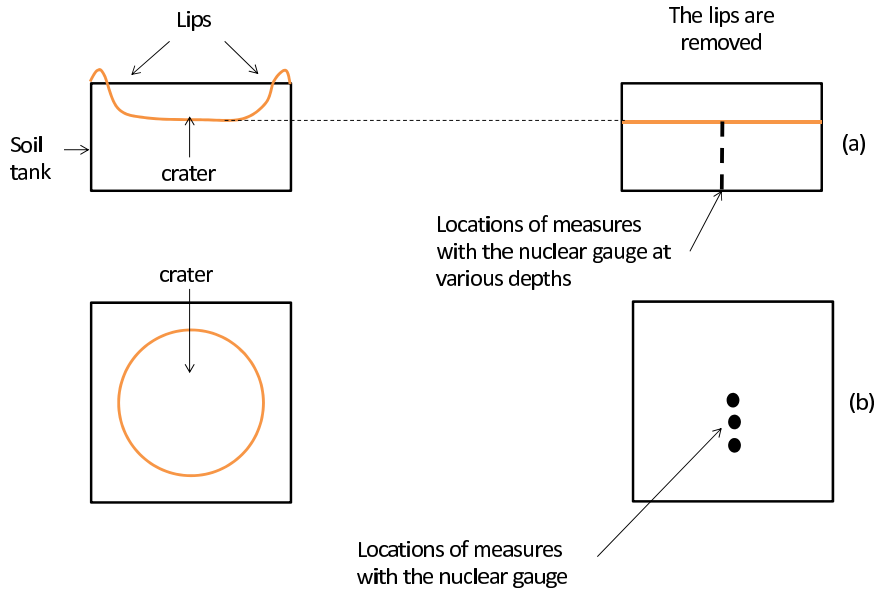

Figure 5.16: Points of measures of density and water content with the nuclear density method for a crater with lips not large enough to perform a measure. (a): side views. (b): top views.

For this first shot, no fat nor aluminium was used to protect the pressure gauges. The time histories of pressures are displayed in figure 5.17.

A force gauge was placed at the bottom of the soil tank. Unfortunately its range of measure was too narrow and the result was clearly saturated. For the next three shots, no force gauge was used.

The first pressure gauge was designed to provide an accurate value of pressure up to 7 MPa. Since the pressure of this gauge was larger than this limit for the first three shots, these three results simply indicate that the pressure at this gauge was more than 7 MPa. A more precise result cannot be considered. Besides no negative pressure was visible on the signal of the first pressure gauge. It could be due to the heat of the detonation since no fat was used. This negative value would correspond to the release following the shock wave. Away from the explosion, the negative part of the curve can be seen on the farthest gauges.

The measures of the density and the water content prior to the test are gathered in tables 5.2 and 5.3 for the various depths of measures. These measures show that the soil was homogeneous before the shot.

Depth of the measure	Water content				
	1st point	2nd point	3rd point	4th point	5th point
0 cm	7%	4.7%	5.4%	5.8%	5%
10 cm	5.8%				
15 cm	5.8%	5.2%	5.8%		
18 cm	5.2%				

Table 5.2: Water content *prior* to the test at various depths and points for the first shot.

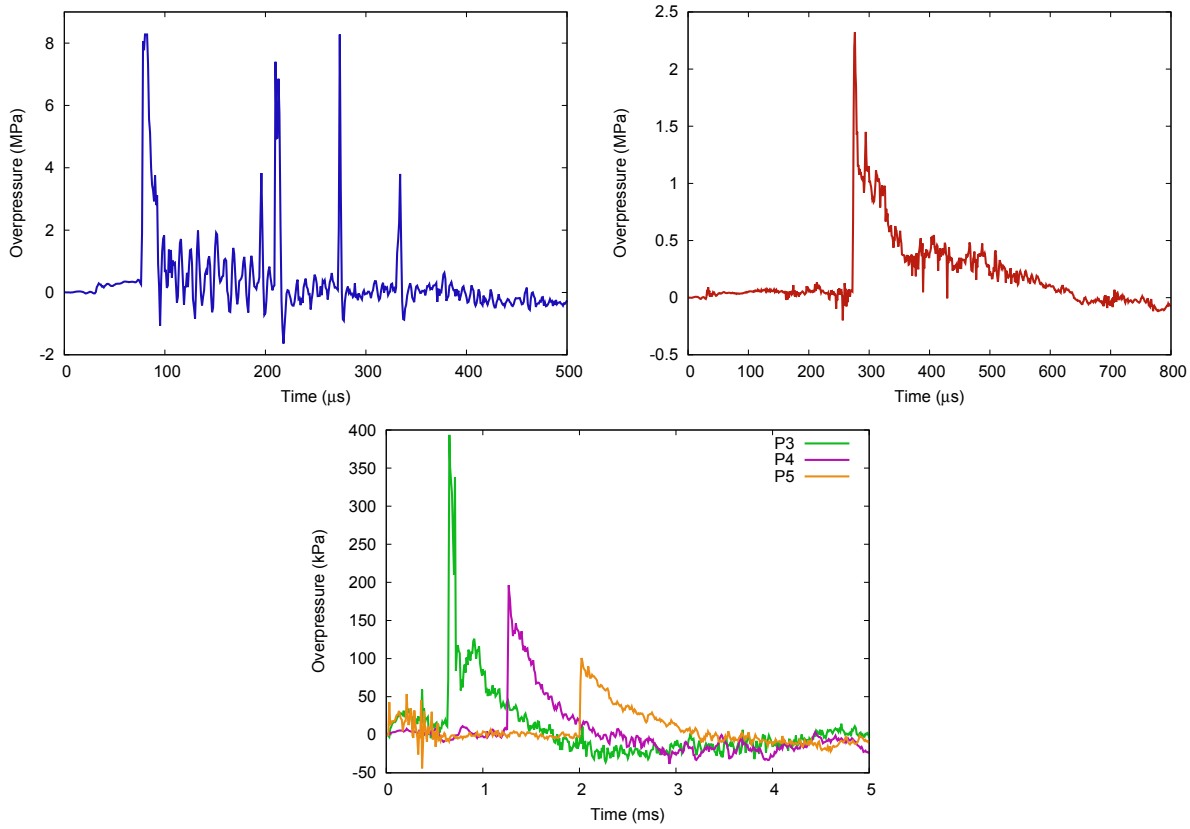

Figure 5.17: Time course of the pressure for the first (top left), second (top right), third, fourth and fifth gauges (bottom) of the first shot.

Depth of the measure	Density 1st point	2nd point	3rd point	4th point	5th point
0 cm	1834 kg.m^{-3}	1831 kg.m^{-3}	1826 kg.m^{-3}	1820 kg.m^{-3}	1824 kg.m^{-3}
10 cm	1782 kg.m^{-3}				
15 cm	1905 kg.m^{-3}	1851 kg.m^{-3}	1878 kg.m^{-3}		
18 cm	1875 kg.m^{-3}				

Table 5.3: Density *prior* to the test at various depths and points for the first shot.

The tables 5.4 and 5.5 respectively present the water content and the density measured by the nuclear density gauge for various depths after the shot. The first point corresponds to the measure on the lip of the crater which can explain the smallest recorded values of water content since the lip is formed from ejecta of soil. Moreover, after the shot, the density increases with the depth of the measure since the explosion has compacted the soil.

Depth of	Water content			
the measure	1st point	2nd point	3rd point	4th point
0 cm	4.2%	5.6%	5.8%	5.3%
5.1 cm		6.1%	6.1%	5.4%
7.6 cm	3.2%	5.1%	4.6%	3.8%
10 cm	3.6%	5.9%	5.8%	4.4%
15 cm	3.7%	5.7%	5.1%	4%
20 cm	4%	5.3%		4.6%

Table 5.4: Water content *after* the shot at various depths and points for the first shot.

Depth of	Density			
the measure	1st point	2nd point	3rd point	4th point
0 cm	1632 $kg.m^{-3}$	1734 $kg.m^{-3}$	1807 $kg.m^{-3}$	1665 $kg.m^{-3}$
5.1 cm		1820 $kg.m^{-3}$	1811 $kg.m^{-3}$	1775 $kg.m^{-3}$
7.6 cm	1826 $kg.m^{-3}$	1843 $kg.m^{-3}$	1860 $kg.m^{-3}$	1867 $kg.m^{-3}$
10 cm	1808 $kg.m^{-3}$	1827 $kg.m^{-3}$	1865 $kg.m^{-3}$	1882 $kg.m^{-3}$
15 cm	1819 $kg.m^{-3}$	1841 $kg.m^{-3}$	1880 $kg.m^{-3}$	1917 $kg.m^{-3}$
20 cm	1808 $kg.m^{-3}$	1880 $kg.m^{-3}$		1940 $kg.m^{-3}$

Table 5.5: Density *after* the shot at various depths and points for the first shot.

5.6.2.2 Second shot - flush charge with a dry soil

This shot was the same as the first one. Since the calibration of the force gauge buried in the soil was not correct, it was not used again.

This time, to prevent drifting signals due to heat and light from the explosion, the pressure gauges were covered with some fat and aluminium powder. The time histories of pressures are displayed in figure 5.18. The second pressure gauge did not provide any exploitable signal.

The measures of density and water content with the nuclear density gauge at various depths are gathered in tables 5.6 and 5.7 for the measures before the shot and in tables 5.8 and 5.9 for the measures after the shot. The measures of water content show that the soil seems to be homogeneous before the soil. Moreover, the density increases as we go deeper, even before the shot.

After the shot, as it was the case for the first shot, the soil is denser as the depth of the measure increases. The water content at the first point which corresponds to the lip of the crater is still the smallest.

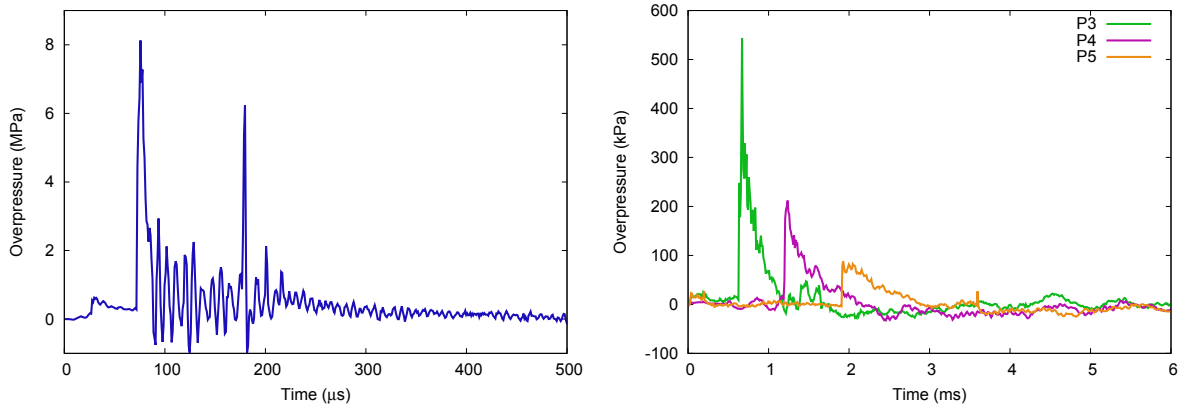

Figure 5.18: Time course of the pressure for the first (left), third, fourth and fifth gauges (right) of the second shot. A gravel may have hit the first gauge, provoking the peak which can be seen at around 180 μs.

Depth of the measure	Water content				
	1st point	2nd point	3rd point	4th point	5th point
0	6.4%	6.7%	5.5%	5.4%	6%
5.1 cm	6.8%				
7.6 cm		6.6%	5.9%	5.8%	5.7%
10 cm	6.7%				
13 cm		6.4%	5.8%	6.7%	7.2%
15 cm	6.2%				
18 cm		6%	6.5%	5.7%	5.7%
20 cm	6.6%				
25 cm		5.7%	5.8%	6.1%	5.3%
30 cm	6%	6.7%	5.7%	5.4%	6.3%

Table 5.6: Water content *prior* to the test at various depths and points for the second shot.

Depth of the measure	Density				
	1st point	2nd point	3rd point	4th point	5th point
0 cm	1780 kg.m^{-3}	1861 kg.m^{-3}	1816 kg.m^{-3}	1768 kg.m^{-3}	1724 kg.m^{-3}
5.1 cm	1813 kg.m^{-3}				
7.6 cm		1825 kg.m^{-3}	1848 kg.m^{-3}	1855 kg.m^{-3}	1856 kg.m^{-3}
10 cm	1789 kg.m^{-3}				
13 cm		1857 kg.m^{-3}	1877 kg.m^{-3}	1839 kg.m^{-3}	1834 kg.m^{-3}
15 cm	1856 kg.m^{-3}				
18 cm		1888 kg.m^{-3}	1889 kg.m^{-3}	1911 kg.m^{-3}	1880 kg.m^{-3}
20 cm	1864 kg.m^{-3}				
25 cm		1958 kg.m^{-3}	1928 kg.m^{-3}	1914 kg.m^{-3}	1906 kg.m^{-3}
30 cm	1895 kg.m^{-3}	1980 kg.m^{-3}	1934 kg.m^{-3}	1932 kg.m^{-3}	1911 kg.m^{-3}

Table 5.7: Density *prior* to the test at various depths and points for the second shot.

Depth of	Water content			
the measure	1st point	2nd point	3rd point	4th point
0 cm	3.8%	7.7%	9.2%	7.8%
5.1 cm	4%	8.5%	7.4%	7.4%
10 cm	4.6%		8.3%	6.6%
13 cm		6.9%		
15 cm	4.5%			8%
18 cm		7.3%	6.4%	
20 cm	4.4%			
23 cm				6.7%
25 cm		7.4%	6.8%	
28 cm				6.5%
30 cm	4.1%	6.3%	7.2%	

Table 5.8: Water content *after* the shot at various depths and points for the second shot.

Depth of	Density			
the measure	1st point	2nd point	3rd point	4th point
0 cm	$1759\,\mathrm{kg.m^{-3}}$	$1722\,\mathrm{kg.m^{-3}}$	$1676\,\mathrm{kg.m^{-3}}$	$1667\,\mathrm{kg.m^{-3}}$
5.1 cm	$1870\,\mathrm{kg.m^{-3}}$	$1799\,\mathrm{kg.m^{-3}}$	$1780\,\mathrm{kg.m^{-3}}$	$1783\,\mathrm{kg.m^{-3}}$
10 cm	$1873\,\mathrm{kg.m^{-3}}$		$1857\,\mathrm{kg.m^{-3}}$	$1809\,\mathrm{kg.m^{-3}}$
13 cm		$1880\,\mathrm{kg.m^{-3}}$		
15 cm	$1852\,\mathrm{kg.m^{-3}}$			$1817\,\mathrm{kg.m^{-3}}$
18 cm		$1871\,\mathrm{kg.m^{-3}}$	$1860\,\mathrm{kg.m^{-3}}$	
20 cm	$1867\,\mathrm{kg.m^{-3}}$			
23 cm				$1865\,\mathrm{kg.m^{-3}}$
25 cm		$1906\,\mathrm{kg.m^{-3}}$	$1894\,\mathrm{kg.m^{-3}}$	
28 cm				$1863\,\mathrm{kg.m^{-3}}$
30 cm	$1883\,\mathrm{kg.m^{-3}}$	$1891\,\mathrm{kg.m^{-3}}$	$1905\,\mathrm{kg.m^{-3}}$	

Table 5.9: Density *after* the shot test at various depths and points for the second shot.

5.6.2.3 Third shot - flush charge with a saturated soil

The shot was carried out for a flush explosive in a saturated soil. 15 liters of water were spread on the first layer of soil before compaction. The compaction led to a puddle of water. A container of 2.8 L was added in the second layer of soil. 15 liters of water were spread on this second layer before compaction. Then the container was removed. Some soil was added to complete the tank and was compacted again.

The time histories of pressures are displayed in figure 5.19.

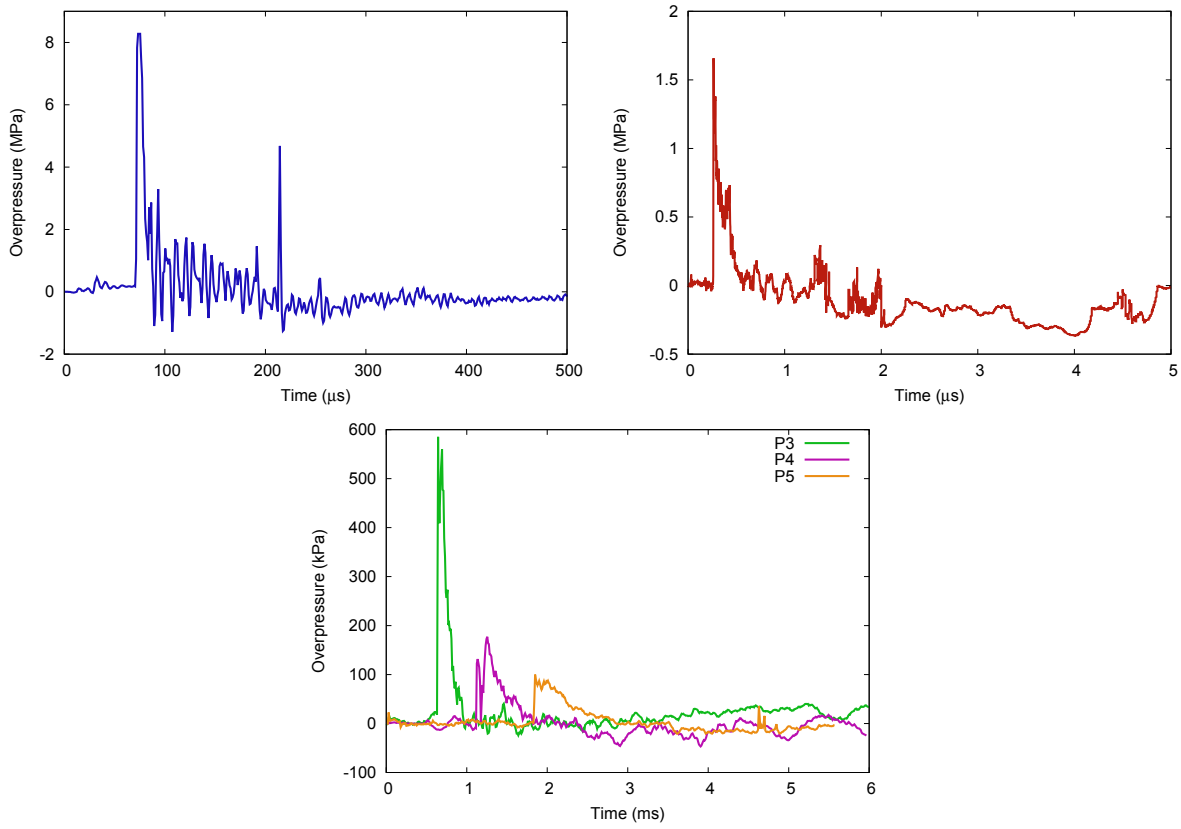

Figure 5.19: Time course of the pressure for the first (top left), second, (top right), third, fourth and fifth gauges (bottom) of the third shot.

The measures of density and water content with the nuclear density gauge at various depths are gathered in tables 5.10, 5.11, 5.12 and 5.13. As for the second shot, the density of the soil was denser before and after the shot as the depth of the measure increases. The water content is homogeneous in the soil before the shot, and the first point after the shot still provides the smallest water content.

Depth of	Water content			
the measure	1st point	2nd point	3rd point	4th point
0 cm	4.8%	5.1%	5%	4.6%
5.1 cm	5.9%	5.9%	4.7%	4.6%
10 cm	5.8%	5.8%	4.5%	4.4%
15 cm				5.2%
18 cm	4.7%	4.7%	4.9%	
20 cm				4.7%
23 cm				4.4%
25 cm	4.7%	4.7%	5.5%	
30 cm	4.6%	4.6%	5.1%	

Table 5.10: Water content *prior* to the test at various depths and points for the third shot.

Depth of	Density			
the measure	1st point	2nd point	3rd point	4th point
0 cm	$1758\,\mathrm{kg.m^{-3}}$	$1808\,\mathrm{kg.m^{-3}}$	$1820\,\mathrm{kg.m^{-3}}$	$1807\,\mathrm{kg.m^{-3}}$
5.1 cm	$1768\,\mathrm{kg.m^{-3}}$	$1768\,\mathrm{kg.m^{-3}}$	$1816\,\mathrm{kg.m^{-3}}$	$1788\,\mathrm{kg.m^{-3}}$
10 cm	$1818\,\mathrm{kg.m^{-3}}$	$1818\,\mathrm{kg.m^{-3}}$	$1787\,\mathrm{kg.m^{-3}}$	$1795\,\mathrm{kg.m^{-3}}$
15 cm				$1818\,\mathrm{kg.m^{-3}}$
18 cm	$1905\,\mathrm{kg.m^{-3}}$	$1905\,\mathrm{kg.m^{-3}}$	$1866\,\mathrm{kg.m^{-3}}$	
20 cm				$1868\,\mathrm{kg.m^{-3}}$
23 cm				$1863\,\mathrm{kg.m^{-3}}$
25 cm	$1961\,\mathrm{kg.m^{-3}}$	$1961\,\mathrm{kg.m^{-3}}$	$1915\,\mathrm{kg.m^{-3}}$	
30 cm	$1978\,\mathrm{kg.m^{-3}}$	$1978\,\mathrm{kg.m^{-3}}$	$1947\,\mathrm{kg.m^{-3}}$	

Table 5.11: Density *prior* to the test at various depths and points for the third shot.

Depth of	Water content			
the measure	1st point	2nd point	3rd point	4th point
0 cm	4.4%	9.8%	8.2%	7.1%
5.1 cm	4.7	8%	6.7%	6.6%
10 cm	3.3%	8.5%	6.8%	6.4%
18 cm	3.7%	7.8%	7.3%	6.7%
25 cm	4.4%	7.6%	7.5%	6.7%
30 cm	3.2%	7.5%	6.7%	6.5%

Table 5.12: Water content *after* the shot at various depths and points for the third shot.

Depth of the measure	Density			
	1st point	2nd point	3rd point	4th point
0 cm	1657 $kg.m^{-3}$	1802 $kg.m^{-3}$	1686 $kg.m^{-3}$	1664 $kg.m^{-3}$
5.1 cm	1759 $kg.m^{-3}$	1831 $kg.m^{-3}$	1886 $kg.m^{-3}$	1821 $kg.m^{-3}$
10 cm	1911 $kg.m^{-3}$	1920 $kg.m^{-3}$	1967 $kg.m^{-3}$	1834 $kg.m^{-3}$
18 cm	1916 $kg.m^{-3}$	1872 $kg.m^{-3}$	1906 $kg.m^{-3}$	1859 $kg.m^{-3}$
25 cm	1949 $kg.m^{-3}$	1943 $kg.m^{-3}$	1952 $kg.m^{-3}$	1888 $kg.m^{-3}$
30 cm	2015 $kg.m^{-3}$	1988 $kg.m^{-3}$	1968 $kg.m^{-3}$	1923 $kg.m^{-3}$

Table 5.13: Density *after* the shot test at various depths and points for the third shot.

5.6.2.4 Fourth shot - flush charge with a saturated soil

This shot was the same as the third one. The procedure followed to prepare the soil tank was the same as the previous shot. However, this time, about 10 liters of water were spread on the complete soil tank. In all, 40 liters of water have been added (against 30 liters in the previous shot). More water was added in order to try to reach complete saturation. The projections of soil seemed more focused, and the crater less deep than for the previous shots.

For this shot, the closest pressure gauge was changed in order to be able to get larger measures (up to the previous 7 MPa) precisely. Unfortunately, this first gauge did not provide any exploitable results. The time histories of pressures are displayed in figure 5.20.

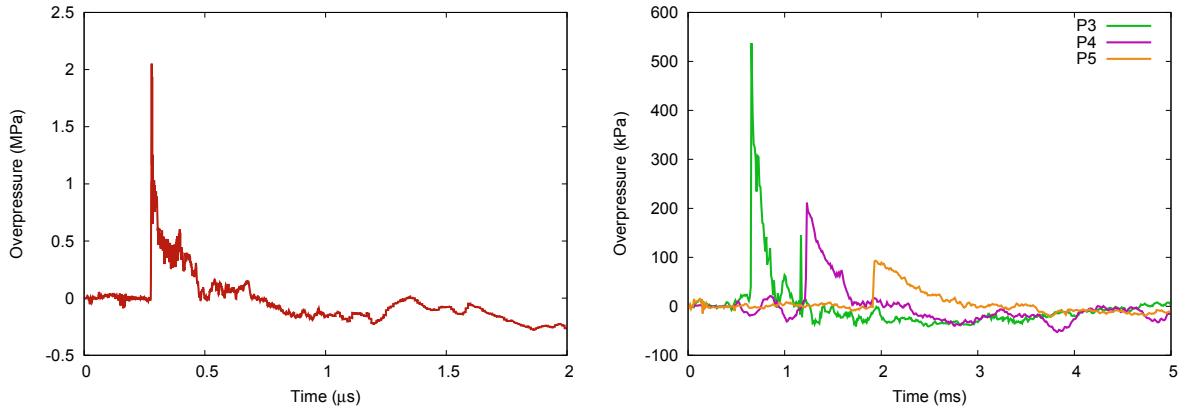

Figure 5.20: Time course of the pressure for the second (left), third, fourth and fifth (right) gauges of the fourth shot.

The measures of density and water content with the nuclear density gauge at various depths are gathered in tables 5.14, 5.15, 5.16, and 5.17. Larger water contents were obtained for this fourth shot compared to the third shot, due to a more important quantity of water spread in the soil tank.

Depth of the measure	Water content 1st point	2nd point
0 cm	10.1%	8.9%
5.1 cm	9.3%	8.5%
10 cm	8.2%	7.9%
15 cm		8.4%
18 cm	8.5%	8.4%
23 cm		8.2%
25 cm	8.5%	
30 cm	9.2%	

Table 5.14: Water content *prior* to the test at various depths and points for the fourth shot.

Depth of the measure	Density 1st point	2nd point
0 cm	1957 $kg.m^{-3}$	1790 $kg.m^{-3}$
5.1 cm	1996 $kg.m^{-3}$	1923 $kg.m^{-3}$
10 cm	1998 $kg.m^{-3}$	1943 $kg.m^{-3}$
15 cm		1973 $kg.m^{-3}$
18 cm	2000 $kg.m^{-3}$	1993 $kg.m^{-3}$
23 cm		1976 $kg.m^{-3}$
25 cm	2049 $kg.m^{-3}$	
30 cm	2034 $kg.m^{-3}$	

Table 5.15: Density *prior* to the test at various depths and points for the fourth shot.

Depth of the measure	Water content 1st point	2nd point	3rd point	4th point
0 cm	7%	10.6%	9.4%	9.9%
5.1 cm	6.2%	9.6%	9.3%	8.7%
10 cm	5.2%	9%	9.9%	9.5%
15 cm		10.1%		8.3%
18 cm	6%		10.3%	9.9%
20 cm		8.9%		
25 cm	5.3%	7.7%	9.7%	
30 cm	4.9%		8.8%	

Table 5.16: Water content *after* the shot at various depths and points for the fourth shot.

Depth of the measure	Density			
	1st point	2nd point	3rd point	4th point
0 cm	1704 kg.m^{-3}	1759 kg.m^{-3}	1803 kg.m^{-3}	1793 kg.m^{-3}
5.1 cm	1824 kg.m^{-3}	1911 kg.m^{-3}	1944 kg.m^{-3}	1949 kg.m^{-3}
10 cm	2000 kg.m^{-3}	2022 kg.m^{-3}	2071 kg.m^{-3}	1975 kg.m^{-3}
15 cm		1950 kg.m^{-3}		1936 kg.m^{-3}
18 cm	1932 kg.m^{-3}		1973 kg.m^{-3}	1901 kg.m^{-3}
20 cm		2014 kg.m^{-3}		
25 cm	1976 kg.m^{-3}	2055 kg.m^{-3}	1993 kg.m^{-3}	
30 cm	1993 kg.m^{-3}		2008 kg.m^{-3}	

Table 5.17: Density *after* the shot test at various depths and points for the fourth shot.

5.6.2.5 Fifth shot - buried charge at 3 cm in a dry soil

For this shot, the charge was buried at 3 cm in a dry soil. The force gauge was changed. It could now measure pressures up to 20 MPa. The value obtained was 9 MPa which may be considered as a reflected value. As a result, the incident pressure may be half of this value, which means 4.5 MPa.

The time histories of pressures are displayed in figure 5.21.

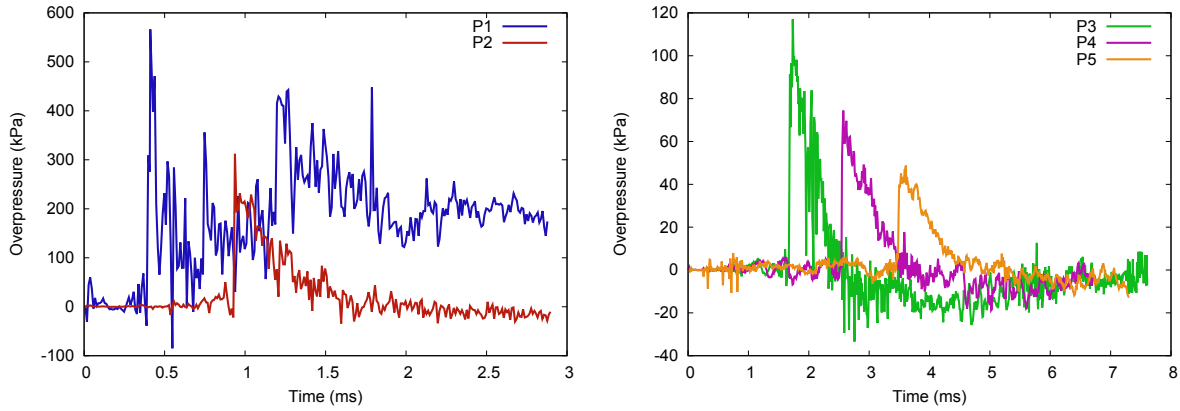

Figure 5.21: Time course of the pressure for the first and second gauges (left) and for the third, fourth and fifth gauges (right) of the fifth shot.

After the shot, there was not enough space on the lip to use the nuclear density gauge. So all the measures were performed at the bottom of the crater. The points of measures are presented in figure 5.16.

The measures of density and water content with the nuclear density gauge are gathered in tables 5.18, 5.19, 5.20, and 5.21. At variance with the shots of flush charges, with an explosive buried at 3 cm, the increase of density as the measure is deeper is even more noticeable.

Depth of	Water content			
the measure	1st point	2nd point	3rd point	4th point
0 cm	4%	4.2%	4.5%	4.5%
5.1 cm	3.8%	4.1%	3.7%	3.9%
10 cm	3%	4.7%	3.9%	3.6%
15 cm	3.4%	4%	4.3%	
18 cm				4.8%
20 cm	3.6%	3.6%	4.7%	
23 cm			4.5%	
25 cm	4.5%			3.8%
30 cm				3.4%

Table 5.18: Water content *prior* to the test at various depths and points for the fifth shot.

Depth of	Density			
the measure	1st point	2nd point	3rd point	4th point
0 cm	1803 $kg.m^{-3}$	1838 $kg.m^{-3}$	1803 $kg.m^{-3}$	1794 $kg.m^{-3}$
5.1 cm	1807 $kg.m^{-3}$	1817 $kg.m^{-3}$	1816 $kg.m^{-3}$	1814 $kg.m^{-3}$
10 cm	1769 $kg.m^{-3}$	1825 $kg.m^{-3}$	1802 $kg.m^{-3}$	1849 $kg.m^{-3}$
15 cm	1839 $kg.m^{-3}$	1889 $kg.m^{-3}$	1856 $kg.m^{-3}$	
18 cm				1839 $kg.m^{-3}$
20 cm	1823 $kg.m^{-3}$	1904 $kg.m^{-3}$	1853 $kg.m^{-3}$	
23 cm			1870 $kg.m^{-3}$	
25 cm	1836 $kg.m^{-3}$			1863 $kg.m^{-3}$
30 cm				1885 $kg.m^{-3}$

Table 5.19: Density *prior* to the test at various depths and points for the fifth shot.

Depth of	Water content		
the measure	1st point	2nd point	3rd point
0 cm	3.8%	4.7%	3.5%
5.1 cm	4.3%	3.5%	4.6%
10 cm	4.4%	4.4%	2.9%
15 cm	3.4%		
18 cm		4.6%	3.6%
20 cm	3.7%		
25 cm	3.3%	4.3%	3.2%
30 cm		3.8%	3.1%

Table 5.20: Water content *after* the shot at various depths and points for the fifth shot.

Depth of the measure	Density 1st point point	2nd point point	3rd point point
0 cm	1522 kg.m^{-3}	1560 kg.m^{-3}	1643 kg.m^{-3}
5.1 cm	1718 kg.m^{-3}	1659 kg.m^{-3}	1668 kg.m^{-3}
10 cm	1768 kg.m^{-3}	1753 kg.m^{-3}	1701 kg.m^{-3}
15 cm	1766 kg.m^{-3}		
18 cm		1760 kg.m^{-3}	1757 kg.m^{-3}
20 cm	1789 kg.m^{-3}		
25 cm	1816 kg.m^{-3}	1802 kg.m^{-3}	1864 kg.m^{-3}
30 cm		1814 kg.m^{-3}	1866 kg.m^{-3}

Table 5.21: Density *after* the shot test at various depths and points for the fifth shot.

5.6.2.6 Sixth shot - buried charge at 3 cm in a saturated soil

For this shot, the charge was buried at 3 cm in a saturated soil. 15 liters of water were added to the first layer, and 10 liters to the second one. It is very difficult to define the detonation time of this shot because the signal provided by the aluminium foils which serve to determine it, is very noisy.

The time histories of pressures are displayed in figure 5.22.

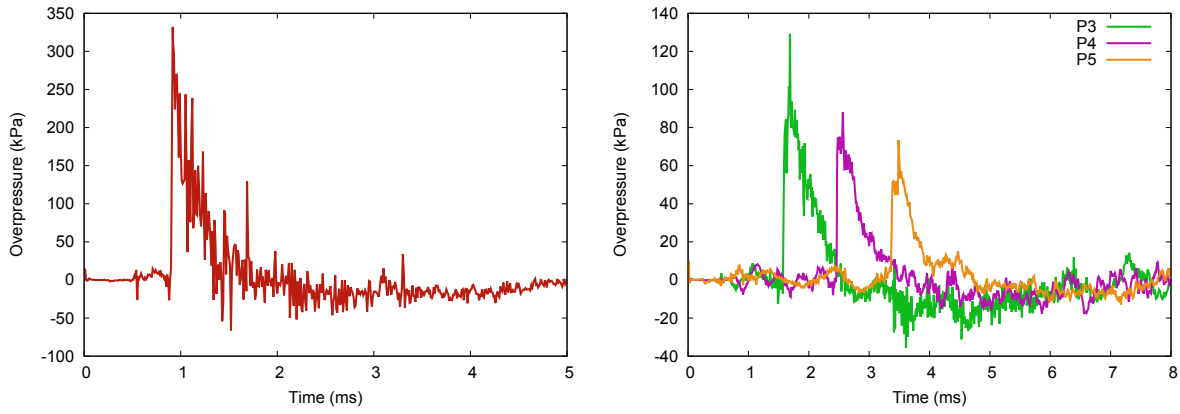

Figure 5.22: Time course of the pressure for the second gauge (left) and for the third, fourth and fifth (right) gauges of the sixth shot.

The measures of density and water content with the nuclear density gauge are gathered in tables 5.22, 5.23, 5.24 and 5.25.

Depth of	Water content			
the measure	1st point	2nd point	3rd point	4th point
0 cm	6.1%	7.6%	6.7%	6.3%
5.1 cm	5.7%	6.5%	6.9%	6.1%
10 cm	6.1%	7.3%	7.1%	6.3%
15 cm		6.5%	6.1%	
18 cm	5.5%			6.6%
20 cm		6.7%	6%	
25 cm	6%			6.7%
30 cm	5.9%			6.6%

Table 5.22: Water content *prior* to the test at various depths and points for the sixth shot.

Depth of	Density			
the measure	1st point	2nd point	3rd point	4th point
0 cm	1847 $kg.m^{-3}$	1836 $kg.m^{-3}$	1880 $kg.m^{-3}$	1881 $kg.m^{-3}$
5.1 cm	1913 $kg.m^{-3}$	1882 $kg.m^{-3}$	1880 $kg.m^{-3}$	1912 $kg.m^{-3}$
10 cm	1912 $kg.m^{-3}$	1858 $kg.m^{-3}$	1932 $kg.m^{-3}$	1963 $kg.m^{-3}$
15 cm		1942 $kg.m^{-3}$	1942 $kg.m^{-3}$	
18 cm	1909 $kg.m^{-3}$			1948 $kg.m^{-3}$
20 cm		1941 $kg.m^{-3}$	1952 $kg.m^{-3}$	
25 cm	1924 $kg.m^{-3}$			1933 $kg.m^{-3}$
30 cm	1920 $kg.m^{-3}$			1898 $kg.m^{-3}$

Table 5.23: Density *prior* to the test at various depths and points for the sixth shot.

Depth of	Water content		
the measure	1st point	2nd point	3rd point
0 cm	7.4%	7.2%	4.8%
5.1 cm	6.1%	6.7%	5.1%
10 cm	7.1%	6.2%	4.4%
15 cm		6.3%	4.4%
18 cm	6.8%		
20 cm		6.9%	4.2%
25 cm	6%	6.7%	4.3%
30 cm	5.7%		

Table 5.24: Water content *after* the shot at various depths and points for the sixth shot.

Depth of the measure	Density 1st point	2nd point	3rd point
0 cm	1714 kg.m^{-3}	1745 kg.m^{-3}	1754 kg.m^{-3}
5.1 cm	1851 kg.m^{-3}	1855 kg.m^{-3}	1833 kg.m^{-3}
10 cm	1843 kg.m^{-3}	1880 kg.m^{-3}	1900 kg.m^{-3}
15 cm		1880 kg.m^{-3}	1864 kg.m^{-3}
18 cm	1855 kg.m^{-3}		
20 cm		1890 kg.m^{-3}	1839 kg.m^{-3}
25 cm	1896 kg.m^{-3}	1882 kg.m^{-3}	1836 kg.m^{-3}
30 cm	1882 kg.m^{-3}		

Table 5.25: Density *after* the shot test at various depths and points for the sixth shot.

5.6.2.7 Seventh shot - buried charge at 3 cm in a dry soil

For this shot, the charge was buried at 3 cm in a dry soil. The force gauge was placed at the bottom of the test tank. On top of the two compacted layers, this time a third layer of about 5 cm was added to complete the test tank. Unfortunately, the grooming machine was out of order. So this third layer was hand-compacted.

The time histories of pressures are displayed in figure 5.23.

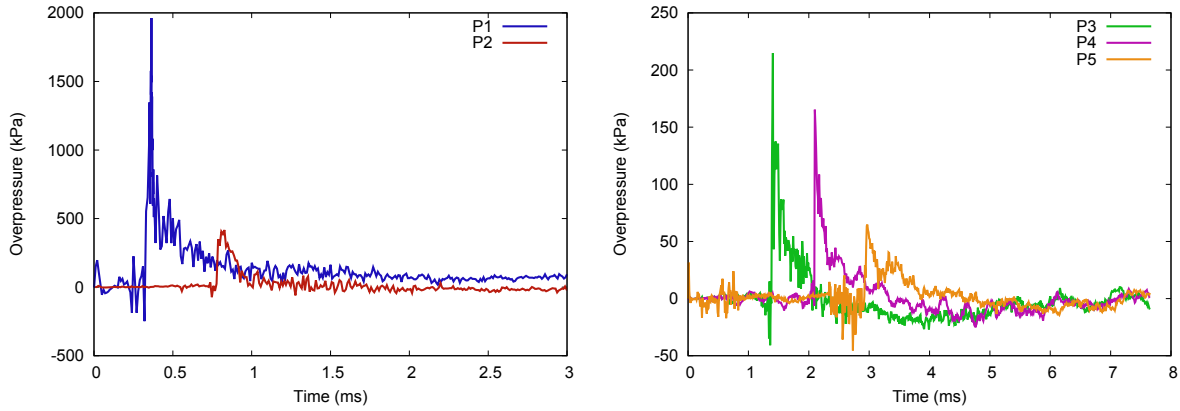

Figure 5.23: Time course of the pressure for the first and second gauges (left) and for the third, fourth and fifth (right) gauges of the seventh shot.

The measures of density and water content with the nuclear density gauge are gathered in tables 5.26, 5.27, 5.28 and 5.29.

Depth of	Water content			
the measure	1st point	2nd point	3rd point	4th point
0 cm	3.2%	4.1%	4.3%	3%
5.1 cm	2.7%	4.7%	3.9%	2.7%
10 cm	2.9%	3.6%	3.2%	2.9%
18 cm	3%	3.6%	3.3%	3%
25 cm	2.8%	4.3%	3.9%	2%
30 cm	3%	3.9%	3.8%	2.7%

Table 5.26: Water content *prior* to the test at various depths and points for the seventh shot.

Depth of	Density			
the measure	1st point	2nd point	3rd point	4th point
0 cm	1663 $kg.m^{-3}$	1756 $kg.m^{-3}$	1681 $kg.m^{-3}$	1646 $kg.m^{-3}$
5.1 cm	1768 $kg.m^{-3}$	1731 $kg.m^{-3}$	1714 $kg.m^{-3}$	1728 $kg.m^{-3}$
10 cm	1782 $kg.m^{-3}$	1815 $kg.m^{-3}$	1722 $kg.m^{-3}$	1712 $kg.m^{-3}$
18 cm	1760 $kg.m^{-3}$	1792 $kg.m^{-3}$	1765 $kg.m^{-3}$	1719 $kg.m^{-3}$
25 cm	1775 $kg.m^{-3}$	1801 $kg.m^{-3}$	1806 $kg.m^{-3}$	1765 $kg.m^{-3}$
30 cm	1766 $kg.m^{-3}$	1812 $kg.m^{-3}$	1794 $kg.m^{-3}$	1789 $kg.m^{-3}$

Table 5.27: Density *prior* to the test at various depths and points for the seventh shot.

Depth of	Water content		
the measure	1st point	2nd point	3rd point
0 cm	5.8%	4.7%	3.8%
5.1 cm	5.7%	5.4%	3.6%
10 cm	5.5%	3.9%	3.5%
18 cm	4.7%	3.9%	3.6%
25 cm	5.6%	4.8%	3.3%
30 cm	5.2%	4.2%	3.8%

Table 5.28: Water content *after* the shot at various depths and points for the seventh shot.

Depth of	Density		
the measure	1st point	2nd point	3rd point
0 cm	1494 $kg.m^{-3}$	1486 $kg.m^{-3}$	1626 $kg.m^{-3}$
5.1 cm	1590 $kg.m^{-3}$	1605 $kg.m^{-3}$	1660 $kg.m^{-3}$
10 cm	1615 $kg.m^{-3}$	1659 $kg.m^{-3}$	1660 $kg.m^{-3}$
18 cm	1649 $kg.m^{-3}$	1695 $kg.m^{-3}$	1695 $kg.m^{-3}$
25 cm	1691 $kg.m^{-3}$	1713 $kg.m^{-3}$	1725 $kg.m^{-3}$
30 cm	1689 $kg.m^{-3}$	1730 $kg.m^{-3}$	1734 $kg.m^{-3}$

Table 5.29: Density *after* the shot test at various depths and points for the seventh shot.

5.6.2.8 Eighth shot - buried charge at 3 cm in a saturated soil

This shot and the last four others took place in January 2014. For all these shots, the nuclear density method was not used. The density and the water content of the soil were determined with a soil sample using the container described in section 5.5 and in figure 5.9.

This shot consisted in the detonation of a buried charge at 3 cm in a saturated soil. About 45 L of water were added to the soil.

The soil was poured and 15 liters of water were spread over the first layer. Then the soil was compacted with the grooming machine. The container was placed in the second layer. 30 liters of water were added and the soil was tamped. The container was removed. The soil tank was completed and hand compacted.

On the high speed camera, the shock wave was observed to deviate from the expected spherical symmetry (maybe due to a gravel, or due to the presence of the first gauge). Besides, the time history of the fourth pressure curve is weird since it seems to record a larger pressure than the third pressure gauge.

The time histories of pressures are displayed in figure 5.24.

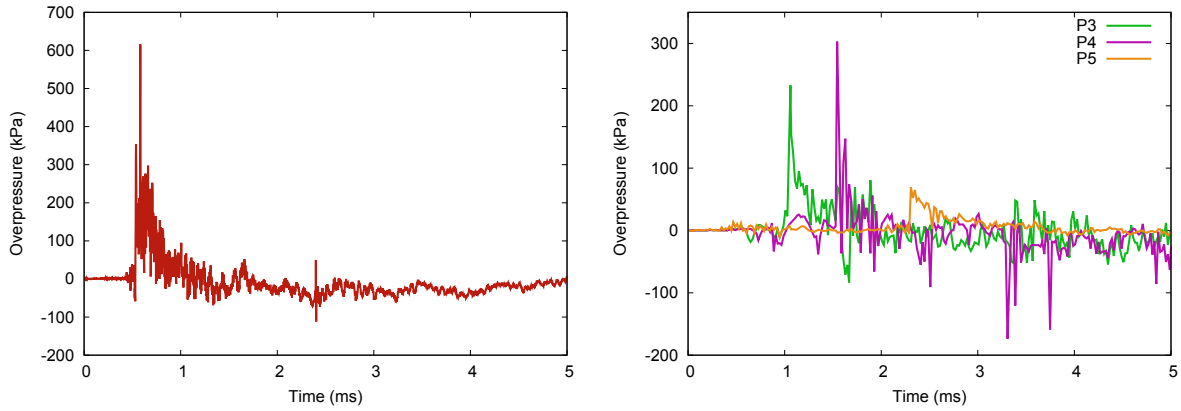

Figure 5.24: Time course of the pressure for the second gauge (left) and for the third, fourth and fifth gauges of the eighth shot.

5.6.2.9 Ninth shot - buried charge at 8 cm in a saturated soil

For this shot, the charge was buried at 8 cm in a saturated soil. About 45 L of water were added to the two layers.

The first layer of soil was poured and watered (adding around 20 L of water), compacted with the grooming machine. Once the soil was tamped, a puddle of water appeared. The container was placed on the opposite side of the puddle of water. A second layer of soil was poured, watered (adding around 25 L of water) and tamped. Some soil was added to complete the soil tank. The final compaction was hand made.

For the detonation of buried charges at 8 cm, the pressure gauges were changed to measure smaller pressures more accurately. However the first gauge was not exploitable.

The time histories of pressures are displayed in figure 5.25.

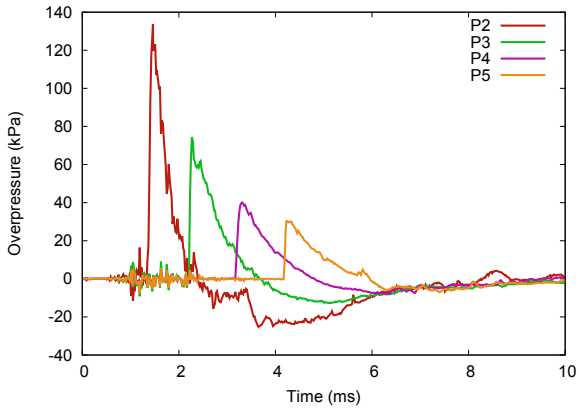

Figure 5.25: Time course of the pressure for the second, third, fourth and fifth gauges of the ninth shot.

5.6.2.10 Tenth shot - buried charge at 8 cm in a saturated soil

This shot is the same as the previous one. About 60 L of water were added to the soil preparation in two layers.

For the first layer of soil, 30 L of water were poured. The soil was compacted with the grooming machine. For the second layer of soil, 30 L of water were also added. This time, the soil was hand tamped. The container was removed. Some soil was added and the tank was hand tamped.

The first pressure gauge was changed since it did not work correctly during the ninth shot.

The time histories of pressures are displayed in figure 5.26.

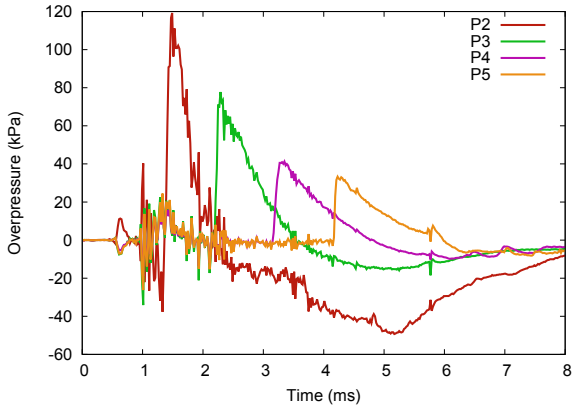

Figure 5.26: Time course of the pressure for the second, third, fourth and fifth gauges of the tenth shot.

5.6.2.11 Eleventh shot - buried charge at 8 cm in a dry soil

For this shot, the charge was buried at 8 cm in a dry soil which was completely hand-tamped. The time histories of pressures are displayed in figure 5.27.

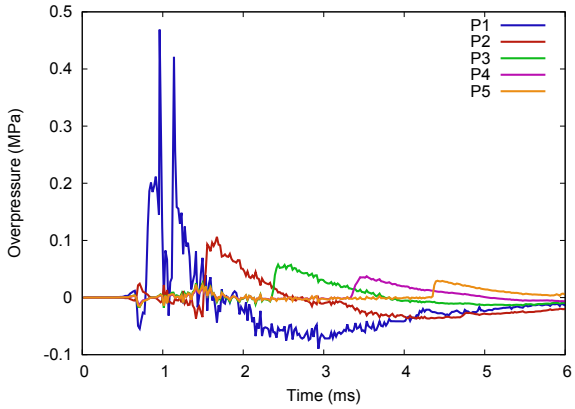

Figure 5.27: Time course of the pressure for the first, second, third, fourth and fifth gauges of the eleventh shot.

5.6.2.12 Twelfth shot - buried charge at 8 cm in a dry soil

This shot is the same as shot eleven. The first layer was tamped with the grooming machine whereas the second layer was hand tamped. The time histories of pressures are displayed in figure 5.28.

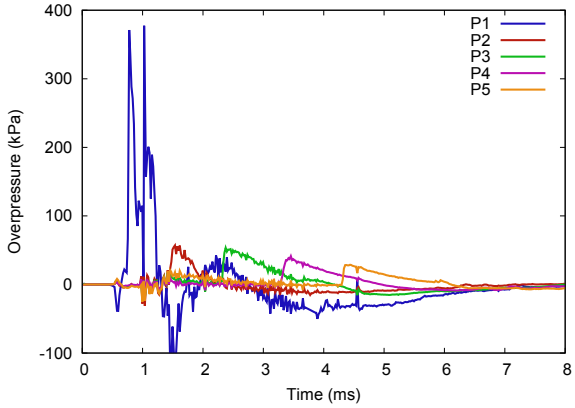

Figure 5.28: Time course of the pressure for the first, second, third, fourth and fifth gauges of the twelfth shot.

5.6.3 Density and water content from the sampling method

A container was placed in the second layer of the soil during the filling of the soil tank. The aim was to have another measure of the density and the water content apart from

those obtained with the nuclear density gauge. With the sampling method, the water content was evaluated by oven drying the soil sample whereas the density was determined by weighing the sample (since the volume was known). The results for each shot (from the third one) are given in table 5.30.

shot number	state of the soil	water content	density
1	dry	-	-
2	dry	-	-
3	saturated	10,5%	2109 $kg.m^{-3}$
4	saturated	8,4%	2021 $kg.m^{-3}$
5	dry	5,0%	1909 $kg.m^{-3}$
6	saturated	6,9%	1938 $kg.m^{-3}$
7	dry	5,0%	1742 $kg.m^{-3}$
8	saturated	6,5%	1818 $kg.m^{-3}$
9	saturated	7,0%	1901 $kg.m^{-3}$
10	saturated	11,6%	1892 $kg.m^{-3}$
11	dry	5,5%	1647 $kg.m^{-3}$
12	dry	5,1%	1576 $kg.m^{-3}$

Table 5.30: Density and water content results with the sampling method.

5.7 Analysis of the results of the shots

The results of the detonation of small buried charges detailed in section 5.6 are here analysed.

5.7.1 Shock wave propagation and soil ejecta

The shock wave drives a density jump. Therefore its propagation can be recorded exploiting the principle of shadowgraphy: its projection on a reflective panel placed in the background of the device is tracked by a high speed camera.

Figure 5.29 shows the propagation of the shock wave for a flush charge, and for an explosive buried at 3 cm. It begins with the detonation of the explosive up to the formation of the detonation products and the soil projections.

In the first set of pictures, three steps can be distinguished: a fire ball expands first, the shock wave follows detected by the pressure propagation and the density change, and finally detonation products spread in air. The sand projections are not well visible.

At variance, for the buried charge, the fire ball is not visible since the detonation occurred in the soil where less oxygen is available. The soil then rises above the explosive creating a kind of camouflet. This corresponds to the soil displacement above the explosive. The shock wave is progressively visible and finally ejecta are clearly distinguishable. The velocity of these ejecta has been evaluated up to 900 m/s.

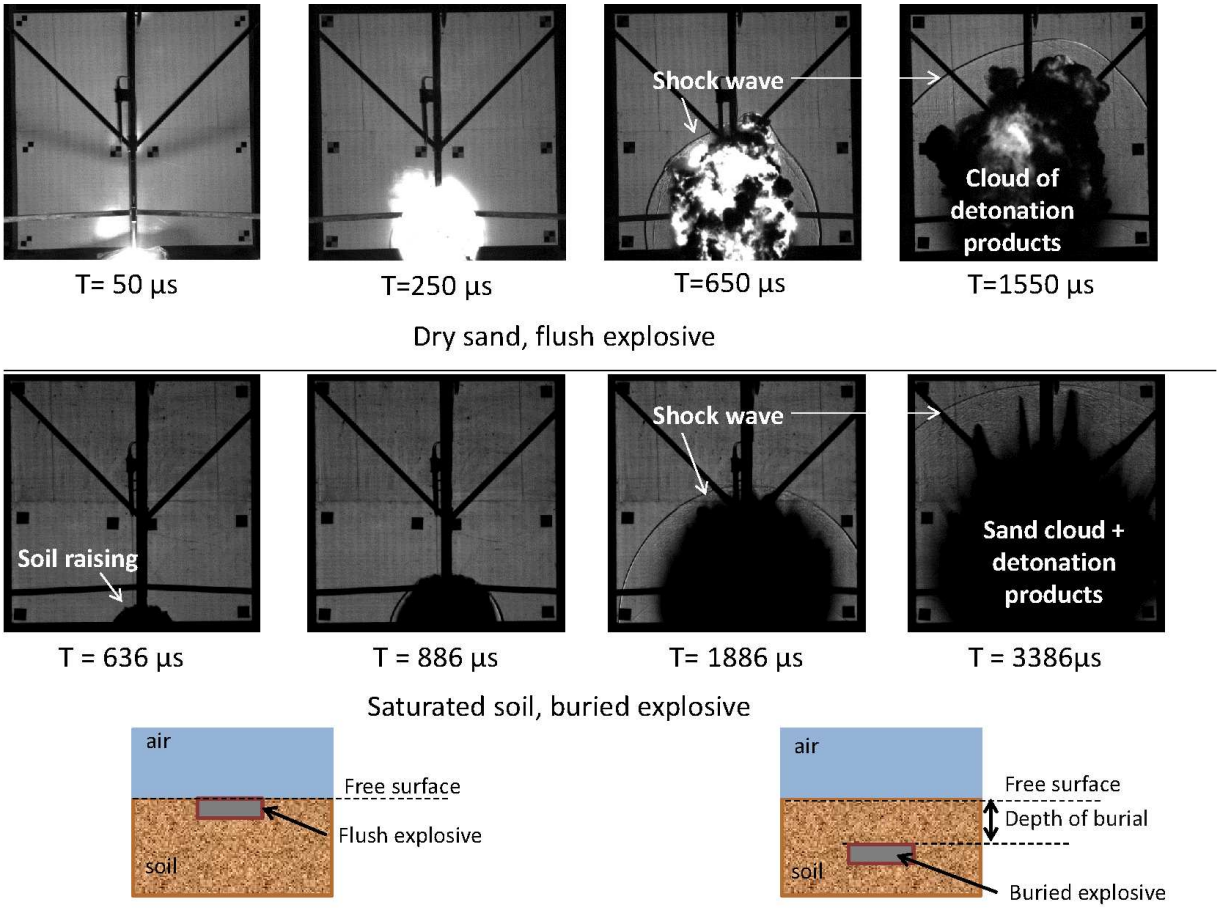

Figure 5.29: Pictures of the detonation and the propagation of the shock wave for a flush explosive in dry soil, and for an explosive buried at 3 cm in saturated soil. In the first set of pictures, the fire ball of the detonation and the shock wave can be noticed. If the pictures were zoomed, the reflections of the shock wave on the structures could be observed. In the second set of pictures, first the soil raising coming from the layer above the explosive, next the shock wave, and finally the detonation products can be successively noticed. When the explosive is buried, no fire ball can be observed.

5.7.2 Remarks on water contents and densities

The apparent mass density and the mass water content respectively defined by equations (1.1.5) and (1.1.17) were measured by two methods: thanks to the nuclear density gauge (see section 1.1.4 for details of this device) and thanks to a soil sample. The results for both methods are given in section 5.6.

The advantage of the nuclear density method is that the density and the water content are evaluated at various points and at various depths whereas the container only provides the density and the water content in one place. The results of the nuclear density gauge are almost instantaneous whereas for the traditional laboratory analyses, the results are known after the test.

For each shot, an average value of the density and the water content was calculated from the results of the neutron density gauge. This value is compared in figure 5.30 to

the results obtained with the sampling method.

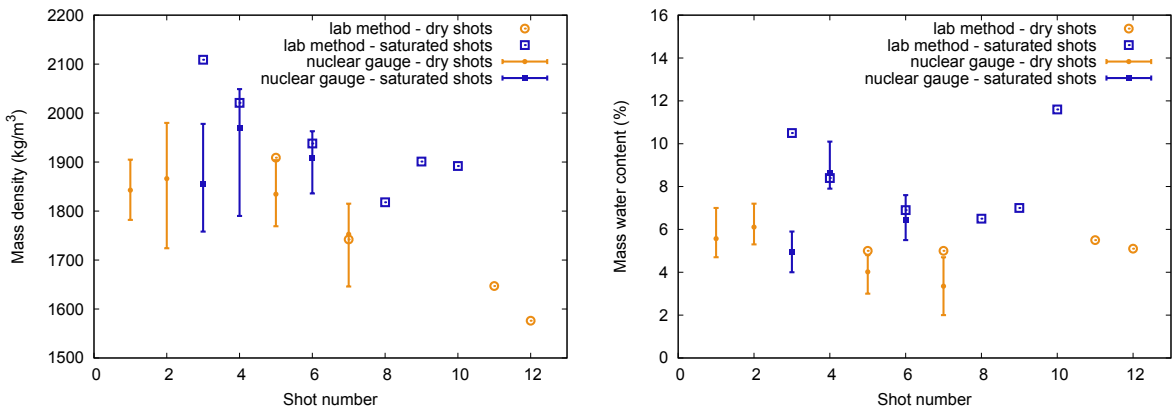

Figure 5.30: Comparison of the results of mass density (left) and mass water content (right) between measures with nuclear density and soil sampling methods.

Except for the third shot, both methods provide close values. It means that the sampling method is adequate to get reliable data of water content and density of the soil.

The measures of the saturated and the dry shots are rather close in these figures. No difference is clear to distinguish a saturated soil from a dry one. We can however deduce that the shot number 10 was saturated since the water content was more important than other shots and that the two last shots (11 and 12) were dry since their densities were much smaller.

Besides, since the soil was stored outside, an important information is the weather forecast. The week before the shots in April, it was raining all day long. On the contrary, during the days of the campaign, the weather was sunny and hot. The results of water content confirm this forecast: the water content of dry soil tanks progressively decreases during the week.

5.7.3 Crater sizes

In our experiments, after each shot, the crater was scanned, which provides the profile of the crater, its diameter, its depth and the height of the lips. From a dedicated software, the volume of the crater was available.

The profiles of craters along one axis obtained from the 3D scan are shown for the three depths of burial (0, 3 and 8 cm) in figure 5.31.

Two important points are worth noticing from these three figures. First, there is no significant difference of crater profiles depending on the state of the soil (whether it is dry or saturated). Second, for a buried charge, the reproducibility seems better for a charge buried at 8 cm than at 3 cm.

For the first notice concerning the state of the soil, it is probably due to the small quantity of explosive (only 100 g) and to the fact that the dry soil was stored in the field. So the difference on water content between what was called a dry soil and a saturated

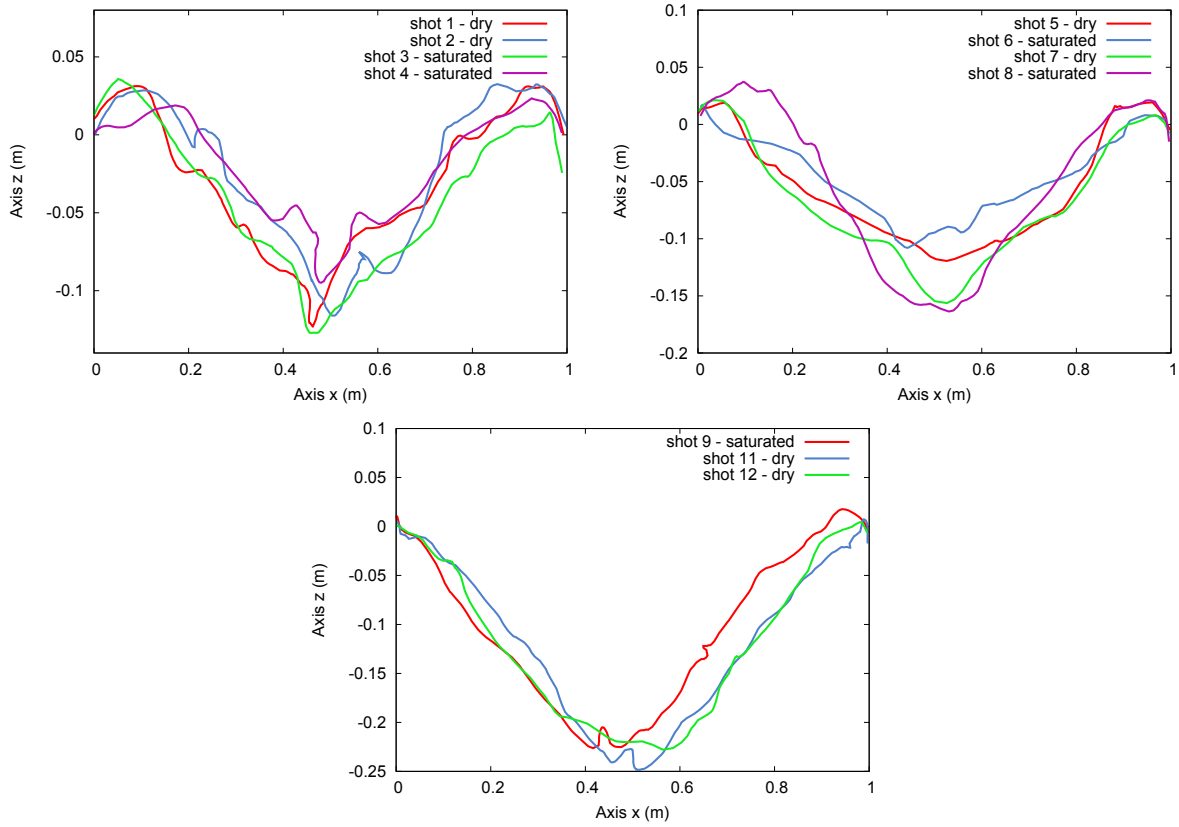

Figure 5.31: Vertical radial cross-sections of the craters for the shots with a flush charge (top left), for the shots with a charge buried at 3 cm (top right) and for the shots with a charge buried at 8 cm (bottom).

soil is not large enough to influence the results. Furthermore it is possible that the saturations were probably not reached as well.

For the second notice concerning the reproducibility, it is possible that the results from a smaller depth are more dependent on the way the soil covering the charge is placed. This dependence is perhaps less important as the depth of burial increases.

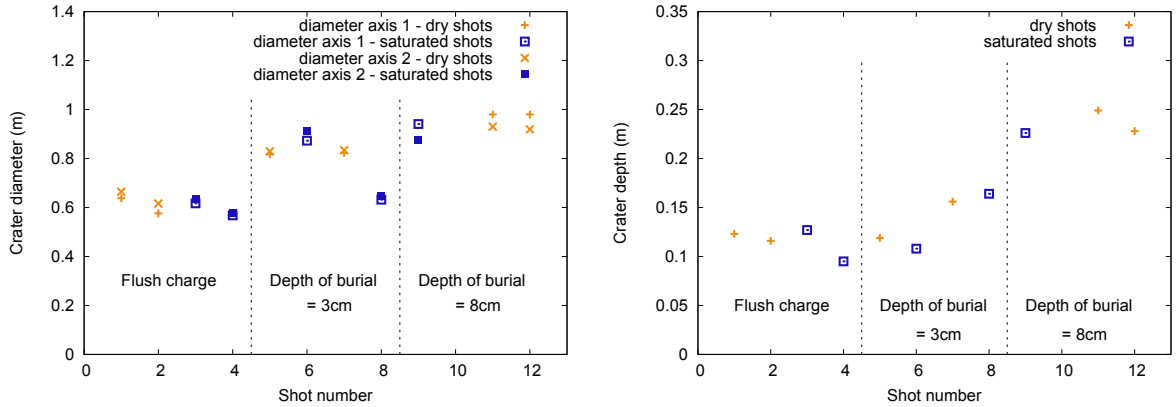

Figure 5.32: On the left, comparison of the crater diameters obtained for the three depths of burial. Since the crater is not completely symmetrical, measures are performed along two orthogonal axes. On the right, comparison of the crater depths obtained during the shots for the three depths of burial. These measures correspond to the lowest point scanned in the crater. So they are the apparent depths. The diameter and the depth of the crater increase with the depth of burial. On the other hand, little difference can be noticed between dry and saturated soil.

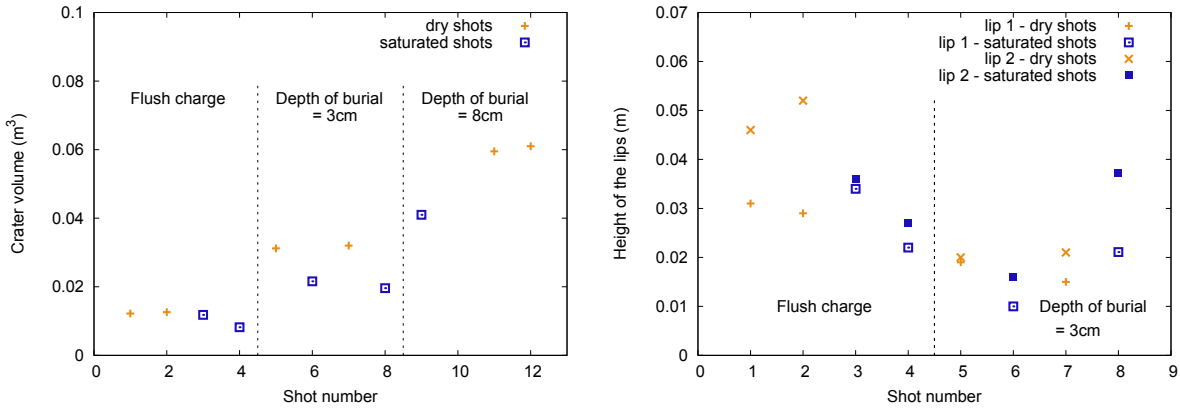

Figure 5.33: On the left, comparison of the crater volumes for the three depths of burial. The crater volumes, calculated by a dedicated software, increase greatly with the depth of burial. Dry shots seem to provide larger craters. On the right, comparison of the heights of the lips for a flush explosive and for a charge buried at 3 cm.

A comparison of the diameter, the depth and the volume of the crater is performed between shots in figures 5.32 and 5.33. The size and the volume of the crater increase with the depth of burial: the volume of a crater for a depth of burial of 3 cm is twice the volume obtained with a flush charge, whereas it is 3 times smaller than for a charge buried at 8 cm.

The influence of the state of the soil (whether it is dry or saturated) seems to increase with the depth of burial: for a flush charge, negligible difference can be noticed whereas, for the depth of burial of 3 cm and 8 cm, shots in dry soil provide larger craters. The water in saturated soils acts like a binder between soil particles.

Figure 5.33 shows the height of the lips for the shots with a flush explosive and a buried explosive at 3 cm. At 8 cm, as shown in figure 5.31, there is hardly any lip on the crater due to the presence of the tank: the soil is expelled outside.

5.7.4 Pressures in the air along a vertical

The maximum pressures recorded at each gauge are displayed in figure 5.34.

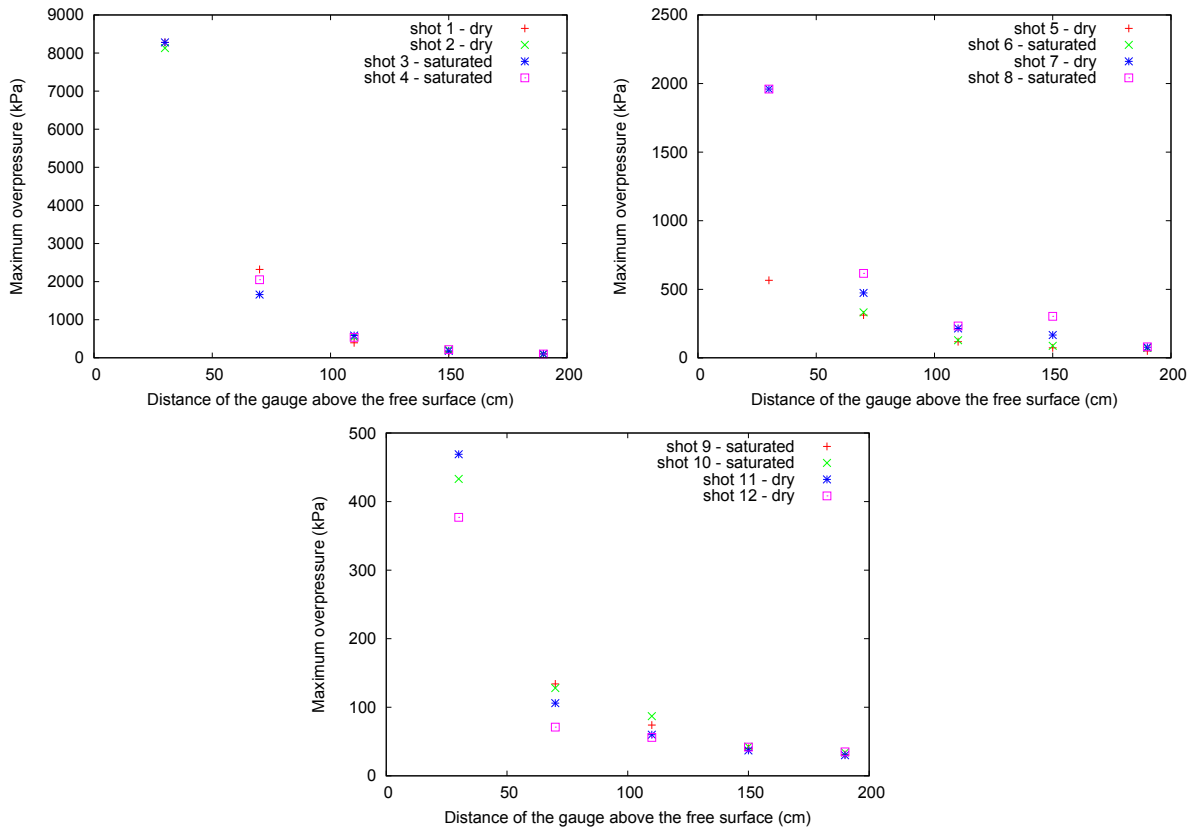

Figure 5.34: Maximum overpressure at the five gauges for the shots with a flush charge (top left), for the shots with a charge buried at 3 cm (top right) and for the shots with a charge buried at 8 cm (bottom).

If instead of linear space scale, a logarithmic scale is used, the maximum pressures

plot linearly, which implies that they can be written in the format

$$P = \frac{k}{d^n} \tag{5.7.1}$$

where P is the pressure in kPa and d corresponds to the distance to the explosive charge in meters.

The parameters k and n depend on the depth of burial as shown in table 5.31. The maximum pressures are replotted in figure 5.35 in logarithmic scale together with the approximation 5.7.1.

	0 cm	3 cm	8 cm
k	682.14	203.1	79.08
n	3.03	2.04	1.39

Table 5.31: Parameters for the three depths of burial (equation 5.7.1).

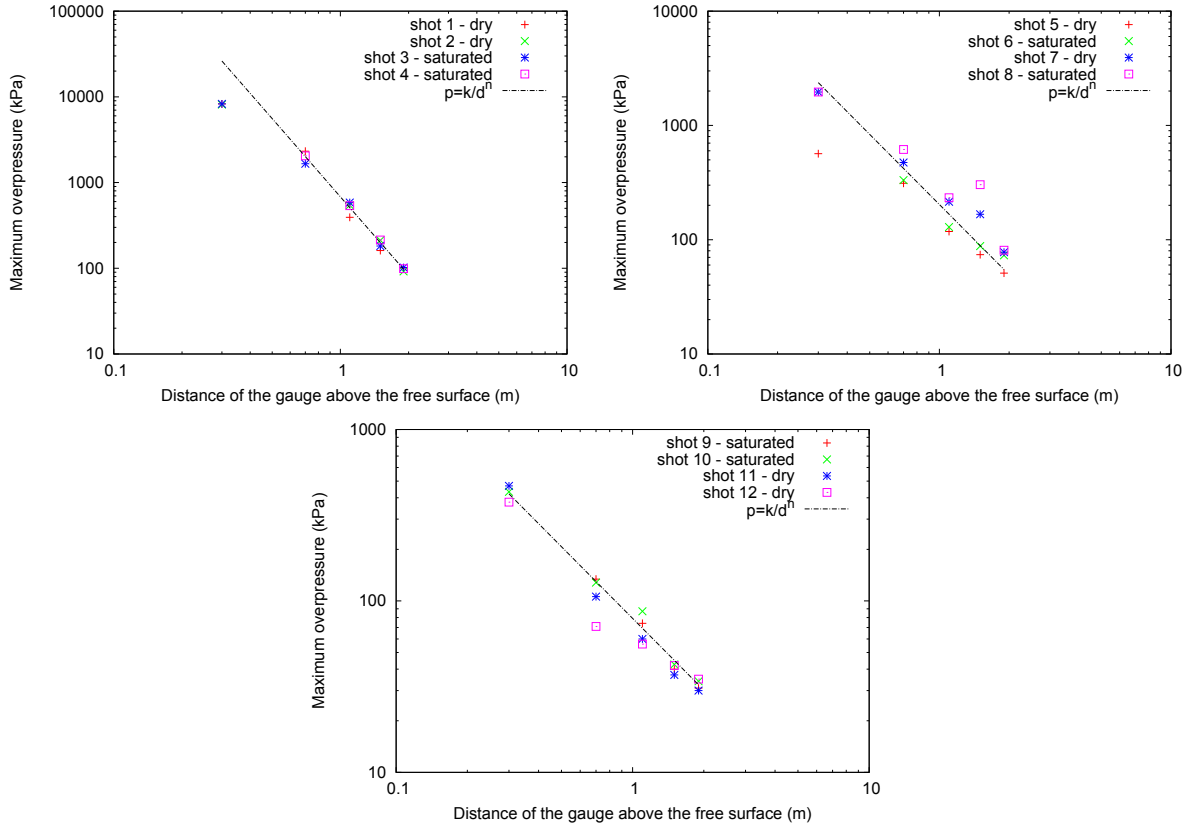

Figure 5.35: Same as figure 5.34 but in logarithm scale.

In figure 5.35 like in figure 5.34, negligible difference can be noticed between dry and saturated shots and no real tendency can be underlined for the two states of soil, and in particularly whether saturated soils provide larger pressures.

5.7.5 Times of arrival of the maximum overpressures

The times of arrival of the maximum overpressures for each shot are recorded in figure 5.36. The records show little dispersion for the flush charges whereas some scattering appears for the deepest charges. The largest dispersion is observed for the charge buried at 3 cm, for which covering the charge with sand might be akward.

While the decrease of the maximum overpressure is exponential according to the distance from the charge, the times of arrival of the maximum overpressure increase exponentially. As a matter of fact, the shock wave is first a detonation wave and propagates in the explosive at the detonation velocity of Chapman Jouguet. In the air, the velocity of the shock wave tends to the sound speed in the air. So the speed of the shock wave begins at around several thousands of meters per second to end at 340 m/s.

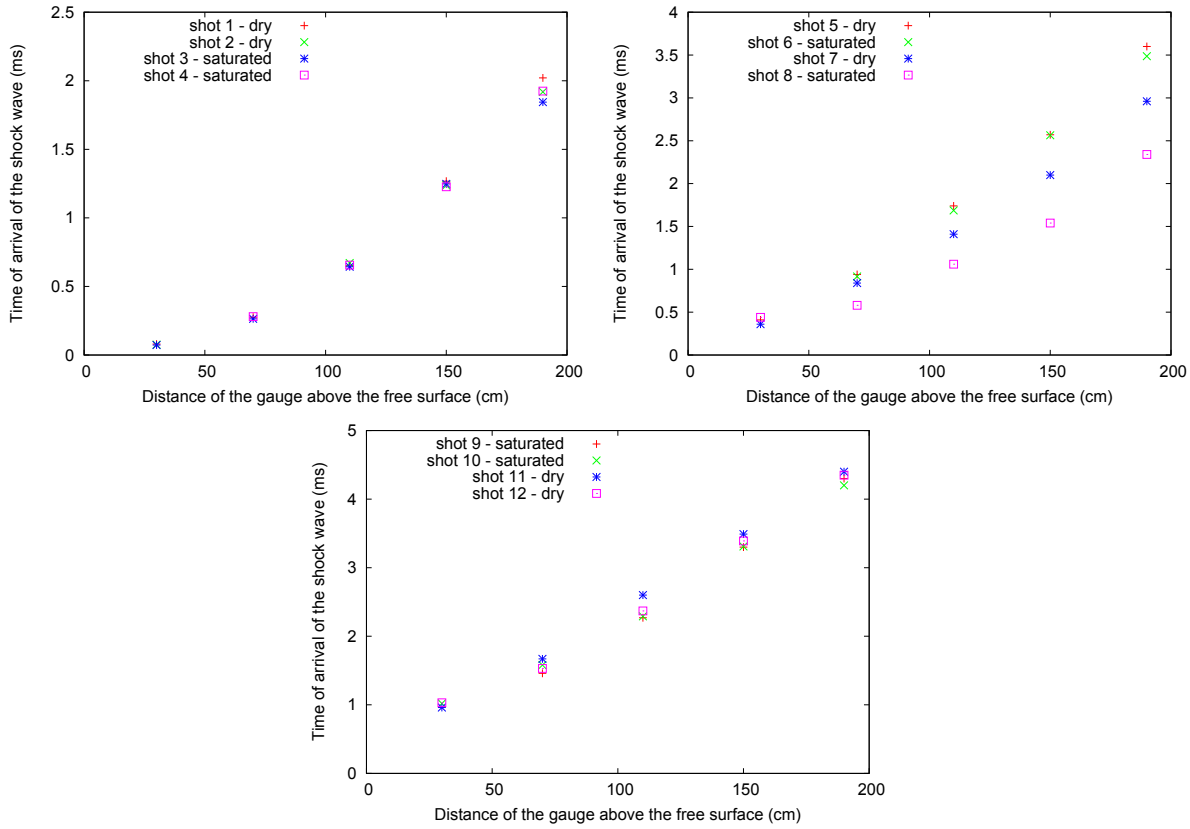

Figure 5.36: Time of arrival of the shock wave at the 5 gauges for the shots with a flush charge (top left), with a charge buried at 3 cm (top right) and with a charge buried at 8 cm (bottom).

Like the pressures, the times of arrival of the maximum overpressures seem similar whether the soil is dry or saturated. In both cases, it is probably due to a too small difference in water content between dry and saturated shots.

5.7.6 Forces measured in soils at the bottom of the soil tank

An attempt was made to measure the force in the soil: a force gauge (very close in its way of working like scales) was placed at the bottom of the tank. For the first shot, the signal of the force gauge was saturated so it was not used for the next three shots until a new one was designed and available. From the fifth shot, the force gauge was changed: the range of pressures which could be measured was then up to 20 MPa.

Unfortunately, as shown in figure 5.37, the results are not really reproducible. As a matter of fact, the result is sensible to many parameters: the way it lays on the soil tank (it may not be completely horizontal which would influence the result), during the compaction the original reference of the force signal can be disturbed...

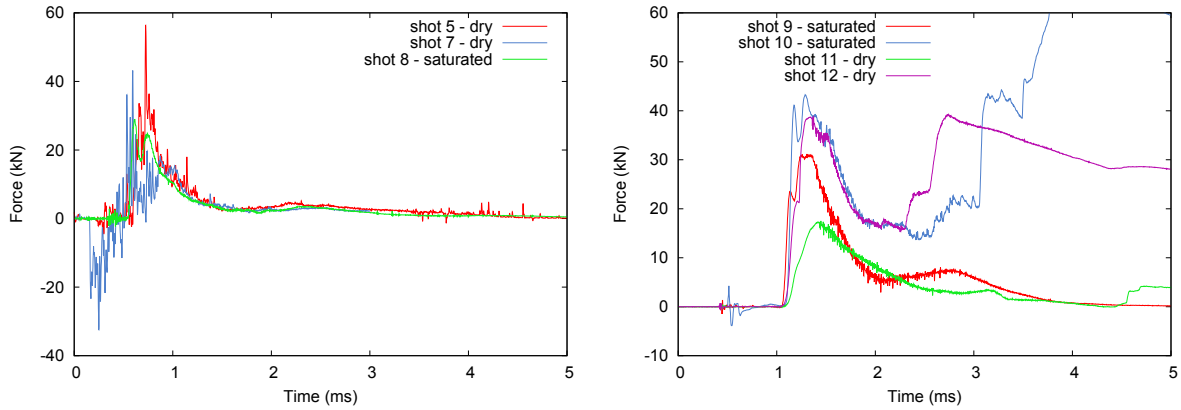

Figure 5.37: On the left, force obtained for the shots with a charge buried at 3 cm. The maximum forces are equal to 55.3, 40.3 and 28.5 kN which are equivalent to pressures of 14.4, 10.5 and 7.4 MPa since the diameter of the force gauge is equal to 70 mm. On the right, for the charge buried at 8 cm, the maximum forces are equal to 23.6, 41.1, 17.3 and 21.6 kN which are equivalent to pressures of 6.1, 10.7, 4.5 and 5.6 MPa.

5.8 Detonation of 100 g of C4 at various depths: simulations versus experiments

The aim of our elastic non linear viscoplastic cap model is to reproduce the most precisely the effects of a buried mine on a structure like a vehicle. In a first step, we try here to repeat the experiments performed at DGA TT reported in section 5.5. We compare the pressures measured at several heights above the soil and the times of arrival of the shock wave. It is also the opportunity to study the influence of the parameters of the model.

For the record, the experiments at DGA TT consisted in the explosion of 100 g of C4 buried at 3 different depths (0, 3 cm and 8 cm) in a dry or in a saturated STANAG soil. The soil tank dimensions were 1 m x 1 m x 0,5 m. The pressure was recorded with 5 gauges located at 30 cm, 70 cm, 110 cm, 150 cm and 190 cm above the free surface of the soil.

5.8.1 Numerical features

In order to save simulation time, the simulations assume a symmetry of revolution about the vertical axis along which sit the pressure gauges. Note that the error due to the fact that the tank is a parallelepided (and not a cylinder) is expected to be small.

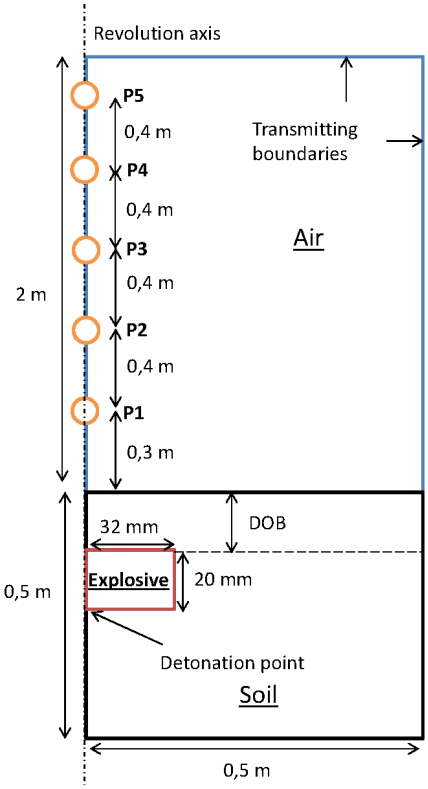

Figure 5.38: Sketch of the configuration run in simulations, with the five fixed pressure outputs (P1 to P5) and the full size of the soil tank. Transmitting boundaries are used to avoid reflections at the borders of the air mesh. The picture is not to scale.

The size of the whole mesh necessary to be able to measure the 5 pressures is 2.50 m x 0.50 m: the height of 2.50 m corresponds to 0.50 m of soil and 2 m of air above the soil. As for the width of the mesh, the soil tank was 50 cm wide.

Transmitting boundaries were used along the boundaries of the air mesh. They were essential. Without them, some huge peaks of pressure occured, corresponding to multiple artificial reflections.The explosive corresponds to the charge used during the experiments: it has a radius of 32 mm and a thickness of 20 mm, which corresponds to 100 g of C4 and provides of density of 1550 kg.m^{-3}. The JWL parameters are given in table 4.7. The point of detonation was located at the bottom of the explosive, along the axis. Actually, the detonator was not a point but had a length (not negligible in our case since it was 1 cm, half of the thickness of the explosive).

In order to have the most realistic results, a condition of atmospheric pressure has been imposed for the boundary conditions of the mesh.

The soil parameters are given in table 2.1.

5.8.2 Pressure for three depths of burial (0, 3 and 8 cm)

The pressure profiles obtained from the detonation of a **flush explosive** are plotted in figure 5.39 at the five outputs. Like in experiments, with the distance, the pressure peaks widen and the decrease of the maximum pressure is exponential.

For each pressure gauge, the maximum value of the pressure and its respective times are compared to experiments in figure 5.40. The results of the simulations fit very well with the experiments.

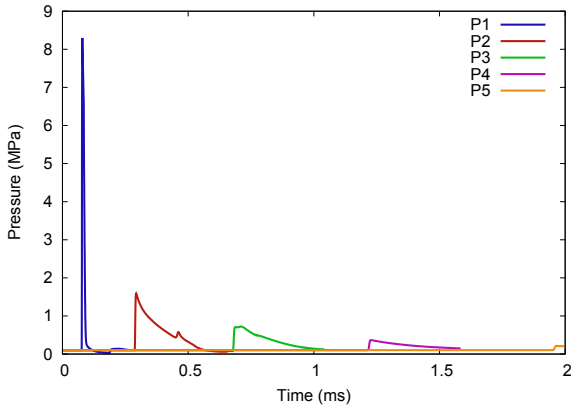

Figure 5.39: Time profiles at the five outputs for a flush charge with an element size of 1 mm.

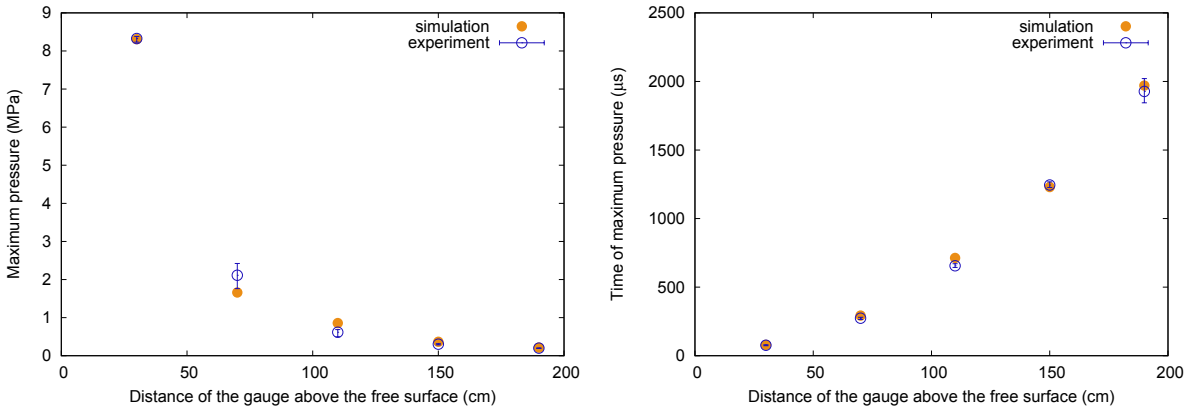

Figure 5.40: Maximum pressures (left) and their respective times (right) at the five outputs for a flush explosive.

The pressure profiles obtained from the detonation of an explosive **buried at 3 cm** are drawn in figure 5.41 at the five outputs. The two first pressure curves are composed of two peaks. One is due to the shock wave while the other one is due to the peak of pressure of the detonation products. Between these two peaks, the pressure curve decreases to a very small value which corresponds to the stress in the soil. As a matter

of fact, the five outputs are fixed so the pressure is displayed whatever the material is, whether it corresponds to aerial pressure or to stresses in the soil (see figures 5.45 and 5.46).

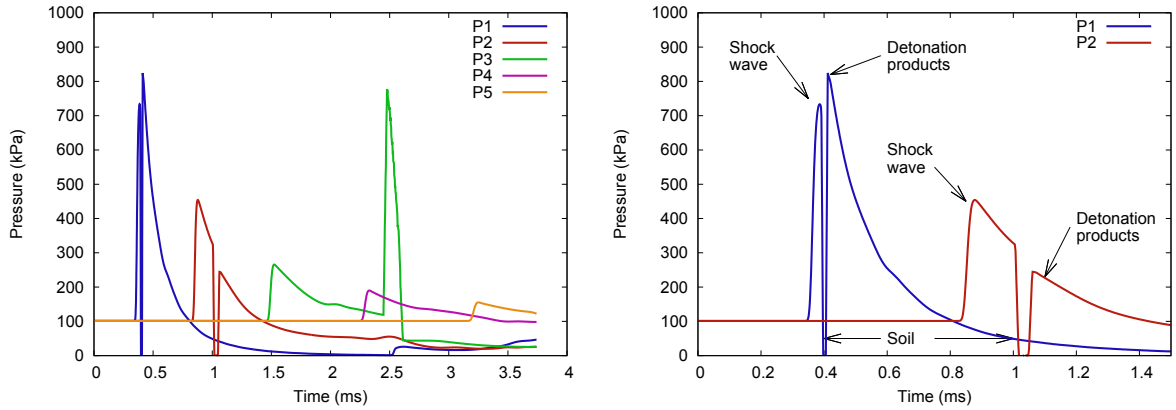

Figure 5.41: Pressure profiles at the five outputs (left) and at the two first outputs (right) for a depth of burial (DOB) of 3 cm and a mesh size of 5 mm. Two pressure peaks appear on the first and the second pressure curves. The first peak corresponds to the shock wave whereas the second one corresponds to the peak of pressure in the detonation products, because of the expansion of the soil (figure 5.46). Another peak, later this time, can be noticed on the third curve. It is due to the decrease of the soil bubble, and the fall of the soil.

For the third history of pressure, a second later peak can be noticed (at around 2.5 ms); this peak is due to the fall of the bubble containing the detonation products.

The maximum pressures and the respective times are compared for each gauge to experiments in figure 5.42. The simulations fit with the experiments[1].

For this depth of burial, the results of experiments are scattered. This has two origins. First it can be due to the preparation of the soil. In this case, contrary to the case of a flush explosive, the results of the pressure depend on the soil which has been put back above the explosive after it was positioned. It is very difficult to place the soil in the same way above the explosive for all experiments. Second, there is very little soil above the explosive (just 3 cm). For such a little thickness, every difference (in thickness, in the granulometry since the soil is heterogeneous) may have consequences on the results.

The pressure profiles obtained from the detonation of an **explosive buried at 8 cm** are drawn in figure 5.43 at the five outputs. As for a depth of burial of 3 cm, two peaks exist for the first and second pressure profiles. Once again the first peak corresponds to the shock wave while the second peak corresponds to the pressure peak of the detonation products inside the soil bubble. This time, the second peak of the first output curve is

[1]except for the pressure of the first output: we can wonder if the problem comes from the simulations or from the experiments. In the latter case, some gravels could have hit the pressure gauge increasing artificially the pressure.

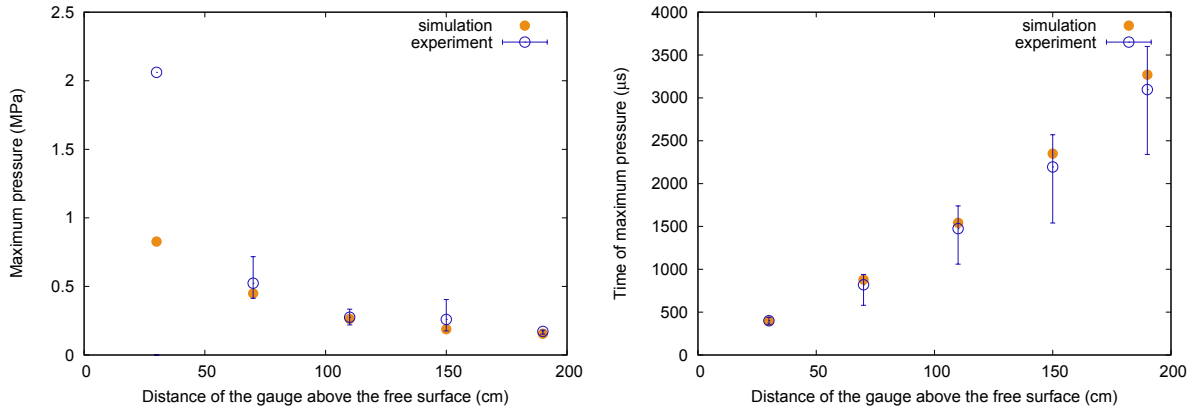

Figure 5.42: Maximum pressures (left) and their respective times (right) at the five outputs for a DOB of 3 cm. Apart from the first output where a huge pressure difference exists between the experiments and the simulations, all the other simulation outputs fit with the experiments.

much larger than the first one. The second time pressure curve is very strange since the peak is not sharp but round.

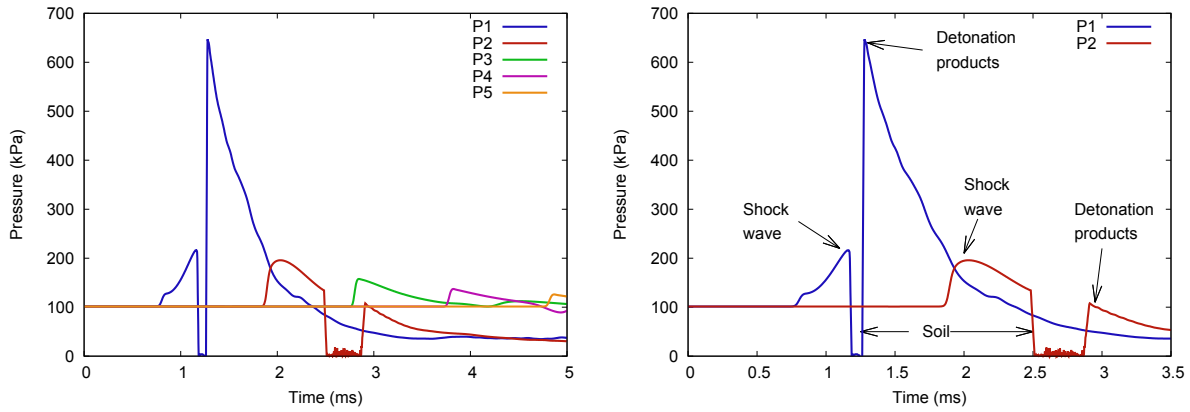

Figure 5.43: Pressure profiles at the five outputs (left) and at the two first outputs (right) for a depth of burial of 8 cm and a mesh size of 5 mm. Two pressure peaks can be noticed for the two first curves as for a depth of burial of 3 cm. This time, the second peak of the first curve is much larger than the first peak. It is worth noticing that the pressure peak of the second curve is not sharp but very round, which is strange.

The maximum pressures and their respective times are compared to experiments for each pressure gauge in figure 5.44. The simulations fit with the experiments for the maximum pressures, but a time shift exists between the experiments and the simulations. The soil was not exactly prepared in the same way for the experiments with an explosive buried at 3 cm and for those with a charge buried at 8 cm. The soil in the experiments with an explosive buried at 3 cm was highly compacted with the grooming machine. At variance, for the experiments with an explosive buried at 8 cm, only the deepest layer of

the tank soil was compacted with the machine. The other layers were tamped manually. The soil was thus less tamped and the density of the soil just beneath the explosive may be much smaller than the density of the rest of the soil tank.

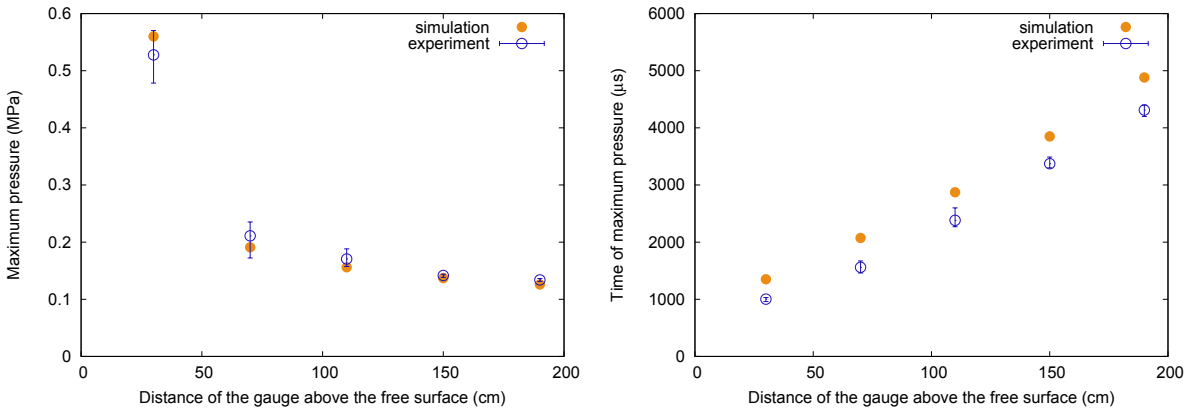

Figure 5.44: Maximum pressures (left) and their respective times (right) at the five outputs for a DOB of 8 cm. All the pressures fit with the experiments. An almost constant time shift exists between the simulations and the experiments. The soil and in particular the upper soil layer was less tamped in the experiments with this depth of burial. Perhaps the density of the soil was smaller which provoked this time shift.

Figures 5.45 and 5.46 shows the contours of the pressure propagation compared to the volume fraction of soil, at two different times for a depth of burial of 3 cm. The shock wave propagates just in front of the soil like in experiments (see figure 5.29).

The pressure peak of the first output for the two depths of burial (3 and 8 cm) can be experimentally due to the shock wave as well as a gravel hitting the gauge and increasing artificially the value. The study in the following sections aims at finding the best parameters to reduce this gap existing between experiments and simulations. However to find them, the simulation pressures of the other gauges which fit very well with experiment must not vary too much since the experiment values for theses gauges are due to the shock wave without a doubt.

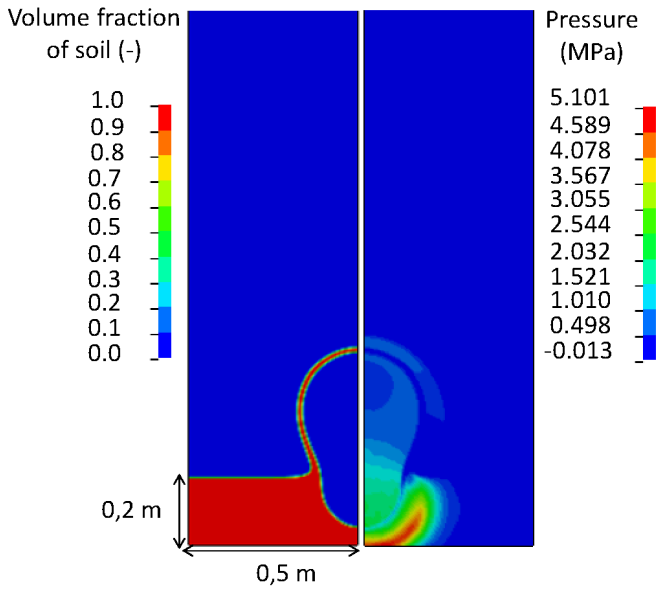

Figure 5.45: Volume fraction of soil (left) and pressure contours (right) due to the detonation of 100 g of C4 buried at 3 cm at t=0.5 ms. On the left, the volume fractions of soil and air are red and blue respectively. On the right, we can see the initial propagation of the shock wave at the same time in the soil and in the air, and the formation of the soil "bubble" consisting of detonation products and soil. In the air, the shock wave propagates in front of the soil expansion like in experiments.

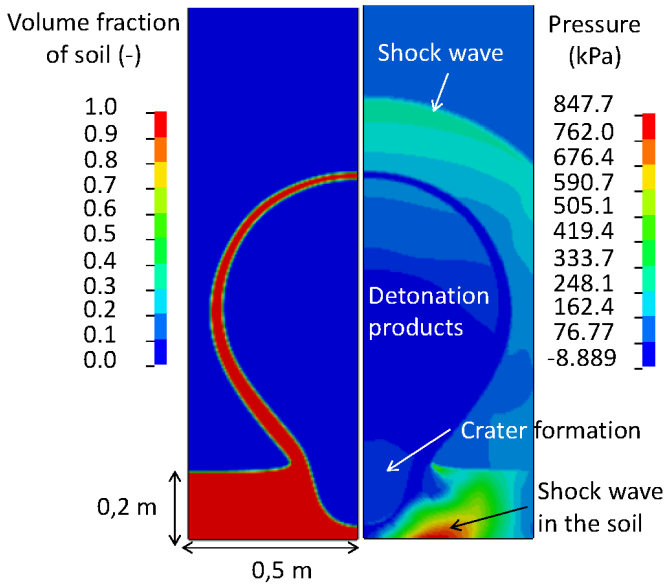

Figure 5.46: Same as figure 5.46 but at t=1.5 ms.

5.9 Influence of experimental details, simulation and soil model parameters

In this section, the influence of all the parameters involved in the simulations is scrutinized. Parameters linked to the experiments, to the finite element mesh and to the soil model are addressed in turn.

5.9.1 Influence of parameters linked to the experiments

The influence of the location of the detonator, the use of polystyrene around the explosive and the size of the soil tank on pressures have been studied.

Influence of the position of the detonator

It is well known that the position of the detonator is very important in order to compare results. As a matter of fact, when locating the detonator on the bottom face of the explosive, all the explosive moves upward. The entire explosive energy has been transferred vertically. At the other extreme, locating a detonator on the upper side of the explosive would tend to orientate the energy of the explosive downward. As a result, the recorded pressures would be smaller. In the experiments carried out at DGA TT, the detonator was not a point but was close to a line (the length of the detonator was equal to 1 cm). Some simulations have been run locating the detonation point in the bottom and in the middle of the explosive to quantify the differences on the pressure signals.

In reality, in simulations, negligible differences could be noticed between the two locations for a flush charge as well as for buried charges (3 and 8 cm). Perhaps it is due to the small quantity of explosive employed, and to the ratio of the detonator length over the thickness of the explosive.

Influence of the polystyrene around the explosive

The explosive was surrounded by polystyrene with a density of $31\,\mathrm{kg.m^{-3}}$ during each experiment (see figure 5.10): 25 mm around the explosive and 25 mm below. The aim was to maintain the position of the detonator once the explosive was placed in the soil. In simulation, some air was used instead of polystyrene since all the parameters of air were known.

In simulation, the influence of the polystyrene around the explosive is small for a depth of burial of 3 cm, whereas the difference is more noticeable for a depth of burial of 8 cm: the pressure peak is a little more important and the pressure signals arrive earlier when the polystyrene surrounds the explosive.

The results of the simulations were compared to the experiments (figure 5.47): since the differences are very little for a depth of burial of 3 cm, the results fit with the experiments. As for a depth of burial of 8 cm, the pressure of the first pressure gauge is still larger in simulation than in experiments. With polystyrene, the other outputs are very close to experiments. In particular, the time shift has decreased.

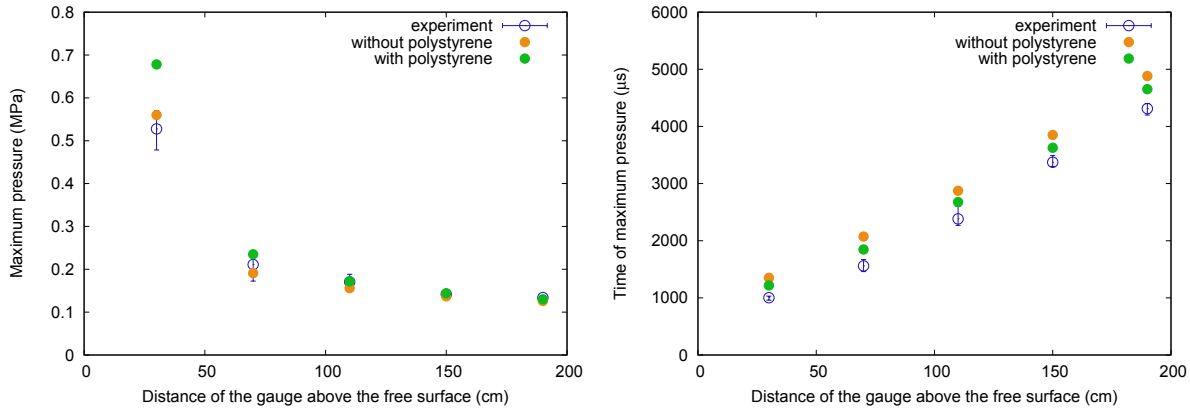

Figure 5.47: Maximum pressures (left) and their respective times (right) for a DOB of 8 cm in experiments, in simulations with and without representing the polystyrene surrounding the explosive. The simulations are closer to the experiments when the polystyrene is taken into account.

The influence of the polystyrene can be explained as follows: the polystyrene is less dense than the soil, so easier to move. Less energy from the explosive is spent. As a result, the pressure peaks are slightly larger. The difference is only slightly since the polystyrene surrounds the explosive but there is no polystyrene above the explosive. The density of polystyrene is smaller than soil so the shock wave propagates faster.

Size of the simulated soil tank

The soil tank which was used in experiments was 0.5 m high and 1 m side. In order to save simulation time, the height of this soil tank was reduced to 0.2 m. The width of the mesh size remained at 0.5 m. The comparison between the two soil tank sizes was made for an element size of 5 mm. For a DOB of 3 cm, there is a slight difference in the times of arrival of the shock wave. This difference disappears with a DOB of 8 cm where the times of arrival are almost identical.

5.9.2 Influence of numerical parameters

The influences of the element size and the convection schemes associated with the ALE and Euler approaches are studied here.

Influence of the element size

The element size is worth testing since it can alterate or improve the quality and accuracy of the results. The shock wave is thin just after the detonation of the explosive. Thus several elements should be in the thickness of the shock wave to avoid pressure diffusion. Various element sizes were tested (1, 2, 5 and 10 mm for a flush explosive, and an element size of 2 and 5 mm for an explosive buried at 3 and 8 cm). The results of the pressure profiles are presented in figure 5.48.

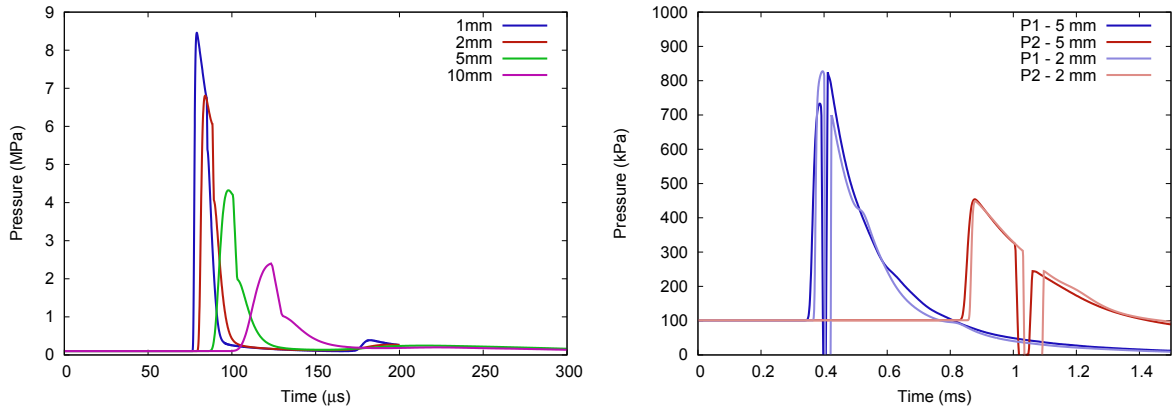

Figure 5.48: On the left, pressure profiles at the first output for a flush charge. A decrease of the element size prevents the diffusion of the pressure. Thus the slope of the pressure peak is stiffened, the value of the peak of pressure is increased, and the duration of the pressure peak is decreased. On the right, pressure profiles at the two first outputs for a charge buried at 3 cm with 2 element sizes (2 and 5 mm). The resulting pressures and in particular the maximum pressures are alike.

For a flush explosive, the element size has a very important influence on the result. Diffusion increases with the element size. Thus, a decrease of the element size stiffens the slope of the pressure peak, increases the value of the peak of pressure, and decreases the duration of the pressure peak. When the element size is large, since the pressure is averaged on the elements, the pressure peak is missed. At variance, when the element size is small, more elements are used to discretized the shock wave which enables to have the right increase in pressure.

The pressure peak was multiplied by 3.4 (from 2.5 MPa to 8.5 MPa) as the element size changes from 10 mm to 1 mm, and the duration of the pressure peak was increased from 25 μs for an element size of 1 mm to 80 μs for an element size of 10 mm. Morever the shock wave occurs earlier with a smaller element size (at 75 μs instead of 105μs).

However as shown in figure 5.48, as the time of arrival of the shock wave seems to be close to convergence, the difference of the pressure peak between an element size of

1 mm and 2 mm suggests that a smaller element size would be necessary to converge also on pressure.

For explosives buried at 3 and 8 cm, element sizes of 2 and 5 mm were compared. The influence is not as much important as for a flush explosive. As a matter of fact, with a buried explosive, the shock wave first propagates in the soil, which has a stronger resistance than air and which is energy consuming. Thus, the thickness of the shock wave rapidly increases which explains why the element size is less important.

For a DOB of 3 cm, the maximum overpressure is very close for the two element sizes, but a slight time shift between the curves exists as shown in figure 5.48. For a DOB of 8 cm the tendencies are the same, and the time shift between the curves seems to be equal for the two depths of burial.

For the following simulations, an element size of 5 mm was chosen for the simulations of explosives buried at 3 and 8 cm whereas for the simulations involving flush explosives, an element size of 1 mm was used.

Influence of the algorithm of convective transport

Two algorithms to convect the nodal and material variables through the ALE or Euler meshes are available in LS Dyna: a first order accurate method called Donor Cell and a second order accurate method called Van Leer. Up to now, the first order method was used.

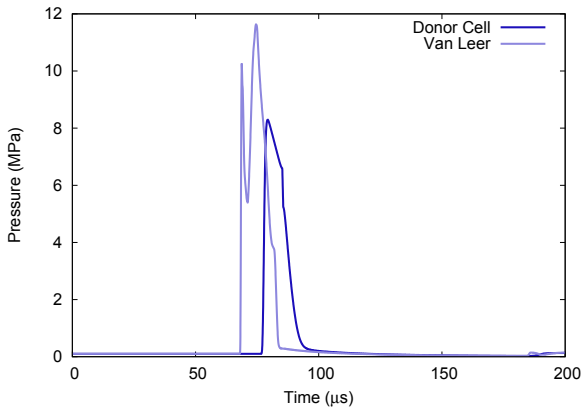

Figure 5.49: Pressure profiles at 30 cm above the free surface of the soil, for a flush charge, for the Van Leer and Donor Cell algorithms, with an element size of 1 mm. The difference of the results between the two numerical methods is important: in particular, the pressure peak is larger and the shock wave arrives earlier with the Van Leer algorithm.

In the case of a flush charge, the pressure peak is larger with the Van Leer method than with the Donor cell method for the first peak as shown in figure 5.49: it is equal to 11.8 MPa with the Van Leer method and only to 8.2 MPa with the Donor Cell method. This difference of pressure between the two algorithms remain the same for all the gauges for a flush charge.

The time of the maximum pressure is also different according to the numerical method which is used. The Van Leer Method provides earlier pressure peaks and this tendency increases with the distance.

For charges buried at 3 and 8 cm, the tendency observed for the flush charges is the same but the differences between the two algorithms are smaller (figure 5.50): the pressure peaks are larger with the Van Leer algorithm and the signals are slightly earlier compared to the Donor Cell algorithm. However with the Van Leer algorithm, unstable pressures appear, in particular for the first output.

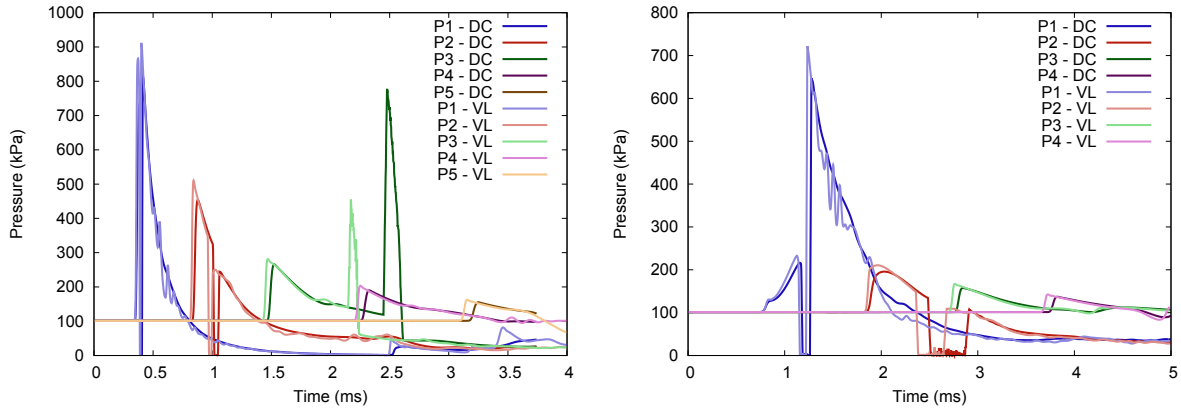

Figure 5.50: Pressure profiles at the five outputs for charges buried at 3 cm (left) and at 8 cm (right), with the Van Leer (VL) and Donor Cell (DC) algorithms. The differences between the two algorithms are less important than with a flush explosive. However using a second order accurate algorithm provides an unstable pressure signal at the first output.

The simulations were compared to the experiments for a charge buried at 3 and 8 cm in figures 5.51 and 5.52. The second order accurate method provides results closer to experiments, in particular for an explosive buried at 8 cm for which the time shift exiting between experiments and simulations is reduced.

The second order accurate algorithm provides results closer to the experiments in particular concerning the time of the maximum pressure. However, to avoid the numerical instabilities that appear on the curve of the first output, the first order accurate algorithm is still used in the following simulations.

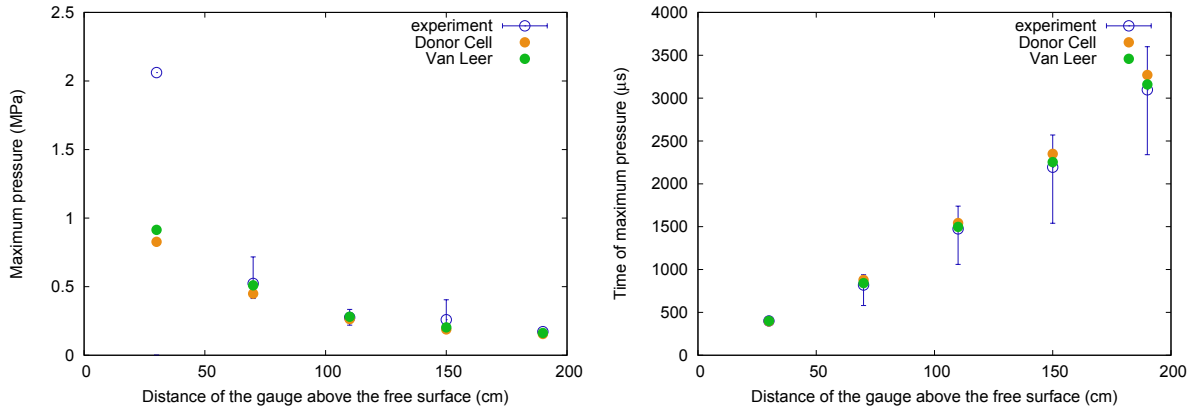

Figure 5.51: Maximum pressures (left) and their respective times (right) at the five outputs for a DOB of 3 cm in experiments, and with the Van Leer and Donor cell algorithms.

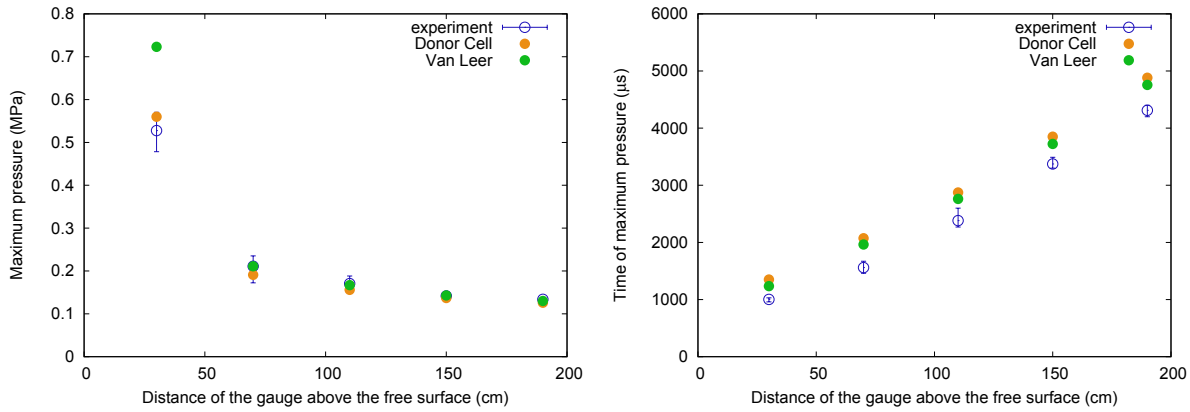

Figure 5.52: Same as figure 5.51 but for a DOB of 8 cm. The maximum pressure at the first output is much larger in simulations than in experiments. The other maximum pressures for the two algorithms are close. The time shift decreases using the second order accurate algorithm.

5.9.3 Influence of the parameters of the soil model

A parametric study has been performed to assess the qualitative and quantitative influences of the soil model parameters. In turn, we address the influence of the parameters defining the elastic stiffening, the yield surface and the hardening rule.

5.9.3.1 Influence of the time dependence

In our model, viscoplasticity is defined with the term η/f_0^N (see equation (2.3.3)). f_0 is a normalizing constant with the same unit (Pa) as f the yield surface. $N \geq 1$ is the Perzyna exponent. η corresponds to the inverse of a characteristic time (1/s). The variations of $1/\eta$ and f_0 are equivalent when $N = 1$.

As previously noticed, the value of η which is the inverse of a time (or of f_0) influences the behaviour of the soil. The soil behaves almost elastically when the viscoplastic parameter η is small. Plasticity is retrieved when the intrinsic viscoplastic time is very small, which means for a large value of η.

The reference values of the viscoplasticity parameters are the following: $N = 1$, f_0 =100 kPa and $\eta = 200\,\mathrm{s}^{-1}$. Three values of N and η were tested ($N = 2$, 3 and 4, and $\eta = 2$, 20 and $2000\,\mathrm{s}^{-1}$).

Figures 5.53 and 5.54 show the volume fraction of soil for three values of η (20, 200 and $2000\,\mathrm{s}^{-1}$) for a depth of burial of 3 and 8 cm respectively. Decreasing the value of η increases the dilatation. At variance, with a value of $\eta = 2000\,\mathrm{s}^{-1}$, the thickness of the soil above the detonation products is small. In this case, the volume fraction of soil falls below 1 on the shock wave front.

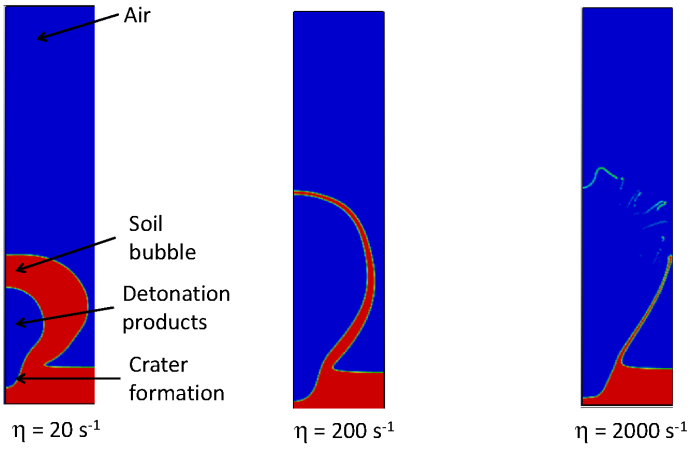

Figure 5.53: Contours of the volume fraction of soil for a depth of burial of 3 cm, for $\eta = 20$, 200 and $2000\,\mathrm{s}^{-1}$ at $t = 2$ ms. The red color denotes the presence of the soil and the blue color the air.

The results of pressure when $\eta = 20\,\mathrm{s}^{-1}$ are very delayed compared to the experiments for the two depths of burial. When $\eta = 200$ and $2000\,\mathrm{s}^{-1}$, the results are closer, but compared to the experiments, $\eta = 2000\,\mathrm{s}^{-1}$ provides the closest pressure results to the experiments for the two depths of burial. This would tend to say that the viscoplasticity

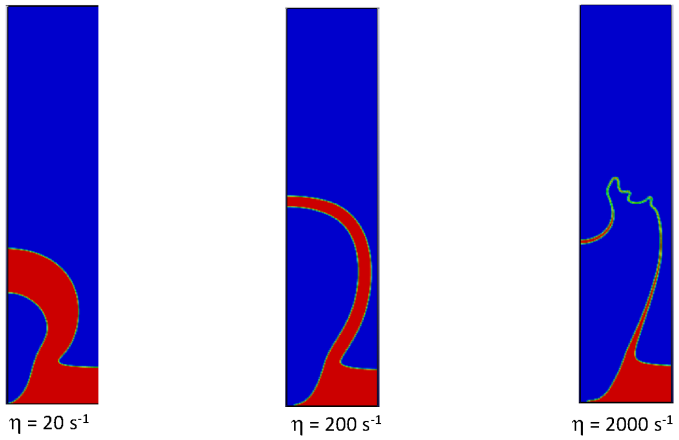

Figure 5.54: Same as figure 5.53 but for a depth of burial of 8 cm at $t = 5$ ms.

which helps in particular the calculations to run must be used but that the time dependence should not be too significant (since increasing the value of η makes the behavior more plastic and less viscoplastic).

All values of exponents N provide close results to experiments.

5.9.3.2 Parameters of the stiffening curve

The parameters of the stiffening curve (ρ_0, K_0, K_{wg}, ν_0) are involved in equations (3.6.5), (3.6.6) and (3.6.7).

Influence of the initial bulk modulus K_0

The value at zero stress of the bulk modulus is equal to 100 MPa. This value was taken from Tong and Tuan (2007) and confirmed by the values available in Bardet (1997) in relation to the nature of the soil and its compaction. The initial bulk modulus is used in the stiffening routine to calculate the current bulk modulus of the soil in relation to the value of the mean stress I_1. In order to evaluate the influence of this elastic modulus, two other values (50 and 500 MPa) have been tested. The initial Poisson's ratio is kept constant with a value of 0.25.

For a DOB of 3 cm, an initial bulk modulus of **50 MPa** results in 10 μs delay in the pressure propagation. The pressure peaks are smaller by a tiny margin than for the standard value of 100 MPa (between 1 to 3 kPa smaller for all gauges). **For a DOB of 8 cm** the tendencies are the same as for the DOB of 3 cm except that for this depth of burial, the differences in time and pressure are much noticeable. The pressure signals are delayed between 10 and 60 μs and the pressure peaks are between 2 to 70 kPa smaller for an initial bulk modulus of 50 MPa.

For a DOB of 3 cm, with an initial bulk modulus of **500 MPa** (figure 5.55), the pressure waves arrive a little earlier, between 20 to 50 μs. The pressure peaks are slightly

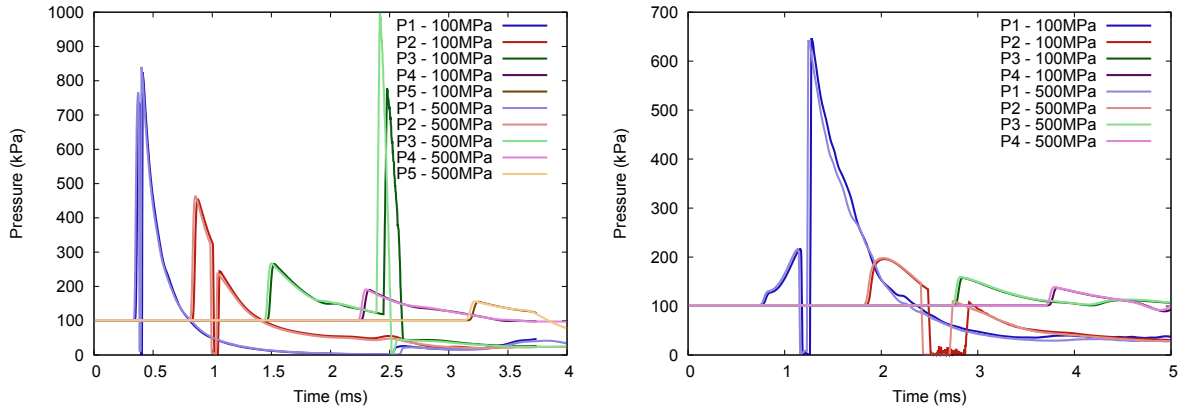

Figure 5.55: Time profiles of the pressures at the five outputs for charges buried at 3 cm (left) and 8 cm (right) for $K_0 = 100$ and 500 MPa. With an initial bulk modulus of 500 MPa, the waves arrive a little earlier, but the peaks are very close for the two elastic moduli.

larger. Once again, **for a DOB of 8 cm** (figure 5.55) the difference is more noticeable. The pressure signals arrive 50 μs earlier but the pressure peaks are between 1 to 7 kPa larger.

The influence of the initial bulk modulus can be explained as follows: the soil is more rigid when the initial bulk modulus is increased. Thus the shock wave propagates faster since the speed of sound is larger. It also means that the quantity of the energy transmitted to the air is more important, provoking larger pressure peaks.

Compared to the experimental data, the initial bulk modulus of 500 MPa provides the closest results to the experiments.

Influence of the bulk modulus K_{wg}

The bulk modulus K_{wg} of the mixture of solid grains and water weighted by their volume fractions plays a role in the stiffening curve of the soil, and in particular is derived from the slope towards which the pressure-density curve tends at large pressure.

Zakrisson et al. (2012) took a value of K_{wg} equal to 66 GPa which is much larger than what could be reasonably expected. The bulk modulus of quartz is about 36 GPa and the bulk modulus of water is 2 GPa.

The value of the bulk modulus K_{wg} which was chosen for all the simulations of this chapter was equal to 36 GPa, since the soil was considered to be dry. Here, two other values of K_{wg}, 20 and 66 GPa, have been tested.

For a bulk modulus K_{wg} of **66 GPa**, the results of the pressure profiles were exactly the same as for a bulk modulus of 36 GPa, for the two depths of burial (3 or 8 cm). In

fact, the increase of the bulk modulus K of the soil is not so high. So it does not reach the value of 66 GPa, providing a similar result.

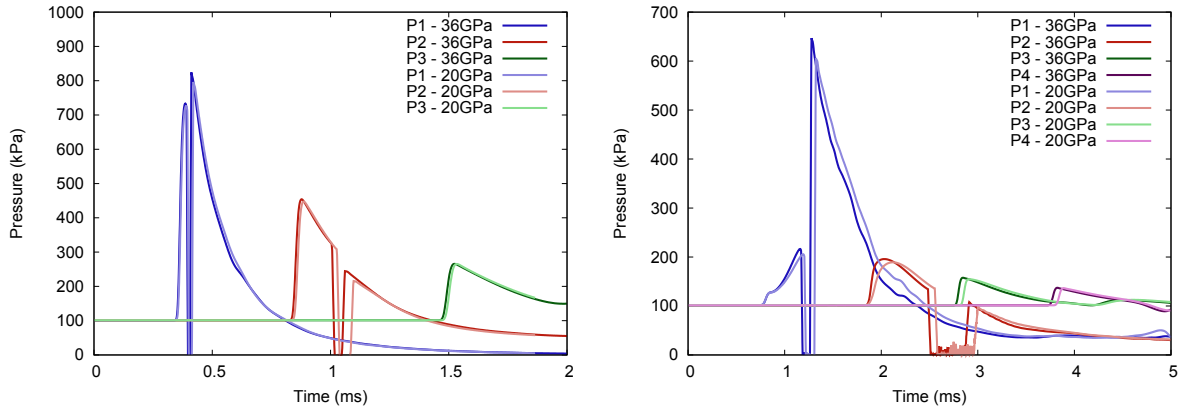

Figure 5.56: Comparison of the pressure profiles at the five outputs for charges buried at 3 cm (left) and 8 cm (right) for $K_{wg} = 20$ and 36 GPa. With a bulk modulus K_{wg} equal to 20 GPa, the pressure waves are slightly delayed.

For a bulk modulus K_{wg} of **20 GPa**, for a **DOB of 3 cm**, the pressure profiles arrived a little later, and the peaks are slightly smaller (figure 5.56). When K_{wg} is equal to 20 GPa, the increase of the bulk modulus of the soil is limited. So the maximum speed of sound (calculated from K) is smaller which can explain a delayed shock wave and smaller pressure peaks since the soil is less rigid and transmits less energy to the air. As for a **DOB of 8 cm** (figure 5.56), the tendency is the same as for a DOB of 3 cm, except that for this depth of burial, the difference between the two values of K_{wg} is much noticeable, in particular concerning the time of arrival of the waves.

Influence of the initial density ρ_0

During our experiments at DGA TT reported in section 5.5, the soil was prepared in two layers which were moistened and tamped. A hole was dug in the center of the free surface, with a diameter slightly larger than the diameter of the explosive and the polystyrene. Once the explosive was placed, the soil was moved back above the explosive without tamping, the free surface being simply smoothed.

The soil above the explosive does not have the same density as the rest of the soil tank. This density can be close to the density obtained by the pluviaton method where the soil is poured from a certain height. In our experiments, the velocity at which the soil is poured is quasi equal to zero, and the height is very small.

Dave and Dasaka (2012) performed pluviation experiments at several speeds and heights. Their results are reproduced in figure 5.57. The density is related to the velocity and the height of pouring. From these data, we may consider that, in our case, the density above the explosive could be 60% of the density of the rest of the soil. Since the mean soil density is equal to 1900 kg.m^{-3}, the soil above the explosive could be equal to 1140 kg.m^{-3}.

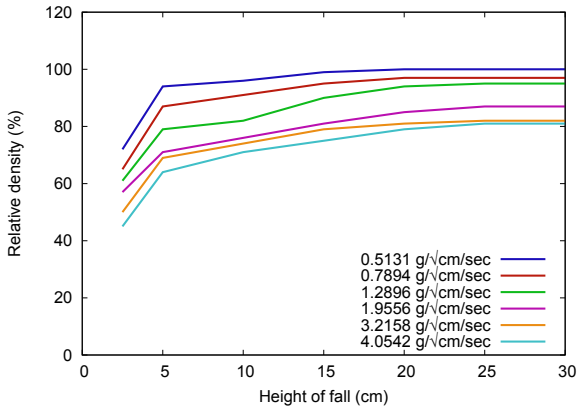

Figure 5.57: This figure is taken from Dave and Dasaka (2012). It represents the density according to the velocity and the height of pouring. The faster and the higher the pluviation occurs, the larger the density is. Our case corresponds to the smallest density, since the velocity and the height are the lowest possible.

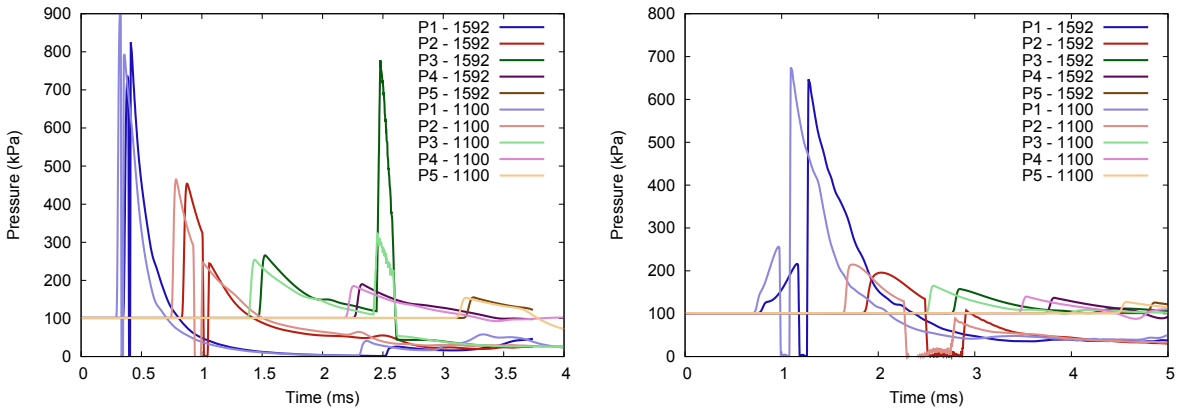

Figure 5.58: Comparison of the pressure profiles at the five outputs for charges buried at 3 cm (left) and 8 cm (right) for $\rho_0 = 1592$ and 1100 kg.m^{-3}. With an initial density of 1100 kg.$^{-3}$, the pressures are in advance and slightly larger.

Simulations have been run with an initial density of 1100 kg.m^{-3} to evaluate the differences with a density of 1592 kg.m^{-3}. Figure 5.58 shows the comparison of pressures for the two initial densities. The time shift between the pressure curves is important for the two depths of burial: the pressures are in large advance with an initial density of 1100 kg.m^{-3}. As for the pressure peaks, they are slightly increased.

A decrease of density provokes a larger sound speed in the soil: the shock wave propagates faster in a lighter soil which explains that the pressure signals arrive earlier. Moreover with a smaller density, the soil above the explosive is lighter so easier to move. Less energy of the detonation is spent to push the soil upward. As a result, the pressure peaks are larger.

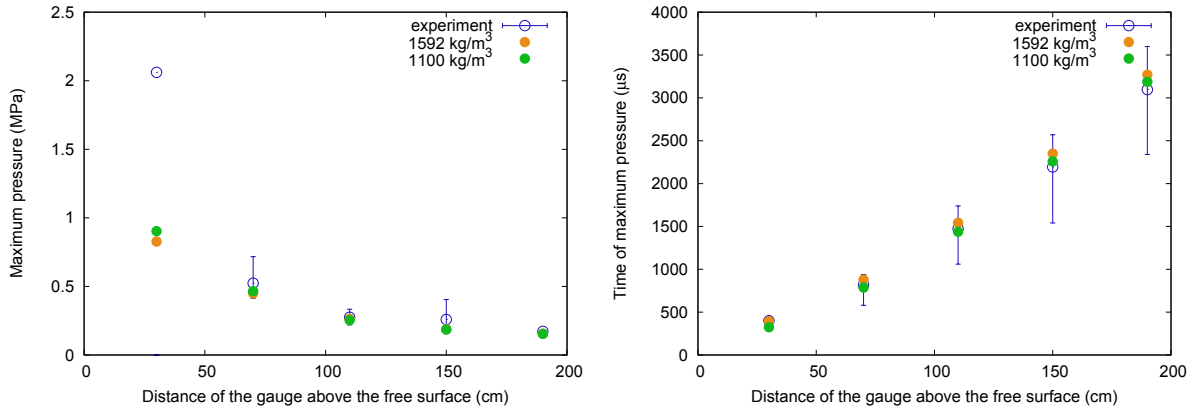

Figure 5.59: Maximum pressures (left) and their respective times (right) at the five outputs for a DOB of 3 cm in experiments, in simulations with initial densities $\rho_0 = 1592$ and 1100 kg.m^{-3}. Except for the first peak, we obtained the closest results to experiments with the smallest density.

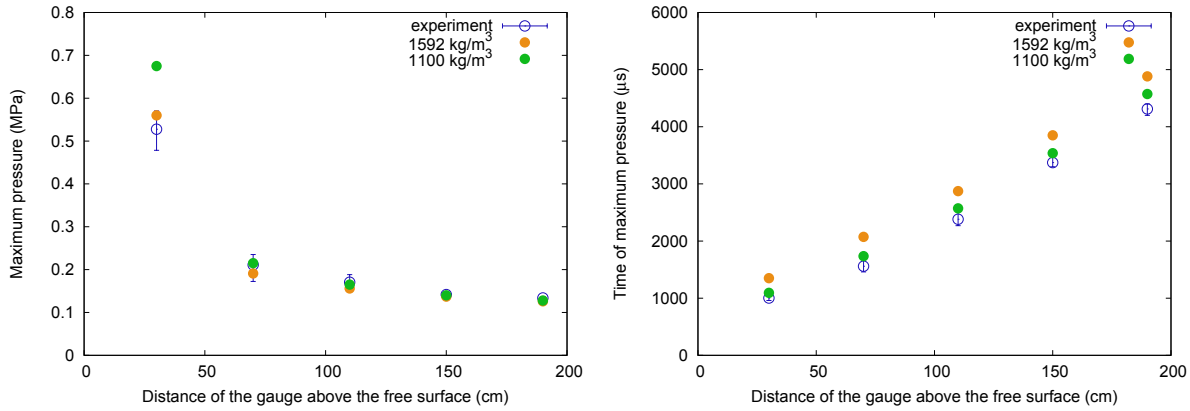

Figure 5.60: Same as figure 5.59 but for DOB of 8 cm. Except for the first peak, all the pressures provided close results compared to the experiments. Moreover with an initial density of 1100 kg.m^{-3}, all the time results were almost in the range of the experiments.

The results of the simulation for the depth of burial of 3 cm (figure 5.59) and 8 cm (figure 5.60) were compared to the experiments: the time shift which existed between the simulations and the experiments for a depth of burial of 8 cm is reduced: the difference between simulations and experiments become little. The density of 1100 kg.m^{-3} provides the closest results to experiments.

In fact, the density appears, as expected, to be a very important parameter in the soil model parameters.

For this simulation, the initial density was 1100 kg.m^{-3} over the whole soil tank, which does not correspond to the reality, since apart from the soil above the explosive, the rest of the soil tank has a larger density.

5.9.3.3 Soil layers with different densities

In order to take into account several densities in the soil tank, some simulations have been run, considering two soil layers with two different densities. The density of the first layer is equal to 1300 kg.m^{-3} whereas the density of the second layer which corresponds to the rest of the soil tank is equal to 1592 kg.m^{-3}. The various configurations tested are shown in figure 5.61. The thickness of the first layer is increased from one configuration to another one.

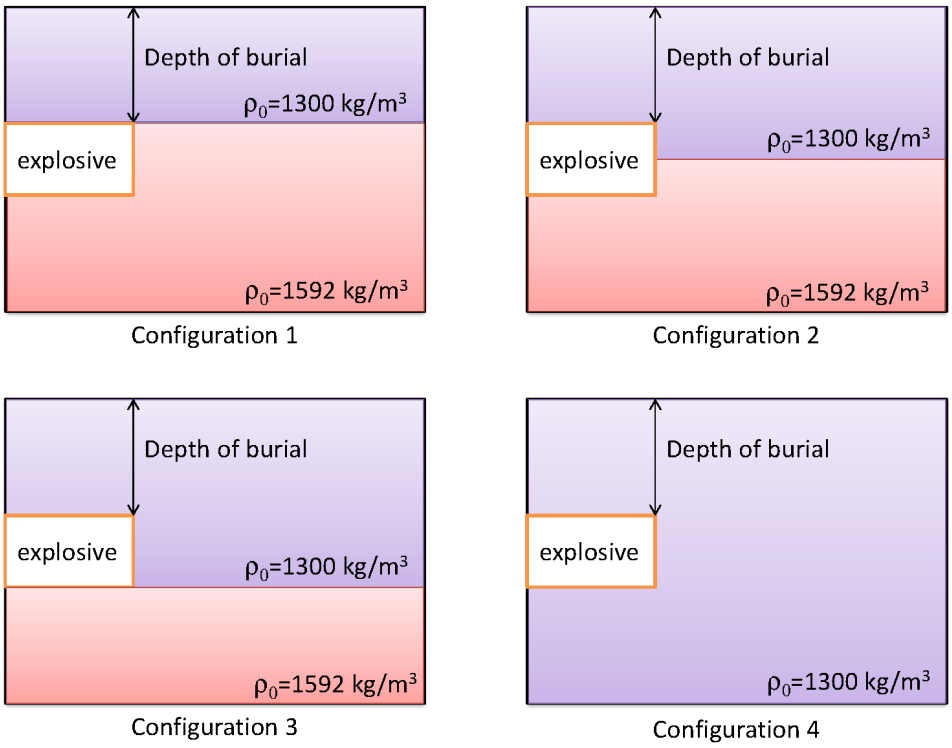

Figure 5.61: Since the density in the soil may not be homogeneous during experiments, some simulations have been run considering different densities inside the same soil tank with four different configurations.

In the first configuration, the thickness of the first layer corresponds to the depth of burial of the explosive. In the second configuration, it is equal to the depth of burial of the explosive plus half of the thickness of the explosive. In the third configuration, the thickness of the first layer corresponds to the depth of burial of the explosive plus the thickness of the explosive. Finally, in the fourth configuration, the entire soil tank has one density, equal to 1300 kg.m^{-3}.

For a **depth of burial of 3 cm**, the results of the four configurations are very close to experiments (for the maximum pressures and their respective times, figure 5.62), except for the first output where a difference in pressure can still be noticed between experiments and simulations.

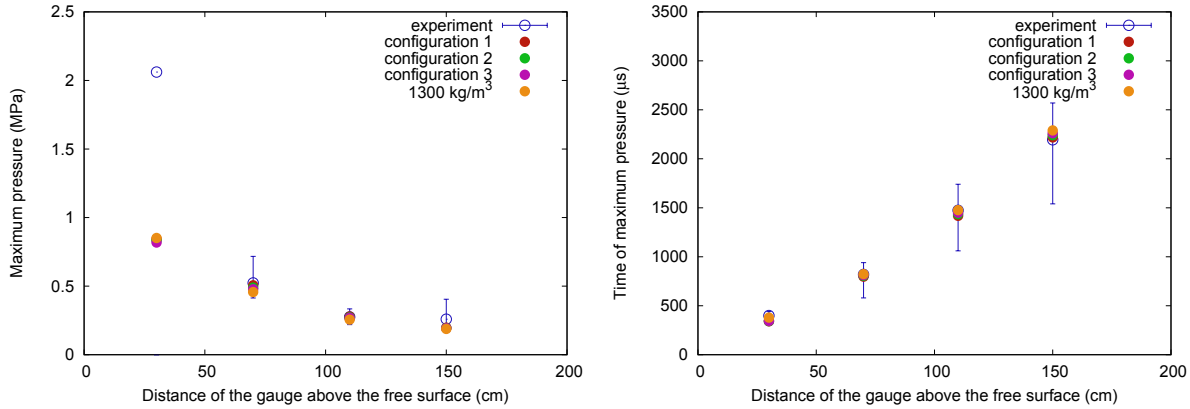

Figure 5.62: Maximum pressures (left) and their respective times (right) at the five outputs for a DOB of 3 cm in experiments, and in simulations with the four configurations sketched in figure 5.61. Except for the first peak, the simulation provided close results compared to the experiments.

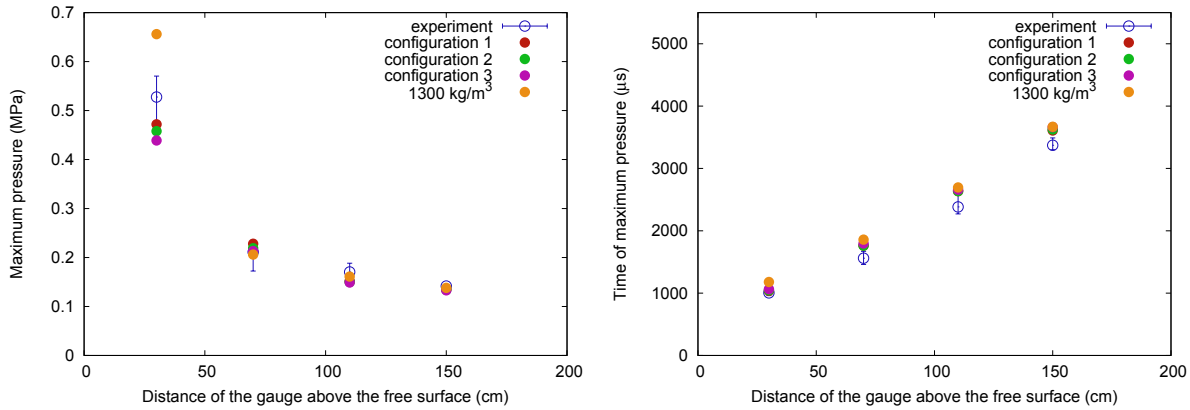

Figure 5.63: Same as figure 5.62 but for a DOB of 8 cm. For the times, considering two layers of soil with different densities provides better results than a smaller density for the whole tank. For the pressure results, the first configuration (corresponding to the thinnest thickness of the first layer) provides the closest results to experiments.

For a **depth of burial of 8 cm**, the time shift which existed between experiments and simulations has decreased while the maximum pressures from simulations are close to experiments (figure 5.63).

As the differences in pressure and time between the three first configurations are little, the first configuration (with the thinnest thickness of the first layer) nevertheless seems to provide the closest results to experiments.

5.9.3.4 Parametric analysis of the soil model

The influence of the parameters defining the yield surface is adressed in this section.

Influence of the α parameter

The α parameter plays a role in the expression of the failure surface

$$F_e(I_1) = \alpha - \gamma \exp(-\beta I_1) + \theta I_1 \tag{5.9.1}$$

and its value is linked to the ordinate to the origin of the yield surface. An increase of the value of α widens the deviatoric size of the yield surface (in fact, the exact value of the deviatoric size of the yield surface is equal to $\alpha - \gamma$). Not any value of α can be chosen. The inequality $0 < M \leq X - (\alpha - \gamma)R$ must be verified, in order that the value of M does not become negative.

To evaluate the impact of the size of the yield surface, the value of the α parameter was multiplied by 10, with a preconsolidation pressure X_0 10 times larger: the parameters $1 \times \alpha$ and $10X_0$ were compared to $10 \times \alpha$ and $10X_0$, with $\alpha = 0.06$ MPa and $X_0 = 1$ MPa.

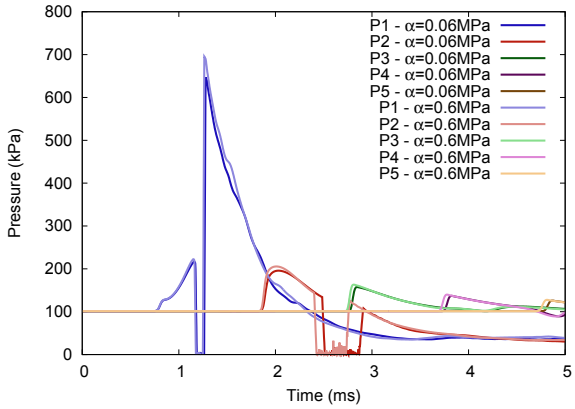

Figure 5.64: Comparison of the pressure profiles at the five outputs for a charge buried at 8 cm for two values of the initial shear stress α (60 and 600 kPa). When the yield surface widens, the pressure signals arrive a little earlier and the pressure peaks are a little increased.

For a DOB of 8 cm (figure 5.64), with a larger yield surface, the slope of the pressure curves is stiffer, the maximum pressure peaks are larger (up to 137 kPa larger for the first peak), and the time of arrival is slightly earlier (about 70 μs earlier). The yield surface is larger so the soil is more elastic. A larger part of the shock wave is transmitted in the

air provoking larger pressure peaks, and a more elastic behavior implies a faster sound speed which explains earlier pressure signals.

However, **for a DOB of 3 cm**, the pressures are very close for the two values of α. The depth of burial of 3 cm is probably too small to notice any significant difference.

Influence of the β parameter

The β parameter plays a role in the definition of the failure surface equation. For all the previous simulations, a value of 3.43×10^{-7} Pa^{-1} was taken for the β parameter. This value comes from Tong and Tuan (2007). Some simulations with $\beta = 0$ and $\beta = 5 \times 10^{-4}\,MPa^{-1}$ were run for a DOB of 3 cm and 8 cm. No significant difference could be noticed.

Influence of the γ parameter

The γ parameter plays a role in the definition of the failure surface equation. For all the simulations, a value of 5.89 kPa was taken for the γ parameter. Some simulations with $\gamma = 0$ were run for a DOB of 3 cm and 8 cm. No significant difference could be noticed. In fact, the two parameters β and γ are involved in the exponential in the failure surface equation. When I_1 increases, $\theta\, I_1$ becomes rapidly predominant in relation to the exponential term. That is why modifications of β and γ have negligible consequences on the pressure results.

Influence of the θ parameter

The θ parameter plays a role in the definition of the failure surface equation. For all the simulations, a value of 0.18257 was chosen for the θ parameter. This value comes from Tong and Tuan (2007). As underlined in equation 2.3.95, the θ parameter is linked to the friction angle of the soil ($\theta = (2/\sqrt{3}) \times \sin\phi/(3-\sin\phi)$). So $\theta = 0.18257$ corresponds to $\phi = 24.2°$.

Some simulations with $\theta = 0$ were run for the two depths of burial. The pressure profiles obtained with $\theta = 0$ have slightly smaller pressure peaks (about 7 kPa smaller). With the distance, the pressure waves are sligthly delayed (about 30 μs later). Figure 5.65 compares the simulation outputs with the experiments. The difference between $\theta = 0$ and $\theta = 0.18257$ tends to decreases with the distance. For the first pressure gauges, $\theta = 0$ provides closer results to experiments.

Influence of the R parameter

The parameter R is involved in the definition of the cap surface. It corresponds to the eccentricity of the cap. For all the simulations, a value of 5.0 was taken for R. To evaluate its influence, some simulations were run with a value equal to 1.5. With such a value, for both depths of burial (3 and 8 cm) (figure 5.66), the pressure arrived earlier (up to 170 μs for a DOB of 8 cm) and the pressure peaks were a little larger (up to 162 kPa for the first peak of a DOB of 8 cm). Moreover, and in particular for the second peak of pressure, in the case of a depth of burial of 8 cm, the slope was stiffer.

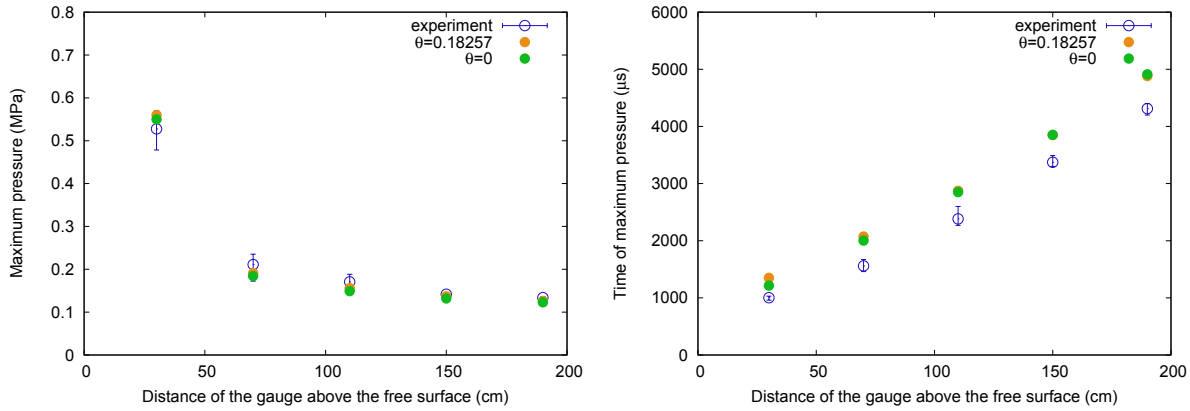

Figure 5.65: Maximum pressures (left) and their respective times (right) at the five outputs for a DOB of 8 cm in experiments, and in simulations with $\theta = 0$ and $\theta = 0.18257$. With $\theta = 0$, the first pressure peak and its first time of arrival are closer to the experiments. Far away, there is no longer differences between the two values of θ.

With a value of $R = 1.5$, the yield surface is larger which implies a larger sound speed and a more elastic soil transmitting a greater energy in the air: the pressure signals arrive earlier with larger pressure peaks.

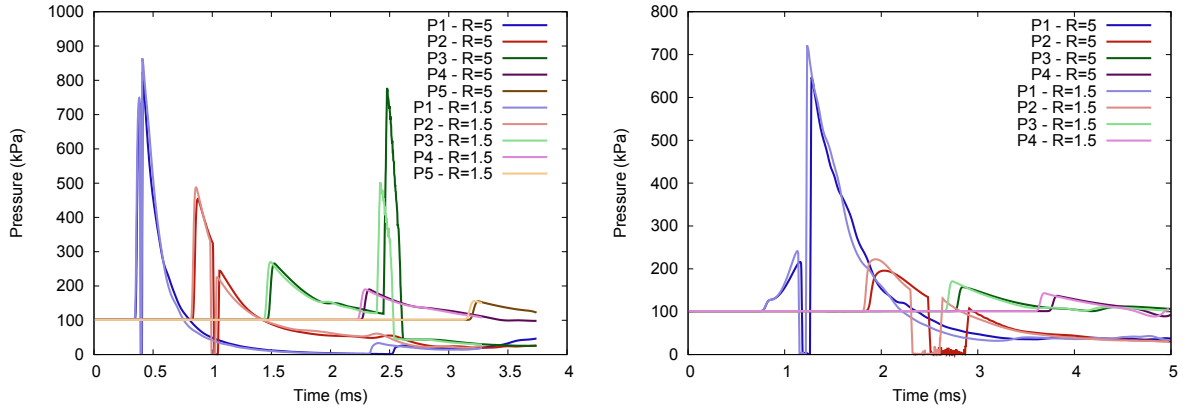

Figure 5.66: Comparison of the pressure profiles at the five outputs for charges buried at 3 cm (left) and at 8 cm (right) for $R = 1.5$ and $R = 5$. The two values of R provide very close pressure results. For a depth of burial of 8 cm, the differences are much more noticeable than for a depth of burial of 3 cm: the pressure peaks are slightly larger and arrive much earlier with $R = 1.5$.

The results of the simulations were compared to the experiments for a depth of burial of 3 cm and a depth of burial of 8 cm. A value of 1.5 provides closer results to experiments, except for the first pressure gauge.

Influence of the T parameter

The tensile cut off parameter sets the extreme position along the I_1 parameter of the cut off surface. For all the simulations, a value of 6.9 kPa was tested. In order to study its influence, a value of 69 kPa was used (figure 5.67). With such a value, the pressure waves arrived later and the pressure peaks were smaller (up to 40 μs late and 27 kPa smaller). This difference was more noticeable with a DOB of 8 cm (up to 118 μs late and 19 kPa smaller). This is a little strange because the soil is more elastic.

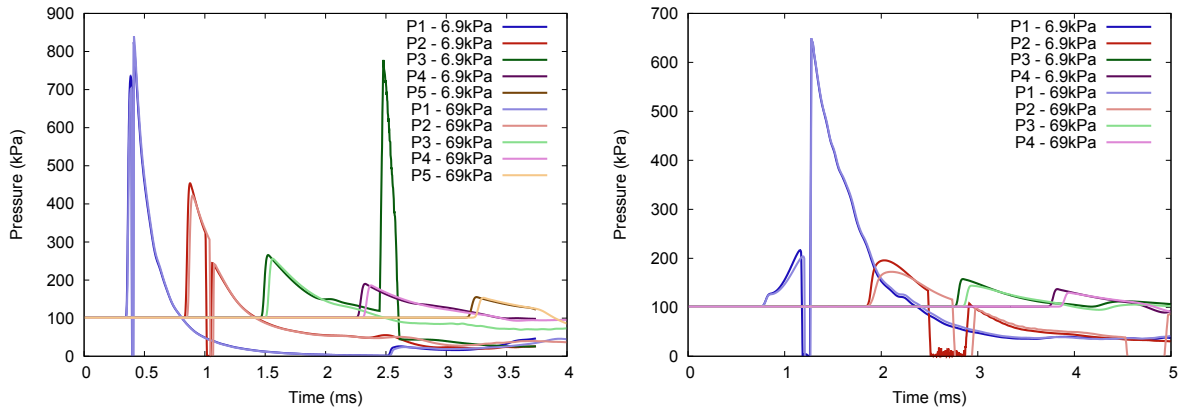

Figure 5.67: Comparison of the pressure profiles at the five outputs for charges buried at 3 cm (left) and at 8 cm (right) for T = 6.9kPa and 69kPa. With T=69 kPa, the pressure waves are delayed and the pressure peaks are smaller, which is strange since the soil is more elastic.

5.9.3.5 Parameters of the hardening law

In this part, the influence of the parameters defining the hardening law is studied.

Influence of the preconsolidation pressure X_0

X_0 corresponds to the preconsolidation pressure of the soil, and the extremity of the cap surface. This parameter is also used in the definition of the hardening expression.

To evaluate the influence of the cap, a very large value X_0 = 1000 GPa was used, so that plasticity due to the cap does not take place but may still be induced by the failure and cut off surfaces.

For the two depths of burial, the pressure waves are much earlier (up to 350 μs earlier for a DOB of 3 cm, and up to 600 μs earlier for a DOB of 8 cm) and much larger (up to 400 kPa larger) (figure 5.68). The slope is also much stiffer. The difference of the peak value decreases with distance. On the contrary, the time shift increases with distance.

This is the second most important parameter. Thanks to a wider yield surface, the stresses are elastic during a longer time. The wave speed is therefore larger which implies the pressure signals to propagate faster. The results of the simulation were compared to experiments in figures 5.69 and 5.70 for an explosive buried at 3 and 8 cm respectively.

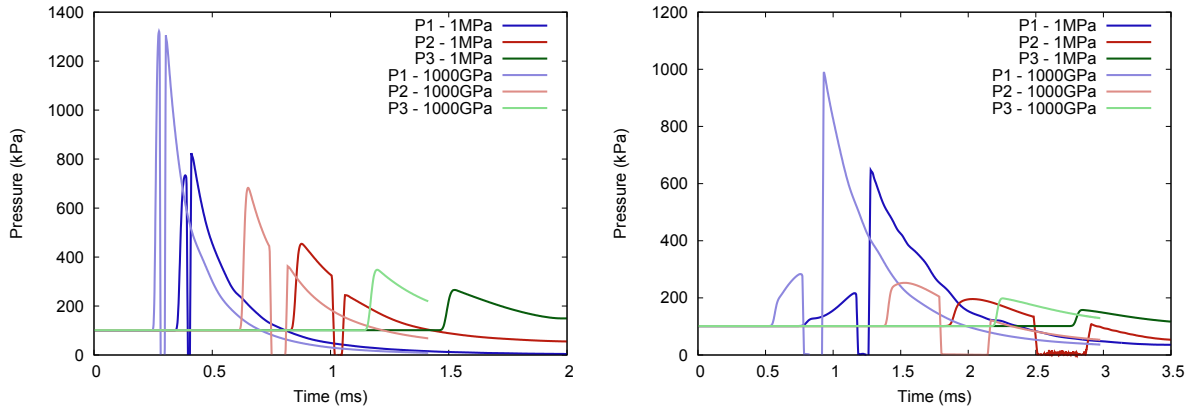

Figure 5.68: Comparison of the pressure profiles at the five outputs for charges buried at 3 cm (left) and 8 cm (right) for $X_0 = 1$ MPa and 1 000 GPa. With a larger cap (so a wider yield surface), the pressure waves arrive much earlier and the pressure peaks are much larger.

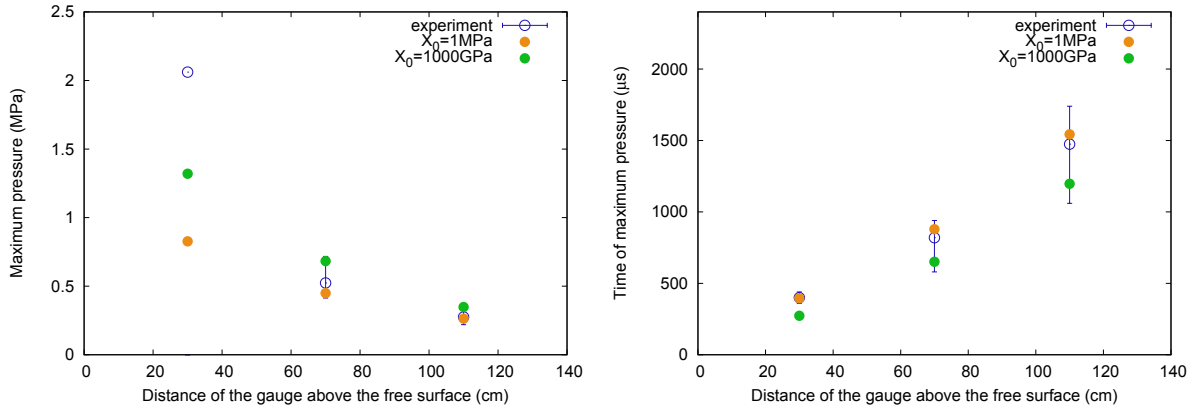

Figure 5.69: Maximum pressures (left) and their respective times (right) for a DOB of 3 cm in experiments, in simulations with $X_0 = 1$ MPa and 1000 GPa. Compared to the experiments, the maximum pressures are too large, except for the first peak which is closer. The times of the maximum pressures are a little too short.

For DOB of 3 cm and 8 cm, the maximum pressures obtained are too large. But as for the time for this maximum pressure, for a DOB of 8 cm, the results of simulations fit with the experiments. At variance, for a DOB of 3 cm, the times of the maximum pressure are a little small.

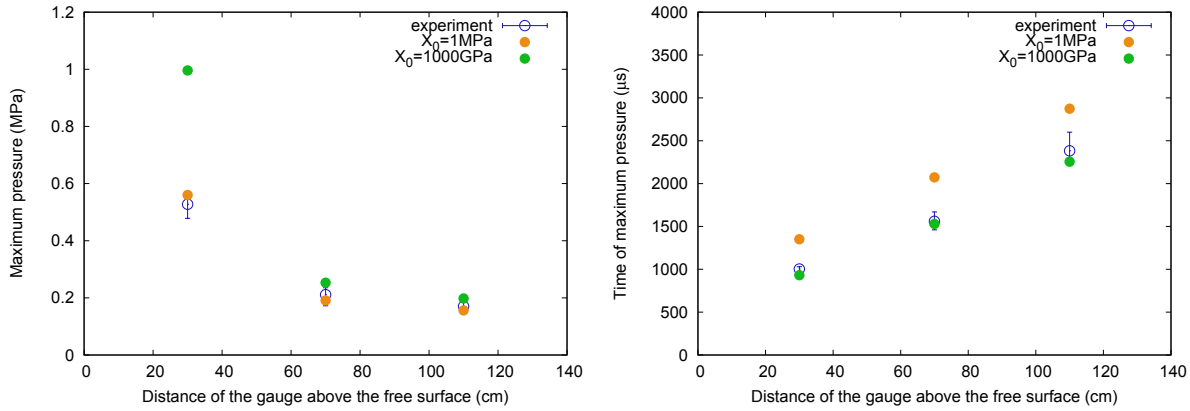

Figure 5.70: Same as figure 5.69 but for a DOB of 8 cm. Like for the depth of burial of 3 cm, the maximum pressures are too large compared to the experiments. As for the times of arrival, an increase of X_0 seems appropriate since the time of the maximum pressure has decreased a lot. The time shift between experiments and simulations does not exist anymore.

Influence of the parameter W

W is a parameter which plays a role in the hardening of the cap. Moreover, the viscoplastic strains tend toward the value of this parameter. For all the simulations, a value of 0.5 was taken. Here two values were tested: 0.2142 (which was the value Tong and Tuan (2007) used) and 0.9. For the value of 0.2142, the differences are very small for a DOB of 3 cm. They are more noticeable for a DOB of 8 cm: the pressure waves arrive later and the pressure peaks are larger. But even it is more noticeable for the DOB of 8 cm, the difference is rather small.

As for the value of 0.9, the curves are very close for the two depths of burial.

5.9.3.6 Conclusions of the parametric study

- The influence of parameters is much more noticeable for a depth of burial of 8 cm than for a 3 cm one. Perhaps, the thickness (3 cm) of the soil above the explosive is not large enough to play a significative role.
- It is important to consider the polystyrene in the simulations, since this matter is easier to move than the soil. The explosive spends less energy to deform the polystyrene and to expand. The resulting pressures are therefore larger.
- To reproduce the experiments, a small value of density must be chosen for the soil above the explosive since this soil is not tamped. Moreover, density is one of the most important parameters.
- The initial cap position X_0 is the second most important parameter. When it is increased, the yield surface is larger. The waves are thus elastic during a longer time. So the pressure waves propagate faster. The pressure peaks are also more important.

Chapter 6

Test rig impulse and deformation of simulating bellies induced by detonation of buried explosives - experiments and simulations

Contents

This chapter is centered around the field measurement and numerical simulations of impulse and deformation of metallic plates due to the detonation of several kilograms of buried explosives.

Before our own impulse and deformation tests, we performed experiments of aerial detonation of TNT that we reproduced in simulation. The aim was to cross-check the JWL parameters of TNT taken from literature regarding our own TNT explosive. The experiments consisted in the aerial detonation of 6 kg of TNT and the pressure was measured at 1, 2, 4 and 8 meters along two orthogonal axes.

Once the JWL parameters were cross-checked, preliminary simulations were run to study the deformation of plates due to the detonation of buried charges. The initial density of the soil, the initial position of the cap, the depth of burial of the explosive and the dimensions of the soil tank were studied.

Finally, our large scale experiments of test rig impulse and of plate deformation were overviewed. Test configurations consisting in various depths of burial, explosive masses, degrees of saturation of the soil, plate thicknesses and stand off distances were shot.

Simulations were run to study the influence of the viscoplastic model parameters on the impulse. The parameters defining the size of the yield surface, in particular the initial cap position and the initial shear stress were found to have the largest influence on impulse.

6.1 Review of large scale experiments to measure impulse and plate deformations due to buried explosion

The effects of an explosion close to a vehicle are of two types:

- local: only a part of the vehicle is deformed;
- and global: the entire vehicle is moved because of the energy tramsitted by the explosion.

The energy transmitted by the detonation to the vehicle is called the impulse.

To measure the effects of buried detonations on vehicles, test rigs are usually designed instead of carrying out experiments on real vehicles which are very expensive. Test rigs consist of a plate representing the vehicle belly. The height is varied to study the effects of the stand off distance.

Some test rigs have been dedicated to measure impulse only (Hlady (2004), Fiserova (2006), Skaggs et al. (2004), Anderson et al. (2011)). The plate is thick enough not to be deformed by the explosion but can freely move.

Hlady (2004) conducted experiments to examine the kinetic energy transferred by 1 kg of C4 to a piston test apparatus (figure 6.1). The impulse was studied for two soils (sand and prairie soils), several water contents and depths of burial. The US Army Research Laboratory developed a similar device called the Vertical Impulse Measurement Fixture (VIMF) (Skaggs et al. (2004)) to measure the vertical impulse for buried charges weighing up to 8 kg, whereas Anderson et al. (2011) determined the impulse transferred

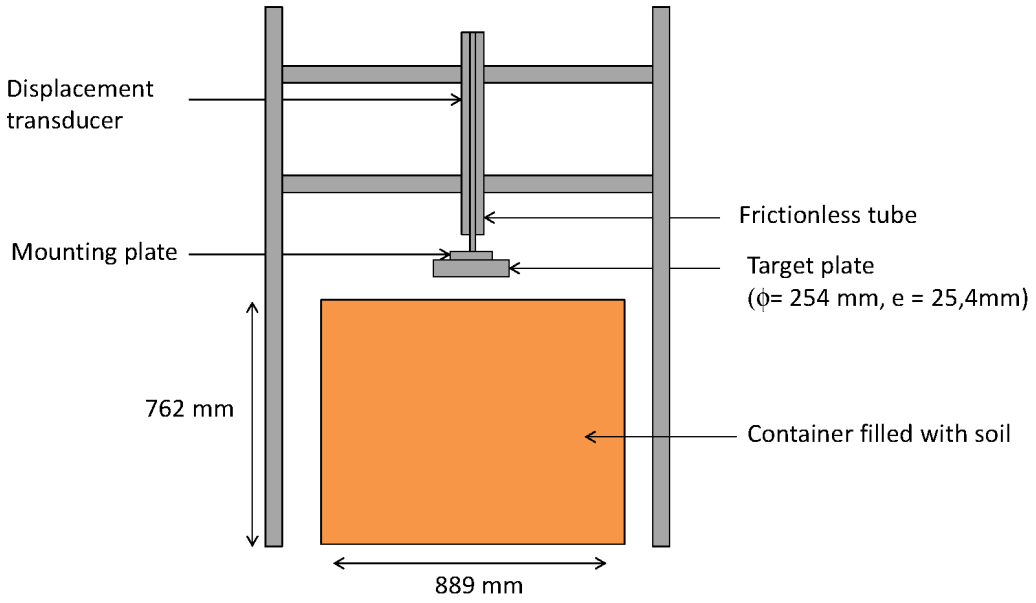

Figure 6.1: Experimental setup of Hlady (2004) consisting of a rigid plate mounted at the bottom of a piston that can freely move vertically. The vertical displacement of the plate leads to the impulse.

to either flat or V-shaped steel plates. In all these cases, the impulse was calculated from the measure of the displacement of the rigid plate. Hlady (2004) and Skaggs et al. (2004) used a linear voltage displacement transducer (LVDT) to measure the height reached by the plate during the trial. Anderson et al. (2011) measured the plate displacement using two cable-pull potentiometers. These were attached between the center of the plate and the ceiling so that the cables were extracted before the experiment started and retracted while the steel plate moves upward.

The impulse can also be obtained from the rotation of an arm. That was performed at DRDC Suffield with the Mine Impulse Pendulum (MIP) to study the effects of soil type, soil water content, depth of burial and explosive type (Bergeron and Tremblay (2000), Bues et al. (2001), Fiserova (2006)). The MIP is a horizontal ballistic pendulum rotating around a fixed axis which measures the impulse of a landmine explosion (figure 6.2). The impulse is obtained from the maximum angle of the arm.

Impulse plugs can also be used to obtain the impulse: they are masses added on the plate and the impulse is deduced from the displacement of the plugs. They were used by Fourney et al. (2010) to determine the spatial repartition of the impulse.

In an alternative approach, Zakrisson et al. (2012) designed a test rig to measure at the same time both impulse and deformation due to buried mine explosions in sand. In these experiments, the transferred impulse was determined thanks to the maximum displacement of the test module in the upward direction. Two independent methods were used: a linear resistive position sensor to register the upward displacement of the test module as a function of time, and a small block of aluminium honeycomb which was mounted above the plate so that the highest displacement of the plate was recorded from the crushing of the honeycomb.

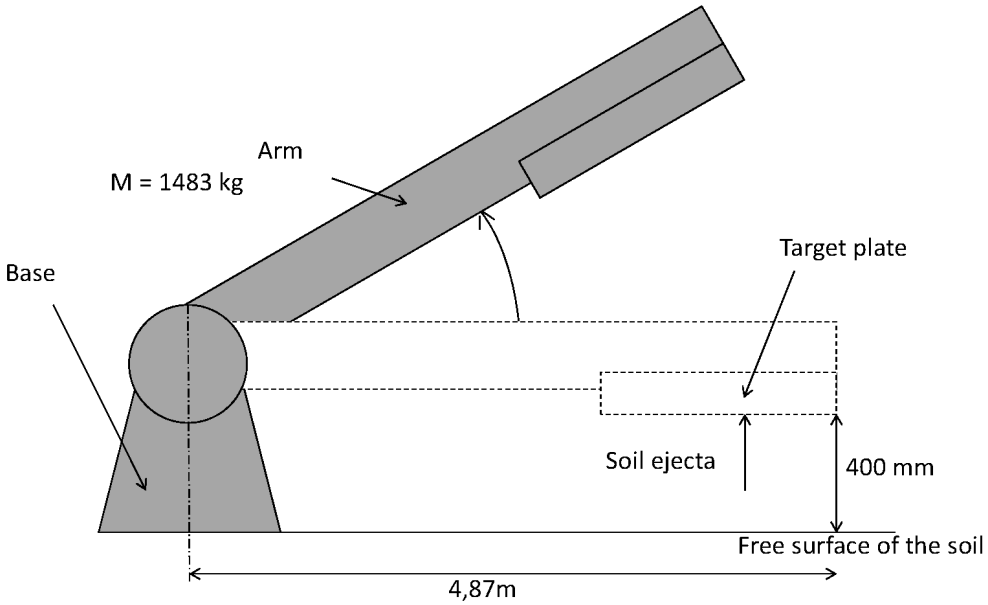

Figure 6.2: Experimental set up called Mine Impulse Pendulum experimental used by Fiserova (2006). It is composed of a rotating arm, a base and a target plate. The maximum angle of the arm provides the impulse.

6.1.1 Calculation of the impulse

The impulse I is defined as $I = mv$. For a rectilinear movement, it can be calculated from the maximum displacement of the device or from its initial velocity. It implies that the displacement takes place in the vertical direction only and the initial velocity is the largest.

The total energy is the sum of kinetic and potential energies:

$$E = E_{kinetic} + E_{potential} \tag{6.1.1}$$

At the time of the explosion:

$$E = \frac{1}{2} m\, v^2 + 0 \tag{6.1.2}$$

where m is the mass of the device and v is its velocity.

At the maximum displacement z_{max}, $v = 0$:

$$E = 0 + m\, g\, z_{max} \tag{6.1.3}$$

where g is the gravity constant and z_{max} the maximum vertical displacement of the plate.

If we neglect dissipative effects and assume the conservation of the total energy:

$$\frac{1}{2} m\, v^2 = m\, g\, z_{max} \tag{6.1.4}$$

The momentum $I = m\, v$ and the corresponding velocity v are obtained:

$$I = m\sqrt{2\, g\, z_{max}} \quad \text{and} \quad v = \sqrt{2\, g\, z_{max}} \tag{6.1.5}$$

6.1.2 Parameters influencing the impulse and the plate deformation

Let us consider a buried explosive, and let us focus on the parameters which influence the impulse and the deformation of structures standing above the location of the buried detonation.

The first and the most important parameter is the **water content** of soil. It is well known that water in soil has an important influence on the impulse.

Hlady (2004) performed buried experiments in a prairie soil (which is a fine grained soil) and in a sand. She found that detonations in wet prairie soil transferred five times more kinetic energy than in dry sand. Increasing the soil density and the water content of a soil could produce up to seven times more energy than under dry sand conditions. In the experiments of Zakrisson et al. (2012) where both impulse and deformations are measured, the water content influence both results, more the impulse than the deformation.

In fact, the parameter to consider is not the water content but the **degree of saturation**. Assaf et al. (2014) showed that increasing the water content has few effects on the impulse as its value is not large enough. When the degree of saturation is close to 1 (so when the soil is so impregnated by water that it looks like quicksand) the difference is really significative on the impulse. Besides a shot in water provides the largest value of impulse and deformation (Fourney et al. (2010)).

In relation to the nature of soil in which the explosive is buried, the **ejecta** contribute to the impulse since they increase the kinetic energy. It is particularly the case when a fine grained soil is used (Hlady (2004)). Besides, Peles et al. (2008) showed that a detonation in a fine-grained soil provokes more damage than in sand. Fourney et al. (2010) even considered that the impulse is primarily due to the ejecta. In the experiments of Hlady (2004), an increase of stand off distance (distance between the plate and the soil) has little effect on the impulse when the detonation occurs in a fine grained soil: the velocity of the projections has not decreased enough. However for the same experiments in sand, a 50% larger stand off distance decreased the impulse by 60%. Sand projections provide much less energy than ejecta from fine grained soils.

The **depth of burial** has also an influence on the impulse and deformation. As the depth of burial increases, even if the resulting blast wave hitting the plate is less important, the kinetic energy and thus the impulse increase with a larger mass of projections (Hlady (2004), Zakrisson et al. (2012)). However, an optimum depth of burial exists where the impulse is the largest. Beyond this value, increasing the depth of burial results in a decrease of the impulse. This optimum value is directly linked to the quantity of explosive. As for the deformation, Zakrisson et al. (2012) showed that a buried explosive provoked a larger deformation than a flush explosive. Moreover the deformation decreases as the depth of burial increases, because it is mostly associated with the shock wave and less with the impact of projections.

6.2 Aerial detonations of 6kg of TNT

The objective here is to get pressures of aerial detonations in order to cross check the TNT parameters of the explosive used in simulations.

At variance with the experiments presented in chapter 5, in this chapter, the explosive of all the experiments is TNT. For the small scale experiments, C4 explosive was used, because such a small quantity of explosive in TNT was not available at DGA TT. C4 is easy to model, so any volume and mass could be produced. In this chapter TNT is used because it is a reference explosive.

6.2.1 Overview of the experiments

Figure 6.3 shows an overview of the experiment setting. An explosive of 6 kg was placed on a 30 mm thick armor steel plate which was at the same level as the soil, to avoid simulating soil. To maintain the detonator in place, a 3.5 cm foam was inserted between the explosive and the steel plate. The explosive was inside its plastic case and was initiated on its bottom center with a 50-g Hexomax booster. The booster is an explosive which links the primary explosive of the detonator to the explosive charge, when the latter could not be initiated directly by the detonator. The booster is more sensitive than the charge and can relay the detonation from the detonator to the explosive.

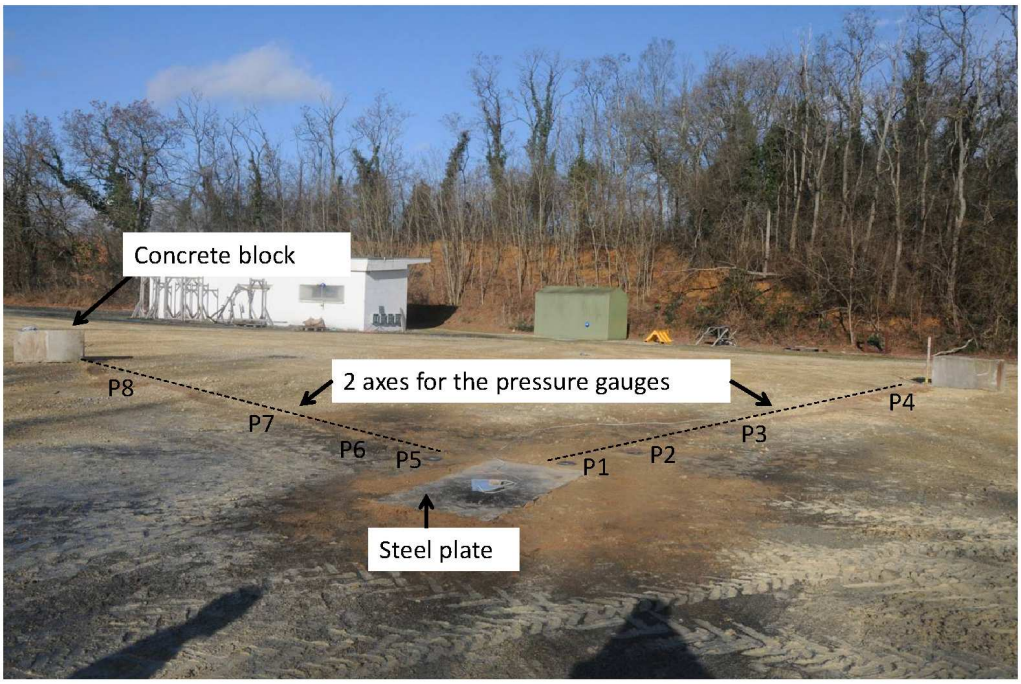

Figure 6.3: Setting of the aerial detonation experiments. Pressure gauges were located along 2 orthogonal axes, at 1, 2, 4 and 8 m from the center of the explosive. Concrete blocks were placed at the end of the two axes to protect wires.

Two sets of pressure gauges were used in two orthogonal axes. They were located at 1 m, 2 m, 4 m and 8 m from the center of the charge. They were at the level of the soil.

Some concrete blocks were located just after the farthest pressure gauges to protect wires. Two aluminium sheets were laid on the explosive charge to synchronise the time of detonation with the measures of the gauges. See section 5.5 for more information about these aluminium sheets.

Two shots were carried out. For the first one, whereas the two closest gauges to the explosive reached saturation, all the other pressure signals provided expected results. For the second shot, the two closest gauges were changed so that they could measure larger pressures. After the shot, one of the two closest gauges was completely buried, whereas the second one was still visible and had very little sand on it. The visible gauge provided a pressure peak of 12 MPa and the buried gauge provided a pressure of 6 MPa. A part of the signal could be linked to the fire ball.

The outputs of the pressure gauges are gathered in the tables 6.1 and 6.2.

Gauge	Distance from the explosive center	Maximum pressure	Time of arrival of the shock wave	Speed of the shock wave at the gauge
P1	0.94 m	4.96 MPa	247 μs	3818 m/s
P2	1.91 m	1.70 MPa	814 μs	1707 m/s
P3	4.01 m	0.345 MPa	3 060 μs	932 m/s
P4	8.00 m	0.066 MPa	11 560 μs	470 m/s
P5	0.93 m	4.97 MPa	248 μs	3805 m/s
P6	1.96 m	1.92 MPa	814 μs	1810 m/s
P7	4.05 m	0.328 MPa	3 340 μs	860 m/s
P8	8.00 m	0.081 MPa	11 545 μs	475 m/s

Table 6.1: Overpressures measured by the pressure gauges and their respective times for the first shot. The gauges P1 to P4 correspond to the first axis, whereas the gauges P5 to P8 correspond to the second axis.

Gauge	Distance from the explosive center	Maximum pressure	Time of arrival of the shock wave	Speed of the shock wave at the gauge
P1	0.93 m	12.26 MPa	247 μs	3768 m/s
P2	1.90 m	2.07 MPa	717 μs	2022 m/s
P3	3.99 m	0.409 MPa	3 030 μs	905 m/s
P4	7.99 m	0.060 MPa	11 370 μs	479 m/s
P5	0.96 m	5.93 MPa	261 μs	3586 m/s
P6	1.99 m	2.21 MPa	777 μs	1941 m/s
P7	4.07 m	0.271 MPa	3 300 μs	830 m/s
P8	8.02 m	0.062 MPa	11 600 μs	475 m/s

Table 6.2: Same as table 6.1 but for the second shot.

6.2.2 Computer simulations of the aerial detonations

The simulations run here reproduce the experiments of aerial detonations. The experimental pressures are compared to the simulations of the first shot at 1 and 2 meters, since the similar gauges of the second shot were not reliable. The numerical parameters for TNT are taken from Dobratz and Crawford (1985) (table 4.7, page 97). The mesh size was 2.2 meters wide and 1 meter high, with an element size of 0.5 mm. Axisymmetric simulations were run. A condition of zero displacement was imposed on the bottom side of the mesh to represent the steel armor plate. Atmospheric pressure was applied to the border of the mesh and transmitting boundaries were considered (figure 6.4). The explosive was initiated at its center on its bottom face. In the simulations, the pressures were displayed at 3.5 cm from the border of the mesh (corresponding to the thickness of the foam) and at 1 and 2 m from the center of the explosive.

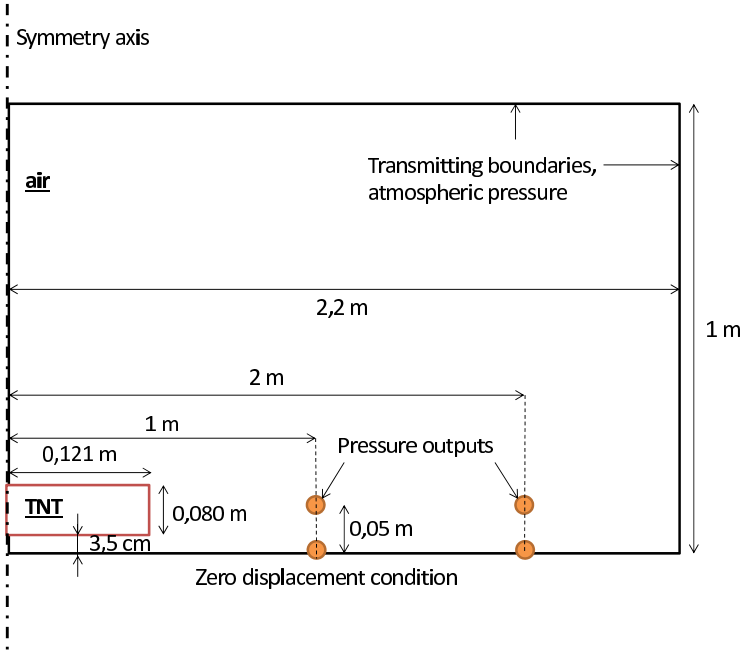

Figure 6.4: Sketch of the simulations of the aerial detonation of 6 kg of TNT. The pressure is displayed at 1 and 2 m from the bottom center of the explosive, which is located at 3.5 cm from the border of the mesh (because of the presence of foam that maintains the detonator upright). The sketch is not to scale.

Figure 6.5 shows the results of simulations compared to the experiments for the two axes of the first aerial shot. For the two axes, the first simulation curve is close to the experiments even if the experimental gauge clipped the maximum pressure. As for the results at 2 m, a slight time shift (30 μs) and slight decrease of the maximum pressure can be observed between the pressure curves in simulation and in experiment.

The JWL parameters of TNT shown in table 4.7 are considered to provide acceptable results. They are adopted for the next simulations of buried TNT explosive reproducing the large scale experiments.

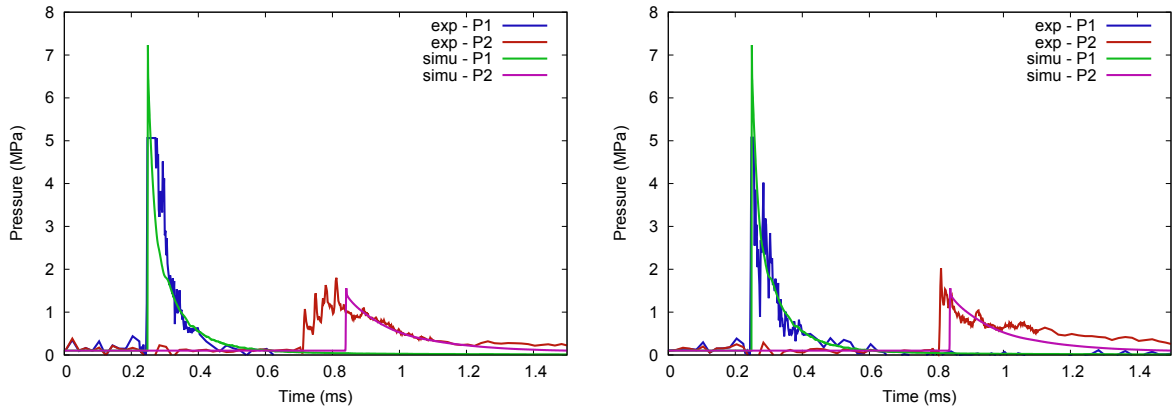

Figure 6.5: Comparison between experiments (noted exp in the figure) and simulations (noted simu in the figure) of the time course of pressure at 1 and 2 m from the center of the explosive. The experiment results correspond to the first (left) and second (right) axes of the first shot. The experimental curve at 1 m along both axes was clipped. Otherwise, the experimental and numerical curves rather fit for the first gauge. For the gauge at 2 m, a time shift exists whereas the intensity of the pressure in simulation is similat to experiments.

6.3 First simulations of the effects on plates of buried explosives

Before considering the large scale experiments and their respective simulations, preliminary simulations modeling the effects of a large quantity of buried explosives are run. First aerial pressures and soil stresses are output at various places to study the shock wave propagation. Then a metallic plate is placed above the free surface of the soil, to quantify the effects of buried explosives on the plate deformation.

6.3.1 Influence of the explosive mass on soil and aerial pressures

Let us focus on the effects of the detonation of several kilograms of buried TNT in the soil and in the air.

The simulations are axisymmetric. Three masses of explosive are tested: 6 kg, 8 kg and 10 kg of TNT, all initiated at the center on their bottom face. Their dimensions are recorded in table 6.4, considering a ratio of one third between the height and the diameter of the explosive. They are all buried at 100 mm below the free surface of the soil which is simulated with our viscoplastic model with parameters given in table 2.1.

In particular, the pressures are displayed at several distances in the soil (at 400, 600 and 800 mm horizontally from the lateral extremity of the explosive), and in the air, at 40, 50 and 60 cm above the free surface. In the air, the distances are chosen since they correspond to the stand off distances of the plates which are later simulated. In the soil, the distances are selected far enough from the explosive so that its expansion does not reach the points of outputs.

The various points of displays in the soil and in the air are shown in figure 6.6.

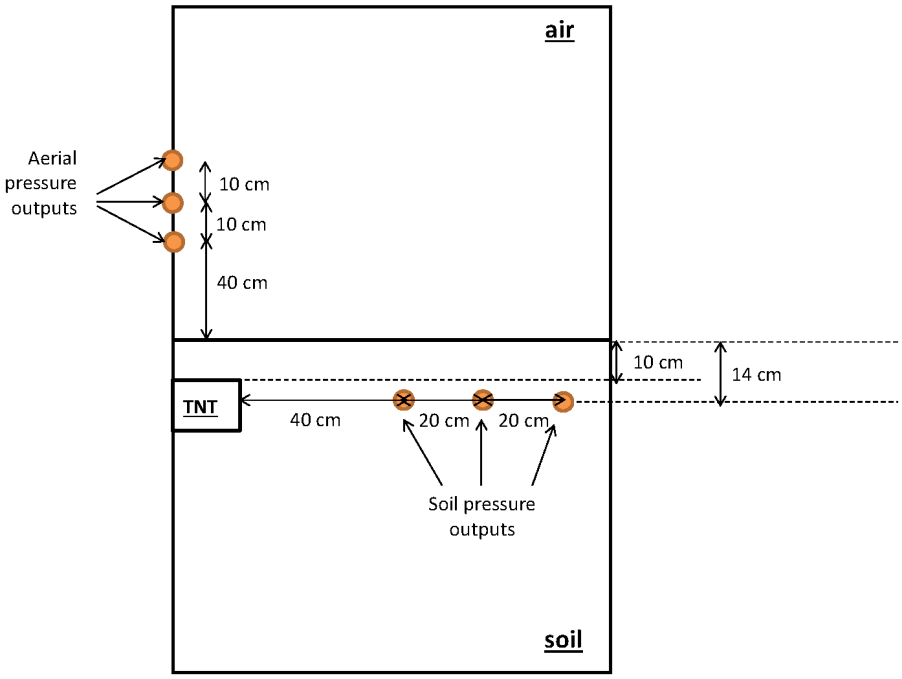

Figure 6.6: Extent of the mesh to simulate the effects of the detonation of several kilograms of TNT on aerial and soil pressures. The outputs are displayed at three fixed horizontally aligned points in the soil and three fixed vertically aligned points in air.

A heavier explosive releases a larger quantity of energy. Since the depth of burial of the three masses of explosive was the same, the aerial pressure is all the more important as the mass of explosive is large.

Moreover, with a large quantity of explosive, the attenuation of the detonation velocity is slower. This is confirmed by the curves: the pressure waves arrive sooner for a larger quantity of explosive.

As in the case of small scale experiments, two peaks can be noticed on each aerial pressure curve. The first one corresponds to the shock wave propagating ahead of the soil bubble. The little small value following the first peak is due to the soil crossing the fixed point of output. The second peak corresponds to the detonation products. The output displays equally the pressure whatever the matter (air or soil) it is related to.

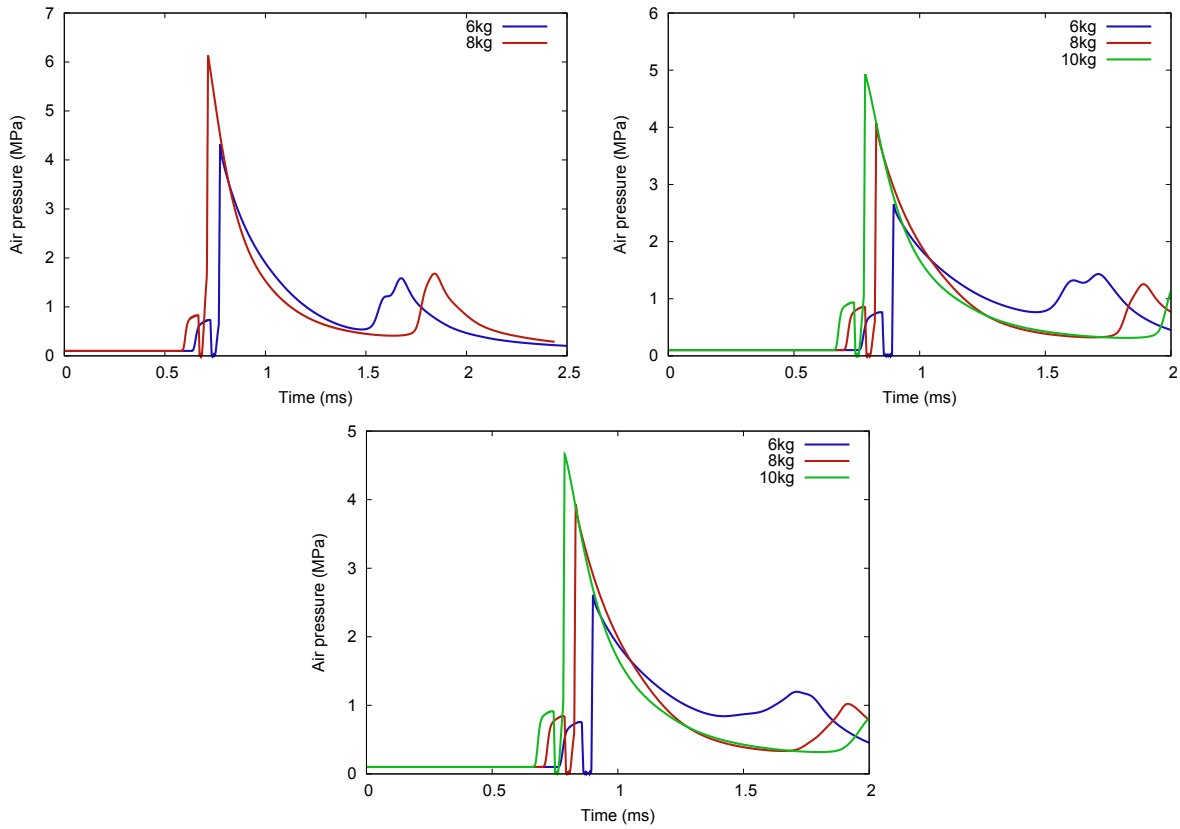

Figure 6.7: Time course of the aerial pressures for various masses of TNT at 400 mm (top left), 500 mm (top right) and 600 mm (bottom) to the free surface. The larger the mass, the sooner the shock wave arrives. The intensity and the duration of the peak increase with the mass of the explosive.

In the soil, the pressure which is equal to the opposite of the mean stress, was output. Close to the detonation point, the pressure rate is large with close values for the three masses of explosive. At variance, far away, the pressure rate decreases. The element size is uniform in all the mesh. This attenuation is thus not due to a larger element size but to the distance: the velocity of the detonation wave progressively decreases as the distance from the detonation point increases. Meanwhile the thickness of the shock wave increases. That is why the pressure rate progressively decreases. At these three points of display, the ratio of pressures between two masses remains the same.

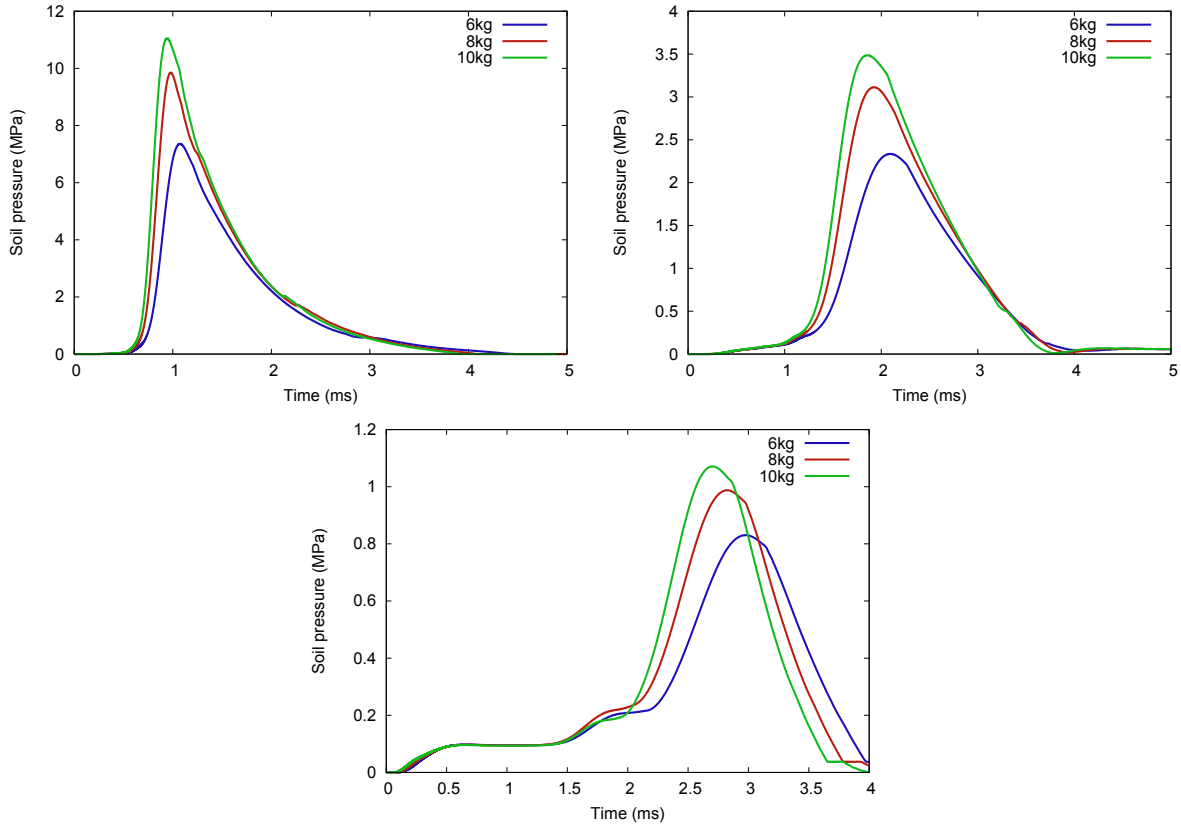

Figure 6.8: Time course of the soil pressures for various masses of TNT at 400 mm (top left), 500 mm (top right) and 600 mm (bottom) from the point of detonation. The pressure peak is almost proportional to the explosive mass at short distance from the charge. The effect of the mass progressively wipes out at larger distances.

6.3.2 Study of plate deformation

Axisymmetric simulations of buried explosives are now run to study the deformation of a plate located above the free surface of the soil. The sketch of figure 6.9 presents a general view of the mesh extent and geometrical aspects of the simulations.

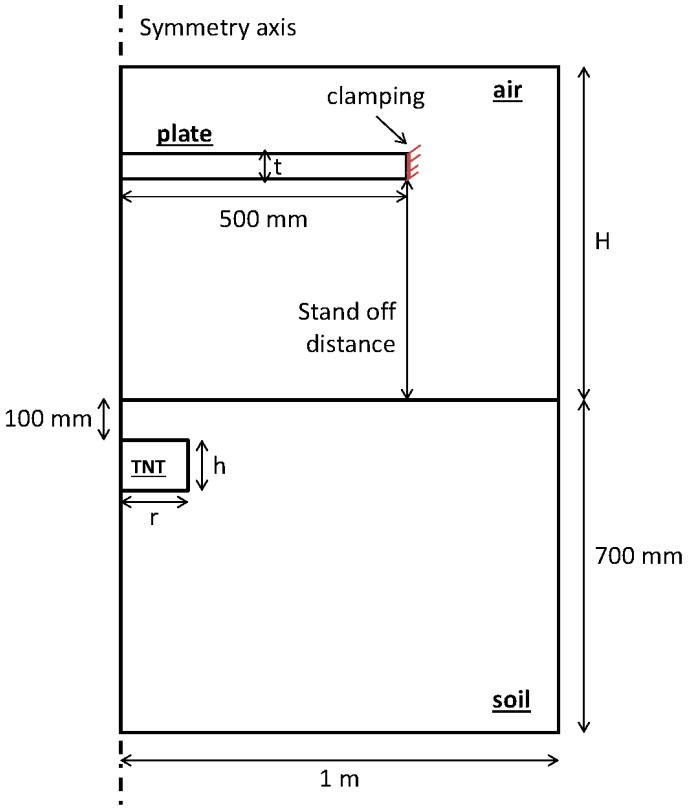

Figure 6.9: Extent of the mesh for the simulations of large quantity of buried TNT (6, 8, and 10 kg) to study its effect on a plate. The explosive has a radius r and a height h. The plate has a thickness t, a radius of 500 mm, and is located at a distance called stand off distance from the free surface of the soil. The extremity of the plate is clamped, allowing no displacement nor rotation. The heigth H of the mesh is chosen according to the stand off distance.

The plate which is simulated is made in RHA (which stands for Rolled Homogeneous Armour, an armour steel). The nodes at the end of the plate are blocked in translation and in rotation as if the plate was clamped. Its radius is equal to 500 mm, and three thicknesses (t) are considered: 30, 40 and 50 mm. The height above the soil at which the plate stands is called the stand off distance. Three stand off distances are tested: 400, 500 and 600 mm.

The plate is modeled with the Johnson Cook law which is detailed in section 4.2.2. The parameters are in table 4.5 (page 96). In LS Dyna, the Johnson Cook law requires to be associated with an equation of state, like the Mie Grüneisen equation of state. The parameters relative to this equation of state are given in table 4.6.

The Lagrangian formulation is used to model the plate, while the air, the explosive and the soil are Eulerian. An interaction is required between the elements of the plate

and the elements of the Eulerian part. This coupling is defined with a penalty method.

The height H of air above the soil depends on the stand off distance. The values of H are in table 6.3.

Stand off distance	H
400 mm	600 mm
500 mm	700 mm
600 mm	800 mm

Table 6.3: Values of H (height of the air mesh) depending on the stand off distance.

Explosives of 6, 8 and 10 kg of TNT with dimensions given in table 6.4 are simulated with JWL parameters provided in table 4.7. The explosives are buried at 100 mm in a soil modeled with our elasto-visco-plastic model with parameters given in table 2.1.

mass	radius (r)	height (h)
6 kg	121 mm	80,0 mm
8 kg	133 mm	88,6 mm
10 kg	143 mm	95,4 mm

Table 6.4: Dimensions of the explosives considering a ratio of one third between the height and the diameter of the explosive.

Next the two most important parameters highlighted in chapter 5 which are the initial density and the preconsolidation pressure X_0 are changed to study their effects on the displacement of the plate. Various depths of burial of the explosive have also been tested. Finally the influence of the width and the depth of the soil tank has been studied.

The comparison between the simulations focused on the displacement of the central point of the plate.

Figures 6.10 and 6.11 show the mass density contours for the detonation of 6 kg of TNT buried at 100 mm below the free surface at various moments, from the detonation time to 2 ms. The first interaction between the explosive and the soil, the propagation of the shock wave in the soil and in the air, and the interaction between the shock wave and the plate are illustrated in these figures.

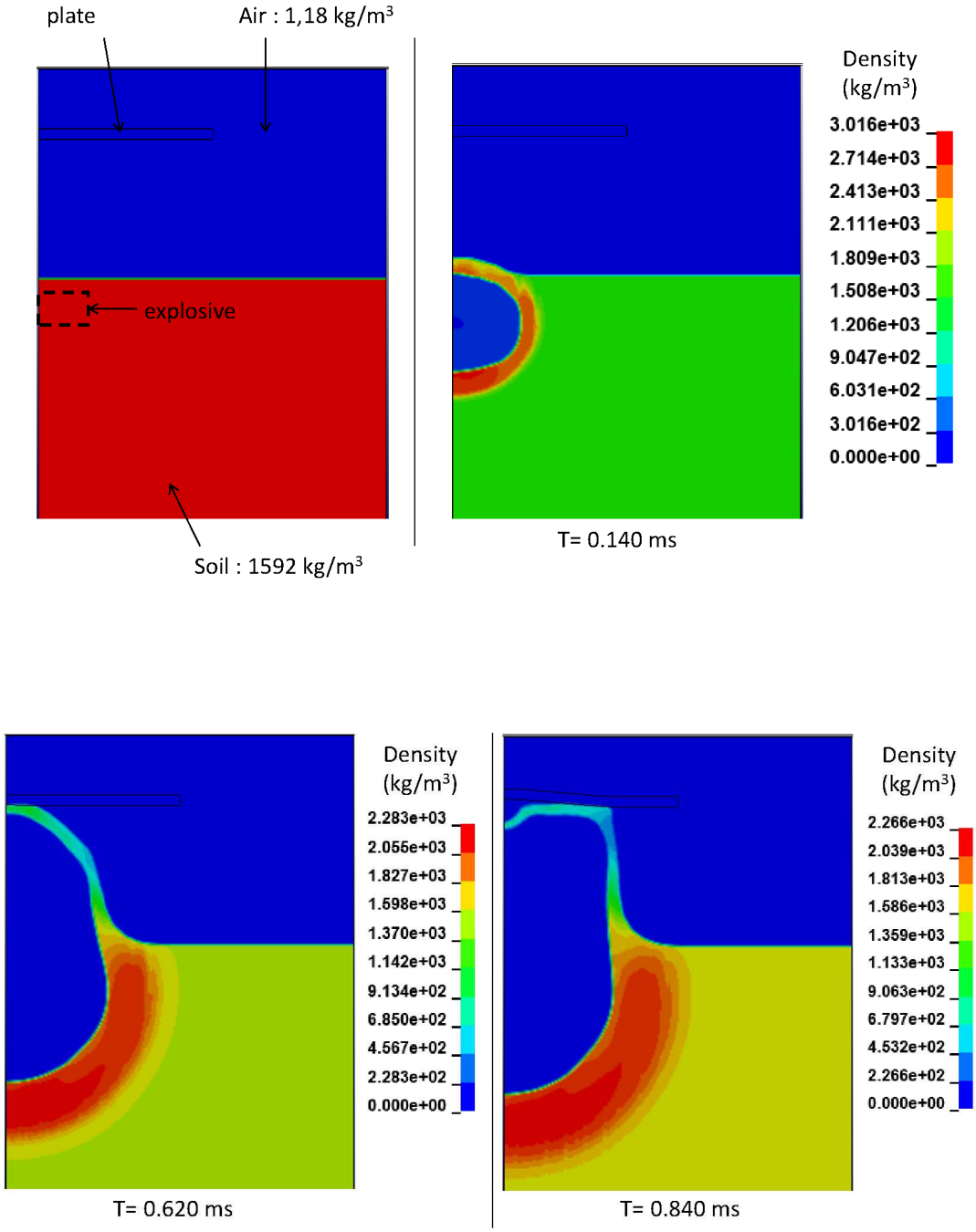

Figure 6.10: Pictures of the mass density contours from the simulations of 6 kg of TNT at $t = 0$, 0.140, 0.620 and 0.840 ms. The plate is 30 mm thick and stands at 400 mm above the free surface. At $t = 0.140$ ms, the shock wave is still in the soil. $t = 0.620$ ms corresponds to the time when the soil just hits the plate. The large difference of density between the soil above and under the detonation products can be noticed. The area below is getting larger and larger, since the bubble of detonation products continues increasing. At $t = 0.840$ ms, the plate is deforming. The soil which has hit the plate seems to bounce down along the axis.

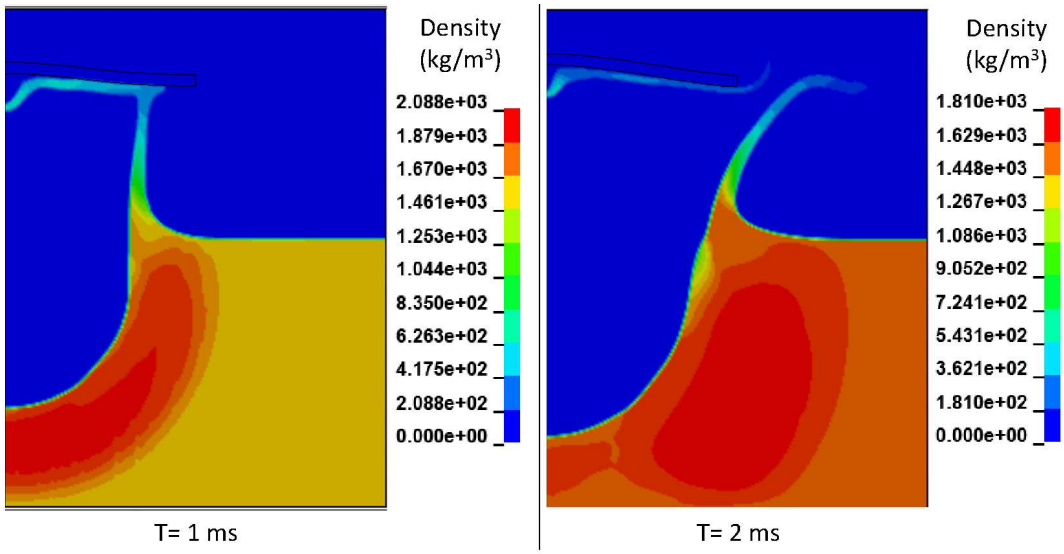

Figure 6.11: Continued from Fig 6.3.2. Mass density at $t = 1\,\text{ms}$ and $t = 2\,\text{ms}$. At $t = 1\,\text{ms}$ the area where the soil is dense is even larger than previously, since the bubble of detonation products continues increasing, and widens. This increase is particularly noticeable in the air. Moreover, the pressure decreases as it propagates in the soil. At $t = 2\,\text{ms}$, the bubble is so wide that the density of its upper part becomes very small and close to the density of the air under atmospheric pressure.

6.3.2.1 Effect of the stand off distance and the plate thickness on displacement

First, the central displacement of the plate has been studied for three masses of explosive (6, 8 and 10 kg of TNT) as illustrated in figure 6.12. Three stand off distances were considered (400, 500 and 600 mm) whereas three thicknesses of the plate were tested (30, 40 and 50 mm).

For a given plate thickness, as the stand off distance increases, the displacement of the plate occurs later and its maximum value is smaller. For a larger stand off distance, the detonation products spent some energy and time just to expand. The difference in time between two curves corresponds to the distance times the detonation velocity of the shock wave. Since the detonation products have less energy, the deformation of the plate is less important.

The plate is more difficult to deform as the thickness of the plate increases, which explains a smaller displacement rate and deformation.

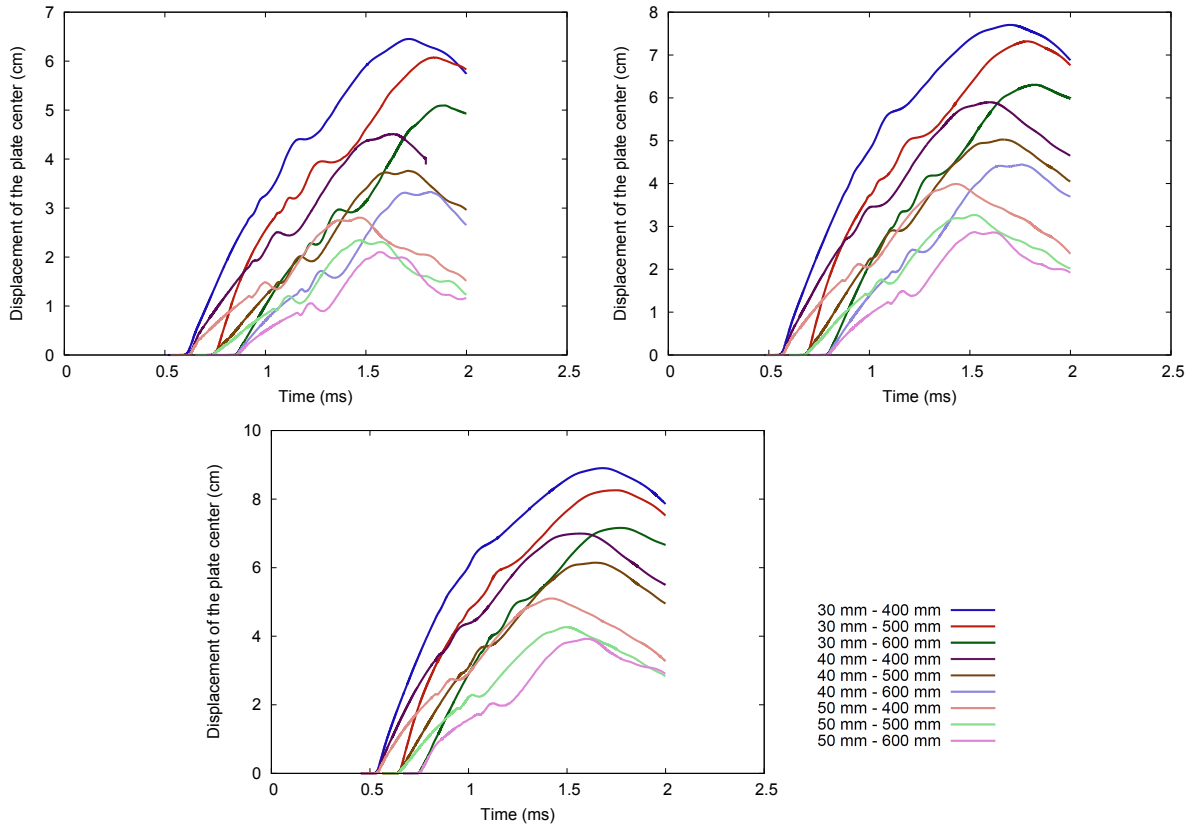

Figure 6.12: Time course of the vertical displacement of the central point of the plate for 6 kg (top left), 8 kg (top right) and 10 kg (bottom) of TNT. Three thicknesses of plate (30, 40 and 50 mm) and three stand off distances were tested (400, 500 and 600 mm).

6.3.2.2 Influence of soil parameters on the plate displacement

In chapter 5, a parametric study was performed to determine the most important parameters of the soil on aerial pressures. The initial density ρ_0 and the initial preconsolidation pressure X_0 were considered as very influential. From these observations, these two parameters were tested here to evaluate their influence on the displacement of the plate. Two initial densities equal to 1300 and 1900 kg.m^{-3}, and an initial preconsolidation pressure equal to $X_0 = 100$ MPa were compared to the reference parameters of our model provided in table 2.1.

The simulations were run for three masses of explosive, a stand off distance of 400 mm and a plate thickness of 30 mm. This configuration was chosen in order to evaluate the influence of parameters more easily since the displacement of the plate is the largest. The displacement of the plate center is shown in figure 6.13.

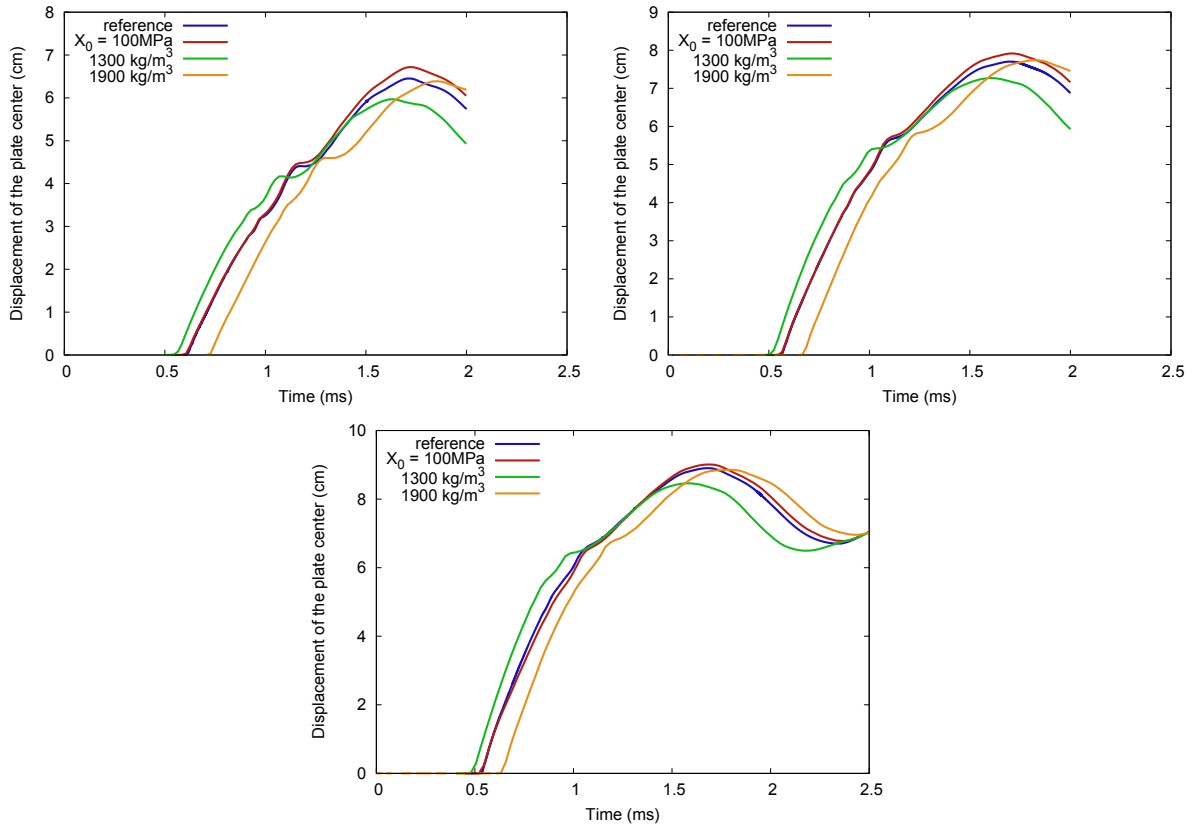

Figure 6.13: Time course of the vertical displacement of the central point of the plate for 6 kg (top left), 8 kg (top right) and 10 kg (bottom) of TNT. The reference curve corresponds to the simulation with the parameters detailed in table 2.1. The other curves differ each by a parameter.

Influence of the density

For the simulations of 100 g of explosive, the pressure signals arrived earlier when the density was decreased. The pressures were also a little larger since the explosive spent less energy to move a lighter soil. In that case, the largest depth of burial was equal to 8 cm; the explosive was 3.2 cm thick with a diameter equal to 6.4 cm. In the simulations we are now interested in, the depth of burial is equal to 10 cm, and the 6kg explosive is 8 cm thick with a diameter equal to 24.2 cm. Comparatively, here, the density of the soil above the explosive does not play an important part compared to the large quantity of explosive.

For a smaller initial density, the displacement of the plate began earlier: a smaller soil density implies a larger sound speed, thus a faster shock wave propagation. The maximum displacement of the plate was smaller for the three masses of explosive when the initial density was decreased. Here the displacement of the plate is due to the energy of the explosion but is also linked to the speed and the mass of the soil which reaches the plate. As mentioned in section 6.1.2, the kinetic energy plays a non negligible part in the impulse. A lighter soil has a smaller mass which causes a smaller displacement.

Influence of the initial cap position X_0

The value of the initial cap position X_0 had a large influence on pressures. A value of 100 MPa was tested for X_0 instead of the initial value of 1 MPa. The width of the yield surface was therefore increased by 100.

With a larger yield surface, the displacement is more important: the soil is more elastic, so less energy of the explosive is spent in plasticity.

However the relative difference of the displacement decreases with the increase of the mass of the explosive: with a mass of explosive of 10 kg, the difference of the plate displacement is very little between the two sizes of yield surface. In this case, the energy of the explosive has more importance on the result than the size of the yield surface.

6.3.2.3 Influence of the depth of burial of the explosive

The simulations of the detonation of three explosive masses were run for five depths of burial (100 mm, 150 mm, 200 mm, 250 mm and 300 mm). The results are shown in figure 6.14.

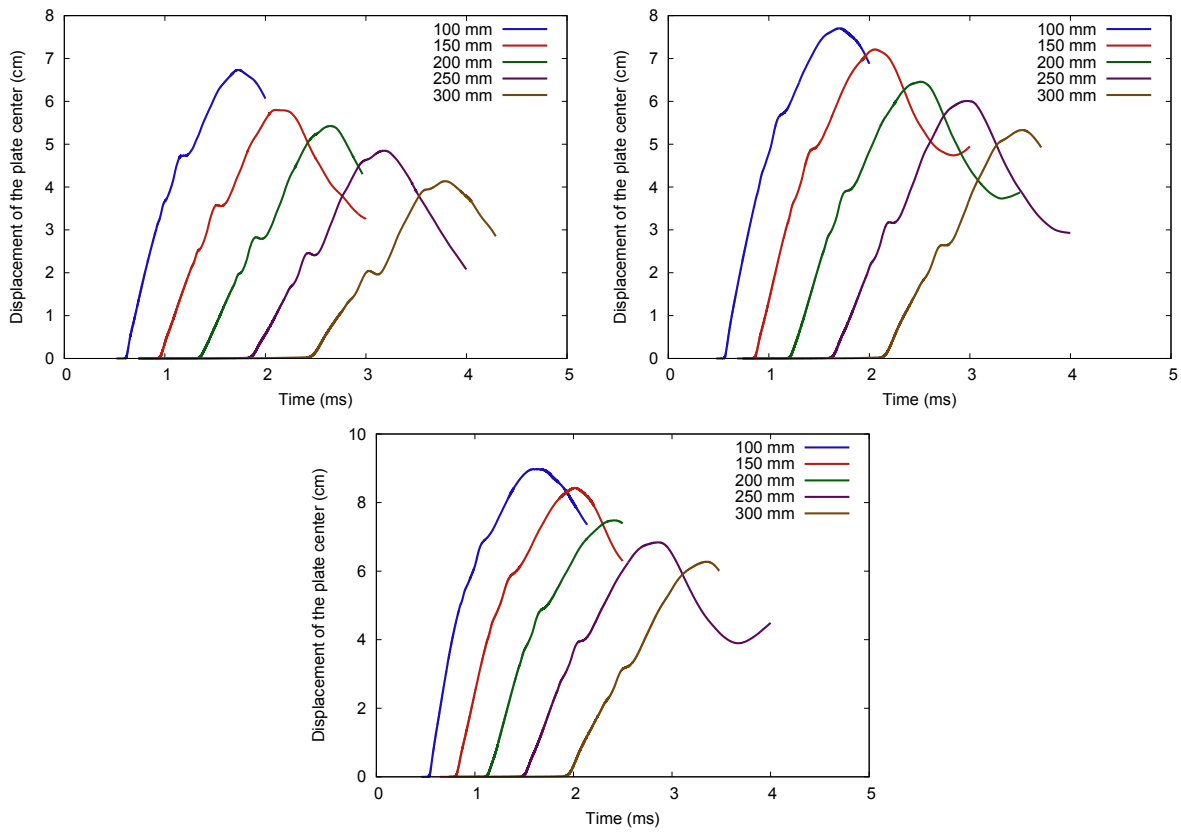

Figure 6.14: Time course of the vertical displacement of the central point of the plate for 5 depths of burial of 6 kg (top left), 8 kg (top right) and 10 kg (bottom) of TNT. The maximum displacement of the plate and the velocity decrease with the increase of the depth of burial. The time shift between two curves increases with the depth of burial.

With a larger depth of burial, the thickness of the soil above the explosive increases. The attenuation of the wave speed is more important in the soil than in the air. Therefore while the 5 depths of burial are regularly spaced (every 50 mm), the time between two displacement curves is not equal. This time is larger as the explosive is buried more deeply.

Moreover, the displacement of the plate and its rate are getting smaller as the depth of burial of the explosive increases. With a deeeper buried explosive, the remaining energy of the explosion at the free surface has decreased which implies a smaller deformation and rate.

6.3.2.4 Influence of the dimensions of the soil tank on the plate displacement

We have to know the dimensions of the soil tank. We need the smallest possible soil tank to prepare the most homogeneous soil. Besides the reflections from the borders should be avoided.

In the following, two parameters are studied:

- the side of the soil tank. In experiments, the surface of the tank is square. Since the simulations are axisymmetric, the influence of the radius is studied instead.
- apart from the soil radius/width, another important dimension of the soil tank is its depth. One current question when preparing the soil tank is how deep the soil must be homogeneous.

Radius of the soil tank

At DGA TT, for the large scale experiments, two soil tanks are available, one with a width of 2 m and one with a width of 3 m. Here, three tank sizes were tested: a soil tank with a radius of 0.25 m, 0.5 m and 1 m for three masses of explosive (6, 8 and 10 kg of TNT, shown in figure 6.15). A condition of zero displacement (horizontally and vertically) was applied to the lateral border of the soil tank.

For the radii of 0.5 and 1 m, the results of the displacement of the plate were exactly the same. A tank radius of 0.25 m increases the displacement of the plate. 0.25 m corresponds to twice the radius of the explosive. So once the explosive has expanded, before the shock wave reaches the plate, the wave has already reflected on the border of the soil tank increasing the stresses in the soil then the displacement of the plate.

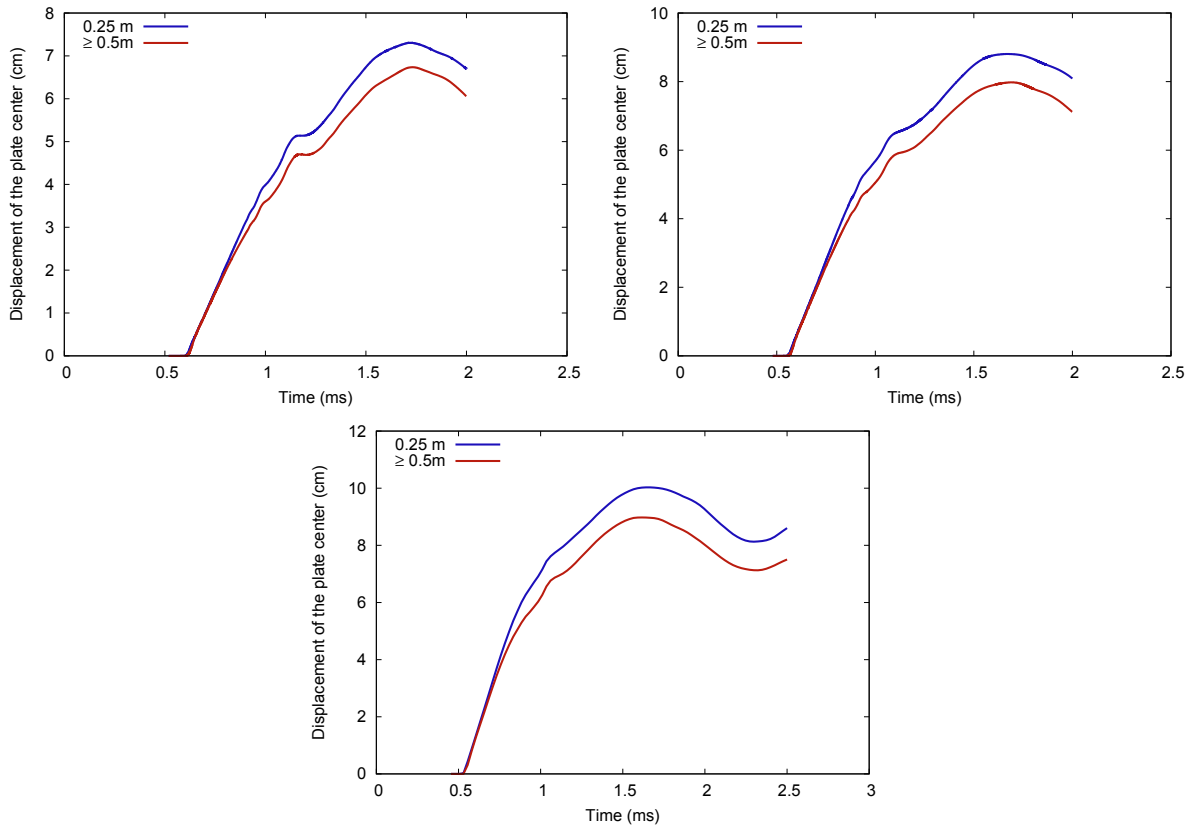

Figure 6.15: Time course of the vertical displacement of the central point of the plate for 6 kg (top left), 8 kg (top right) and 10 kg (bottom) of TNT. Three radii of the soil tank were tested: 0.25, 0.5 and 1 m. The displacement results of 0.5 and 1 m are the same. But decreasing the width of the soil tank from 0.5 m to 0.25 m increases the displacement of the plate.

Depth of the soil tank

Three tank depths were studied: 30 cm, 50 cm and 70 cm, considering a non displacement condition at the bottom of the mesh (which corresponds to the bottom of the soil tank). Three masses of explosive were tested (6 kg, 8 kg and 10 kg shown in figure 6.16).

For a depth of 50 and 70 cm, the results of the displacement of the plate are exactly the same. At variance, a depth of a tank of 30 cm increases the displacement of the plate. In fact, in these 30 cm, there is about 10 cm of soil below the explosive, the thickness of the explosive is about 10 cm which is itself located at 10 cm below the free surface. So with a depth of burial of 30 cm, the shock wave is reflected at the bottom of the soil tank, increasing the stresses of the soil, and driving a larger displacement of the plate.

As a consequence, if the soil in the tank is not removed between two shots, the soil will become denser and denser, due to the detonation of successive explosives. This means that in order not to disturb the plate displacement results, the soil should be removed on a 50 cm depth at least.

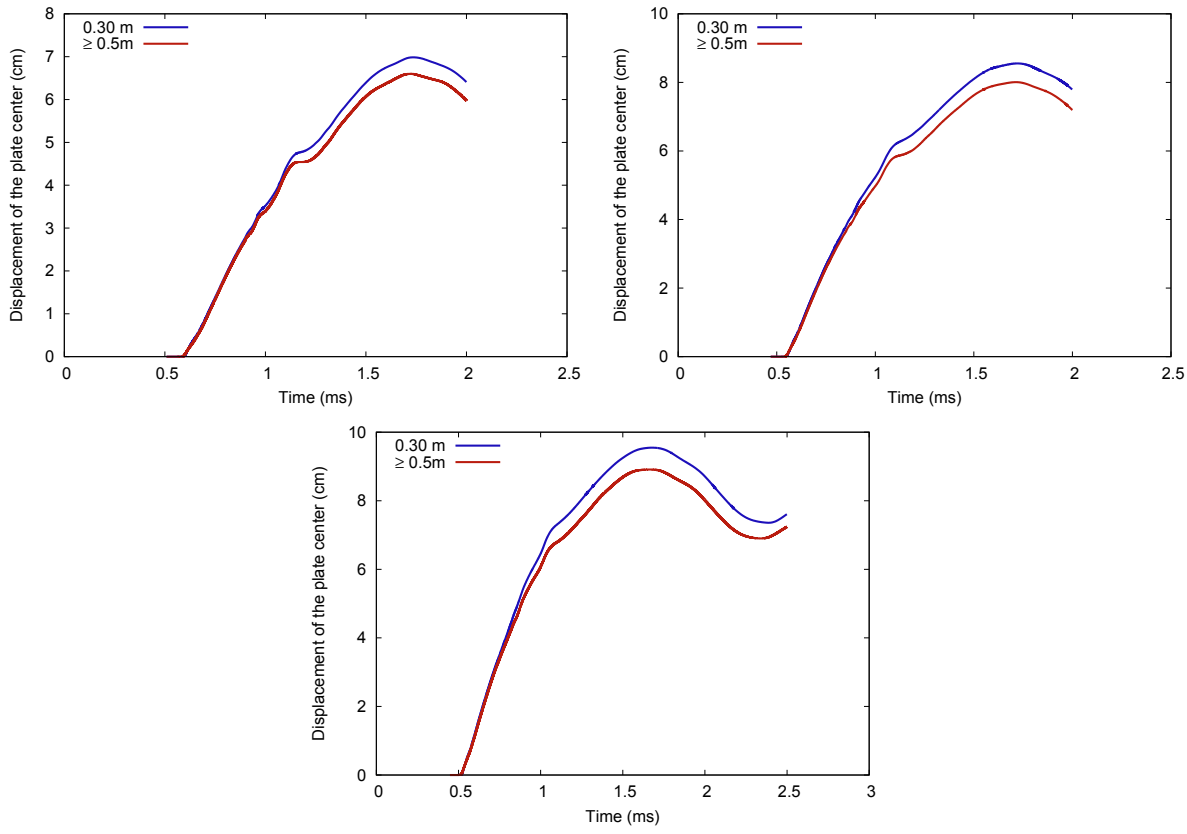

Figure 6.16: Time course of the vertical displacement of the central point of the plate for 6 kg (top left), 8 kg (top right) and 10 kg (bottom) of TNT. Three depths of the soil tank were tested: 30 cm, 50 cm and 70 cm. The displacements of the plate for a soil tank depth of 50 and 70 cm are the same. However, a difference in the displacement can be noticed for a depth of 30 cm.

Different radii and depths have been studied to determine the smallest size of the

tank in order to obtain the same plate displacement. Instead of studying the plate displacement, had the impulse been studied, the dimensions of the tank would have been different.

6.4 Large scale experiments and simulations

In the following, tests carried out at DGA TT between Septembre 2014 and January 2015 to measure the deformation of plates and the impulse transmitted to a test rig by buried detonations are overviewed. Next, simulations are run to study the influence of parameters of our viscoplastic model on impulse.

6.4.1 Overview of our large scale tests

In order to validate our soil model for the effects of buried mines on vehicle bellies, experiments of detonations of large quantities of explosive (up to 8 kg of TNT) was carried out with a test rig developed with the support of Nexter Systems.

The aim of the shots was to measure the deformation of a metallic plate and the impulse transmitted to the device by a buried explosion. A range of soil water contents, depths of burial, stand off distances and plate thicknesses was tested.

Figure 6.17: View of our large scale experimental set up. The deformation of a metallic plate and the impulse transmitted by buried detonations were studied.

The test rig was composed of several parts. The first one was a main assembly of 3 tons with a square opening of 1 m side in its center. An intermediate plate which had

a circular opening with a diameter of 1 m was screwed to this massive part. The plate which was deformed by the explosion was itself screwed to this intermediate plate. The tested plate was a cylinder of Rolled Homogeneous Armor (RHA, armoured steel) with a diameter of 1.46 m. Various thicknesses (between 15 and 50 mm) were tested.

Eight additional ballasts were placed above the main assembly. Each one weighed 450 kg. The whole device weighed around 9 tons without the studied plate which was equal to 650 kg for a thickness of 50 mm.

The distance between the plate and the soil (called stand off distance and noted SO in the following) was adjustable thanks to four feet on which the device was mounted. The four feet directly lied on the soil of the tank: the test rig was 2 m wide while the side of the soil tank was equal to 3 m.

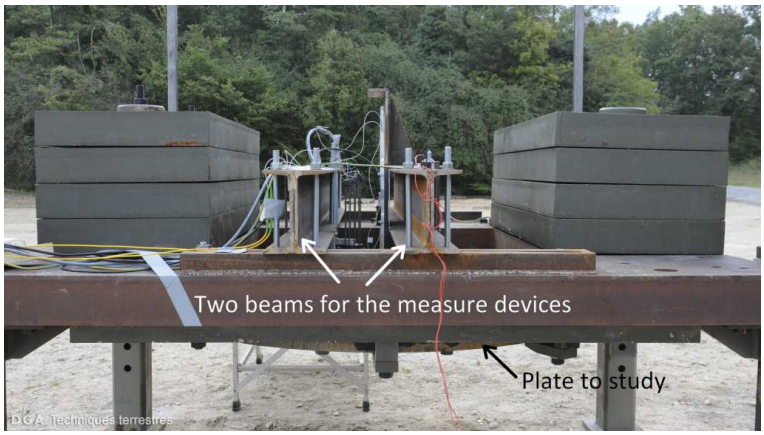

Figure 6.18: Beams across the opening of the assembly on which measure devices were fixed.

Across the opening of the main assembly, two beams were fixed for the measure devices to study the plate deformation. A laser provided the velocity of the displacement of the plate center. A block of metallic deformable rods was used to get time instants of the plate displacement. Each rod was located at a given height above the plate and was associated to an electric resistance with a specific value. All of them formed a voltage divider. When one rod was hit by the plate, the measured voltage was suddenly changed which provides the time of displacement of the plate. Moreover honeycomb structures were used as witnesses of the maximum deformation of the plate. These three measure devices (the laser, the honeycomb structure, the rods) were not located at the same place above the plate. A maximum distance of 10 cm should exist between two measure devices. Figure 6.18 shows the installation of the two beams fixed across the opening of the main ballast. Figure 6.19 illustrates the three measure devices.

As for the global motion of the entire test rig, it was obtained thanks to four check patterns mounted at the end of four shafts fixed on the main assembly. Their displacement was recorded by a high speed camera with a frequency between 2000 and 6000 pictures per second depending on the luminosity of the setting.

When the fire impulse is given by the pyrotechnician, the time between his action and the detonation of the explosive depends on various parameters. In order to get an absolute time and to synchronize all the signals of the measuring instruments, two

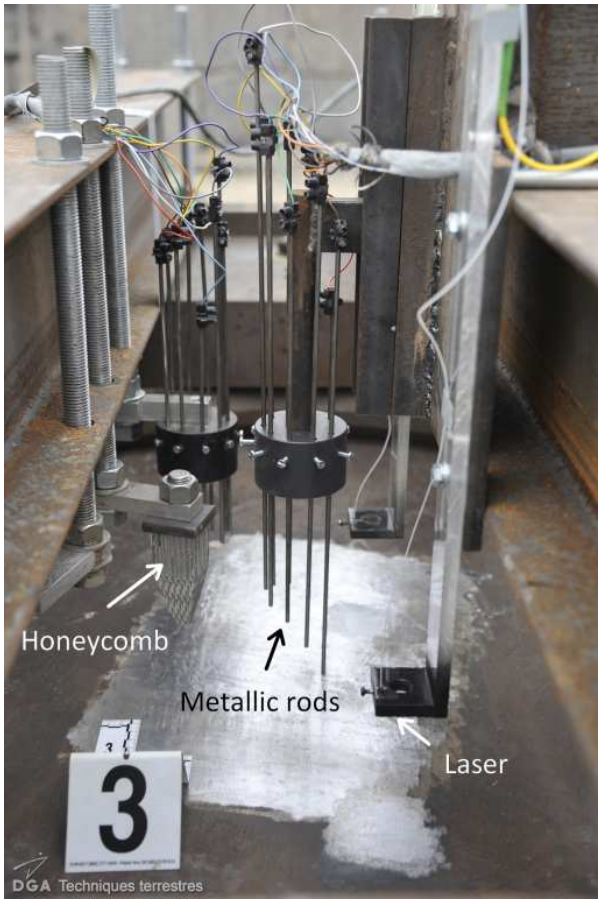

Figure 6.19: Devices to measure plate deformation: honeycomb structure, metallic rods and laser.

aluminium sheets were laid on the buried explosive. This technique was already used for small scale experiments and for aerial detonations, see section 5.5 for more information. Thanks to this technique, the time of arrival of the shock wave at the border of the explosive was obtained.

After each shot, the crater was scanned and the residual deformation of the plate was measured. From shot number 5 onwards, the plate was also scanned after each shot to get its deformed profile.

6.4.2 Soil preparation

The soil the explosive was buried in was the same as in the small scale experiments reported in chapter 5. This was a STANAG sandy gravel soil. The requirements of this soil imposed by a NATO document (AEP55) are detailed in section 1.1.2 and the granulometry of the soil is given in figure 1.3.

For the first six shots, a soil tank with a square opening of 2 m x 2 m was used. The sizes of the craters revealed that the borders of the tank were too close and limited the diameter of the crater. Therefore for the following shots, a larger soil tank (3 m x 3 m) was used.

The soil of the tank was prepared in the same way as for the small scale experiments, that is to say, in two layers. Each one was moistened and compacted. Two containers were placed in the soil tank while preparing the upper layer to get the density and the water content of the soil just before the shot. Both were cylindrical. The first container (called volume 1 in the following) had a radius of 65 mm and a height of 220 mm whereas volume 2 had a radius of 136.5 mm and a height of 100 mm.

6.4.3 Shot configurations

The various shot configurations are presented in table 6.5. Each shot was only carried out once given the degree of saturation of the soil, so all the results must be taken with care since they were not duplicated.

Shot number	Explosive mass	Depth of burial	Stand-off distance	Plate thickness
A	2 kg	100 mm	800 mm	50 mm
B	4 kg	100 mm	800 mm	50 mm
C	4 kg*	100 mm	800 mm	50 mm
D	6 kg	100 mm	800 mm	50 mm
E	6 kg	100 mm	800 mm	50 mm
F	6 kg	100 mm	800 mm	50 mm
1	6 kg	100 mm	800 mm	30 mm
2	6 kg	100 mm	600 mm	30 mm
3	6 kg	100 mm	600 mm	30 mm
4	8 kg	100 mm	600 mm	30 mm
5	8 kg	250 mm	600 mm	30 mm
6	8 kg	100 mm	600 mm	30 mm
7	8 kg	250 mm	600 mm	30 mm
8	8 kg	100 mm	800 mm	30 mm
9	8 kg	100 mm	800 mm	30 mm
10	6 kg	100 mm	1000 mm	25 mm
11	6 kg	100 mm	600 mm	25 mm
12	6 kg	100 mm	600 mm	20 mm
13	8 kg	100 mm	600 mm	25 mm
14	6 kg	100 mm	600 mm	15 mm
15	6 kg	250 mm	600 mm	25 mm

Table 6.5: Shot configurations for the large scale experiments. Except for shot C where the explosive was plastrite, for all the other shots, TNT was chosen.

6.4.4 Impulse and displacement of the plate

The impulse and the deformation of the plate center are gathered in table 6.6.

As mentionned in the description of the test rig, checked patterns were placed at the end of four edges mounted on the main ballast. Their displacement was tracked by a high

speed camera. However after several hundreds of milliseconds following the detonation of the explosive, the checked patterns were hidden behind soil projections and detonation products. Thus the highest position of the device could not be recorded. However, this time was long enough for the test rig to have a linear displacement. From this value, the velocity of the test rig was deduced.

The impulse is generally calculated from the maximum displacement of a device. In our case, the impulse was obtained from the product of the velocity of the device by its mass.

Shot number	Impulse (kN.s)	Displacement (mm)
A	4.0	9
B	7.8	18
C	16.2	17
D	24.9	30
E	14.3	24
F	-	21
1	23.2	46
2	26.1	62
3	22.3	67
4	50.3	113
5	60.2	87
6	28.6	78
7	44.1	65
8	40.9	90
9	25.2	59
10	6.6	-
11	29.2	71
12	31.2	106
13	26.9	90
14	18.9	117
15	32.3	75

Table 6.6: Impulse and displacement of the plate obtained during the large scale experiments. A high speed camera tracked the displacement of the checked patterns which were mounted at the end of four edges on the main ballast. This provided the global displacement of the test rig. The impulse was calculated by the product of the mass of the test rig times its velocity. As for the displacement of the plate, it corresponds to the records of honeycomb structures.

6.4.4.1 Influence of the degree of saturation

For each shot, the density and the water content were measured with two samples of soil. The results are given in table 6.7. The density was obtained by weighing the sample, and the soil was oven dried to get its water content.

These measures provided soil information at two points of the soil tank. The soil was prepared so that these two measures were representative of the entire tank. However a slight difference could exist since the soil in the tank may not be completely homogeneous.

The degree of saturation of the soil can be obtained thanks to the density and the water content. In section 6.1.2, this parameter was considered as crucial and had a real influence on the impulse.

For the record, the degree of saturation S_r of the soil is the ratio of the volume of water over the volume of voids (air and water):

$$S_r = \frac{V_w}{V_v} = \frac{V_w}{V_w + V_a} \quad \Rightarrow \quad V_a = \frac{V_w(1 - S_r)}{S_r} \tag{6.4.1}$$

The water content w is the ratio of the mass of water over the mass of solid grains whereas the soil gravity $G_s = 2.61$ is the ratio of the soil grain density over the water density:

$$w = \frac{M_s}{M_w} = \frac{1}{G_s}\frac{V_w}{V_s} \quad \Rightarrow \quad \frac{V_w}{V_s} = G_s\, w \tag{6.4.2}$$

The soil density ρ is the ratio of the soil mass over the soil volume:

$$\rho = \frac{M}{V} \cong \frac{M_s + M_w}{V_a + V_s + V_w} = \frac{M_s(1+w)}{V_s + V_w\left(1 + \dfrac{1 - S_r}{S_r}\right)} = \rho_s \frac{1+w}{1 + \dfrac{G_s\, w}{S_r}} \tag{6.4.3}$$

Finally the saturation S_r can be obtained from the soil density ρ and the water content w

$$S_r = \frac{\rho\, G_s\, w}{\rho_s(1+w) - \rho} \tag{6.4.4}$$

For our STANAG soil, $G_s = 2.61$ thus $\rho_s = 2610\,\mathrm{kg.m^{-3}}$. Table 6.7 provides for each shot the degree of saturation obtained from the two containers placed in the soil tank.

For most of the shots, the two results are alike. However for shots 5, 9 and 11, a difference is noticeable. For shots 5 and 11, the weather conditions were very bad. Therefore, a degree of saturation of 81% seems more likely for shot 5. For shot 11, the degree of saturation should be closer to 78%.

For shot 9, the two samples were not removed at the same time. The sample which corresponds to the time of the shot provides a degree of saturation of 72%.

Figure 6.20 displays the impulse for 8 kg of TNT explosive in relation to the calculated degree of saturation for various stand off distances and various depths of burial of the explosive. Even if few tests were carried out for each configuration, the tendency remains the same: the impulse increases with the degree of saturation.

When the detonation occurs in a dry soil, the explosion scatters the solid grains and the soil mass which reaches the plate is small. At variance, when a detontation occurs in a saturated sand, the explosion drives water and solid grains where water acts as a binder, and the mass which impacts the target is larger. The impulse is therefore increased.

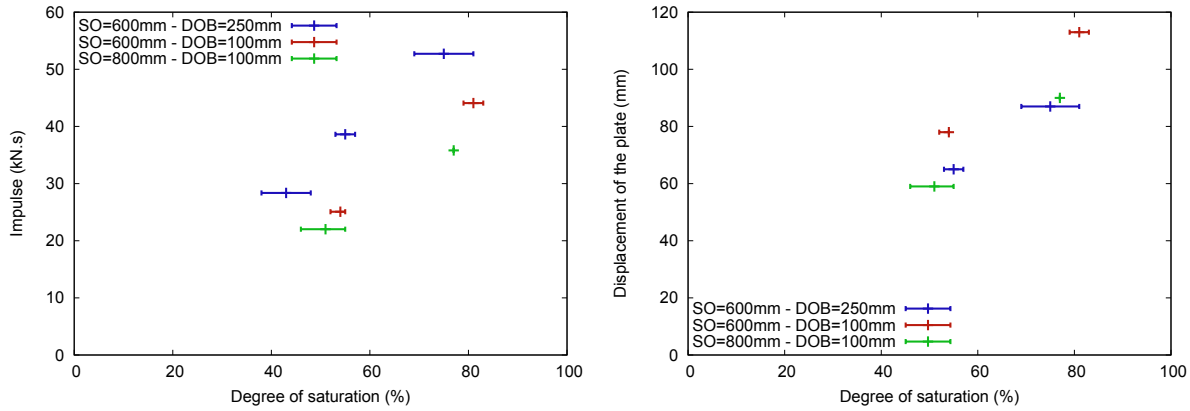

Figure 6.20: Impulse (left) and displacement of the plate (right) in relation to the degree of saturation of the soil due to the detonation of 8 kg of TNT for various shot configurations. The error bars correspond to the measures of the two soil volumes removed from the tank. For all the shot configurations, the impulse and the displacement of the plate are largely increased by the degree of saturation.

Let us now focus on the influence of the degree of saturation on the displacement of the plate center. Zakrisson et al. (2012) in particular recorded larger deformations when the soil was saturated. However the difference of deformation between dry and saturated soil was less marked than for the impulse.

The deformations regarding the degree of saturation for each configuration are plotted in figure 6.20. The tendency is the same as highlighted by Zakrisson et al. (2012): as the water content increases, the deformation is larger.

Apart from the displacement of the plate, the residual value was also measured. Figures 6.21 and 6.22 display the residual displacement of the RHA plates scanned after each shot. The residual displacement obviously depends on the explosive mass but also on the saturation of the soil. In figure 6.21, the residual displacement of the plate was compared for similar shots where the only difference was the degree of saturation. The residual displacement was all the more important as the degree of saturation was large.

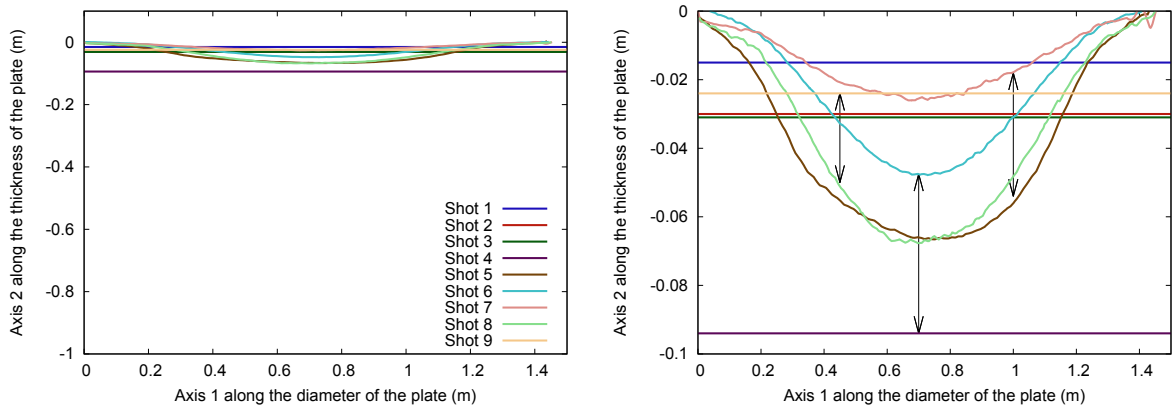

Figure 6.21: Residual displacement of the RHA plate obtained after each shot, for shots number 1 to 9. On the left, the figure displays the residual displacement on scale whereas on the right, the residual displacement is zoomed in order to notice the difference between shots. The arrows relate two similar configurations except for the degree of saturation. The straight lines correspond to the values of the maximum residual displacement when the plate was not scanned.

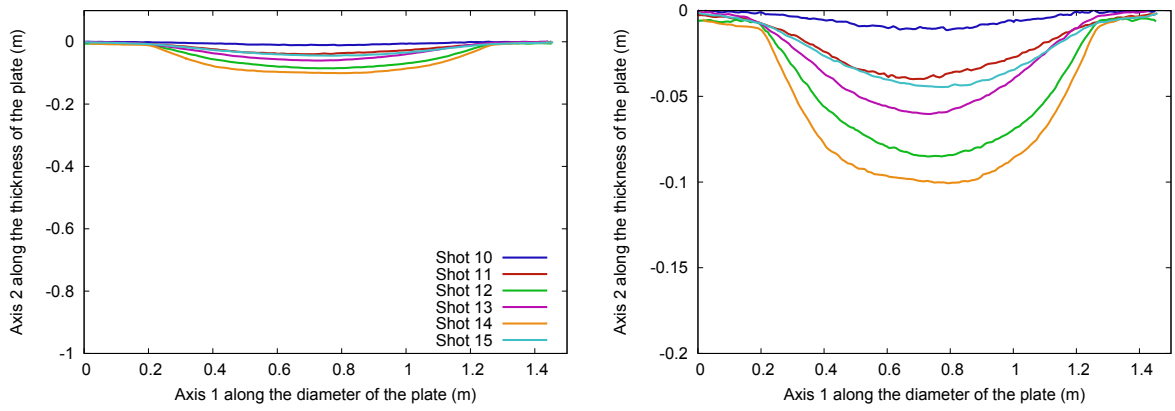

Figure 6.22: Same as figure 6.21 but for shots number 10 to 15.

	Volume 1			Volume 2		
Shot number	Water content (%)	Density ($kg.m^{-3}$)	Saturation (%)	Water content (%)	Density ($kg.m^{-3}$)	Saturation (%)
A	7.6	2040	53	-	-	-
B	11	2097	74	-	-	-
C	9.9	1942	54	-	-	-
D	8.1	1882	42	-	-	-
E	10	2062	67	-	-	-
F	10	2044	65	-	-	-
1	13	-	-	-	-	-
2	10	-	-	-	-	-
3	9.5	1964	54	8.6	2029	57
4	13	2050	79	13	2102	83
5	13	1962	69	14	2058	81
6	12	1853	55	8.9	1964	52
7	9.7	1940	53	10	1956	57
8	11	2106	77	-	-	-
9	13	1999	72	6.9	1931	40
10	9.4	1980	55	7.0	1997	46
11	12	2100	78	9.6	2003	59
12	9.3	1921	50	9.7	1973	56
13	9.5	2003	58	8.4	1967	50
14	7.2	1879	38	8.3	1930	47
15	7.5	1859	38	8.0	1962	48

Table 6.7: Water content, density and degree of saturation of the soil obtained for the two different sample volumes. Both were cylindrical. Volume 1 had a radius of 66.5 mm and a height of 300 mm whereas volume 2 had a radius of 136.5 mm and a height of 100 mm.

6.4.4.2 Influence of the depth of burial of the explosive

Two depths of burial (100 and 250 mm) were tested while considering an explosive mass of 8 kg, a stand off distance of 600 mm, a plate thicknesses of 30 mm and two water contents (a value around 10% and another one close to 14% where there was so much water in the soil that water puddles remained on the surface of the soil tank). The impulse of the test rig and the maximum value of the displacement of the plate center are displayed in figure 6.23.

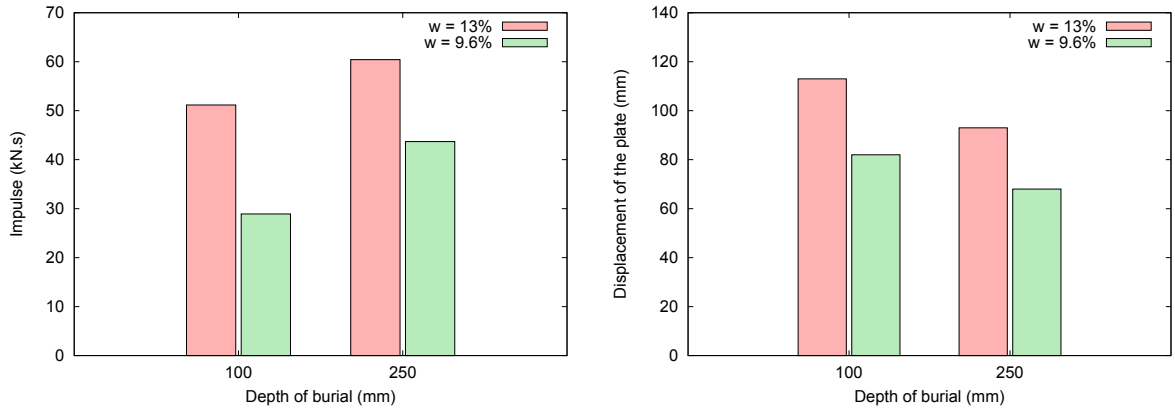

Figure 6.23: Impulse (left) and diplacement of the plate (right) of a 30-mm plate of RHA placed at 600mm above the soil for two depths of burial and two water contents.

Since only two depths of burial and two water contents were tested, the tendencies must be considered with care and other results should be added to confirm the conclusion. If the explosive is buried deeper, the impulse is increased but the displacement of the plate is decreased. The energy transmitted to the plate is more important due to the larger mass of soil projections which compensates the loss of energy from a deeper detonation.

These tendencies were confirmed by Zakrisson et al. (2012) which noticed that as the depth of burial increases, the deformation of the plate decreased while the impulse increases.

6.4.4.3 Influence of the explosive mass and the stand off distance

Explosive masses between 2 and 6 kg have been detonated while considering a plate thickness of 50 mm of RHA and a stand off distance of 800 mm. Moreover the detonation of 6 kg and 8 kg of TNT explosive has also been tested with a plate thickness of 30 mm and a stand off distance of 600 and 800 mm. Since we previously noticed that the water content had a large influence on results, these comparisons were made for the same water content (around 10% in our case). The results are shown in figure 6.24.

As it could be expected, the impulse and the deformation of the plate increased with the explosive mass.

The impulse calculation works on the assumption that the device is entirely indeformable. While the deformation of a 50 mm thick plate is little, it becomes larger with

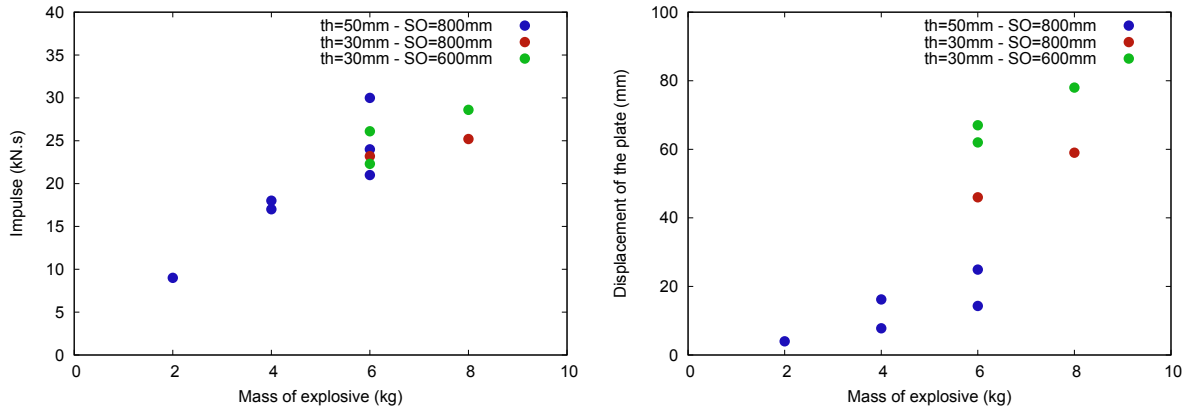

Figure 6.24: Impulse (left) and diplacement of the plate (right) obtained for various masses of TNT explosive. Two stand off distances (600 and 800 mm) and two plate thicknesses (30 and 50 mm) were tested.

a 30 mm thick plate, all the more for an explosive mass of 8 kg. In the case of a plate with a thickness of 30 mm, a part of the energy which could be used for the impulse is thus spent in deforming the plate.

In figure 6.24 the impulse has also been added with a stand off distance of 600 mm (thus closer to the soil) and a plate thickness of 30 mm. At a smaller distance to the soil, the energy of the detonation is more important. However the results for a mass of 6 and 8 kg seem to be aligned with those obtained with a plate thickness of 50 mm. The impulse loss due to the deformation of the thinner plate is compensated by a reduced stand off distance.

6.4.4.4 Influence of the plate thickness on the plate displacement

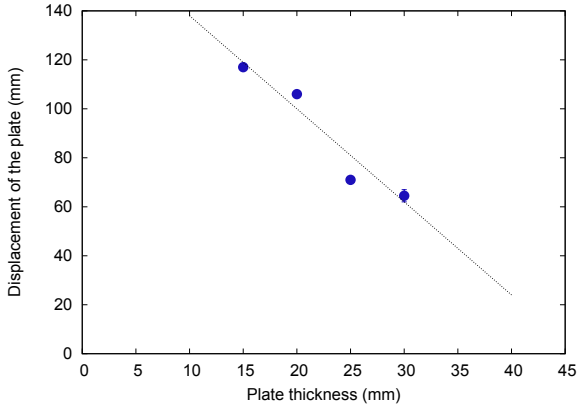

Figure 6.25: Diplacement of the plate in relation to its thickness. For each shot, 6 kg of TNT were detonated at 100 mm below the free surface in STANAG soil with a degree of saturation of about 50%. The plate was placed at 600 mm above the free surface.

The displacement of various RHA plate thicknesses (15, 20, 25 and 30 mm) due to the detonation of 6 kg of TNT buried at 100 mm below the free surface was studied. A stand off distance of 600 mm was chosen. The maximum displacement of the plate center displayed in figure 6.25 seems to decrease almost linearly as the thickness of the plate increases.

6.4.5 Crater patterns

After each shot, when the conditions were good enough, the crater resulting from the detonation of the buried explosive was scanned. The scan of the crater was not possible in case of rain or snow.

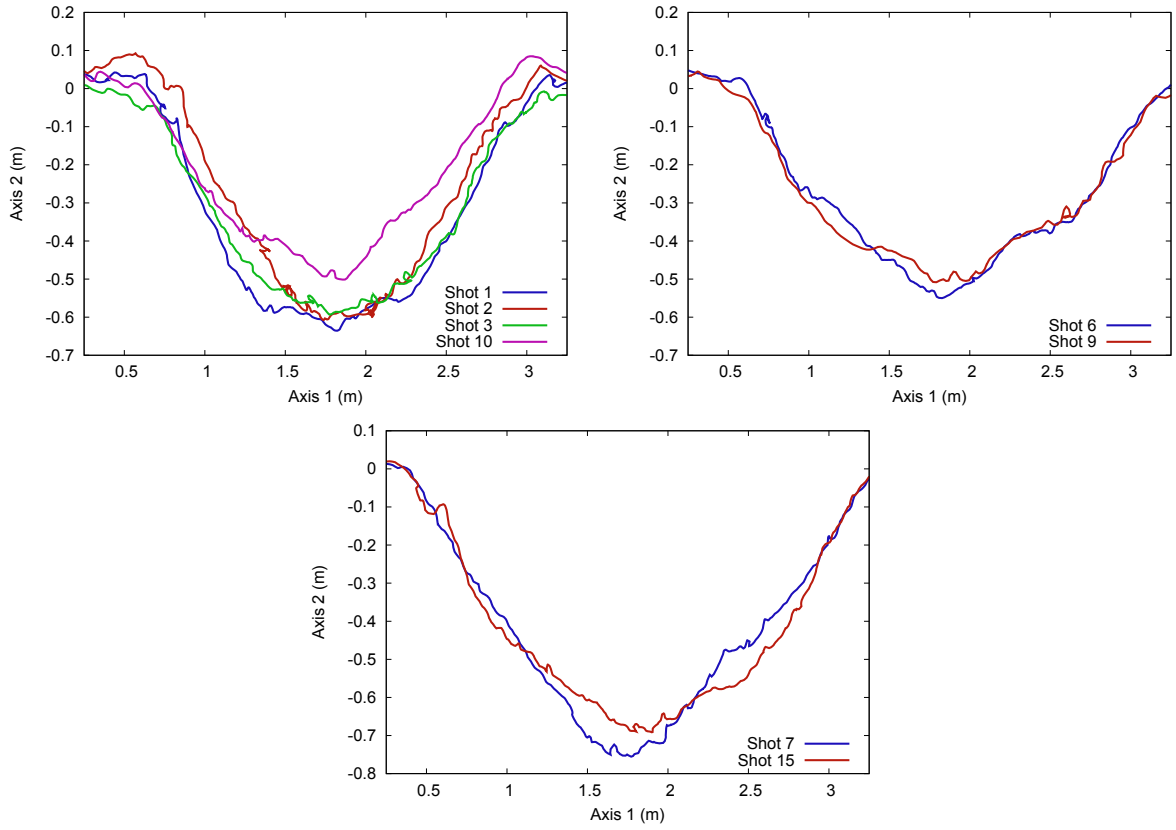

Figure 6.26: Profile of the craters resulting from the detonation of 6 kg (top left) and 8 kg (top right) of TNT buried at 100 mm below the free surface. Bottom: 8 kg of TNT buried at 250 mm below the free surface. Since the test rig is above the buried explosive, the profile of the crater may be slightly modified by the soil that hits the test rig and falls back in the tank.

Figure 6.26 shows the profile of the craters obtained after the detonation of 6 kg and 8 kg of TNT buried at 100 mm and for 8 kg of TNT buried at 250 mm. For close degrees of saturation, the profiles seem similar. Contrary to the craters resulting from the small scale experiments where dry sand led to larger craters, here (in particular for shot number 10) the tendency seems to be the opposite. For shot number 10, 6kg of TNT was buried

at 100 mm below the free surface and the effects of its detonation on a plate situated at 1000 mm above the soil were studied. The water content was smaller than for the other shots. However the smaller crater obtained for this shot is surprising. With such a large stand off distance, fewer projections were expected to fall back in the crater leaving a crater with larger dimensions.

Figures 6.27 and 6.4.5 display a comparison of the main dimensions of the crater (diameter, depth and volume) regarding the mass of explosive and its depth of burial. Once scanned, the volume is calculated with a dedicated software.

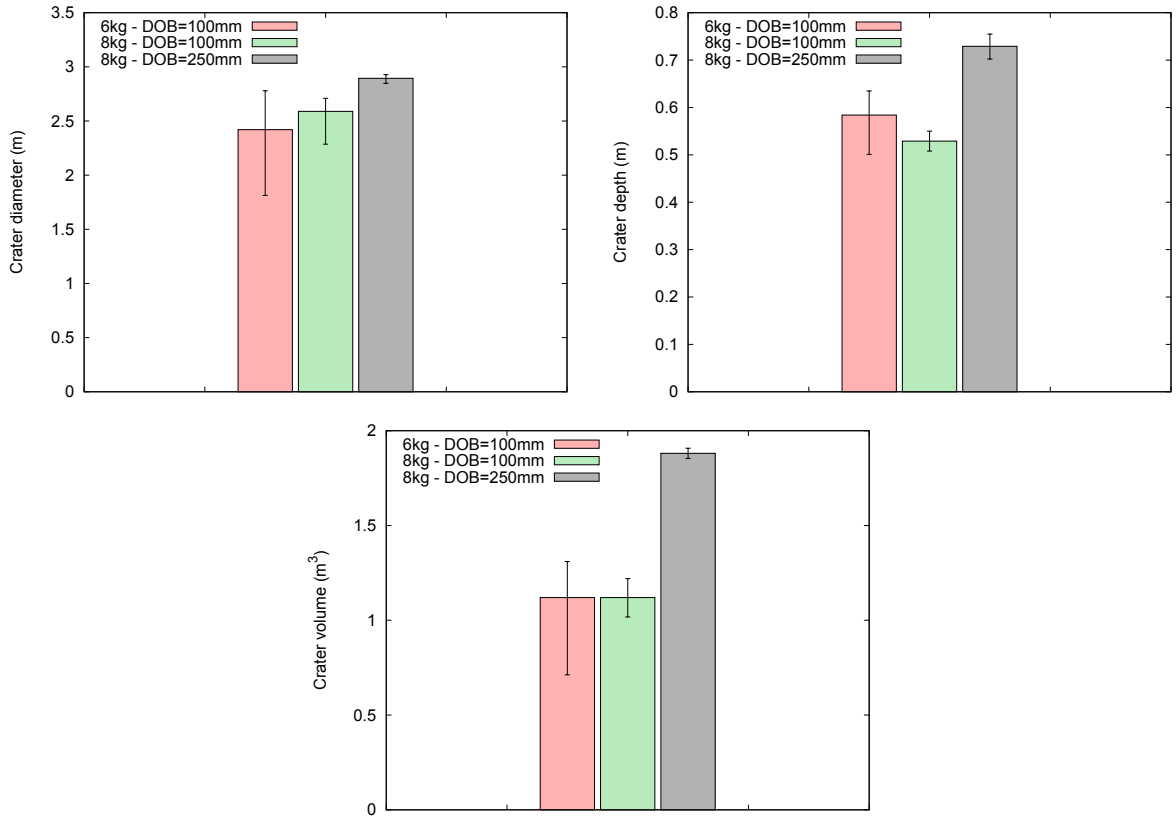

Figure 6.27: Diameter (top left), depth (top right) and volume (bottom) of the scanned craters for shots involving 6 and 8 kg of TNT buried at 100 and 250 mm. (DOB: depth of burial)

These results are a little surprising since the crater depths seem smaller for 8 kg of TNT than for 6 kg. The diameters and the volume seem alike. One expected result is the larger crater dimensions due to a deeper explosion.

6.4.6 Overview of our simulations

The simulations presented in this section reproduce our experiments described in section 6.4.1. Axisymmetric simulations were run and the sketch in figure 6.28 displays the extent of the mesh.

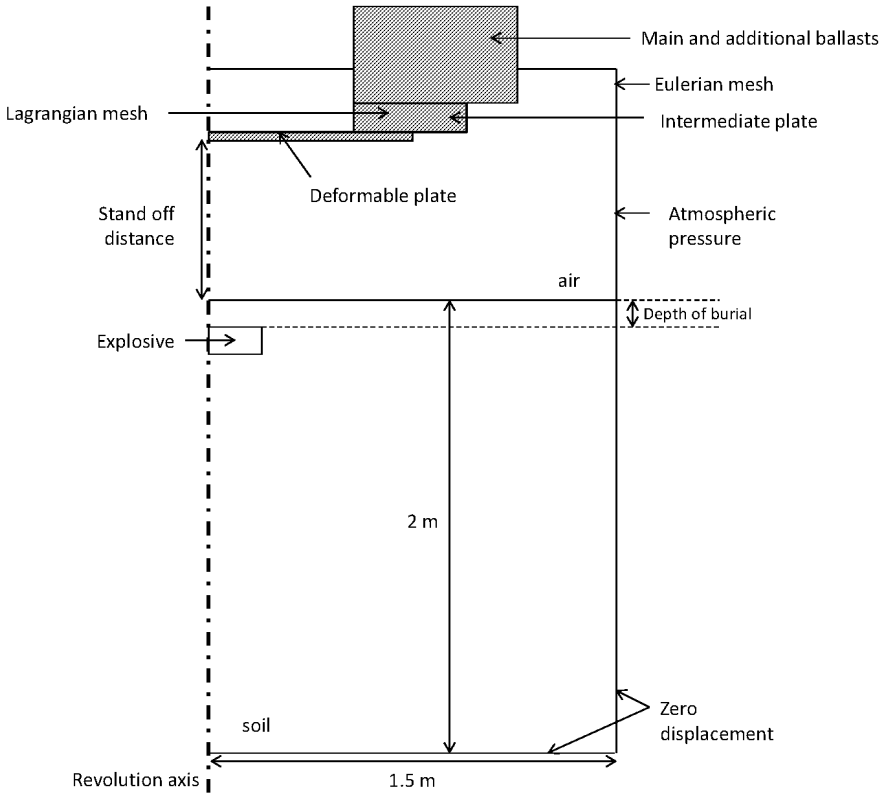

Figure 6.28: Extent of the mesh for the axisymmetric simulations reproducing the large scale experiments. The air, the explosive and the soil are modeled with a Eulerian formulation whereas the plate and the rigid parts are Lagrangian. The average mass of the test rig is the same as in experiments even if the hypothesis of axisymmetry is made.

The studied plate is cylindrical and can deform through the circular opening of the intermediate plate. However the other parts of the test rig do not allow a complete revolution symmetry. Even if the dimensions of the main and additional ballasts are slightly modified for the axisymmetric simulations, the entire mass of the test rig is the same as in experiments.

The air, the soil and the explosive are modeled with a Eulerian formulation. At variance, the other parts are Lagrangian. A Johnson Cook law associated with an equation of state is used for the plate. The parameters are given in tables 4.5 and 4.6. The other Lagrangian parts are considered rigid so that LS Dyna avoids calculations in such elements. Their masses are only taken into account for inertia.

A contact is imposed between the rigid parts and the plate. Contacts between deformable and rigid parts are possible by providing a Young's modulus of the rigid parts which is only used for calculating the stiffness of the spring of the contact. Since the

rigid parts of the simulation and the deforming plate are screwed in experiments, one node common to the plate and to the rigid parts is merged so that the two parts remain connected during the entire simulation.

A zero displacement condition is imposed to the nodes of the border of the mesh of the soil part while the atmospheric pressure is applied to the border of the mesh.

An interaction between the Eulerian and Lagrangian parts is established.

In the Eulerian parts, the air is modeled with a polynomial equation and the parameters are given in section 4.2.4. The parameters of the explosive are provided in table 4.7 while the parameters of the soil are gathered in table 2.1. As in experiments, the detonation point of the explosive is located on the center of its bottom face and the depth of burial is the distance between the upper face of the explosive and the free surface of the soil.

The displacement of some nodes of the plate is output to get its displacement. Moreover some nodes of the rigid part are displayed to obtain the global displacement of the test rig and to calculate its impulse thanks to its velocity.

The sensitivity of the element size of the mesh was studied: while a slight difference on the displacement of the plate center can be noticed, there is negligible consequence on the impulse. Therefore an element size of 5 mm was chosen for the entire mesh.

6.4.7 Influence of the parameters of our viscoplastic model on the impulse

In the following simulations, let us consider just one of the experimental configurations of table 6.6 to study the influence of various parameters of the model on the impulse. Let us simulate the detonation of 8 kg of TNT buried at 100 mm below the surface of the soil. The studied plate is placed at 600 mm above the soil.

Our viscoplastic model is defined by three regions in the $(I_1, \sqrt{J_2})$ plane (see section 2.3): a cutoff surface, a failure surface and a cap surface.

In order to know which region of the yield surface is activated according to the location in the soil, figure 6.29 shows the isocontours of the three regions of the yield surface at various times, from the time when the shock wave enters in the soil to the time of the interaction of the soil with the plate.

When a detonation occurs in the soil, first stresses increase significantly in the vicinity of the explosive (with values around 10 GPa). The stress state immediately jumps out of the yield surface and activates the cap. Thanks to the viscoplastic behavior of the soil, the stress state can be outside the yield surface. Therefore, the cap hardens to try to reach the stress state and at the same time, the bulk modulus of this zone of large stress increases quickly to reach the grain-mixture bulk modulus. Therefore, thanks to a larger bulk modulus, the soil resists the detonation.

Once the shock wave is passed, the stresses decrease quickly to much smaller values (around 10-100 MPa). In our model, the cap can harden but cannot soften. Therefore when the stresses decrease, the cap is not activated anymore but the failure surface is. As a matter of fact, the stress state remains close to the failure surface between the moment

when the shock wave is passed and when the soil hits the plate. When the soil reaches the plate, the cap surface is activated again. Moreover, the soil bubble undergoes tensile stresses when it expands, as shown in figure 6.29.

After the explosive detonation, the shock wave propagates and reaches the free surface of the soil. A part of the shock wave continues its way in the air, while the other part is reflected in the soil. As the same phenomenon occurs in metals, when the reflected wave meets compressive wave, it turns into tensile wave.

Let us try now a different yield surface of the soil, with a cap surface far enough not to be activated. As figure 6.29 shows the isocontours of the three parts of the yield surface for a "small" yield surface (α which delimits the height of the yield surface was equal to 0.06 MPa and X_0 which provides the width of the yield surface was equal to 1 MPa), figure 6.30 displays the isocontours of the parts of the yield surface for a much larger yield surface (where $\alpha = 10$ MPa and X_0=100 GPa).

In this case, the cap is never activated because X_0 is very large. Instead the failure surface is first activated and when the shock wave is reflected on the free surface of the soil, a tensile wave is created and the cut off surface is activated. As a matter of fact, since the yield surface is very large, the wave remains elastic a longer time and the stresses become much larger. Therefore the stresses are more tensile with a wider yield surface because the stresses were more compressive before being reflected on the free surface of the soil.

In the following, we consider a cap surface close enough to the origin to be activated. Therefore, the main parameters to study regarding their influence on the impulse are the parameters of the failure surface, of the cap surface and the elastic moduli.

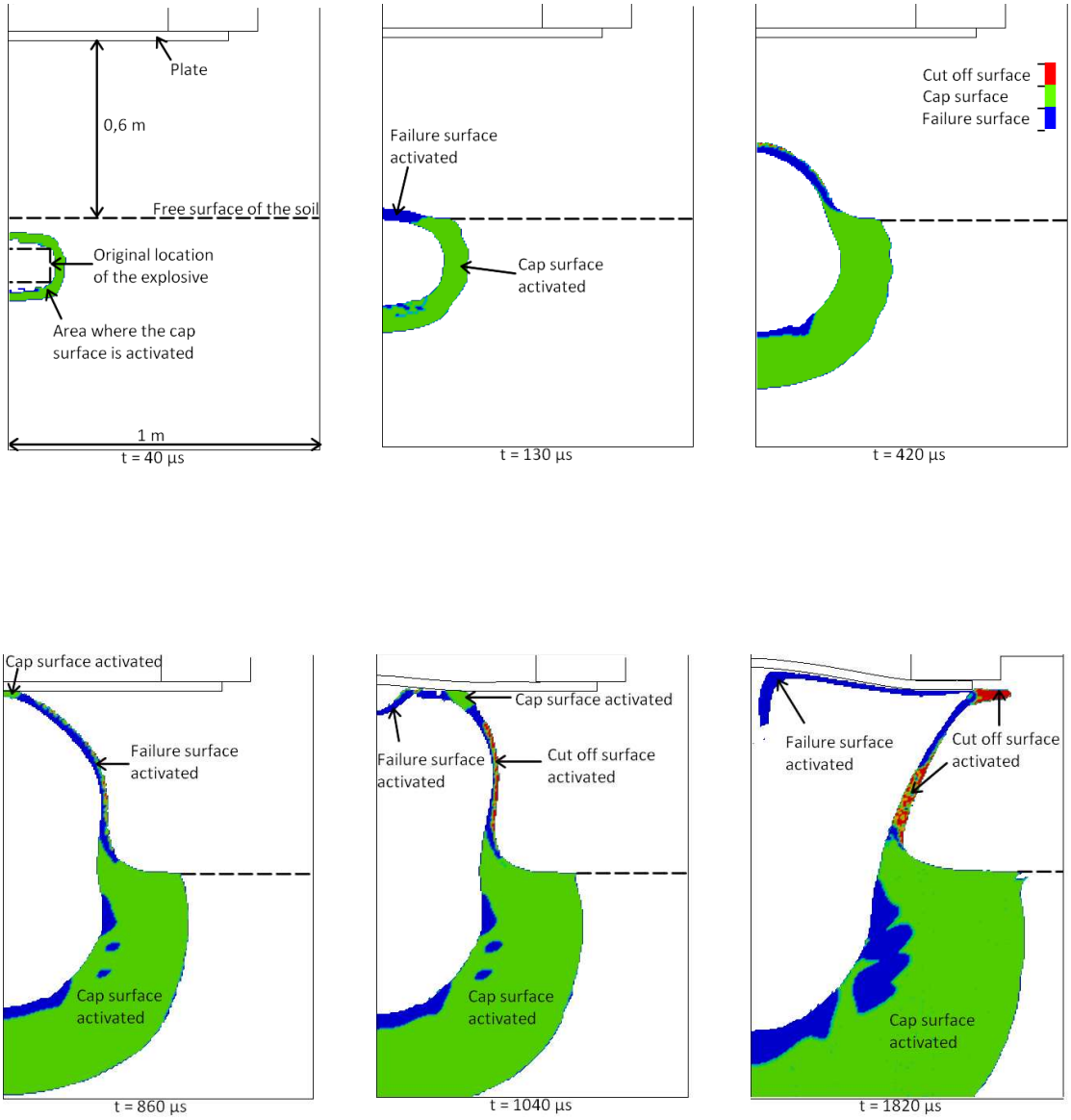

Figure 6.29: Isocontours of the three regions of the yield surface of the soil. At first, since the stresses are very large, the soil undergoes a large compression and the cap surface is activated in the soil all around the explosive. In the soil above the explosive, the failure surface is activated once the shock wave is passed in the air. When the soil hits the plate, the soil undergoes compression again and the cap surface is thus activated. Some tension is also output because of the extension of the soil bubble.

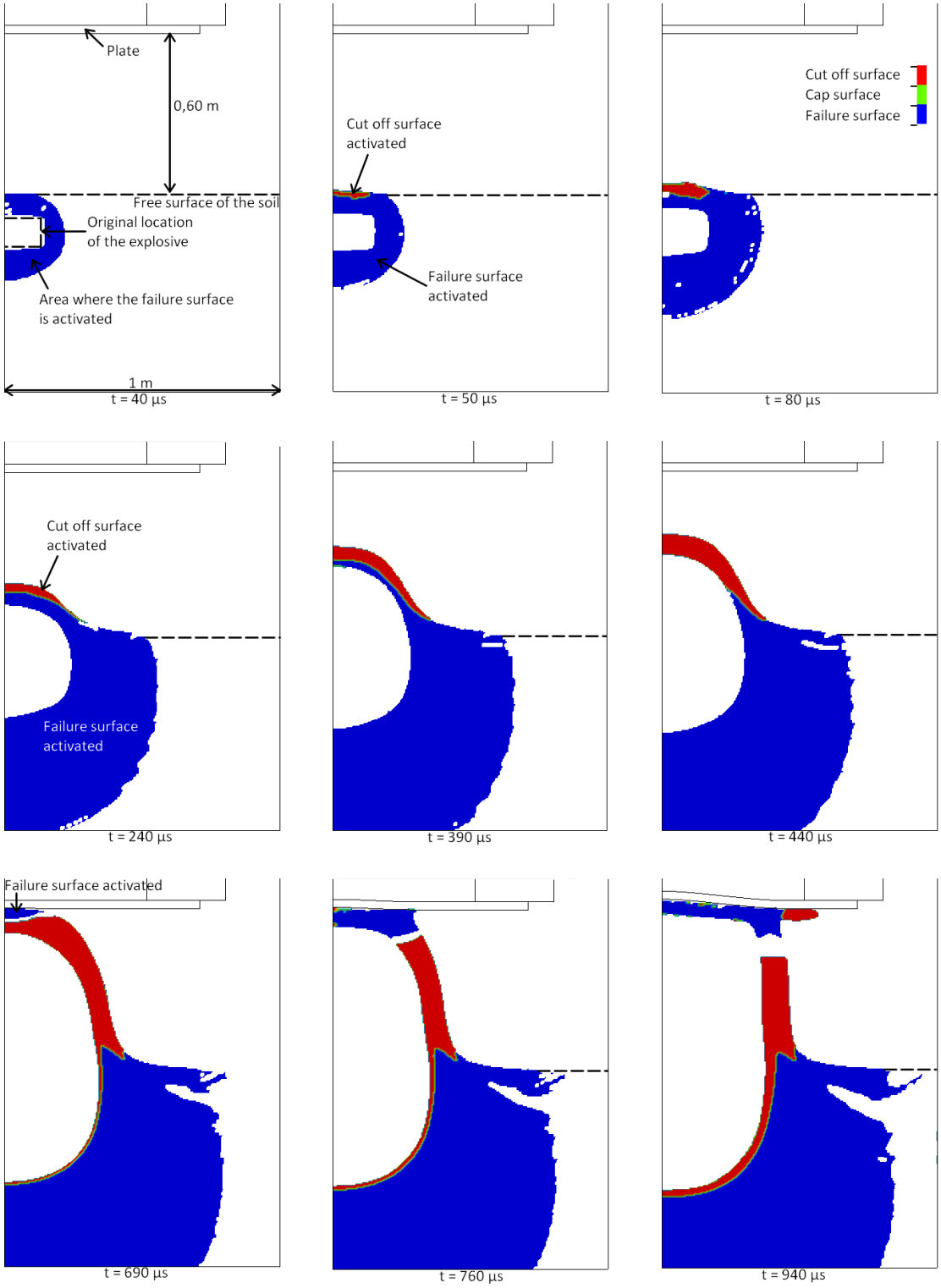

Figure 6.30: Isocontours of the three regions of the yield surface of the soil in the case where the cap surface is far ($X_0 = 100\,\text{GPa}$). Since the cap surface cannot be activated, the failure surface is first activated instead. When the shock wave is reflected on the free surface, a tensile wave propagates and the cut off surface is activated. As the soil moves upward, the area of the tensile stresses increases. When the soil hits the plate, since the cap surface is too far and cannot be activated, the failure surface is activated again. As the soil bubble widens, tensile stresses appear again.

6.4.7.1 Influence of the parameters of the failure surface on impulse

In experiments, we noticed in section 6.4.4.1 that the degree of saturation of the soil plays an important role on the impulse. As a matter of fact, as the water content increases, water plays a more and more important role.

Therefore as the degree of saturation increases, the yield surface of the soil can tend to the yield surface of water. The yield surface of the saturated soil would therefore be very close to the hydrostatic axis, and the cap surface would be pushed back to the infinity. For our viscoplastic model, it means that the initial shear stress α would decrease a lot, whereas the initial failure slope θ would tend to 0 and the initial cap position X_0 would be very large.

To study the influence of the size of the failure surface (in particular along the deviatoric axis $\sqrt{J_2}$), let us consider two values for the initial cap position X_0: 200 MPa (implying that the cap surface is activated at least during the first interaction between the explosive and the soil, when the shock wave enters the soil), and 100 GPa (implying that the cap surface is far enough not to be activated).

Various values of α have been tested. Figure 6.31 shows the variation of impulse as a function of α.

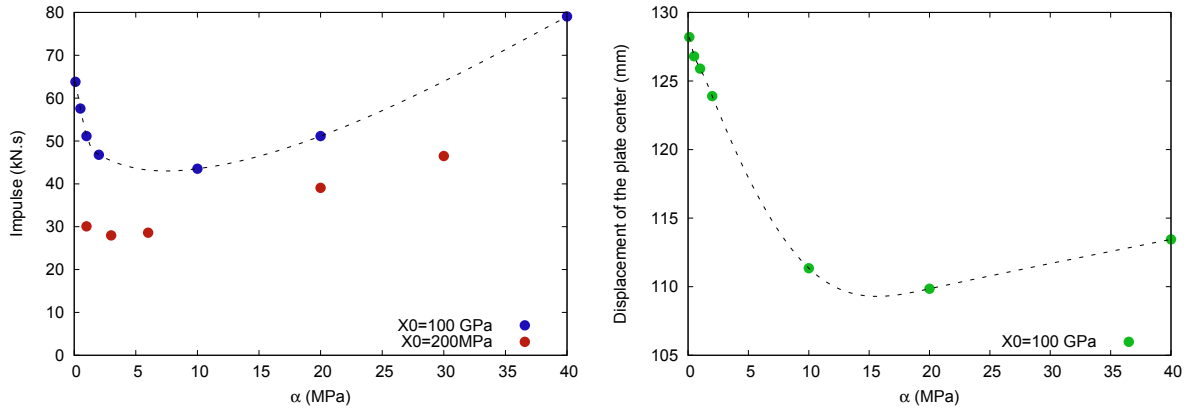

Figure 6.31: Influence of the initial shear stress α on impulse (left) for two values of X_0 and on the displacement of the place center (right) for $X_0 = 100$ GPa.

As shown in figure 6.31, the evolution of the impulse is not monotonic. As α tends to 0, the impulse increases, because the behavior of the soil tends to a behavior of a fluid. At variance, when the value of α becomes large enough, more elasticity is produced. So less energy of the detonation is spent in plasticity which can explain larger values of impulse. The displacement of the plate center also provides a non monotonic curve: as α tends to 0, the displacement largely increases. The displacement increases again as the yield surface becomes very large.

These simulations have been run with the parameter θ equal to 0. In fact, as θ decreases and tends to 0, the impulse increases, as shown in figure 6.32.

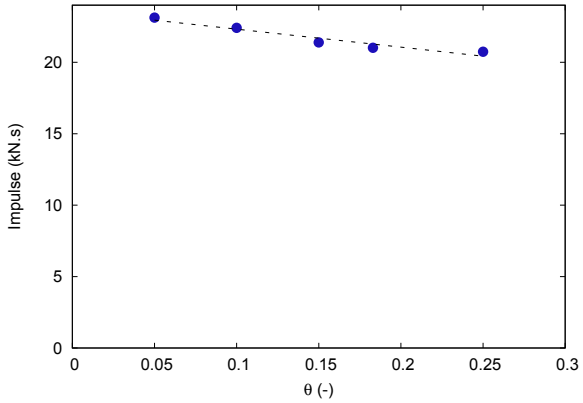

Figure 6.32: Influence of the value of θ on impulse. The slope θ and the friction angle ϕ are related in the following way: $\theta = (2/\sqrt{3}) \times \sin\phi/(3 - \sin\phi)$ or in inverse form $\sin\phi = 3\sqrt{3}\theta/(2 + \sqrt{3}\theta)$

6.4.7.2 Influence of the initial cap position X_0

As noticed in figure 6.29, if the initial cap position X_0 is small enough, the cap surface is activated. As the value of X_0 increases, the stresses are elastic for a longer period of time before becoming viscoplastic. Various values of X_0 have been tested, considering the parameter α equal to 1 MPa. Figure 6.33 presents the impulse obtained.

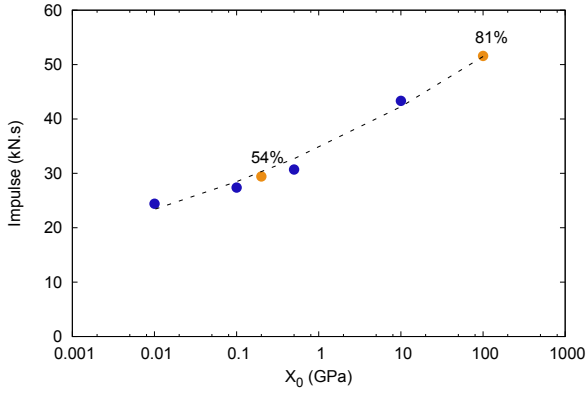

Figure 6.33: Influence of the initial value of the cap limit X_0 on impulse. For X_0=200 MPa and 100 GPa, the impulses are very close to those obtained in experiments for shots 6 and 4 respectively. The only difference between these two shots was the degree of saturation of the soil. For shot 4, it was equal to 81% whereas it was equal to 54% for shot 6. If all the other parameters are fixed, the initial value of the cap X_0 can be linked to the degree of saturation of the soil.

When the cap surface is initially pushed away (so as the value of X_0 is large), the resulting impulse is larger since the stresses are elastic for a longer time in particular during the initial compression at the interaction between the soil and the explosive. Less energy is thus spent in plasticity leading to larger impulses.

Since the increase of impulse is very large compared to the variation of impulse obtained with the modification of other parameters, it seems that the initial soil compression is the period during which the largest energy of the explosive is spent.

Moreover, with $X_0 = 200\,\text{MPa}$ and $100\,\text{GPa}$, we obtained impulses in simulation close to the experimental results for shots 6 and 4. The degrees of saturation of these shots were equal to 54 and 81% respectively. Therefore, if we consider that all the other parameters of the model are given, the parameter X_0 could be linked to the degree of saturation of the soil. However, we only have two similar experiments. So we cannot cross check the impulses obtained with the other values of X_0 of the curve with experiments.

Grujicic et al. (2009) proposed a dependence of each parameter of the model of Tong and Tuan (2007) on the degree of saturation. In the same way, these two points of simulation correlated with experiments can be used to define a dependence of X_0 with respect to the degree of saturation, such as $X_0(S_r) = 10^{10\,S_r+3}$. For a dry soil, $S_r = 0$ and $X_0(S_r = 0) = 1\,\text{kPa}$ which means that the yield surface would be very small. At variance, for a saturated soil, $S_r = 1$ and $X_0(S_r = 1) = 100000\,\text{GPa}$. In this case, the cap would be so far that it would be equivalent to a yield surface without a cap, as suggested by Fox et al. (2014).

6.4.7.3 Influence of the density and the elastic moduli

To complete the test of the main parameters, here the influence of the initial soil density and the elastic moduli is studied.

When the elastic moduli (the bulk modulus K and the shear modulus G) are larger while keeping the Poisson's ratio constant, the resulting impulse increases modeslty.

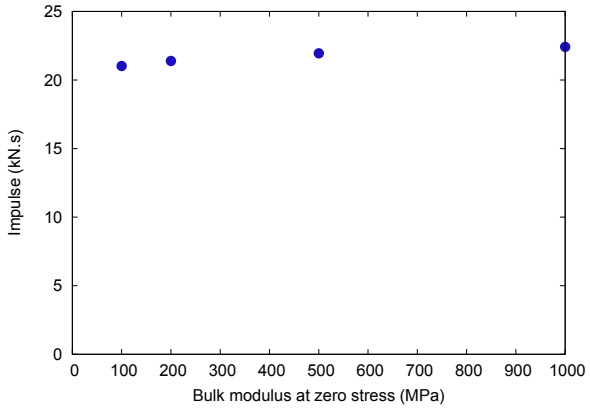

Figure 6.34: Influence of the the bulk modulus at zero stress on impulse. A slight increase of impulse is obtained as the bulk modulus is larger.

As for the density, as it increases, the mass of the soil which hits the test rig is larger. So this heavier soil drives the test rig upwards quicker. As shown in figure 6.35, even if the impulse increases with density, the influence of this parameter is little.

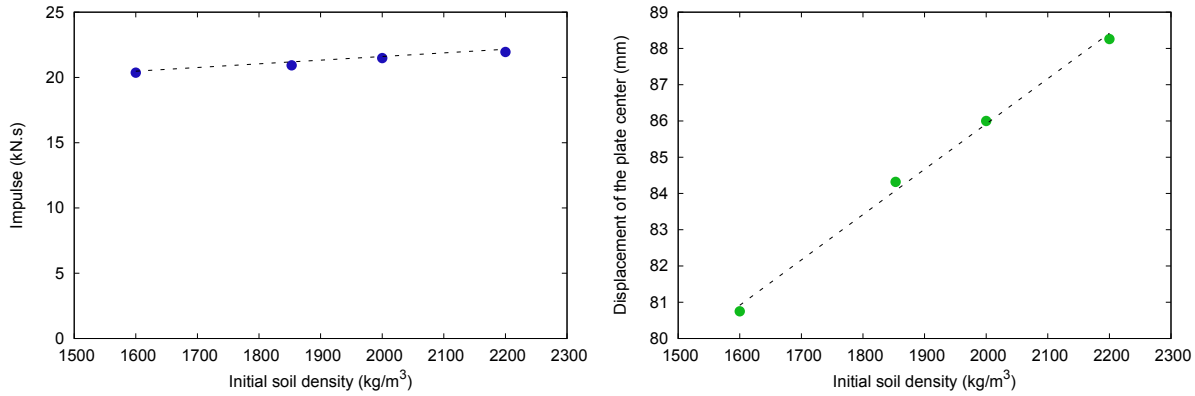

Figure 6.35: Influence of the initial density of the soil on impulse (left) and on the displacement of the plate center (right).

6.4.7.4 Summary of the influence of the main parameters of the model

In the above sections, we studied the influence of various parameters of our model on the impulse. As they all influence the impulse, their roles do not have the same weight.

Given the possible densities which can be taken by the soil, the variation of the impulse is small. This is also the case of the elastic moduli: the variation of the impulse is little for reasonable values of elastic moduli.

The two parameters which have the largest influence on the impulse of the test rig are the initial shear stress α and the initial cap position X_0 which means that the size of the yield surface plays the largest role. The failure slope θ also influences the impulse but much less compared to the two previous parameters.

In fact, the dimensions of the yield surface and in particular the value of the initial cap position X_0 can be linked to the degree of saturation of the soil. We validated two points of the curve for one configuration of shots with two degrees of saturation. One relation between the initial cap position X_0 and the degree of saturation S_r was proposed so that the model can apply to any degree of saturation.

Outlook and perspectives

The aim of this work was to obtain a soil model to correlate simulations with experiments of buried mine detonations. STANAG soil defined in AEP 55 relative to STANAG 4569 was used. In this NATO document, soil is saturated. But a model of soil reliable with any water content was of interest.

We developed a viscoplastic cap model for soils subjected to explosions. In order that the soil resists the detonation, the elastic moduli increased with stresses thanks to a stiffening curve. This curve also allowed to account for the water content of the soil. The bulk modulus at zero stress was calculated in relation to the initial void ratio while the bulk modulus of the grain-water mixture depended on the bulk moduli of water and grains weighted by their volume fractions.

We first validated our model with experiments performed at DGA TT involving small quantity of explosive buried at three various depths in STANAG soil. However, the difference of water content between each shot was little. The soil was never completely dry. As a result even if the simulations fitted the experiments, the influence of water content on pressure could not be highlighted in the experiments and in the simulations.

A second experimental campaign allowed to evaluate the influence of water content, and more specifically of the degree of saturation. In these experiments, the impulse transmitted by the detonation of several kilograms of buried TNT explosive to a test rig, and the deformation of a plate standing for a vehicle floor were measured. The impulse and the deformation of the plate increased with the degree of saturation. Numerical simulations were then run to evaluate the influence of the parameters of our viscoplastic model on impulse. The size of the yield surface, in particular the initial cap position X_0 and the initial shear stress played the largest role. In fact, a relation between the degree of saturation and the parameter X_0 was proposed so that the size of the yield surface evolved with the initial water content of the soil. In this way, the soil model could reproduce the experiments for any degree of saturation.

The following points deserve further research:

1. A stiffening curve was added to our viscoplastic cap model so that the soil resisted the detonation. The curve was taken from the experiments of Zakrisson et al. (2012). The maximum stresses involved in these curves were little since the experiments were carried out up to 1 GPa. However the soil has to sustain several gigapascals close to the detonation. Therefore to improve the stiffening curve of the model, similar laboratory experiments should be carried out with larger stresses.

This would require to develop a dedicated device. STANAG soil is very heterogeneous and contains particles with large grain sizes (up to 40 mm). In order to be representative of STANAG soil, the sample should be large enough.

2. The water content was accounted for in various parameters of our viscoplastic model (in the density, the bulk modulus at zero stress, the bulk modulus of the solid-grain mixture, the initial cap position). As a matter of fact, the soil was considered from the point of view of a single phase solid. At variance, it could be modeled as a porous medium. During a detonation, the water is trapped in the soil. Thus the pore water plays a large role since the explosion is an undrained phenomenon. The stress path in a porous medium is totally different from a stress path in a single phase solid.

3. When reproducing large scale experiments, we noticed that plasticity contributed to dissipate energy and that the definition of the size of the yield surface in particular in the first moment after the detonation was crucial to get the right impulse. An energetic study would be interesting to evaluate the different origins of energy dissipation and their respective weights. One source of energy dissipation could be linked to grain fracture. The shape and the size of the grains could change because of the detonation.

4. A damage law could be added to the soil model. The bulk modulus of grain water mixture K_{wg} could be modified considering that once the shock wave has crossed the soil medium, solid grains do not have the same stiffness anymore. The slope of the stiffening curve could also be changed. However this latter modification would require laboratory tests to validate the modifications of the curve.

Bibliography

[1] Abu Sayeed M., Suzuki K., Rahman M. M. Strength and deformation characteristics of granular materials under extremely low to high confining pressures in triaxial compression. *International Journal of Civil and Environmental Engineering*, **11**(4), 2011.

[2] AEP 55, *Procedures for evaluating the protection level of logistic and light armoured vehicles*, Volume 2, Edition C, Version 1, (NATO, 2014).

[3] Ambrosini R. D., Luccioni B., Danesi R., Riera J., Rocha M. Size of Craters Produced by Explosive Charges on or Above the Ground Surface. *Shock Waves*, **12**(1):69-78, 2002.

[4] Ambrosini R. D., Luccioni B., Danesi R. Influence of the soil properties on craters produced by explosions on the soil surface. *Mecanica Computacional*, **23**:571-590, 2004.

[5] An J. *Soil behavior under blast loading*. PhD thesis, University of Nebraska, USA, 2010.

[6] An J., Tuan C. Y., Cheeseman B. A., Gazonas G. A. Simulation of Soil Behavior Under Blast Loading. *International Journal of Geomechanics*, **11**(4):323-334, 2011.

[7] Anderson C. E., Behner T., Weiss C. E. Mine blast loading experiments. *International Journal of Impact Engineering*, **38**:697-706, 2011.

[8] Arlery M., Gardou M., Fleureau J. M., Mariotti C. Dynamic behaviour of dry and water-saturated sand under planar shock conditions. *International Journal of Impact Engineering*, **37**:1-10, 2010.

[9] Assaf Z., Ran E., Golan G., Drori O., Katalan I. K. The influence of soil conditions on the blast intensity for sand, clayey sand and gravel with silt. In *28th International Symposium on Ballistics*, 1623-1633, 2014.

[10] Baker W. E. *Explosions in the air*, University of Texas, Austin, USA, 1973.

[11] Baker W. E., Westine P. S., Dodge F. T. *Similarity methods in engineering dynamics*. Elservier, Amsterdam, The Netherlands, 1991.

[12] Bangash M. Y. H. *Impact and explosion, Analysis and Design*. CRC Press, Boca Raton, Florida, USA, 1993.

[13] Bardet J. P. *Experimental Soil Mechanics*. Prentice Hall, New Jersey, USA, 1997.

[14] Barsotti M. A., Puryear J. M. H., Stevens D. J., Alberson R. M., McMahon P. Modeling mine blast with SPH. In *12th International LS DYNA Users Conference*, 2012.

[15] Bergeron D., Walker R., Coffey C. *Detonation of 100-Gram Anti-Personnel Mine Surrogate Charges in Sand, A Test Case for Computer Code Validation*. Report of Defense Research Establishment Suffield, Canada, 1998.

[16] Bergeron D. M., Tremblay J. E. Canadian research to characterise mine blast output. In *16th International Symposium on the Military Aspects of Blast and Shock*, 501-511, 2000.

[17] Bowles J. E. *Foundation analysis and design*. 4th edition, McGraw-Hill, New York, USA, 1988.

[18] Bragov A. M., Lomunov A. K., Sergeichev I. V., Tsembelis K., Proud W. G. Determination of physicomechanical properties of soft soils from medium to high strain rates. *International Journal of Impact Engineering*, **35**:967-976, 2008.

[19] Brown J. L., Vogler T. J., Chhabildas L. C., Reinhart W. D., Tornhill T. F. *Shock Response of Dry Sand*. SANDIA Report, SAND2007-3524, Sand Dynamics and Energetic Materials Department, USA, 2007.

[20] Bues R., Hlady S. L., Bergeron D. M. *Pendulum measurement of land mine blast output, Volume 1: Theory and implementation*. Report of Defence Research Establishment Suffield, Canada, 2001.

[21] Bull J. W., Woodford C. H. Camouflets and their effects on runway supports. *Computer and Structures*, **69**(6):695-706, 1998.

[22] Buxton R. *The effects of porous sea bottoms on the propagation of underwater shock waves using the $P-\alpha$ equation of state.* Thesis report, Pennsylvania State University, USA, 2009.

[23] Carroll M. M., Holt A. C. Static and dynamic pore collapse relations for ductile porous materials. *Journal of applied physics*, **43**:1626-1636, 1972.

[24] Cernica J. N. *Geotechnical engineering, Soil mechanics*. John Wiley & Sons, New York, USA, 1995.

[25] Chapman D. J., Tsembelis K., Proud W.G. The Behaviour of Water Saturated Sand under Shock-loading. In *Proceedings of the Society for Experimental Mechanics (SEM) Annual Conference And Exposition on Experimental and Applied Mechanics*, Paper 400, 2006.

[26] Converse F. J. Foundations subjected to dynamic forces, Chapter 8 of *Foundation Engineering*. McGraw-Hill, New York, USA, 1962.

[27] Curran D. R., Seaman L., Shockey D. A. Dynamic failure of solids. *Physics Reports (Review Section of Physics Letters)*, **147**(5):253-388, 1987.

[28] Dave T. N., Dasaka S. M. Assessment of portable traveling pluviator to prepare reconstituted sand specimens. *Geomechanics and Engineering*, **4**(2):79-90, 2012.

[29] Dobratz B. M., Crawford P. C. *LLNL Explosives Handbook: Properties of Chemical Explosives and Explosive Simulants*, Report UCRL-5299, Rev. 2 of Lawrence Livermore National Laboratory, University of California, 1985.

[30] Drake J. L., Little C. D. Ground shock from penetrating conventional weapons. In *On the interaction of non-nuclear munitions with structures*, Colorado Springs, Colorado, USA, 1983.

[31] Duvaut G., Lions J. L. *Les Inéquations en Mécanique et en Physique*, Dunod, Paris, France, 1972.

[32] Felice C. W. *The response of soil to impulse loads using the Split-Hopkinson Pressure Bar technique*. Report of Air Force Weapons Laboratory, Air Force Systems Command Kirtland Air Force Base, NM, USA, 1986.

[33] Felice C. W., Brown J. A., Gaffney E. S., Olsen J. M. An investigation into the high strain-rate behavior of compacted sand using the split-Hopkinson pressure bar technique. In *Proceedings of the Second Symposium on the Interaction of Non-Nuclear Munitions with Structures*, 391-396, 1987.

[34] Field J. E., Walley S. M., Bourne N. K., Huntley J. M. Experimental methods at high rates of strain. *Journal de Physique IV. Colloque C8, supplément au Journal de Physique III*, **4**, 1994.

[35] Field J. E., Walley S. M., Proud W. G., Goldrein H. T., Siviour C. R. Review of experimental techniques for high rate deformation and shock studies. I*nternational Journal of Impact Engineering*, **30**:725-775, 2004.

[36] Fiserova, D. *Numerical analyses of buried mine explosions with emphasis on effect of soil properties on loading*. PhD thesis, Cranfield University, UK, 2006.

[37] Fourney W. L., Leiste H. U., Hauch A., Jung D. Distribution of Specific Impulse on Vehicles Subjected to IED's. In *Proceedings of the IMPLAST 2010 Conference*, 2010.

[38] Fox D. M., Lee J. S. The influence of water, dry sand, and unsaturated sand constitutive behavior on the blast response of a rigid target. *International Journal of Impact Engineering*, **65**:163-173, 2014.

[39] Fung Y. C. *A first course in continuum mechanics*. Second Edition, Prentice Hall, New Jersey, USA, 1977.

[40] Gailly B. (1996). *Etude du comportement dynamique et de la rupture de trois aciers à blindage*. PhD Thesis, Ecole Nationale des Mines de Paris, France, 1996.

[41] Grujicic M., He T., Pandurangan B., Bell W. C. Development, parameterization, and validation of a visco-plastic material models for sand with different levels of water saturation. *Journal of Materials: Design and Applications*, **223**:63-81, 2009.

[42] Hallam M. G., Heaf N. J., Wootton L. R. *Dynamic of marine structures*. Report UR 8, 2nd edition, CIRIA Underwater Engineering Group, 1978.

[43] Henrych J. *The dynamics of explosion and its use*, Chapter 5, Elsevier, New York, USA, 1979.

[44] Herrmann W. Constitutive equation for the dynamic compaction of ductive porous materials. *Journal of applied physics*, **40**:2490-2499, 1969.

[45] Hlady S. L. Effect of soil parameters on land mine blast. In *18th Military Aspects of Blast and Shock*, 2004.

[46] Hunt R. E. *Geotechnical engineering techniques and practices*. McGraw-Hill, New York, USA, 1986.

[47] Jackson J. G., Ehrgott J. Q., Rohani, B. *Loading rate effects on compressibility of sand*. Final Report of Structures Laboratory, US Army Engineer Waterways Experiment Station, MS, USA, 1980.

[48] Johnson G. R., Cook W. H. A constitutive model and data for metals subjected to large strains, high strain rates and high temperatures. In *Proceedings of the 7th International Symposium on Ballistics*, 541-547, 1983.

[49] Kalinski M. E. *Soil mechanics lab manual*. Second edition, John Wiley and Sons, Inc. USA, 2011.

[50] Kim D., Ha S. Effects of particle size on the shear behavior of coarse grained soils reinforced with geogrid. *Materials*, **7**:963-979, 2014.

[51] Kolsky H. An investigation of mechanical properties of materials at very high rates of loading. In *Proceedings of the Physical Society*, 676-700, 1949.

[52] Laine L., Sandvik A. Derivation of mechanical properties for sand. In *Proceedings of the 4th Asia-Pacific Conference on shock and impact loads on structures*, 361-368, 2001.

[53] Livermore Software Technology Corporation (LSTC), *LS-Dyna theoretical manual*, Livermore, California, 2014.

[54] Luccioni B. M., Ambrosini R. D. Craters produced by underground explosions. *Mecánica Computacional*, **25**:1603-1614, 2006.

[55] Lun A. C. Y. *Influence of grain size distribution on shear strength of sand*. Bachelor thesis, Universiti teknologi Malaysia, 2011.

[56] Martin B. E., Chen W., Song B., Akers S. A. Moisture effects on the high strain-rate behavior of sand. *Mechanics of Materials*, **41**:786-798, 2009.

[57] Materials Sciences Corporation. *Methodology for improved characterization of land mine explosions*, Presentation at the Technical Interchange Meeting SBIR Phase II Plus Program, Contract DAAD17-01-C-0111, Horsham, PA, USA, 2006.

[58] Meyers M. A. Dynamic Behavior of Materials, John Wiley & Sons, New York, USA, 1994.

[59] Niroumand H., Kassim K. A. Analytical and numerical study on explosion into/on cohesion less soils. *European Journal of Scientific Research*, **46**(4):554-562, 2010.

[60] Peles S., Touati D., Azulay I., Neuberger A. Numerical simulation of mine detonation beneath a generalized add-on armor structure. In *Proceedings 24th International Symposium of Ballistics, volume 1*, 439-447, 2008.

[61] Perzyna P. Fundamental problems in viscoplasticity. *Advances in applied mechanics*, **9**(2):244-368, 1966.

[62] Ramasany et al. In-vehicle extremity injuries from improvised explosive devices: current and future foci. *Philosophical transactions of the Royal society. Biological sciences*, **366**:160-170, 2011.

[63] Riedel W., Wicklein M., Thoma K. Shock properties of conventional and high strength concrete: Experimental and mesomechanical analysis. *International Journal of Impact Engineering*, **35**:155-171, 2008.

[64] Ross C. A., Thompson P. Y., Charlie W. A., Doehring D. O. Transmission of Pressure Waves In Partially Saturated Soils. *Experimental Mechanics*, **29**(1):80-83, 1989.

[65] Salot C. *Modélisation du comportement mécanique d'un matériau granulaire composite par la méthode des éléments discrets*. PhD thesis, University of Grenoble, France, 2007.

[66] Simo J. C., Hughes T. J. R. *Computational inelasticity*, Springer-Verlag, New York, USA, 1998.

[67] Skaggs R. R., Watson J., Adkins T., Gault W., Canami A., Gupta A. D. *Blast loading measurements by the vertical impulse measurement fixture (VIMF)*. Army Research Laboratory Report ARL-TR-3383. Aberdeen Proving Ground, MD, USA, 2004.

[68] Song B., Chen W., Luk V. Impact compressive response of dry sand. *Mechanics of Materials*, **41**:777-785, 2009.

[69] Steinberg D. J. *Equation of state and strength properties of selected materials*. Report of Lawrence Livermore National Laboratory, California, USA, 1996.

[70] Swensen D. A., Denison M. K., Guilkey J., Harman T., Goetz R. *A software framework for blast event simulation*. Report of Reaction Engineering International, Salt Lake City. USA, 2006.

[71] Tasneem N. *Study of wave shaping techniques of Split Hopkinson Pressure Bar using finite element analysis*. Master of Science thesis, Wichita State University, Kansas, USA, 2005.

[72] Thompson D., Luke E., Newman J. C. III, Janus J. M., Blades E., Tong X., Moore C. *Development of a strategy for simulating blast-vehicle interactions*. Report of US Army RDECOM-TARDEC, MI, USA, 2010.

[73] Tong X., Tuan C. Y. Viscoplastic cap model for soils under high strain rate loading. *Journal of Geotechnical and Geoenvironmental Engineering*, **133**(2):206-214, 2007.

[74] Wang J. *Simulation of landmine explosion using LS Dyna 3D software: benchmark work of simulation of explosion in soil and air*. Report of Defence Science and Technology Organisation (DSTO), DSTO-TR-1168, Weapons Systems Division, Aeronautical and Maritime Research Laboratory, Australia, 2001.

[75] Wang Z., Hao H., Lu Y. A three-phase soil model for simulating stress wave propagation due to blast loading. *International Journal for numerical and analytical methods in geomechanics*, **28**:33-56, 2004.

[76] Wardlaw A. B., McKeown R., Chen H. *Implementation and application of the $P - \alpha$ equation of state in the DYSMAS code*. Report NSWCDD/TR-95/107 of Naval Surface Warfare, USA, 1996.

[77] Westine P. S., Morris B. L., Cox P. A., Polch E. Z. *Development of computer program for floot plate response from land mine explosions*. Technical report 13045 of US Army Tank-Automotive Command, Warren, Michigan, USA, 1985.

[78] Wilkins M. L. *Calculations of elastic plastic flow*, University of California, Lawrence Radiation Laboratory, Livermore, California, USA, 1963.

[79] Williams K., Poon K. *A numerical analysis of the effect of surrogate anti-tank mine blasts on the M113*. Report of Defence Research Establishment, Canada, 2000.

[80] Wünnemann K., Collins G. S., Melosh H. J. A strain-based porosity model for use in hydrocode simulations of impacts and implications for transient crater growth in porous targets. *Icarus*, **180**:514-527, 2006.

[81] Zakrisson B., Häggblad H-Å, Jonsén P. Modelling and simulation of explosions in soil interacting with deformable structures. *Central European Journal of Engineering*, **2**(4):532-550, 2012.

Abstract: In recent conflicts, vehicles have been facing underbelly attacks involving a large quantity of buried explosive. A part of the energy is absorbed by the deformation of the belly. Still the vehicle is subjected to the impulse transmitted by the detonation which may severely injure occupants. The intensity of the impulse is highly dependent on three main parameters which are the degree of saturation of the soil, the nature of the soil in which the explosive is buried and the depth of burial of the charge. Computer simulations should follow the complete process of the explosion, including the early interaction of the charge with the soil, the expansion of the detonation products, the propagation of the shock wave up to the vehicle floor, and the large deformation of the soil projections. The mechanical information transmitted up to the floor level should be sufficiently accurate because the impact on the vehicle is the key target of the simulations. Developing a constitutive soil model is therefore a challenging task.
The soil model is visco-plastic with a hardening cap surface, a failure surface to limit shear stresses and a cut off surface against excessive tension. The entire yield surface is smooth so that the plastic strain increments are continuous. A stiffening mechanism is introduced to account for air compression and accommodate the huge stresses in the immediate neighborhood of the charge. The water content of the soil is also taken into account.
Two sets of experiments were carried out at DGA TT to serve as a reference for computer simulations. A first campaign involved small quantity of explosive at several depths of burial. The aerial pressures were measured at various heights and compared to simulations. The second set of experiments used a test rig to measure both the deformation of a floor simulating plate and the impulse transmitted by the buried explosion. A range of soil water contents, depths of burial of the explosive, plate thicknesses and stand off distances has been explored. For all the experiments, the sandy gravel STANAG soil defined in AEP 55 of STANAG 4569 has been used.
Eulerian simulations were run and fit with these experiments. The roles of the three parts of the yield surface, of the elastic stiffening and plastic hardening mechanisms could be assessed. The initial soil density and the initial cap position were found to have the largest influence on aerial pressures. As for the impulse transmitted to the metallic plate, it was observed to be mostly controlled by the degree of saturation of the soil.

Keywords: Buried mines, partially saturated soils, finite elements, impulse, viscoplastic cap surface

Résumé: Au cours des conflits récents, les véhicules ont été sujet à des attaques impliquant une grande quantité d'explosif enterré. En général, les planchers sont visés, et leurs déformations absorbent une partie de l'énergie. Le véhicule subit également une impulsion, transmise par la détonation, qui peut blesser gravement les occupants. L'intensité de l'impulsion dépend principalement de trois paramètres: le degré de saturation du sol, la nature du sol dans lequel l'explosif est enterré, et la profondeur d'enfouissement de la charge.
Les simulations numériques doivent reproduire le processus intégral de l'explosion, incluant l'initiale interaction entre la charge et le sol, l'expansion des produits de détonation, la propagation de l'onde de choc jusqu'au plancher du véhicule, et la grande déformation des projections de sol. L'information mécanique transmise jusqu'au niveau du plancher doit être suffisamment précise car les effets sur le véhicule constituent l'objectif des simulations. Développer un modèle constitutif de sol est par conséquent délicat.
Le modèle de sol est visco-plastique avec un cap écrouissable, une surface de rupture pour limiter les contraintes de cisaillement et un cut off contre les contraintes excessives de tension. La surface de charge est entièrement lisse afin que les incréments de déformation plastique soient continus. Un mécanisme de rigidification est présenté pour tenir compte de la compression de l'air et des très grandes contraintes dans l'environnement immédiat de la charge. Le taux d'humidité du sol est également pris en compte.
Deux séries d'essais ont été réalisés à DGA TT pour servir de référence pour les simulations numériques. Une première campagne a mis en jeu de petites quantités d'explosif à plusieurs profondeurs d'enfouissement. Les pressions aériennes ont été mesurées à plusieurs hauteurs et comparées aux simulations. Un moyen d'essai a été utilisé lors de la seconde campagne d'essais pour mesurer à la fois la déformation d'une plaque représentant un plancher de véhicule, mais aussi l'impulsion transmise par l'explosion enfouie. Un certain nombre de taux d'humidité, profondeurs d'enfouissement, épaisseurs de plaques et gardes au sol a été étudié. Au cours des essais, le sol STANAG, composé de sable et de graviers, défini dans l'AEP 55 relatif au STANAG 4569, a été utilisé.
Des simulations Eulériennes ont été réalisées et sont en accord avec les résultats d'essais. Le rôle des trois parties de la surface de charge, des mécanismes de rigidification élastique et d'écrouissage plastique a été évalué. La masse volumique initiale du sol et la position initiale du cap sont les paramètres ayant la plus grande influence sur les pressions aériennes. Quant à l'impulsion, elle est principalement contrôlée par le degré de saturation du sol.

Mots clés: Mines enfouies, sols partiellement saturés, éléments finis, impulsion, surface de charge viscoplastique